

AD-A034 088

XONICS INC SANTA MONICA CALIF

THEORETICAL STUDIES OF HIGH-POWER ULTRAVIOLET AND INFRARED MATE--ETC(U)

JUN 76 M SPARKS, C J DUTHLER

F/G 20/6

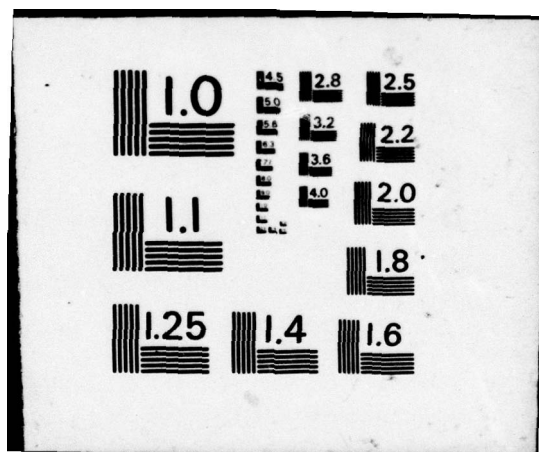
DAHC15-73-C-0127
NL

UNCLASSIFIED

1 of 3
ADA034088

REF ID: A6212





MDA034088

Unclassified

SECURITY CLASSIFICATION OF THIS PAGE (When Data Entered)

REPORT DOCUMENTATION PAGE		READ INSTRUCTIONS BEFORE COMPLETING FORM
<p>9. Technical rept. no. 7, 1 Jan - 30 Jun 76</p> <p>10. THEORETICAL STUDIES OF HIGH-POWER ULTRAVIOLET AND INFRARED MATERIALS.</p> <p>11. M. Sparks and C. J. Duthler</p>		<p>12. REPORT DATE 30 June 1976</p> <p>13. NUMBER OF PAGES 230 (231 p.)</p> <p>14. SECURITY CLASS. (for this report) Unclassified</p>
<p>15. PERFORMING ORGANIZATION NAME AND ADDRESS Xonics, Incorporated 1333 Ocean Avenue Santa Monica, California 90401</p> <p>16. CONTROLLING OFFICE NAME AND ADDRESS Defense Supply Service Room 1D245 - The Pentagon Washington, D. C. 20310</p> <p>17. MONITORING AGENCY NAME & ADDRESS (if different from Controlling Office) Defense Advanced Research Projects Agency 1400 Wilson Boulevard Arlington, Virginia 22209</p>		<p>18. PROGRAM ELEMENT, PROJECT, TASK AREA & WORK UNIT NUMBERS DAHC15-73-C-0127</p> <p>19. DISTRIBUTION STATEMENT (of this Report) This document may be further distributed only with specific prior approval of the Defense Supply Service, Washington, D. C.</p> <p>20. DISTRIBUTION STATEMENT (of the abstract entered in Block 20, if different from Report) 'A'</p> <p>21. SUPPLEMENTARY NOTES</p>
<p>22. KEY WORDS (Continue on reverse side if necessary and identify by block number) adsorption, alkali halides, band gap, band structure, coating, density of states, dielectric, dielectric constant, dielectric reflectors, electron-avalanche breakdown, high-power optics, impurities, infrared, laser, lithium fluoride, localized states, materials, multi-phonon, optical coating, optical properties, overlap integrals, phonons, polyethane, polymers, reflectors, Slater orbitals, spectra, surface states, theory, thin-film, tight binding,</p> <p>23. ABSTRACT (Continue on reverse side if necessary and identify by block number) (1) The thin-film-improvement methods suggested in the previous technical report, which is briefly summarized here in conference-publication form, could result in greatly improved reflectors for wavelengths from $\sim 10 \mu\text{m}$ to $\sim 120 \text{ nm}$. (2) Recently measured values of the optical absorption coefficient $\beta = 3-7 \text{ cm}^{-1}$ at $10.6 \mu\text{m}$ now show that the absorptance A can be less than the current desired value of 10^{-4} for very thin ($\sim 100 \text{ nm}$) polymer films. Such thin films possibly could afford protection against adsorption of, and attack by, water and other contaminants. The discrepancy between high measured moisture penetration through unsupported pin-hole-free films and such observations as the</p>		

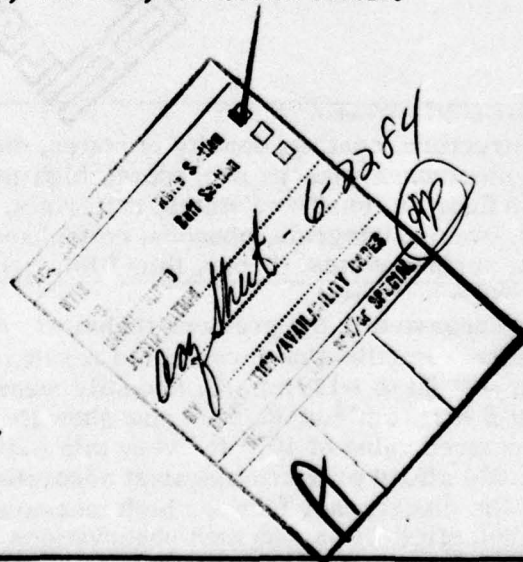
Unclassified

SECURITY CLASSIFICATION OF THIS PAGE(When Data Entered)

protection of CsI for one month at 89 percent RH by a deposited polymer film may be explained as follows: Polymer coatings produced by plasma polymerization are known to nucleate growth at high-energy surface sites which are also the attack sites for water. The reactive plasma species act in a scrubbing reaction to remove the impurities or reduce the defect energies, then immediately passivate these sites with highly cross-linked or crystalline globules. (3) The calculated width of the valence band agrees well with the experimental value for LiF, but the calculated values are smaller than the experimental values for several other alkali halides. (4) Closed-form expressions are given for the integrals $\int X_a \mathcal{L} X_b d\mathbf{r}$ for $\mathcal{L} = 1$ (overlap), $\mathcal{L} = -\frac{1}{2} v^2$ (kinetic-energy), and $\mathcal{L} = Z/r_a$ (nuclear-Coulomb-attraction) for any Slater-atomic orbitals X having principal quantum numbers from 1 to 6. (5) By using our tight-binding valence-band wave functions and diagonalizing the Hamiltonian matrix for a model 15-layer LiF slab, we find that: The Madelung energy pushes a narrow band of surface states (confined to the surface layer) out of the top of the conduction band. Both bulk and surface-layer densities of states show broader peaks near the top and bottom of the band. The bulk density of states, which is approached rather closely even in the second atomic layer, generally resembles previously calculated densities but has considerably more resolution. (6) The substitution of ions that are larger than the host ions in alkali halides is expected to lead to absorption at frequencies below the band gap since the Madelung energy (a good zeroth-order approximation to the band gap) decreases as the lattice spacing increases. Only parts per million of substitutional ions may give $\beta = 1 \text{ cm}^{-1}$, a typical observed value. The formulation required to obtain quantitative results is developed. (7) In readdressing the problem of electron-avalanche breakdown, the Boltzmann equation is reduced to a practical transport equation by making simple approximations. (8) It is shown that infrared absorption in alkali halides is dominated by processes generating an odd number of optical phonons ($\omega = 3\omega_{\text{op}}, 5\omega_{\text{op}}, \dots$). The results afford a practical, greatly simplified computation scheme and explain recent observations of well-defined peaks in β at $3\omega_{\text{op}}$. The theory avoids two inadequacies of diatomic-molecule approaches (peaks near $n\omega_{\text{op}}$ for all n and gross overestimates of vertex-correction factors).

19. KEY WORDS (Cont'd):

transport equation, two-photon, ultraviolet, vacuum ultraviolet, visible region, water protection, windows, electronic levels.



Unclassified

SECURITY CLASSIFICATION OF THIS PAGE(When Data Entered)

TABLE OF CONTENTS

<u>Section</u>		<u>Page</u>
	Contents of Present and Previous Reports	ix
	Preface	xiii
A	Introduction and Summary	1
B	Polymer Coatings for Protection of Optical Components	15
	I. Introduction	17
	II. Infrared Absorption by Moisture at $10.6 \mu\text{m}$	20
	III. The Alkali Halides	27
	IV. Moisture Protection from Bulk Properties of Polymer Films	34
	V. Surface Interactions Limiting Water Permeability	44
	VI. Polymer Adsorption of Water	58
	VII. Infrared Absorption by Polymers	60
	VIII. Experimental Testing of Polymer Films	71
C	Electronic Properties of the LiF Valence Band, Surface States and the Local Density of States Near the Surface	81
Appendix	Explicit Form of the Hamiltonian for the N Layer LiF Slab	99
D	Localized Electronic States in Alkali Halides Associated with a Substitutional Anion Impurity	102
E	Classical Transport Equation for Electron-Avalanche Breakdown	133
F	Evaluation of Two-Center Integrals of Slater Atomic Orbitals	144
G	Quasiselection Rules for Multiphonon Absorption in Alkali Halides	162
	I. Introduction	163
	II. Absorption Mechanism	166

TABLE OF CONTENTS (Cont'd)

<u>Section</u>		<u>Page</u>
G	III. Derivation of Quasiselection Rule	169
	IV. Calculation of the Anharmonic Contribution to the Absorption Coefficient	180
	V. Vertex Renormalization Factors	186
	VI. Conclusions	190
	VII. Acknowledgments	192
H	→ Irradiance Limits for Vacuum-Ultraviolet Material Failure	195
	1. Introduction	195
	2. Metallic Reflectors	197
	3. Transparent Materials	197
	4. Summary and Conclusions	201
I and	Materials for High-Power Window and Mirror Coatings and Multilayer-Dielectric Reflectors	206
	1. Introduction	206
	2. High Absorptance of Films	207
	3. Suggested Measurements	210
	4. Material Selection Guidelines and Suggested Materials	211
	5. Protective Coatings	215
	6. Stresses	216
	7. Laser Heating and Damage	216
	8. Acknowledgments	217

LIST OF ILLUSTRATIONS

<u>Section</u>	<u>Figure</u>	<u>Title</u>	<u>Page</u>
B	1	Transmittance of 5 μm of distilled water.	21
	2	(a) Infrared absorption spectrum of water vapor in a carbon dioxide atmosphere. (b) Reference spectrum to indicate the absorption bands of carbon dioxide.	22
	3	Comparison of the water vapor absorption of the atmosphere in the (a) 1.7-3.0 μm region, and (b) the 8.5-11.5 μm region for a 0.3 km path in the Chesapeake Bay area.	23
	4	Calculated transmission from 8.0 to 15.0 μm for precipitable water vapor concentrations of from 0.1 to 100 cm.	25
	5	(a) Calculated 10.59 μm transmittance of water vapor at 77 F in a sea level atmosphere vs. the path length for selected relative humidities. (b) Path to 1 mm of precipitable water as a function of temperature and relative humidity.	26
	6	Mass increase of a 2.5 cm diameter polished NaCl disc when exposed to water vapor at 300 K.	28
	7	Anion size vs. the Mulliken electronegativity and the hydration energy.	31
	8	Sorption isotherms for methyl bromide and different density polyethylenes at C.	42
	9	Spectrum of commercial atactic polystyrene film approximately 25 μm thick.	61
	10	Spectrum of n-C ₂₄ H ₅₀ at -160 C.	63
	11	Infrared spectrum of oriented polyethylene.	64
	12	(a) Infrared spectrum of uncoated NaCl crystal and the same crystal coated with plasma-polymerized ethylene. (b) General spectrum of a vinyl group or a vinyl group with an alkane substitute. (c) Infrared spectrum of NaCl coated with plasma-polymerized ethylene after 30 days exposure to the atmosphere.	66
	13	Infrared spectrum of uncoated NaCl and NaCl coated with plasma-polymerized ethane.	67

LIST OF ILLUSTRATIONS (Cont'd)

<u>Section</u>	<u>Figure</u>	<u>Title</u>	<u>Page</u>
B	14	(a) Infrared spectra of CsI window uncoated, and coated with different thicknesses of plasma-polymerized polychlorotrifluoroethylene. (b) Conventionally polymerized polytetrafluoroethylene. (c) Conventionally polymerized polychlorotrifluoroethylene showing the C-Cl stretching frequency at 10.2 μm that is absent in (a).	69
	15	(a) Infrared spectrum of isotactic polypropylene. (b) Infrared spectrum of polyethylene terephthalate.	70
C	1	The local density of states for the valence band of a LiF slab with a (100) surface.	89
	2	A comparison of the local valence band density of states for the LiF slab in the outermost atomic layer with that in the first interior layer.	93
	3	The local valence band density of states in the outermost layer for the LiF slab, for the case where the shift in Madelung energy of the surface orbital is accounted for.	94
	4	The sharp feature in the local density of states at the surface, plotted as a function of distance from the surface.	96
G	1	In the higher-order-dipole moment mechanism the absorbed photon directly creates n final state phonons (a). Only the fundamental Reststrahl phonon couples to the radiation field in the anharmonic lattice mechanism (b).	167
	2	Ion displacements for acoustical and optical normal modes of a linear diatomic lattice with ions of equal mass, upper curves. Relative displacement of ions, lower curves.	176
	3	Dependence of the spatial phase on the phonon wave vector and heavy to light ion masses.	178
	4	Dependence of the magnitude of the Fourier transformed relative displacement on the phonon wave vector and heavy to light ion mass ratio.	181
	5	Relaxation frequency of the fundamental Reststrahl mode as a function of frequency.	183

LIST OF ILLUSTRATIONS (Cont'd)

<u>Section</u>	<u>Figure</u>	<u>Title</u>	<u>Page</u>
G	6	Comparison of the 80 K theoretical absorption coefficient to the 80 K data.	184
	7	Higher-order three-phonon diagram involving an intermediate-state phonon.	187
H	1	Reflectance of aluminum as a function of frequency.	203
	2	Absorption coefficient of an ionic solid as a function of frequency.	203
	3	Sketch of aluminum-film laser-cavity mirror.	203
	4	Frequency dependence of the nonlinear refractive index for a solid consisting of molecular oscillators.	204
	5	Frequency dependence of the nonlinear refractive index for a broad-band solid, such as LiF.	204
	6	Failure irradiances for various mechanisms.	205
I	1	Transmission spectra of (a) liquid water and of (b) water vapor.	208
	2	Positions of absorption peaks of some possible coating contaminants.	209
	3	Attenuated-total-reflection spectra: (a) This ATR spectrum for a ThF_4 coating deposited on a ZnSe substrate clearly shows the spectrum of contaminating water. (b) This ATR spectrum of ZnSe on BaF_2 illustrates the difficulty of interpreting ATR-spectrum results.	212
	4	Schematic illustration of coatings used to distinguish between absorption at the film surface, in the bulk of the film, and at the film-substrate interface.	213

LIST OF TABLES

<u>Section</u>	<u>Table</u>	<u>Title</u>	<u>Page</u>
B	1	Solubilities of the alkali halides and the alkali hydroxides in gm/100 cc of water.	30
	2	Theoretical and experimental values of the surface tensions of the {100} faces of the alkali halides.	33
	3	Permeabilities and solubilities of water in organic polymers.	37
	4	Critical surface tensions of various polymeric solids.	47
	5	Nucleation rate of critical-sized water droplets as a function of the supersaturation ratio P_b/P_0 , for water alone and several water-polymer combinations.	53
	6	Maximum supersaturate ratio and cooling rate for $10\mu\text{m}$ -thick films of typical polymer types assuming a cooper droplet nucleation rate of 10^6 nuclei/cm ³ s and a temperature range of $10\text{ C} < T_0 < 100\text{ C}$.	56
D	1	Symmetry coordinates for an impurity ion which interacts only with its nearest neighbors.	127
	2	The form of the Green's function matrix in the space of the impurity ion.	129
	3	The form of the perturbing matrices ΔH .	130
F	1	Unnormalized Overlap Integrals.	153

CONTENTS OF PRESENT AND PREVIOUS REPORTS

1. March 1972

1. Introduction
2. Calculation of Multiphonon Absorption Coefficients
3. Calculation of Extrinsic Absorption Coefficient
4. Effects of Pressure on Operation of Windows
5. Recommendations for an Experimental Program
6. Experimental Data from the Literature
7. Nonlinear Processes

App. A Elementary Introduction to the Theory of Infrared Absorption Spectra

2. June 1972

1. Introduction
2. Calculation of Multiphonon Absorption Coefficient
3. Green's Function Analysis and Sjolander-Type Approximations
4. Rigid-Ion, Next-Near-Neighbor Model for the Scattering Hamiltonian
5. Pressure-Induced Optical Distortion in Laser Windows
6. Plans for Continued Research

App. A Tabulation of Pressure-Induced Optical-Distortion Results
App. B Eigenvectors for the Rigid-Ion, Next-Near-Neighbor Model

3. December 1972

- A. Introduction
- B. Theory of Multiphonon Infrared Absorption
- C. Theory of Infrared Absorption and Material Failure in Crystals Containing Inclusions
- D. Collection of Experimental Results for $\beta(\omega)$
- E. References to Previous Multiphonon Calculations

4. June 1973

- A. Introduction
- B. Theory of Infrared Absorption and Material Failure in Crystals Containing Inclusions
- C. Theory of Multiphonon Absorption in Insulating Crystals
- D. Temperature Dependence of Multiphonon Infrared Absorption
- E. Theory of Infrared Absorption by Crystals in the High Frequency Wing of Their Fundamental Lattice Absorption
- F. Temperature Dependence of the Absorption Coefficient of Alkali Halides in the Multiphonon Regime
- G. Temperature and Frequency Dependence of Infrared Absorption as a Diagnostic Tool
- H. Short-Pulse Operation of Infrared Windows without Thermal Defocusing

5. December 1973

- A. Introduction
- B. Extrinsic Absorption
- C. Extrinsic Absorption in $10.6 \mu\text{m}$ Laser Window Materials Due to Molecular-Ion Impurities
- D. Very High-Intensity Effects
- E. Explanation of Laser-Damage Cone-Shaped Surface Pits
- F. Nonlinear Infrared Absorption from Parametric Instabilities of Phonons
- G. High-Power $2\text{-}6 \mu\text{m}$ Window-Material Figures of Merit with Edge Cooling and Surface Absorption Included
- H. High-Power $10.6 \mu\text{m}$ Window-Material Figures of Merit with Edge Cooling and Surface Absorption Included
- I. Explicit Exponential Frequency Dependence of Multiphonon Infrared Absorption
- J. Quasiselection Rule for Infrared Absorption by NaCl-Structure Crystals
- K. The Absorption Coefficient of Alkali Halides in the Multiphonon Regime: Effects
- L. Vertex Corrections for Multiphonon Absorption
- M. Negligible Intrinsic-Absorption Processes
- N. Summary of Publications and Results
- App. Simple Pendulum Instability

6. June 1974

- A. Introduction and Summary
- B. Intensity Limits of High-Intensity Vacuum Ultraviolet Materials
- C. Multiphoton Absorption
- D. Calculated Reflectance of Aluminum in the Vacuum Ultraviolet
- E. Total-Internal-Reflection Devices
- F. The Scattering and Absorption of Electromagnetic Radiation by a Semi-Infinite Crystal in the Presence of Surface Roughness
- G. Infrared Absorption by the Higher-Order-Dipole-Moment Mechanism
- H. Stimulated Raman and Brillouin Scattering: Parametric Instability Explanation of Anomalies
- I. Extrinsic Absorption in $10.6 \mu\text{m}$ Laser Window Materials
- J. Erratum, High-Power $2\text{-}6 \mu\text{m}$ Window-Material Figures of Merit with Edge Cooling and Surface Absorption Included
- K. List of Recent Publications

7. December 1974

- A. Introduction and Summary
- B. Stimulated Raman Scattering: Enhanced Stokes Gain and Effects of Anti-Stokes and Parametric Phonon Processes
- C. Enhanced Stimulated Raman Scattering and General Three-Boson Parametric Instabilities
- D. Theory of Laser-Materials Damage by Enhanced Stimulated Raman Scattering
- E. Surface Roughness and the Optical Properties of a Semi-Infinite Material; The Effect of a Dielectric Overlayer
- E. App. Construction of the Green's Functions for the Electromagnetic Wave Equation

7. December 1974 (Cont'd)

- F. Theory of Laser Heating of Solids: I. Metals
- G. Current Status of High-Intensity Vacuum Ultraviolet Materials
- H. Impurity Absorption in Halide Window Materials
- I. List of Recent Publications

8. June 1975

- A. Introduction and Summary
- B. Current Status of Electron-Avalanche-Breakdown Theory
- C. Preliminary Theory of Electron-Avalanche Breakdown in Dielectric by Laser and dc Fields
- D. VUV Window Failure by Multiphoton Absorption and Electron Defocusing, Avalanche, and Absorption
- E. Optical Distortion from the Nonlinear Refractive Index
- F. Studies of Optical Properties of Alkali Halide Crystals
- G. A Possible Mechanism for Extrinsic Absorption in Insulators below the Fundamental Absorption Edge
- H. Multiphonon Absorption of Alkali Halides and Quasiselection Rules
- I. Enhanced Stimulated Raman Scattering and General Three-Boson Parametric Instabilities
- J. List of Publications

9. December 1975

- I. Summary of Results
- II. Near-Term Recommendations
- III. Background Information
- IV. Possible Sources of Additional Absorption in Coatings
- V. Suggested Measurements
- VI. Other Problems
- VII. Laser Heating of Coatings
- VIII. Laser Damage of Coatings
- IX. Laser Damage of Detached Coatings
- X. Guidelines for Selecting New Materials
- XI. Candidate 10.6 μm Coating Materials
- XII. Candidate 2-6 μm Coating Materials
- XIII. Excerpts and Results from Literature, with Comments

10. June 1976

- A. Introduction and Summary
- B. Polymer Coatings for Protection of Optical Components
- C. Electronic Properties of the LiF Valence Band; Surface States and the Local Density of States Near the Surface
- App. Explicit Form of the Hamiltonian for the N Layer LiF Slab

10. June 1976 (Cont'd)

- D. Localized Electronic States in Alkali Halides Associated with a Substitutional Anion Impurity
- E. Classical Transport Equation for Electron-Avalanche Breakdown
- F. Evaluation of Two-Center Integrals of Slater Atomic Orbitals
- G. Quasiselection Rules for Multiphonon Absorption in Alkali Halides
- H. Irradiance Limits for Vacuum-Ultraviolet Material Failure
- I. Materials for High-Power Window and Mirror Coatings and Multilayer-Dielectric Reflectors

PREFACE

This Seventh Technical Report describes the work performed on Contract Number DAHC15-73-C-0127 on Theoretical Studies of High-Power Ultraviolet and Infrared Materials during the period from January 1, 1976 through June 30, 1976. The work on the current contract is a continuation of that of the previous Contract Number DAHC15-72-C-0129.

The following investigators contributed to this report:

Dr. C. J. Duthler, principal research scientist

Mr. M. R. Flannery, research assistant

Mr. K. G. Hamilton, research assistant

Dr. T. D. Holstein, consultant, University of California, Los Angeles

Dr. A. A. Maradudin, consultant, University of California, Irvine, California

Dr. D. L. Mills, consultant, University of California, Irvine, California

Dr. L. J. Sham, consultant, University of California, San Diego, California

Dr. M. Sparks, principal investigator.

Previously reported results are not repeated in the present report, with the exception of Sec. I, which is a summary of the coatings study reported in the Sixth Technical Report, 31 December 1975, prepared for presentation at the Eighth Annual Symposium on Optical Materials for High Power Lasers, and parts of Sec. H, which is primarily a review of some recent results.

A. INTRODUCTION AND SUMMARY

I. Scope of the Program

The scope of our program continues to change as the interest in high-power materials is shifting. As current interest in the visible and ultraviolet regions is increasing, it is appropriate to recall that the field of high-power optical materials has been changing for the last fifteen years or so. For the first two years of the Xonics program, which began in December of 1971, the primary concern was in obtaining high-power infrared windows. At the beginning of the period the interest was primarily in the CO₂ laser wavelength of 10.6 μm . In the infrared region, the wavelength range from 2 to 6 μm , which includes the HF and DF lasers, also has been of interest. The high-power neodymium-glass laser at 1.06 μm has been important, especially in the laser-fusion programs.

Since December of 1973 the interest of our program has been shifting from the infrared region to the vacuum-ultraviolet region. The high-power excimer lasers, particularly the xenon laser which operates at 172 nm (7.2 eV), stimulated considerable interest in the vacuum-ultraviolet region, and there is current interest in a high-power 350 nm laser.

The first laser was, of course, the ruby laser which operates in the visible region, and interest in the visible region is again increasing. High-power lasers are becoming available at more and more wavelengths, and serious consideration is now being given to the free-electron laser, which possibly could operate tunably from the infrared region at $\sim 10 \mu\text{m}$ to the X-ray region at $\sim 0.1 \text{ nm}$. The attending materials problems tend to be more severe, more limiting (possibly

Sec. A

preventing lasing in some cases), and more difficult to solve as high powers become available at more and more frequencies.

II. Materials Problems of Optical Coatings and Multilayer-Dielectric Reflectors for High-Power Applications

The Sixth Technical Report (31 December 1975) was devoted to coatings and dielectric reflectors. A summary of the results, which was prepared for publication, is given in Sec. I of the present report.

It was shown that current difficulties in achieving satisfactory coatings are by far more likely to be technical difficulties, such as contamination of the coating, rather than fundamental limitations. If the suggestions to improve deposition techniques lead to satisfactory low-absorptance coatings, the results will be more widely useful than originally realized. In particular, the thin-film-improvement methods could result in greatly improved reflectors for wavelengths from $\sim 10 \mu\text{m}$ to $\sim 120 \text{ nm}$ (10 eV). Such improvement is possible since (1) metallic reflectors have very large intrinsic values of absorptance for all wavelengths from $10 \mu\text{m}$ to their useful limit of $\sim 14 \text{ eV}$, (2) the intrinsic absorptance of multilayer-dielectric reflectors is extremely low, and (3) the current relatively high experimental values of the absorptance of multilayer-dielectric reflectors probably are limited by the same technical difficulties as are the infrared coatings.

The major unsolved question of the previous technical report on coatings was that of the usefulness of polymer coatings in protecting films and substrates from attack by water and other contaminants including those in hostile laser-cavity environments and in preventing adsorption. This problem is discussed in the following subsection (III).

III. Polymer Coatings for Protection of Optical Components

In addition to the well known problem of protecting such hygroscopic materials as some of the alkali halides from moisture attack, protection of optical components from such hostile environments as those found in some laser cavities may be required in certain applications. Also, in the Sixth Technical Report (31 December 1975) it was shown that moisture adsorbed on surfaces of optical components and absorbed in the pores of coatings on these components possibly may prevent the successful operation of some systems by giving rise to an optical absorptance that is greater than the tolerable level. Thus, it would be extremely important if polymer coatings could be used for thin hydrophobic layers or for protective layers. Our preliminary investigation of the use of polymers for these functions indicated that further studies were needed to answer two important questions. First, there is conflicting experimental evidence as to whether or not pin-hole-free polymer coatings can prevent moisture penetration into alkali halides. A vast amount of experimental results on moisture-vapor transmission through unsupported pin-hole-free polymer films suggests that such films cannot prevent moisture-vapor penetration to the degree required unless the penetration through films deposited on solids is much less than that through unsupported films. Second, measured values of optical absorptance of polymer films suggest that the absorptance is too great unless the currently measured absorptance values are impurity dominated by contaminants that can be removed from the polymers.

Even though neither of these questions has been answered with certainty, the results of Sec. B are that the probability of obtaining satisfactory polymer coatings is sufficiently great that studies of polymer coatings should be continued.

Sec. A

Recent measured values of the $10.6\mu\text{m}$ absorption coefficient, $\beta = 3-7\text{ cm}^{-1}$, show that the absorptance A can be less than the current desired value of 10^{-4} for very thin ($\sim 100\text{ nm}$) films. It has not yet been determined if β can be reduced to $\sim 0.5\text{ cm}^{-1}$, which is needed in order to give $A = 10^{-4}$ for a one-quarter optical wavelength thickness at $10.6\mu\text{m}$. The lowest optical absorption at $10.6\mu\text{m}$ appears to be in hydro-, fluoro-, and chlorocarbon polymers, respectively, with the absorption resulting from included diamers and carbon-carbon double bonds.

It is believed that pin-hole-free polymer coatings can be deposited successfully. However, measurements of moisture-vapor transmission rates on unsupported pin-hole-free polymer films indicate that a sufficient amount of water to give rise to $A = 10^{-4}$ will penetrate through a typical polymer film within seconds. By contrast, a $1\text{-}\mu\text{m}$ thick polychlorotrifluoroethylene film has protected cesium iodide for one month at 88.8 percent relative humidity. It is proposed that this discrepancy can be explained as follows: polymer coatings produced by plasma polymerization are known to nucleate growth at high-energy surface defects or impurities, which are also the attack sites for water. The reactive plasma species act in a scrubbing reaction to remove the impurities or reduce the defect energies, and then immediately passivate these sites with highly cross-linked or crystalline globules of very low moisture penetrability. We had previously established that absorption of water by the polymer film (as opposed to transmission through the film) should not be a problem. In addition to the small amount of water absorbed, hydrophobic polymer films with no contamination and extremely small voids prevent moisture condensation within the film even when significantly supersaturated, because the energy of condensation of a droplet is limited by the volume of the void to less than that required for the polymer-water surface energy of the droplet.

IV. Problems Related to the Optical Properties of Alkali Halides

Our interest in the optical properties of the alkali halides was originally stimulated by our rough estimate of the strength of the two-photon absorption in lithium fluoride, which indicated that two-photon absorption was the most important effect that limited the use of transparent materials in the vacuum-ultraviolet region. In an attempt to refine the calculated value of the two-photon absorption, it was found that the current understanding of the optical properties of the alkali halides was not sufficiently well developed to allow an accurate, tenable two-photon calculation to be made. The current lack of a satisfactory theory of the simple, so-called one-photon, optical properties of the alkali halides is discussed below. In subsequent investigations it was found that the same wave functions needed in the two-photon calculation also were needed in four other important areas of our program. At present the electron wave functions are needed in:

- two-photon and multiphoton absorption calculations,
- electron-avalanche-breakdown calculations,
- impurity-absorption calculations,
- electronic-surface-state-absorption calculations, and
- post-Hartree-Fock corrections to one-photon optical properties.

The one-photon problems include the following: It is generally agreed that the best Hartree-Fock calculations give a value of the band gap of 23.0 eV, which is much greater than the experimental value of ~13 eV. However, recent calculations have claimed fair agreement with the experimental absorption spectrum of LiF and have attributed the absorption edge to interband transitions rather than to the excitons. Because of the neglect of several physical effects which are known

Sec. A

to be large and the adjustment of parameters to fit experimental data, the apparent fair qualitative agreement of these calculations with experiment may be coincidental, and the results have been questioned.

The approximations that were made are: neglect of the large (~ 4 eV) interaction of the bare electrons with the polarization field (i.e., electron-charge correlation), use of a local approximation for the exchange potential (i.e., use of Slater exchange or $X\alpha$ exchange), neglect of electron-hole correlation, and neglect of local field effects (e.g., Lorentz-Lorentz correction) in calculating the dielectric constant. The first three of these effects have been included in a recent calculation by Mickish, Kunz, and Collins.¹ Qualitative agreement with experiment was again obtained, with the absorption edge now being attributed to exciton absorption. Thus, even the nature of the absorption edge is controversial, and the important effect of local field corrections and exchange-exciton effects have been neglected. Furthermore, the electronic polarization effects, both long range and short range, may not have been treated correctly.

The available Hartree-Fock wave functions are so complicated that excessive numerical analysis would be required, to the point of making some calculations impractical. What is more important, we would have little faith in the results since these wave functions do not even predict the one-photon properties. Thus, a simple set of wave functions is needed for the calculations listed, and an indication is needed that these wave functions are reliable in spite of the difficulties in the theory of the simple optical properties.

A very simple set of wave functions should be sufficient for our calculations for the following reasons. The advent of new mathematical methods (use of

Sec. A

gaussian-type orbitals rather than Slater-type orbitals) and large digital computers has made possible Hartree-Fock-Slater calculations of the energy bands of alkali halides, using a large set of basis functions, at many points in the Brillouin zone to within a hundredth of an electron volt. Then in order to explain the band gap, corrections of the order of 10 eV are required, and the accuracy of this correction may be only a few electron volts. Thus, simple wave functions that reproduce the Hartree-Fock band gap to within say two or three electron volts should be quite sufficient for the investigations listed.

To date the following have been calculated for lithium fluoride:

- the tight-binding wave functions for the valence band and the nearly free-electron wave functions for the conduction band,
- the band gap,
- the width of the valence band, and
- valence-band localized states.

The valence-band wave functions contain two simple exponential terms obtained by numerically fitting the two-term wave functions to the more complicated atomic Hartree-Fock-Roothaan wave functions. The conduction-band wave functions are plane waves that are orthogonalized to the valence-band states, and a pseudopotential is used in calculating the energies. Our value of 24.4 eV calculated for the band gap by using these wave functions agrees to within 1.5 eV with the best current Hartree-Fock value of 23.0 eV.

The great discrepancy between the experimental band gap of \sim 13 eV and the Hartree-Fock value of 23 eV has been tentatively identified in our present program as a conduction-band problem. If subsequent investigations verify this result,

Sec. A

it is expected that our valence-band wave functions may be quite accurate, and they can be used with confidence in the subsequent calculations listed above.

Our calculated value of the width of the valence band of lithium fluoride agrees with the experimental value to within the accuracy to which the width could be extracted from the experimental data. However, the theoretical values for several other alkali halides are smaller than the experimental values, the difference becoming greater as the masses of the elements increase. It appears that technical difficulties in the experiments could explain the discrepancy. Preliminary discussions with experimentalists in the field confirm that this is a likely explanation. Additional contributions to the theoretical width will be evaluated, the calculations will be made for the other alkali halides, and the experimental broadening will be considered in subsequent reports.

The results of the optical-properties studies are used in the following four subsections (V-VIII).

The next specific optical-properties tasks to be performed are as follows: Using the simple lithium-fluoride wave functions, evaluate the importance of the post-Hartree-Fock effects including electronic polarization, our new mechanical-polarization effect, local-field effects, and correlation effects. Next the wave functions, the Hartree-Fock band gap, the width of the valence bands, and the post-Hartree-Fock corrections will be calculated for the other fluorides, then for the other alkali halides. For lithium fluoride, the wave functions will be used in the two-photon-absorption calculation, the electron-avalanche-

Sec. A

breakdown calculation, the impurity-absorption calculation, and the surface-electronic-state absorption calculation as discussed in other subsections of the present section. Finally, these calculations will be repeated, first for the other fluorides and then for the remaining alkali halides.

V. Evaluation of Two-Center Integrals of Slater Atomic Orbitals

In the calculations of the valence-band width discussed above and in a number of our other calculations, the values of several types of two-center integrals are needed. In Sec. F the values of these integrals are calculated and tabulated in closed form. In particular, expressions are given from which the values of overlap integrals $\int x_a x_b d^3 r$, kinetic-energy integrals $-\frac{1}{2} \int x_a \nabla^2 x_b d^3 r$, and nuclear-Coulomb-attraction integrals $Z \int x_a (1/r_a) x_b d^3 r$ are obtained in closed form for any Slater atomic orbitals x having principal quantum numbers from one to six. The a's and b's above denote the two different centers. Previous calculations of Roothaan² were available for n equals one and two.

VI. Electronic Properties of the LiF Valence Band; Surface States and the Local Density of States Near the Surface

Using our tight-binding valence-band wave functions and diagonalizing the Hamiltonian matrix for a model 15-layer lithium-fluoride slab, the following results are obtained in Sec. C: Including the Madelung energy pushes a band of surface states out of the top of the conduction band. These surface states, which are spatially confined to the surface layer, are believed to be features of the lithium-fluoride (100) surface, not of the model used. Both bulk and surface-layer densities of states show peaks near the top and bottom of the

Sec. A

band, in addition to the narrow surface state. The bulk density of states, which is approached rather closely even in the second atomic layer, generally resembles previously calculated densities but has considerably more resolution.

VII. Impurity Absorption in the Vacuum-Ultraviolet Region

Our study of impurity absorption consists of two parts. The first is an extensive tabulation of impurity spectra in the vacuum-ultraviolet, ultraviolet, and visible regions. It is anticipated that a future technical report will be devoted to this tabulation.

The second part is a study of possible absorption mechanisms, in addition to well known mechanisms covered in the tabulation. One possible source of the great, relatively structureless, observed values³ of vacuum-ultraviolet absorption coefficients was proposed in Sec. G of the Fifth Technical Report (30 June 1975). Another possible source, which has also been studied experimentally,⁴ is substitutional ions in alkali halides. The cross sections for electronic absorption are extremely large, the absorption coefficient having a typical value of 10^6 cm^{-1} for solid densities of $\sim 10^{23} \text{ cm}^{-3}$. Thus, only parts per million of halide or alkali substitutional impurities are expected to be required to give rise to the typical observed values of $\beta \approx 1 \text{ cm}^{-1}$.

An extremely rough argument suggests that the substitution of ions that are larger than the host ions should lead to absorption at frequencies below the band gap. The Madelung energy is a good zeroth-order approximation to the band gap for the alkali halides, and the Madelung energy decreases as the lattice spacing increases. Thus, the effective band gap for the impurity, roughly speaking, decreases for large ions, and absorption below the pure-material gap is expected.

This zeroth-order argument is being refined in order to develop a believable, intuitive explanation of the impurity absorption process, and a formal treatment of the problem has been developed. The formal results are given in Sec. D, where a tight-binding calculation of localized electronic states pushed out of the top of the valence band is formulated. These impurity states are not to be confused with the intrinsic surface states discussed in Sec. A-VI. Numerical results for specific cases of interest will be included in future reports.

VIII. Electron-Avalanche Breakdown

In the present program we attempted to calculate the electron-avalanche breakdown in the vacuum-ultraviolet region using existing theories. It was found that the theories were not only inadequate in the vacuum-ultraviolet region, but that they were also inadequate quite generally and in particular in the visible and infrared regions where so many electron-avalanche-breakdown studies have been made. We proposed new theories of electron-avalanche breakdown and showed that very rough estimates indicated that the theories could explain the experimental results quite well.

At this point the following investigations are needed to determine if the proposed theory is indeed viable. First, the previous results, some of which were obtained largely by intuitive-type arguments, need to be verified by carrying out the program outlined by Ted Holstein which uses a difference-differential transport equation. The estimated values of the matrix elements used in the theory need to be verified by calculations employing the wave functions that are being developed in the study of the optical properties of alkali halides discussed below.

The progress to date on the transport-equation approach is included in Sec. E of the present report. It is seen in that section that we are taking a fresh, first-principles look at the problem of electron-avalanche breakdown. Starting from the Boltzmann transport equation, making a quasi-isotropy approximation, using the Fokker-Planck expansion, and making other simple approximations gives a practical transport equation. Within the framework of this theory, a current density, a conductivity tensor, and relaxation rates are introduced.

The theory will be generalized to include the large-quantum processes in which the electron can change energy by a great amount, as discussed in the Fifth Technical Report (30 June 1975). Exciton-forming collisions also will be included. Finally, the theory will be extended to determine the magnitude and the frequency dependence of the breakdown field for picosecond pulses in view of the great current interest in short-pulse experiments.

IX. Multiphonon Absorption

The last vestiges of our multiphonon calculations are in Sec. G, where a quasiselection rule that multiphonon infrared absorption in alkali halides prefers final states containing an odd number of optical phonons explains the recent observation of a well-defined peak in the low-temperature infrared absorption of several alkali halides at a frequency corresponding to the sum of three optical phonons. The quasiselection rule results from the relative ionic displacements for optical modes being approximately in phase with the individual ion displacements, while the relative ionic displacements for acoustical modes are approximately 90° out of phase. The further realization that the magnitude of the Fourier-transformed optical-mode relative displacement is nearly independent of the wave

Sec. A

vector greatly reduces calculation effort by reducing an extremely tedious multiple sum to a thermally and frequency weighted density of states of distinct phonon branches. The theory avoids the two inadequacies of diatomic-molecule approaches: (a) that peaks near all integral multiples of the fundamental frequency are predicted, and (b) that molecular models have led to gross overestimates of vertex correction factors, which are shown here to be small.

X. Irradiance Limits for Vacuum-Ultraviolet-Material Failure

Section H of the present report contains a paper presented at the 1976 Eighth Annual Symposium on Optical Materials for High Power Lasers, Boulder, Colorado. There are only minor differences in the results of Sec. H from the latest results of previous reports.

REFERENCES

1. D. Mickish and A. Kunz, *J. Phys. C* 6, 1723 (1973); D. Mickish, A. Kunz, and T. Collins, *Phys. Rev. 9*, 4461 (1974).
2. C. Roothaan, *J. Chem. Phys.* 19, 1445 (1961).
3. T. Tomiki and T. Miyata, *J. Phys. Soc. Japan* 27, 658 (1969).
4. D. Hinks and S. Susman, *Phys. Stat. Sol. (b)* 52, K53 (1972).

B. POLYMER COATINGS FOR PROTECTION OF OPTICAL COMPONENTS

M. Flannery

Xonics, Incorporated, Santa Monica, California 90401

and

Department of Physics, The University of Southern California,
Los Angeles, California 90007

It was shown previously that the use of polymer coatings in protecting optical components from attack by water or other contaminants and in preventing contaminant adsorption possibly could be precluded by either great optical absorption or great water-vapor transmission through the polymer. Even though neither of these questions has been answered with certainty, the results are that the probability of obtaining satisfactory polymer coatings is sufficiently great that studies of polymer coatings should be continued. Recently measured values of the $10.6\text{ }\mu\text{m}$ absorption coefficient $\beta = 3.7\text{ cm}^{-1}$ show that the absorptance A can be less than the current desired value of 10^{-4} for very thin ($\sim 100\text{ nm}$) films. It has not yet been determined if β can be reduced to $\sim 0.5\text{ cm}^{-1}$, which is needed in order to give $A_f = 10^{-4}$ for a one-quarter optical wavelength thickness at $10.6\text{ }\mu\text{m}$. The lowest optical absorption at $10.6\text{ }\mu\text{m}$ appears to be in hydrocarbon, fluorocarbon, and chlorocarbon polymers, respectively, with the absorption resulting from included diamers and carbon-carbon double bonds. It is believed that pinhole-free polymer coatings can be deposited successfully. However, measurements of moisture-vapor-transmission rates on unsupported pinhole-free polymer films indicate that a sufficient amount of water to give rise to $A_f = 10^{-4}$ will penetrate through a typical polymer film within seconds. By contrast, a one-micron-thick

polychlorotrifluoroethylene film has protected cesium iodide for one month at 88.8 percent relative humidity. It is proposed that this discrepancy can be explained as follows: Polymer coatings produced by plasma polymerization are known to nucleate growth at high-energy surface defects or impurities, which are also the attack sites for water. The reactive plasma species act in a scrubbing reaction to remove the impurities or reduce the defect energies, and then immediately passivate these sites with highly cross-linked or crystalline globules of very low moisture penetrability. We had previously established that absorption of water by the polymer film (as opposed to transmission through the film) should not be a problem. In addition to the small amount of water absorbed, hydrophobic polymer films with no contamination and extremely small voids prevent moisture condensation within the film even when significantly supersaturated, because the energy of condensation of a droplet is limited by the volume of the void to less than that required for the polymer-water surface energy of the droplet.

I. INTRODUCTION

High-power infrared windows are sensitive to moisture absorbed on the surface or diffused into the bulk because of the very strong infrared absorption of water. Additionally, some windows may suffer direct physical attack by hydrolysis or swelling of the window or its antireflection coating. In particular, the alkali halides used in windows and coatings can be virtually destroyed by water-vapor corrosion. It has tacitly been assumed that surface adsorption or attack by environmental moisture could be prevented by coating the window faces with a thin, pinhole-free layer of a suitable hydrophobic polymer. However, there is ambiguous evidence on the ability of thin, pinhole-free films deposited on window substrates to meet the requirements of sufficiently low moisture permeability and a value of $A_f = 10^{-4}$ for the infrared absorption per surface. Simple diffusion calculations using the published water-vapor permeabilities of polymers indicate that films of the order of $1 \mu\text{m}$ thick would allow an unacceptable amount of water through in approximately two seconds. On the other hand, there is experimental evidence^{1,2} that polymer films of this thickness have provided protection for extended periods of time, for example, completely protecting deliquescent CsI for at least a month at 88.8 percent relative humidity. Although infrared spectra have been measured for many of these films,^{1,2,3} they are not of sufficient sensitivity to estimate the absorption coefficient in the range of interest ($A_f \approx 10^{-4}$) for the most transparent films, and there appear to be no laser-damage measurements at present. Finally, most experimentalists have reported good adhesion of their polymer films to electronic and optical substrates.³

In this report we investigate the importance of the following effects on the moisture protection of the alkali halides by polymers:

- 1) Infrared absorption of liquid and vapor forms of water at $10.6 \mu\text{m}$ to determine tolerable concentration limits.
- 2) Surface defects and impurities that may provide nucleation sites for moisture attack on alkali-halide crystals.
- 3) Physical properties of polymer films that may reduce their moisture permeability.
- 4) Film-crystal surface interactions that passivate moisture-attack sites on the crystal surface.
- 5) Interactions between the polymer and water vapor that may prevent condensation above the dew point.
- 6) Surface free energies and wettabilities of polymers to determine the equilibrium amount of adsorbed moisture.
- 7) Infrared absorption of polymers and polymer films to determine their absorption coefficient at $10.6 \mu\text{m}$.

The results are:

- 1) Two monolayers of liquid water formally produce an absorption of 10^{-4} per surface, but any reasonable concentration of free water vapor produces negligible absorption.
- 2) High-energy surface defects and impurities, particularly hydroxyl ions, initiate moisture attack. Removal or passivation of these features greatly enhances the crystal's resistance to hydrolysis.
- 3) High degrees of cross-linking and high crystallinity produce polymers with significantly lower moisture permeabilities.

- 4) Film-crystal surface interactions reduce the free energy at the interface, but the amount appears to be too small to have a large effect over a gross surface. Some interactions are considered that reduce moisture attack on the high-energy sites of the crystal, but the details of the mechanisms and their effectiveness are not known.
- 5) Limitation of the size of condensation droplets by the pore sizes of hydrophobic polymers makes it energetically favorable for water to remain as a supersaturated vapor unless the cooling is quite rapid.
- 6) Free surface energies, and hence the wettability of polymers, increase as one moves from fluoro-, to hydro-, to chlorocarbon polymers. The fluoropolymer surfaces normally adsorb much less than a monolayer of water, as should hydrocarbons that are free of double bonds or aromatic rings.
- 7) Hydrocarbons free of double bonds or aromatic rings may have the lowest absorption at $10.6 \mu\text{m}$. Fluoropolymers may also be acceptable, but chloropolymers appear to have too much intrinsic absorption from the fundamental molecular vibrations.

II. INFRARED ABSORPTION BY MOISTURE AT $10.6\mu\text{m}$

In the previous report it was shown that approximately two monolayers (formally using a thickness of $\sim 0.6\text{ nm}$) of liquid water are sufficient to produce an absorption of 10^{-4} per surface, which gives an absorption coefficient of $\beta \sim 950\text{ cm}^{-1}$ at $10.6\mu\text{m}$. This value was calculated from the absorption spectra in Fig. 1, which was estimated to be $5\mu\text{m}$ thick, based on an average of thicknesses calculated from measured values of the absorption at several frequencies.⁴

In Fig. 1, the absorption on the high-frequency side of the band at $3\mu\text{m}$ is due to asymmetric stretching and that on the low-frequency side is due to symmetric stretching, while the fundamental bending mode produces the band at $6\mu\text{m}$. The broad, smooth appearance of these absorption lines is due to the strong hydrogen bonding in liquid water that produces a distribution of effective masses and bond strengths. The bending and stretching of the hydrogen bonds themselves produce the very broad absorption around $13.5\mu\text{m}$, which contributes most of the absorption at $10.6\mu\text{m}$. This is clearly indicated by comparing the spectrum of liquid water in Fig. 1 with that of water vapor, which is free of hydrogen bonding, in Fig. 2. A better estimate of the relative absorption of water vapor at $2-3\mu\text{m}$ and at $10.6\mu\text{m}$, can be made from the atmospheric spectrum of Fig. 3, which is free of the Fabry-Perot interferences of the absorption cell used in Fig. 2.

At $10.6\mu\text{m}$, two computations were made for the absorption coefficient of water vapor β_{pv} (with $\beta\ell = \beta_{\text{pv}}\ell_{\text{cond}}$, where ℓ_{cond} is the equivalent thickness of liquid if the precipitable vapor were condensed). The first was computed

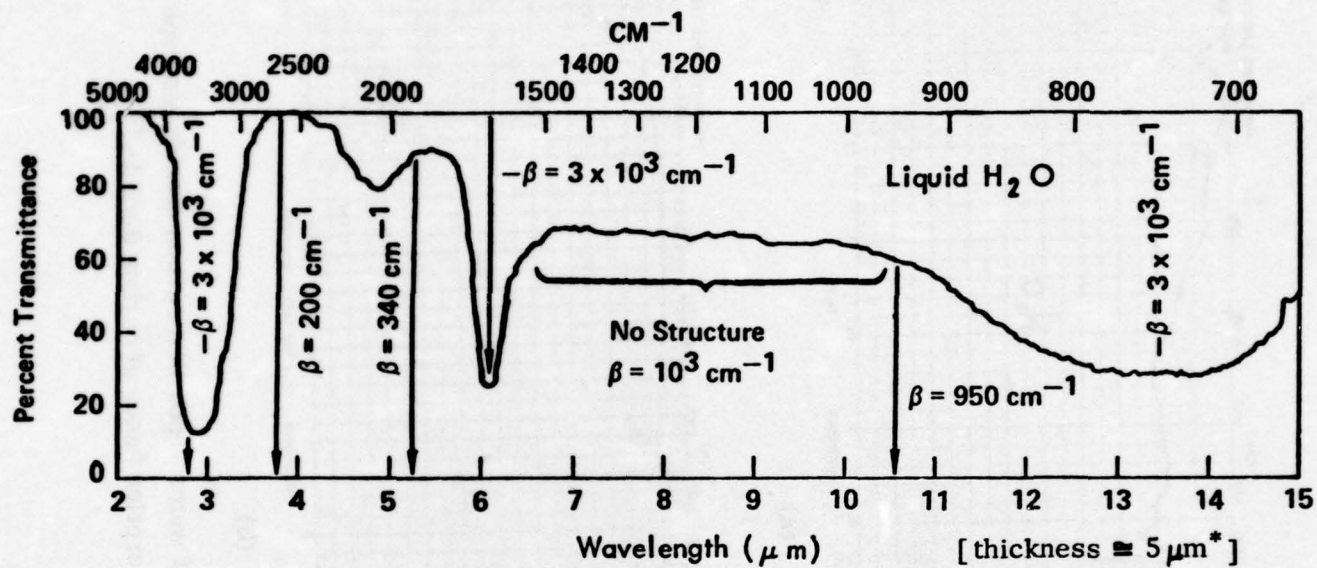


Fig. 1. Transmittance of $5 \mu\text{m}^*$ of distilled water.^{4a} [*The thickness was calculated from the average value of $\lambda = -\beta^{-1} \ln T$ at 2.9, 4.9, 6.1, 10.6, and 13 μm , using the values of β given in Ref. 4.]

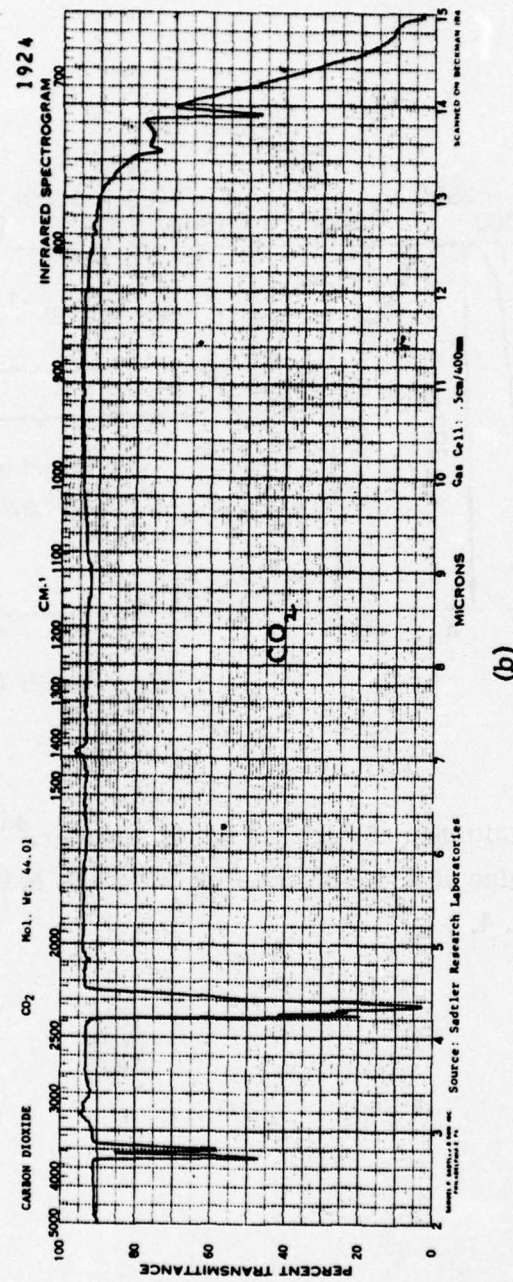
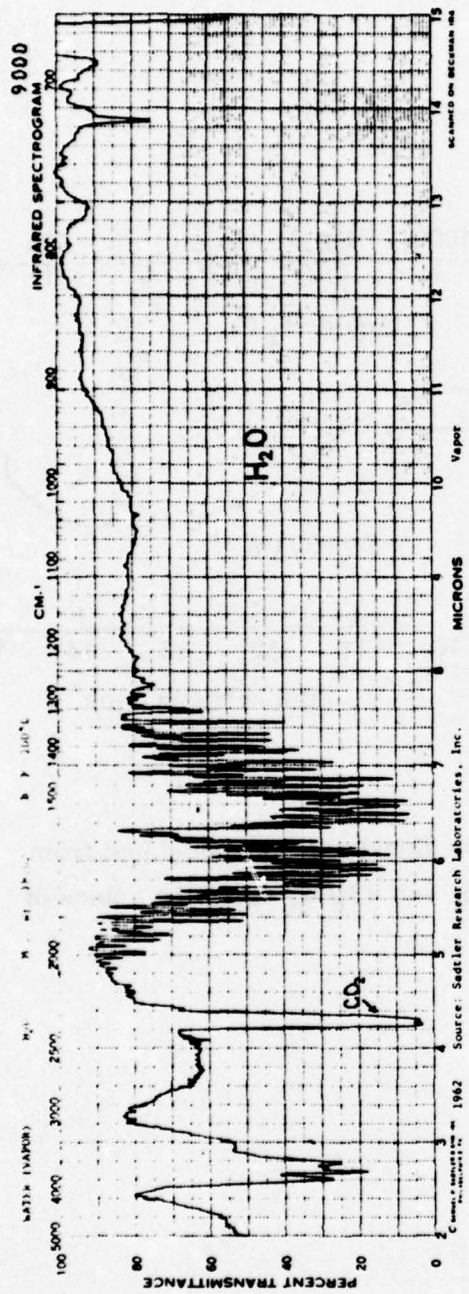


Fig. 2. (a) Infrared absorption spectrum of water vapor in a carbon dioxide atmosphere.
(b) Reference spectrum to indicate the absorption bands of carbon dioxide.^{4a}

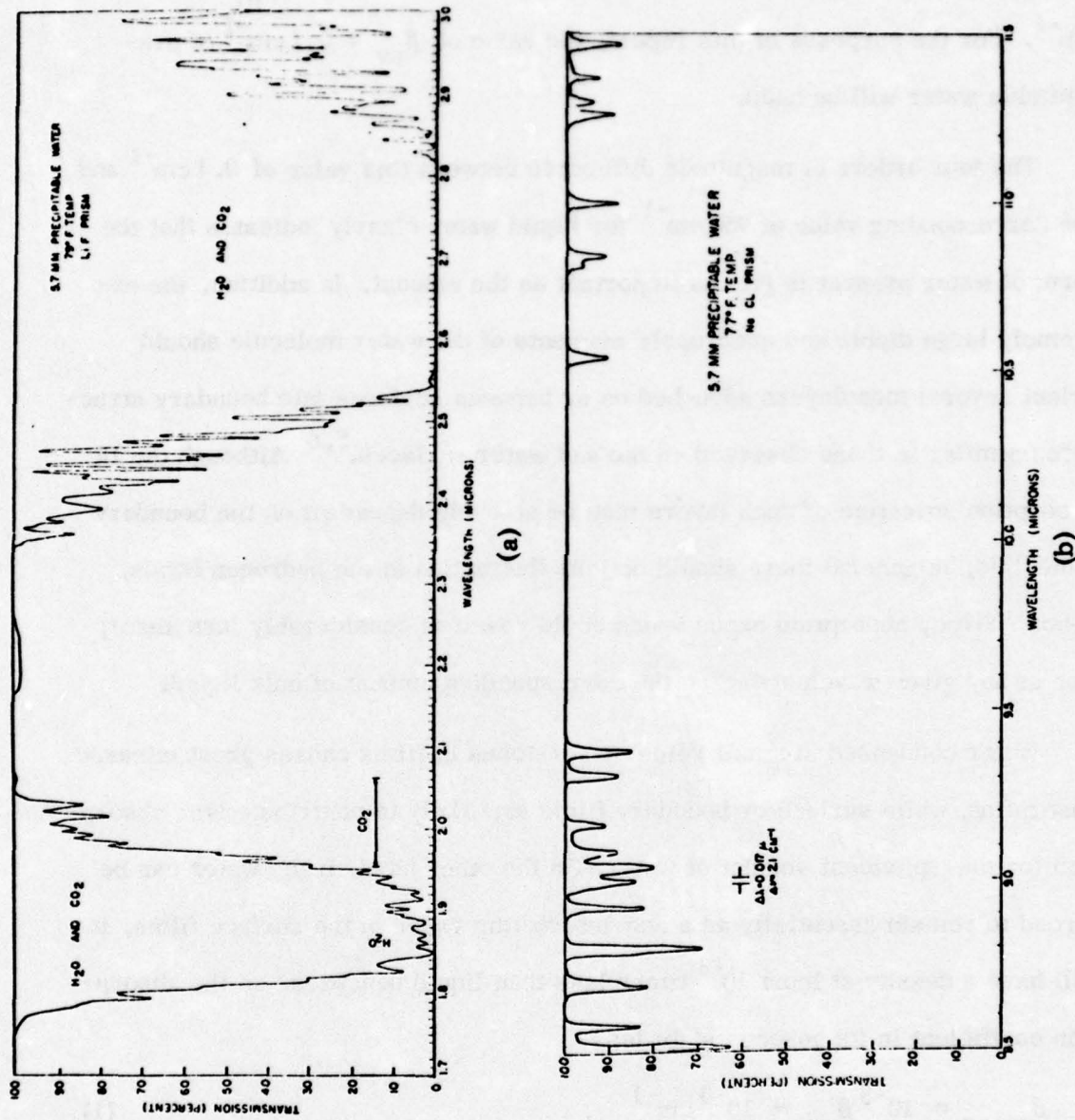


Fig. 3. Comparison of the water vapor absorption of the atmosphere in the (a) 1.7-3.0 μm region, and (b) the 8.5-11.5 μm region for a 0.3 km path in the Chesapeake Bay area.^{4b}

directly from Fig. 4 and yields $\beta_{pv} \sim 0.096 \text{ cm}^{-1}$ of precipitable water vapor.

The second calculation was made by taking the calculated $10.59 \mu\text{m}$ transmittance of water vapor from Fig. 5a and using Fig. 5b to convert the relative humidity to centimeters of precipitable water. This result was $\beta_{pv} \sim 0.117 \text{ cm}^{-1}$. For the purposes of this report, the value of $\beta_{pv} = 0.1 \text{ cm}^{-1}$ of precipitable water will be used.

The four orders of magnitude difference between this value of 0.1 cm^{-1} and the corresponding value of 950 cm^{-1} for liquid water clearly indicates that the form of water present is just as important as the amount. In addition, the extremely large dipole and quadrupole moments of the water molecule should orient several monolayers adsorbed on or between surfaces into boundary structures similar to those observed on ice and water surfaces.^{5,6} Although the IR absorption spectrum of such layers may be strongly dependent on the boundary materials, in general there should be less fluctuation in the hydrogen bonds, hence sharper absorption bands which could result in considerably less absorption at any given wavelength than the corresponding amount of bulk liquid.

Water condensed in small voids or scratches in films causes great infrared absorption, while surface or boundary films are likely to contribute less absorption for the equivalent amount of water. On the other hand, if the water can be forced to remain essentially as a non-interacting vapor in the surface films, it will have a density at least 10^{-3} times less than liquid densities, so the absorption coefficient in its gaseous state is:

$$\beta_{\text{vapor}} = 10^{-3} \beta_{pv} = 10^{-4} \text{ cm}^{-1} , \quad (1)$$

which is negligible in any surface film.

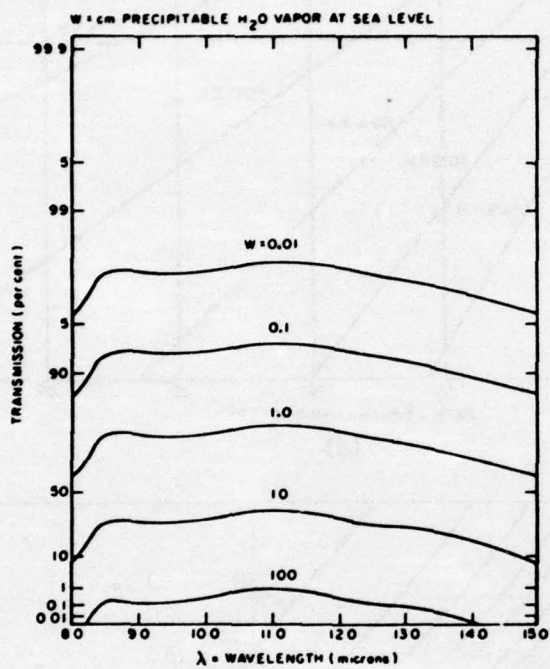
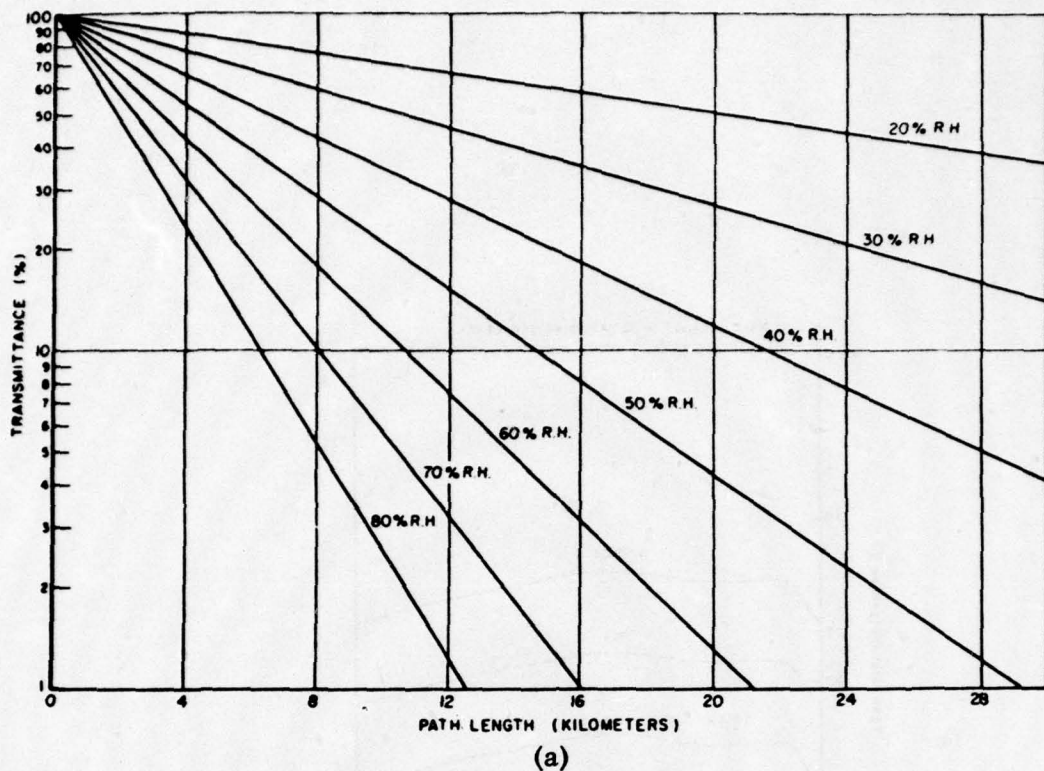
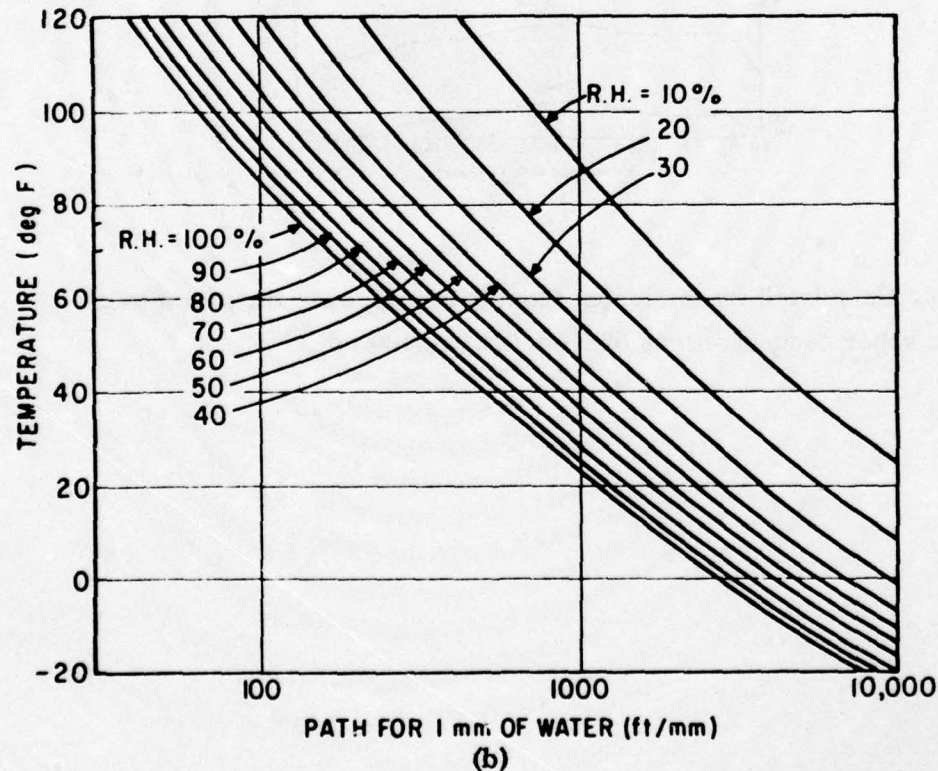


Fig. 4. Calculated transmission from 8.0 to 15.0 μm for precipitable water vapor concentrations of from 0.01 to 100 cm.⁴⁶

Sec. B



(a)



(b)

Fig. 5. (a) Calculated $10.59\mu\text{m}$ transmittance of water vapor at 77 F in a sea level atmosphere vs. the path length for selected relative humidities. (b) Path to 1 mm of precipitable water as a function of temperature and relative humidity.^{4b}

III. THE ALKALI HALIDES

The alkali halides are particularly attractive as window materials and as low-index layers in antireflection coatings⁷ because of their low intrinsic absorption at 10.6 μm . Unfortunately they are also the most moisture sensitive of all the candidate materials at this wavelength and will require moisture protection or passivation if they are to be used in uncontrolled environments.

At a given temperature, the nature of moisture attack on a soluble material is best characterized by the ambient vapor pressure, $P_{\text{H}_2\text{O}}$, relative to the vapor pressures of the pure solvent, $P_{\text{H}_2\text{O}}^{\circ}$, and the saturated solution $P_{\text{H}_2\text{O}}^*$.⁸ The three regions of interest are:

- 1) Dew point or precipitation region, where $P_{\text{H}_2\text{O}} \geq P_{\text{H}_2\text{O}}^{\circ}$;
- 2) Deliquescence region, where $P_{\text{H}_2\text{O}}^* < P_{\text{H}_2\text{O}} < P_{\text{H}_2\text{O}}^{\circ}$;
- 3) Efflorescence region, where $P_{\text{H}_2\text{O}} \leq P_{\text{H}_2\text{O}}^*$.

The value of $P_{\text{H}_2\text{O}}^*$ can be found from vapor pressure data, which show, for example, that from 20 to 90 C, a saturated KCl solution maintains an 80 percent relative humidity, while a saturated NaCl solution maintains a 75 percent relative humidity.

For a polished NaCl disc, P. A. Young⁹ found the uptake of moisture as a function of relative humidity shown in Fig. 6. The rapid weight increase in the deliquescence region of NaCl, between 75 and 100 percent relative humidity, appears to be consistent with the expected behavior of a hygroscopic or deliquescent material.

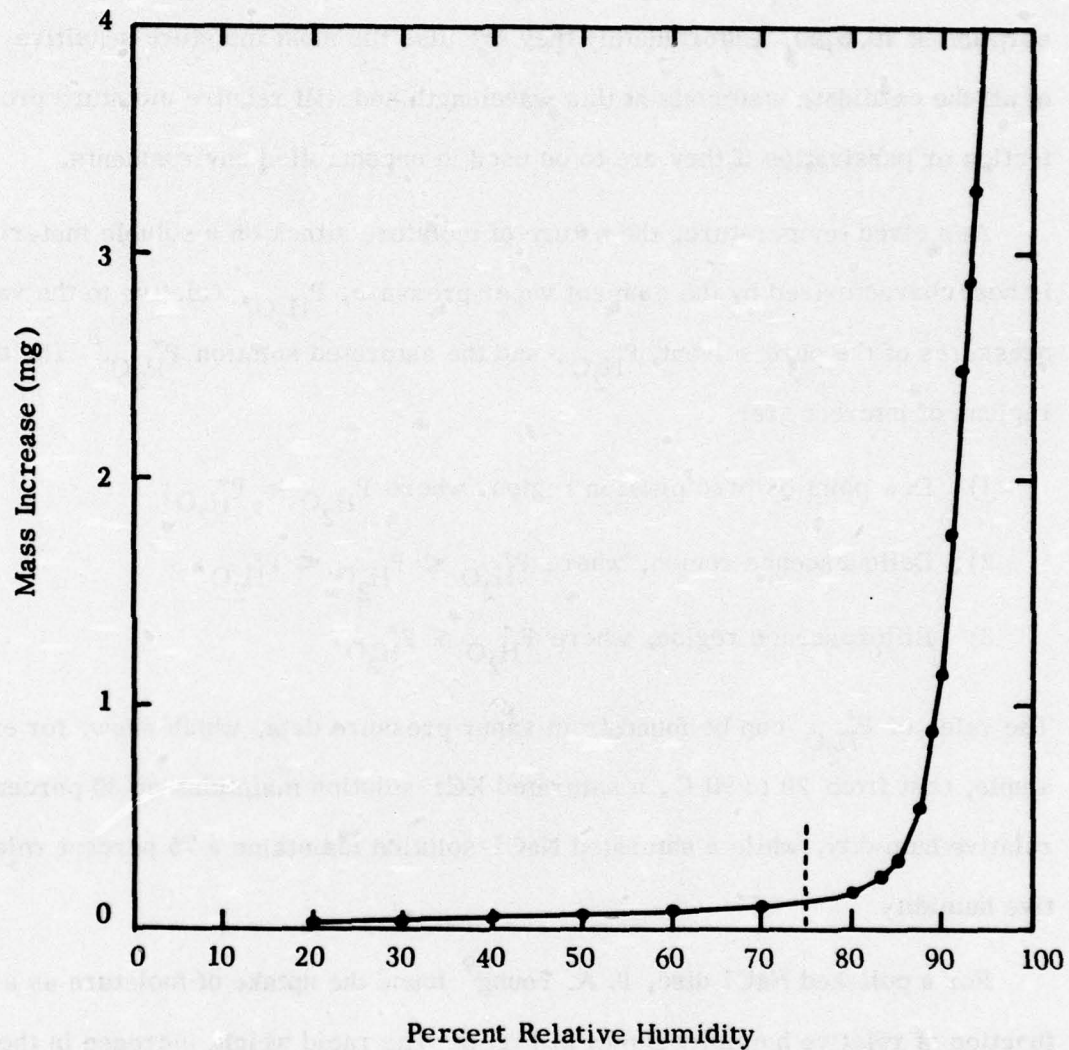
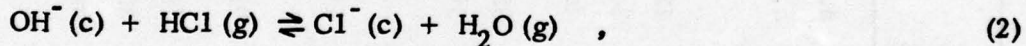


Fig. 6. Mass increase of a 2.5 cm diameter polished NaCl disc when exposed to water vapor at 300 K. Exposure time was 30 min for each value of the relative humidity. The dashed vertical line is the vapor pressure of a saturated solution of NaCl for temperatures between 20 and 90 C.⁹

This behavior might seem to contradict the well known result that pure powdered NaCl and KCl are nonhygroscopic at all normal pressures and temperatures. Table 1 shows the solubilities and the hygroscopicity or deliquescence behavior of the alkali halides along with the alkali hydroxides. The ubiquitous nature of water and the deliquescence of the hydroxides suggests the possibility that NaOH was the chief cause of the behavior observed by P. S. Young. Additional evidence was provided by Pastor and Braunstein¹¹ who plotted the Mulliken electronegativity and hydration energy of the hydroxide and halide ions vs. the ionic radius r_{X^-} , as shown in Fig. 7. Since the hydroxide ion falls naturally into the halide sequence between Cl⁻ and F⁻ in both electronegativity, which characterizes electron transfer processes, and hydration energy, which characterizes ion exchange properties, OH⁻ is the most natural impurity that could condition a deliquescent behavior in KCl or NaCl.

This suspicion was confirmed when KCl was found to be indefinitely stable in the efflorescence region if it was carefully processed in a reactive CCl₄ atmosphere to exchange the surface OH⁻ for Cl⁻ by the scrubbing reaction



where c stands for the crystalline and g the gaseous states, respectively.¹² Furthermore, when freshly cleaved KCl surfaces were annealed in a reactive atmosphere, the stability of the crystal against moisture attack could be extended through the deliquescence region into the dew-point region. Short residence above the dew point indicates that this process resulted in a surface free energy that is lower for the solid-gas interface than for the solid-liquid interface.

Table 1. Solubilities of the alkali halides and the alkali hydroxides in gm/100 cc of water. Superscript is the temperature in degrees centigrade.¹⁰

Alkali Metals Halogens	Li	Na	K	Rb	Cs
F	0.113 ²⁵ 0.27 ¹⁸	4.0 ¹⁵ 5.0 ¹⁰⁰	92.3 ¹⁸ very soluble ¹⁰⁰	130.6 ¹⁸	367.1 ⁸
		42 ⁰	107.15	167. ²⁰	395.5 ¹⁵
OH	12.8 ²⁰ 17.5 ¹⁰⁰	347.100	178.100	deliquescent	very deliquescent
	hygroscopic				
Cl	63.7 ⁰ 130. ⁹⁵	35.7 ⁰ 39.12 ¹⁰⁰	34.7 ²⁰ 56.7 ¹⁰⁰	77 ⁰ 138.9 ¹⁰⁰	162.2 ^{0.7} 259.6 ^{89.5}
				deliquescent	
Br	154 ⁴ 254. ⁹⁰	116 ⁵⁰ 121.100	53.5 ⁰ 102.100	98 ⁵ 205.2 ^{113.5}	124.3 ²⁵ very soluble ¹⁰⁰
	deliquescent	hygroscopic	slightly hygroscopic		
I	165 ²⁰ 430. ⁸⁰	184 ²⁵ 302.100	127.5 ⁰ 208.100	152. ¹⁷ 163. ²⁵	44 ⁰ 160. ⁶¹
		hygroscopic	slightly deliquescent		

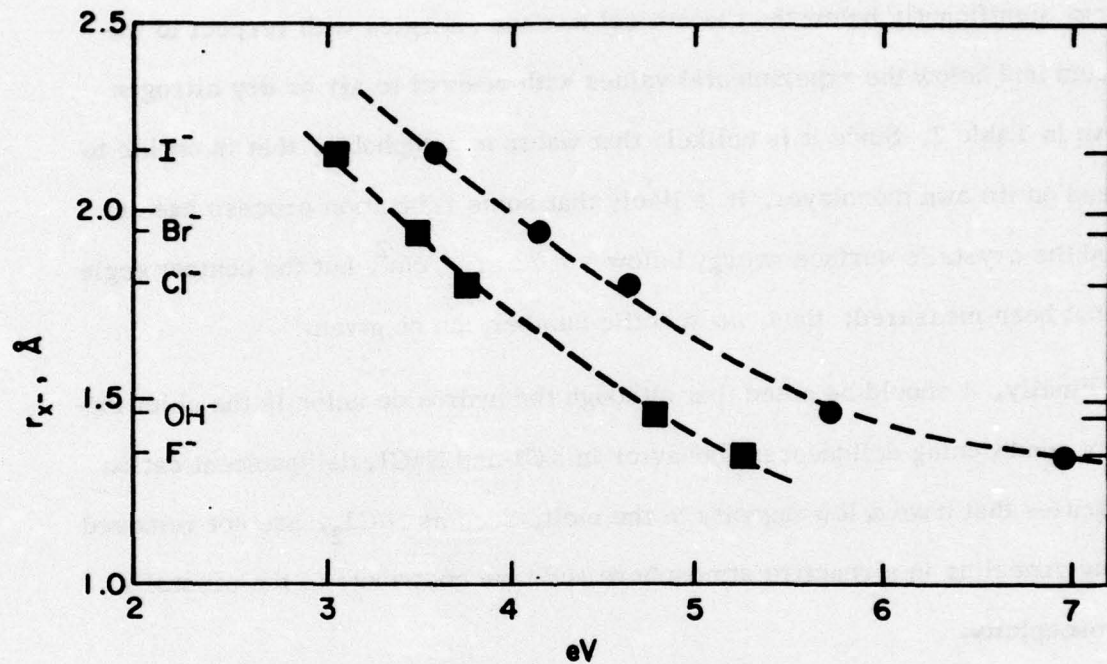


Fig. 7. Anion size vs. the Mulliken electronegativity (●) and the hydration energy (■).¹¹

Therefore, except at local high-free-energy sites such as impurities or unannealed defects, water will not wet the surface, and the microscopic dewdrops formed at these nucleation sites do not coalesce into a film. Since spreading should occur if the surface energy of the crystal is greater than that of water, $\gamma_{H_2O} = 72 \text{ ergs/cm}^2$, annealing in a reactive atmosphere apparently reduces the crystal's (100) surface energy significantly below the theoretical surface energies with respect to the vacuum and below the experimental values with respect to air or dry nitrogen shown in Table 2. Since it is unlikely that water is autophobic, that is unable to spread on its own monolayer, it is likely that some relaxation process has reduced the crystal's surface energy below $\gamma = 72 \text{ ergs/cm}^2$, but the contact angle has not been measured; thus, no specific number can be given.

Finally, it should be noted that although the hydroxide anion is the chief impurity conditioning deliquescent behavior in KCl and NaCl, deliquescent cation impurities that have a low fugacity in the melt, such as $NiCl_2$, are not removed during annealing in a reactive atmosphere and may contribute to the crystal's hygroscopicity.

These mechanisms of surface attack and passivation are important clues to protective interactions that occur between crystal and polymer during the coating process, particularly if it involves very reactive monomers or diamers in plasma form.

Table 2. Theoretical and experimental values of the surface tensions of the {100} faces of the alkali halides.¹³

	<u>Theoretical</u>	γ (dynes/cm)	<u>Experimental</u>
LiF	494		340
LiCl	624		—
LiBr	591		—
LiI	546		—
NaF	741		—
NaCl	438		227
NaBr	386		—
NaI	341		—
KF	495		—
KCl	264		110
KBr	229		—
KI	191		—
RbF	427		—
RbCl	222		—
RbBr	192		—
RbI	176		—
CsF	371		—

IV. MOISTURE PROTECTION FROM BULK PROPERTIES OF POLYMER FILMS

There are two properties of polymers that will be important in determining their suitability as moisture barriers for high-power optics: permeability and solubility. The transmission of a penetrant through a high-integrity polymer layer normally occurs by an activated diffusion process.¹⁴ After condensing on the surface, the penetrant dissolves in the surface layers, migrates through the bulk driven by a concentration gradient, and evaporates at the low-concentration surface. The transmission rate J is defined as the amount of penetrant passing per unit time through a unit area normal to the flow, that is

$$J = Q/At \quad , \quad (3)$$

where Q is the total amount of penetrant passed through area A in time t . Under steady-state conditions, the rate of permeation will be a constant proportional to the concentration gradient (Fick's first law of diffusion),

$$J = D \frac{\partial c}{\partial x} \quad , \quad (4)$$

where c is the concentration of penetrant in the film, x is the distance along the flow direction, and D is the diffusion constant. For homogeneous materials, for which the diffusion constant is independent of concentration, (4) may be integrated over the sample thickness ℓ to give

$$J = D(c_1 - c_2)/\ell \quad , \quad (5)$$

where c_1 and c_2 are the equilibrium concentrations of penetrant in the surface layers on each side of the sample. The equilibrium concentration of penetrant

in a surface layer is proportional to the partial pressure of the ambient gaseous phase p ,

$$c = Sp, \quad (6)$$

where S is the solubility of the penetrant in the polymer. When Henry's law is obeyed there is a linear relationship between concentration and pressure, and the solubility of one penetrant will be a function of temperature only, independent of any other penetrant concentration. In this case the transmission rate is

$$J = DS(p_1 - p_2)/\ell \quad (7)$$

which gives a working definition of the permeability constant,

$$P \equiv DS = \frac{J\ell}{(p_1 - p_2)} = \frac{Q\ell}{At(p_1 - p_2)}, \quad (8)$$

where (3) was used for J in the last step. Most experimental data on polymers is given in terms of the solubility and permeability constants, rather than the diffusion constant. Under isothermal conditions, the atmospheric gases, other than water vapor, obey the assumptions used above over a wide range of pressures, temperatures, and polymers. Water often deviates strongly from these linear relationships because it is well below its critical temperature and therefore condenses easily, is a relatively good solvent of some polymers, and interacts by hydrogen bonding.

However, if there is very little interaction between the polymer and water, for coating applications the only important thermodynamic dependence of the permeability, diffusivity or solubility is on the temperature. Over small temperature ranges, the temperature dependence of P , D or S can be represented by an

Arrhenius-type relation,

$$X = X_0 \exp \left\{ -E_X / RT \right\} , \quad (9)$$

where X stands for P , D , or S and E_X is the apparent activation energy for that process. For the solubility coefficient, E_S is the apparent heat of solution into the polymer given by

$$E_S = \Delta H_{\text{cond}} + \Delta H_m \quad , \quad (10)$$

where ΔH_{cond} is the molar heat of condensation and ΔH_m is the partial molar heat of mixing. For the permanent atmospheric gases above their critical points, ΔH_{cond} is very small and E_S is just ΔH_m . The heat of solution for these gases is small and positive so the solubility increases slowly with temperature. For more condensable vapors such as water, E_S is negative due to the contribution from the heat of condensation, and the solubility decreases with increasing temperature. The activation energy E_D for diffusion is associated with the energy required to form a hole in the polymer for the solute molecule against the cohesive forces of the polymer matrix, plus that required to force the molecule through the matrix. If the penetrant does not plasticize the matrix, E_D will normally be positive and larger than E_S , so their sum, the permeability energy, is positive and the permeability increases with increasing temperature.

Table 3 lists the water solubilities and permeabilities for some of the more hydrophobic polymers which have surface energies less than 50 ergs per cm^2 . The permeabilities were calculated from the transmission rates given by Baer¹⁴ with the exception of the values for the parylene polymers which come from S. M. Lee.¹⁵ Polychlorotrifluoroethylene, with $S = 10^{-2}$ weight percent and

Table 3. Permeabilities and solubilities of water in organic polymers.

Polymer	Temperature. C	S { weight % H_2O , 24-hr im- mersion, 1/8" thick sample }	P { $\frac{gm\ \mu m}{cm^2\ s\ mmHg}$ }
Polyethylene (0.92 g/ml) ~ 60%*	39	< 0.1	1.70
(0.94 g/ml) ~ 69%	37	< 0.1	0.945
(0.95 g/ml) ~ 75%	38	< 0.1	0.429
(0.96 g/ml) ~ 81%	37	< 0.1	0.270
Polypropylene	38	0.005-0.03	0.556
Polyvinyl chloride	38	0.03	2.05
Polyvinylidene chloride ("Saran")	39	< 0.1	0.091-0.424
Polyvinyl fluoride	40	< 0.5	2.64
Polychlorotrifluoroethylene ("Kel-F")	40	< 0.01	0.287
Fluorinated poly(ethylene-propylene)	40	< 0.01	0.414
Polytetrafluoroethylene ("Teflon")	40	0.00	0.287
Chlorinated polyether	36	0.01	0.499
Polyethylene terephthalate ("Mylar")	39	0.03-2.5	1.818
Polycarbonate	20	0.35	5.62
Parylene C	40	-	0.122
Parylene D	40	-	0.124
Parylene N	40	-	0.852

* % of polymer in a crystalline state

$P = 2.9 \times 10^{-9} \text{ g } \mu\text{m}/\text{cm}^2 \text{ s mmHg}$ at 40°C , is typical of the low moisture absorption, low-permeability polymers in Table 3. For a film of this polymer $1 \mu\text{m}$ thick, the mass of absorbed water per unit area is

$$q_w = \rho S \ell = 2.1 \times 10^{-8} \text{ g/cm}^2 , \quad (11)$$

where the density of the polymer is $\rho = 2.1 \text{ g/cm}^3$. The transmission rate is given by

$$J = \frac{Q}{At} = \frac{(p_1 - p_2)P}{\ell} = 1.6 \times 10^{-7} \text{ g/cm}^2 \text{ s} \quad (12)$$

if $p_1 = P_{\text{H}_2\text{O}}^\circ (40^\circ\text{C}) = 55.32 \text{ mmHg}$ and $p_2 = 0 \text{ mmHg}$. While these vapor pressures are typical of those used in transmission measurements on unsupported films, a more realistic steady-state boundary condition at the salt surface would be $p_2 = P_{\text{H}_2\text{O}}^* (\text{KCl}) = 0.8 P_{\text{H}_2\text{O}}^\circ (40^\circ\text{C})$ which reduces the transmission rate by a factor of five. Two monolayers of water have a surface mass density given by

$$q_2 = 2 \left[\frac{N_0 \rho}{m} \right]^{2/3} = 6.2 \times 10^{-8} \text{ g/cm}^2 , \quad (13)$$

where N_0 is Avogadro's number, m the molecular mass and ρ the density of water. Thus only two seconds are required to transport enough water to reach the acceptable limit for optical absorption, and several minutes should be sufficient to dissolve the salt surface and release the film.

Most experimental work on high-quality, pinhole-free films is in direct conflict with these dire theoretical predictions. Hollahan, et al.¹ reported no apparent attack on crystals of NaCl coated with $0.98 \mu\text{m}$ of polytetrafluoroethylene for five days, or on hygroscopic CsI coated with $1.2 \mu\text{m}$ of polytetrafluoroethylene for

30 days, when both samples were exposed to 88.8 percent relative humidity at 20 C. Tibbitt, et al.² reported protection of NaCl for a month against the atmosphere at room temperature when coated with 15 μm of polyethylene or 5 μm of polyethane. In addition, the infrared spectrum of the polyethane film showed no change after exposure to the atmosphere, although it was not sensitive enough to detect the absorption from two monolayers of water.

In the remainder of this section we discuss the physical properties that can modify the bulk permeability of a polymer layer, with particular emphasis on the properties relevant to plasma polymerized films. The following properties tend to be progressively more effective at increasing the water-vapor permeability:

- Amorphous polymers
- $T > T_{\text{glass}}$
- Solvent entrapment
- Sintered polymers
- Plasticizers
- Polar, hydrophilic polymers,

while the following properties progressively decrease the permeability:

- Polar, hydrophobic polymers
- Nonpolar polymers
- Major polymer chains oriented perpendicular to the diffusion path
- High degree of cross-linking
- High crystallinity or $T < T_{\text{glass}}$.

Consider the first group of polymer properties. Amorphous polymers tend to be less tightly packed than crystalline polymers, which leaves more room for diffusion of such small molecules as water. In addition, if the temperature is above the glass temperature of the polymer, the matrix flows or creeps more easily, reducing the energy required for diffusion.¹⁶ Solvent entrapment occurs because the polymer was "blown" from a solution resin or extruded from a powdered resin with the aid of a lubricant. The former is common for films of nylon or acrylics while the latter is common for the fluoropolymers.¹⁷ In addition, fluoropolymers are often produced by extrusion of powders with heat, producing a sintered network of small voids. Both of these properties allow water to diffuse through voids or solvent-filled voids at much higher rates than through solid polymers. Plasticizers may act somewhat as trapped solvents, but are usually added to insure low crystallinity or cross-linking with resultant high permeability. Finally, polar, hydrophilic polymers react with water to form distended gels which pass the water by very rapid self-diffusion. In this case the addition of hydrophobic plasticizers may dramatically reduce the permeability because it prevents the interaction between the polymer and water.

Consider the properties which decrease the permeability. Polar, hydrophobic polymers are distinguished from their hydrophilic counterparts by having internal and external surface energies lower than those of water. Nonpolar polymers have even lower surface energies, but the dissimilar chemical nature of the polymer and water contributes most of the reduction in permeability and solubility. The last three factors in the list all act to decrease the permeability by increasing what has been called the tortuosity factor, which accounts for anomalously long

diffusion paths caused by obstructions, such as cross links, or gross regions of crystallites where the penetrant is completely excluded. The effect of crystallinity is clearly seen in the more than six-fold reduction in the permeability for the different density polyethylenes as the crystallinity varies from 60 to 81 percent as shown in Table 3. Cross-linking severely limits absorption because the additional bonds prevent swelling beyond a certain limit. Crystallinity has a similar effect if the penetrant is not a solvent of the polymer and is excluded from the crystallites.

Figure 8 shows absorption data for methyl bromide in different densities or crystallinities of polyethylene. In Fig. 8a the mass of sorbed vapor (defined as absorbed plus adsorbed) has been normalized to the total mass of the polymer for the three different crystallinities. This results in three different sorption isotherms, which proffers the unlikely interpretation that the different crystallinities correspond to significantly different chemical potentials with respect to the solvent. When the mass of vapor is normalized to the amorphous content of each sample as in Fig. 8b, one isotherm results, providing strong evidence that the crystalline portions of the polymer are effectively impermeable to the solvent.

The data given by Baer¹⁴ in Table 3 come from a wide variety of sources so the actual state of the polymer is in doubt. Commercial plastic films are not likely to be highly crystalline or highly cross-linked, but are likely to have entrapped solvents or polymerizing agents as well as pinholes and voids. For these reasons, very thin polymer layers made by plasma polymerization, which are obviously solvent-free and known to be highly cross-linked and defect-free in some cases,^{19, 20} are likely to have $S < 10^{-3}$ weight percent and $P < 10^{-10}$ $\text{g}\mu\text{m}/\text{cm}^2 \text{s mmHg}$. The parylenes listed in Table 3 have been produced in this

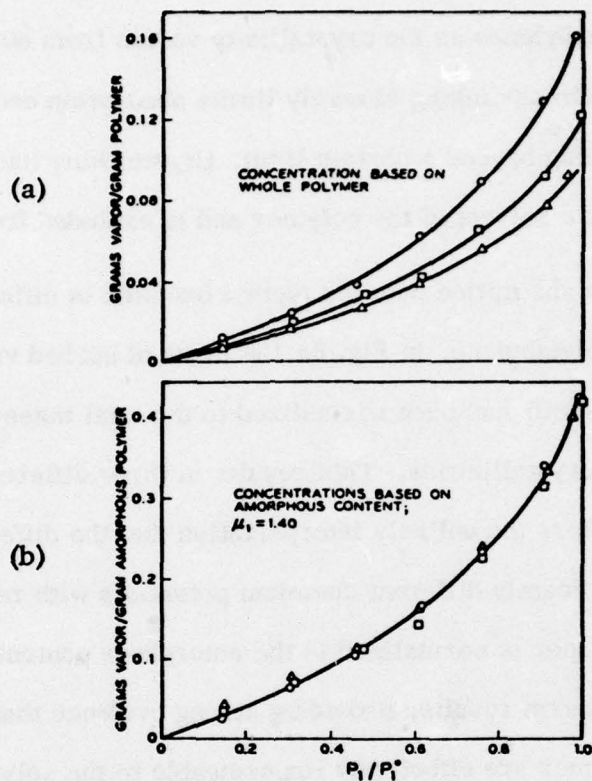


Fig. 8. Sorption isotherms for methyl bromide and different density polyethylenes at C: ¹⁸

- 0.922 g/cm³, 60 percent crystalline
- 0.938 g/cm³, 69 percent crystalline
- △ 0.954 g/cm³, 78 percent crystalline.

way and have among the lowest permeabilities, but the method of removing them from the substrate is not indicated by Lee,¹⁵ so it is possible they suffered damage during removal which increased their permeability. If the films had been deposited on a soluble substrate such as the alkali halides, the substrate could be dissolved leaving the film physically undamaged. This procedure will be necessary for unsupported testing of the very thin films used in antireflection and environmental coatings for infrared optics.

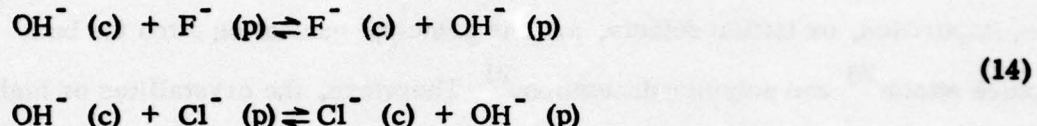
V. SURFACE INTERACTIONS LIMITING WATER PERMEABILITY

It is clear from the results of the previous section that permeabilities measured on unsupported polymer films must differ by some four or five orders of magnitude from values for films deposited on solid substrates if they are to account for the extended protection of CsI reported by Hollahan, et al.¹ Since it is unlikely even these high quality films can account for such a large discrepancy, it appears that one of the following mechanisms is responsible for the additional moisture protection:

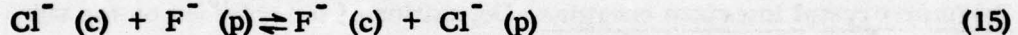
- Interaction between the substrate surface and the polymeric plasma to chemically passify the surface or its moisture attack sites
- Nucleation of polymer deposition at moisture-attack sites to provide preferential protection from low local permeabilities
- Reduction in the surface energy at the crystal surface from the crystal-air value to the crystal-polymer value
- Limitation on the size of condensation droplets by the pore sizes of hydrophobic polymers making it energetically unfavorable for water to condense, and allowing attack on the crystal by vapor only.

Chemical passification. During plasma polymerization, a large number of highly reactive species that are formed by dissociation may participate in surface-scrubbing reactions to remove undesirable surface ions such as OH^- . For example, Hollahan, et al., note that plasma-polymerized polychlorotrifluoroethylene does not have the strong absorption from the C-C1 bond at 972 cm^{-1} typical of the conventionally polymerized polymer. This indicates that the chlorine was almost completely dissociated from the diamers prior to polymerization

and replaced by fluorine. Therefore, it is certain that such species as Cl^- , Cl , and Cl_2 are present in the plasma, and it is very likely that F^- , F , and F_2 also are present because the C-F bond strength is $\sim 100 \text{ kcal mol}^{-1}$ (4.3 eV per bond) compared to $\sim 85 \text{ kcal mol}^{-1}$ for the C-Cl bond. During the initial moments of polymer deposition these species can remove the hydroxide ions by such scrubbing reactions as



where p stands for the plasma state and c for the crystal. There may also be some replacement reactions involving the anions of the salt crystal that are in high-energy surface sites. For example,



could occur in NaCl or KCl . The scrubbing reactions take place very fast because of the high activity and concentration of reactants in the plasma, but they will be effective only for less than 0.1 s because they are shut off once a monomeric layer is deposited. Under these conditions, plasma-polymerized deposition may remove the immediate surface hydroxide ions, which are likely to be the nucleation sites for moisture attack, and then effectively passivate the site with a polymer coating.

Replacement reactions such as (15) may be contraproductive because they usually increase the optical surface absorption while having an ambiguous effect

on the crystal's hygroscopicity. Referring to Table 1 indicates that the conversion of NaCl to NaF will significantly reduce the surface solubility, but conversion of KC1 to KF will make the surface deliquescent.

Nucleation of deposition. The data on different percentage crystalline polyethylenes given in Fig. 8 and Table 3 indicate that perfect polymer crystallites are not permeable to nonsolvent penetrants. High-energy regions, such as cleavage steps, impurities, or lattice defects, are the principal nucleation sites for both moisture attack²⁰ and polymer deposition.²¹ Therefore, the crystallites or highly cross-linked globules are preferentially located directly over the most interactive surface features of the substrate. This self-tailoring of the polymer film to the surface defects in conjunction with a mechanism to prevent diffusion along the polymer-substrate interface could significantly reduce the effective permeability below that measured for the unsupported film.

Polymer-crystal interface energies. Deposition of the polymer on the substrate brings the salt surface into intimate contact with a polymer surface usually consisting of fluorines, chlorines, or hydrogens. This juxtaposition reduces the free surface energy of the interface f_{cp} below that of the crystal γ_c by the surface energy of the polymer γ_p ,

$$f_{cp} = \gamma_c - \gamma_p . \quad (16)$$

As a first approximation the value of the free energy of a polymer-crystal interface could be found by subtracting the polymer surface energies in Table 4 from the crystal surface energies in Table 2. If this were correct, then most polymer-crystal combinations would have $f_{cp} > \gamma_{H_2O} = 72 \text{ ergs/cm}^2$, indicating that

Table 4. Critical surface tensions of various polymeric solids.²²

<u>Polymeric Solid</u>	γ_p <u>Dynes/Cm at 20 C</u>
Polymethacrylic ester of ϕ' -octanol	10.6
Polyhexafluoropropylene	16.2
Polytetrafluoroethylene	18.5
Polytrifluoroethylene	22
Poly(vinylidene fluoride)	25
Poly(vinyl fluoride)	28
Polyethylene	31
Polytrifluorochloroethylene	31
Polystyrene	33
Poly(vinyl alcohol)	37
Poly(methyl methacrylate)	39
Poly(vinyl chloride)	39
Poly(vinylidene chloride)	40
Poly(ethylene terephthalate)	43
Poly(hexamethylene adipamide)	46

water reaching the surface can reduce the interface energy by condensing at the interface and separating the polymer from the crystal. In fact, as noted at the end of Sec. III, Pastor and Braunstein have found that water does not wet the surface of high quality KCl or NaCl crystals, indicating that $\gamma_c < \gamma_{H_2O}$. Thus, f_{cp} will be significantly less than γ_{H_2O} and it will not be energetically favorable for a very thin layer of water to condense between the film and the substrate.

This estimate of the interface energy is crude at best because it requires the coating process to take place in thermodynamic equilibrium, ignoring the kinetic nature of coating growth. Similar objections apply to calculations of the reversible work of adhesion of the film per unit area based on the reduction of surface energy when the solid is coated with a monolayer of monomers or diamers.^{3, 14}

Limitation of condensation by polymer pore sizes. In the precipitation region, even if the crystal is not hygroscopic, the moisture may permeate through the polymer, condense at the polymer-crystal interface, and begin to dissolve the salt. It appears that this could be prevented if the polymer has sufficiently hydrophobic surfaces, the cracks and voids in the coating are small near the polymer-crystal interface, and the polymer is free of any contaminants that reduce its hydrophobic properties. The objective is to keep the water in vapor form by confining it to such small hydrophobic voids that the energy gained by condensation is less than that required to form the liquid water-polymer interface.

For a system consisting of two phases of a substance separated by a plane interface, the temperature, chemical potential, and pressure must be constant throughout the system. If the interface is curved, there will be additional forces exerted and the pressures of the two phases will no longer be equal. For a sphere

of liquid with radius r_0 surrounded by saturated vapor, the surface pressure difference is given by

$$p_l - p_v = \frac{2\gamma}{r_0} , \quad (17)$$

where γ is the surface-tension coefficient, p_l the pressure in the liquid, and p_v the pressure in the vapor. Equation (17) gives only the pressure difference, but the pressures of the two phases can be calculated separately,

$$p_l - p_0 = \frac{2\gamma}{r_0} , \quad (18)$$

$$\frac{p_v}{p_0} = 1 + \frac{2v_l \gamma}{r_0 k_B T} , \quad (19)$$

where p_0 is the common pressure of the phases with a plane interface at temperature T , v_l the molecular volume of the liquid, and k_B is Boltzmann's constant. Since γ must be positive for the drop to be in equilibrium, the vapor pressure in equilibrium with a liquid drop is greater than the saturated vapor pressure over a plane liquid surface, and increases with decreasing drop radius. These expressions are only valid if the vapor is regarded as an ideal gas and $(p_v - p_0)/p_0 \ll 1$; the latter implies that the drop is relatively large.

For small drops and large vapor pressures, (19) should be replaced by the Kelvin equation²³

$$\ln \left(\frac{p_v}{p_0} \right) = \frac{2\gamma v_l}{r_0 k_B T} , \quad (20)$$

which requires very small drops to have substantially higher equilibrium vapor pressures than Eq. (19). This equation can be used to approximate condensation

Sec. B

within an idealized spherical void of a hydrophobic polymer if the surface tension is replaced by an effective surface tension²⁴

$$\gamma_e = \gamma_{H_2O} - \gamma_p . \quad (21)$$

Now consider the nucleation of a water droplet in a supersaturated vapor. The probability of creating a droplet of radius r is proportional to $\exp(-G/k_B T)$, where G is the Gibbs free energy required to form one droplet,

$$G = \frac{4\pi}{3} r^3 g + 4\pi r^2 \gamma \quad (22)$$

and g is the increase in Gibbs free energy per unit volume. The condition for equilibrium is

$$\left(\frac{\partial G}{\partial r}\right)_{r=r_0} = 0 , \quad (23)$$

which gives $r_0 = -2\gamma/g$. If this value is substituted in Eq. (20), g is found to be negative for $p_v > p_0$ and equal to zero for $p_v = p_0$. Thus, there is a critical droplet radius in a supersaturated vapor at which the droplet would tend neither to grow nor evaporate, while all droplets tend to evaporate for $p_v \leq p_0$. Therefore, the Gibbs free energy required to form a stable droplet is just that of a droplet of the critical radius,

$$G_0 = \frac{4\pi}{3} \gamma r_0^2 . \quad (24)$$

The concentration of critical-sized droplets is just

$$n_0 = n_v e^{-G_0/k_B T} , \quad (25)$$

where n_v is the concentration of vapor molecules. These droplets will become supercritical if one more molecule is added. From the kinetic theory of gases, the number of gas molecules striking a unit area per unit time is $n_v \bar{v} / 4$, where \bar{v} is the average velocity. Since the surface area of the droplet is $4\pi r_0^2$, the time required for one molecule to hit the droplet is $(n_v \bar{v} \pi r_0^2)^{-1}$ and the nucleation rate per unit volume is just:

$$I = \pi r_0^2 \bar{v} n_v^2 \exp(-4\pi\gamma r_0^2 / 3k_B T) . \quad (26)$$

Since r_0 is a known function of the pressure, and the vapor obeys the ideal gas law, the nucleation rate is given in terms of the pressure.

The pre-exponential factor in (26) is relatively independent of pressure because the concentration is proportional to the pressure and r_0 is inversely proportional to the logarithm of the pressure. Since the polymer surface completely shields a portion of the droplet surface from impinging vapor molecules and obstructs the free passage of vapor molecules to the remaining surface, the time required for the droplet to gain an additional molecule is probably several orders of magnitude larger than estimated from kinetic gas theory and the pre-exponential factor correspondingly smaller. In addition, Eq. (25) assumes that the whole volume is filled with vapor and should be corrected for the volume fraction occupied by the polymer. If this correction is about 10^{-3} then Eq. (26) predicts nucleation rates about 10^5 times greater than actually expected in clean polymers. However, the nucleation rate given by Eq. (26) is most sensitive to errors or variations in the surface tension of the polymer since $I \sim \exp \gamma^3$ according to (26) with r_0 given by (20).

Table 5 shows the nucleation rate and critical droplet radius vs the supersaturation ratio p_v/p_0 : for pure water, $\gamma_{H_2O} = 72 \text{ ergs/cm}^2$, and for water in a typical fluoropolymer, $\gamma_e = 52 \text{ ergs/cm}^2$; a hydrocarbon polymer, $\gamma_e = 42 \text{ ergs/cm}^2$; and a chlorocarbon polymer, $\gamma_e = 32 \text{ ergs/cm}^2$. N_{H_2O} is the number of water molecules in a critical-sized droplet. In rare-gas liquids approximately two molecular layers are necessary to form the surface.²⁵ If this same criterion is applied to water, then the smallest droplet radius for which (22) is meaningful is $r_0 \sim 0.6 \text{ nm}$, which gives $N_{H_2O} \sim 30$ molecules. The results of Table 5 can be expressed in terms of the supercooling, $T - T_0$, instead of the supersaturation ratio by using Clapeyron's equation,

$$p_v - p_0 = \frac{q}{T_0(u_v - u_f)} (T - T_0) \quad , \quad (27)$$

where q is the molecular heat of transition from the metastable vapor phase to the liquid phase.

If a polymer is characterized by its maximum void radius r^* and surface tension γ_p , then a maximum supersaturation ratio could be found from Eq. (20) by setting $r_0 = r^*$ and $\gamma = \gamma_e$ which insures there is no condensation within the polymer at lower pressure ratios. However, this is not the optimum choice for $(p_v/p_0)_{\max}$ because it may correspond to extremely large values of the nucleation rate, which makes the film very sensitive to fluctuations in p_v/p_0 , or to $I \sim 0$, thereby underestimating the protective ability of the film. A better definition for $(p_v/p_0)_{\max}$ is $(p_v/p_0)_{I=I^*}$, where I^* is an acceptable nucleation rate depending on such things as the film thickness, damage incurred per nucleation, acceptable damage levels per unit area, and the number of temperature or

Table 5 shows the nucleation rate and critical droplet radius vs the supersaturation ratio p_v/p_0 : for pure water, $\gamma_{H_2O} = 72 \text{ ergs/cm}^2$, and for water in a typical fluoropolymer, $\gamma_e = 52 \text{ ergs/cm}^2$; a hydrocarbon polymer, $\gamma_e = 42 \text{ ergs/cm}^2$; and a chlorocarbon polymer, $\gamma_e = 32 \text{ ergs/cm}^2$. N_{H_2O} is the number of water molecules in a critical-sized droplet. In rare-gas liquids approximately two molecular layers are necessary to form the surface.²⁵ If this same criterion is applied to water, then the smallest droplet radius for which (22) is meaningful is $r_0 \sim 0.6 \text{ nm}$, which gives $N_{H_2O} \sim 30$ molecules. The results of Table 5 can be expressed in terms of the supercooling, $T - T_0$, instead of the supersaturation ratio by using Clapeyron's equation,

$$p_v - p_0 = \frac{q}{T_0(v_v - v_l)} (T - T_0) \quad , \quad (27)$$

where q is the molecular heat of transition from the metastable vapor phase to the liquid phase.

If a polymer is characterized by its maximum void radius r^* and surface tension γ_p , then a maximum supersaturation ratio could be found from Eq. (20) by setting $r_0 = r^*$ and $\gamma = \gamma_e$ which insures there is no condensation within the polymer at lower pressure ratios. However, this is not the optimum choice for $(p_v/p_0)_{\max}$ because it may correspond to extremely large values of the nucleation rate, which makes the film very sensitive to fluctuations in p_v/p_0 , or to $I \sim 0$, thereby underestimating the protective ability of the film. A better definition for $(p_v/p_0)_{\max}$ is $(p_v/p_0)_{I=I^*}$, where I^* is an acceptable nucleation rate depending on such things as the film thickness, damage incurred per nucleation, acceptable damage levels per unit area, and the number of temperature or

Table 5. Nucleation rate of critical-sized water droplets as a function of the supersaturation ratio P_v/P_0 , for water alone and several water-polymer combinations. Parameters used in Eq. (26) are $T = 300\text{ K}$, $\bar{v} = 5.94 \times 10^4 \text{ cm/s}$, $v_l = 3 \times 10^{-23} \text{ cm}^3$, $P_0 = 27 \text{ mmHg}$ at 300 K , and n_v is found by using the perfect gas law.

P_v/P_0	$\gamma_{H_2O} = 72 \text{ ergs/cm}^2$			$\gamma_e = 52 \text{ ergs/cm}^2$			$\gamma_e = 42 \text{ ergs/cm}^2$			$\gamma_e = 32 \text{ ergs/cm}^2$		
	r_0 nm	N_{H_2O}	$\frac{I}{\text{nuclei}} \frac{\text{cm}^3}{\text{s}}$	r_0 nm	N_{H_2O}	$\frac{I}{\text{nuclei}} \frac{\text{cm}^3}{\text{s}}$	r_0 nm	N_{H_2O}	$\frac{I}{\text{nuclei}} \frac{\text{cm}^3}{\text{s}}$	r_0 nm	N_{H_2O}	$\frac{I}{\text{nuclei}} \frac{\text{cm}^3}{\text{s}}$
1.25	4.68	14,000	0	3.38	5,400	0	2.73	2,834	0	2.08	1,250	10^{-33}
1.5	2.57	2,400	0	1.86	900	10^{-51}	1.50	472	10^{-14}	1.14	209	10^9
1.75	1.86	905	0	1.35	340	10^{-14}	1.09	180	10^6	0.83	80	10^{18}
2	1.51	476	10^{-44}	1.09	180	10	0.88	95	10^{13}	0.67	42	10^{21}
3	0.95	120	1	0.69	45	10^{17}	0.55	24	10^{22}	0.42	10	10^{25}
4	0.75	60	10^{10}	0.54	22	10^{21}	0.44	12	10^{24}	0.34	5	10^{26}
20	0.35	6	10^{37}	—	—	—	—	—	—	—	—	—

pressure cycles expected during the component's lifetime. This choice will never be too large, but if r^* is very small, $(p_v/p_0)_{r_0=r^*}$ will be larger than $(p_v/p_0)_{I=I^*}$ and an intermediate value should be chosen.

Originally it was hoped that the critical sizes given in Table 5 would be smaller than the expected polymer voids for a supersaturation ratio large enough to allow a polymer exposed to 100 percent relative humidity at its maximum environmental temperature to be cooled to its minimum temperature without droplet formation. For example if $T_{\max} = 50^\circ\text{C}$, $P_{\text{H}_2\text{O}}^{\circ} = 92.5\text{ mmHg}$ and $T_{\min} = 0^\circ\text{C}$, $P_{\text{H}_2\text{O}}^{\circ} = 4.58\text{ mmHg}$, then $p_v \approx 20$, which gives $r_0 = 0.35\text{ nm}$ and $I \sim 10^{37}\text{ nuclei/cm}^3\text{ s}$ for pure water vapor. Since there are likely to be many voids of this size in polymers, there will be a large amount of condensate in a film subject to such extreme saturation.

Since the whole environmental range cannot be accommodated, it is necessary to specify a maximum cooling rate for a thin film that allows sufficient water-vapor diffusion out of the film to keep the supersaturation ratio and hence the nucleation rate below specified values. The maximum cooling rate allowed without condensation in the film is given approximately by

$$\left(\frac{\partial T}{\partial t}\right)_{\max} \sim \frac{(T - T_0)_{\max}}{\tau_d} = \frac{T_0 (v_v - v_\ell)}{\tau_d q} \left[\left(\frac{p_v}{p_0}\right)_{\max}^{-1} \right], \quad (28)$$

where $(T - T_0)_{\max}$ is the maximum supercooling and τ_d is the out-diffusion time for supersaturated water vapor through one surface of a thin film maintained at saturation. From Carslaw and Jaeger,²⁶ the condition

$$D \tau_d / \ell^2 \sim 1 \quad (29)$$

will insure that diffusion has reduced the supersaturation ratio to ten percent of its original value everywhere in the film. The diffusion constant for the best projected films is

$$D = \frac{P}{S} \cong \frac{10^{-10} \text{ g } \mu\text{m}/\text{cm}^2 \text{ s mmHg}}{2 \times 10^{-13} \text{ g}/\text{cm}^2 \mu\text{m mmHg}} = 500 \mu\text{m}^2/\text{s} \quad , \quad (30)$$

while typical measured values are 10^2 - 10^4 times larger. Therefore, the out-diffusion time calculated from Eq. (29) is 10^{-2} s for a $1\mu\text{m}$ thick film and 1 s for a $10\mu\text{m}$ thick film. However, there is probably a significant boundary resistance to transferring a molecule of water from the supersaturated polymer matrix to either a surface film of water or an atmosphere saturated with water vapor. For thin films this resistance will place a lower limit on the effective diffusion time used in Eq. (28). Since no data on this effect has been found for a supersaturated film, care should be exercised when drawing conclusions based on Eq. (29) for the diffusion time.

Table 6 gives the maximum cooling rate for $10\mu\text{m}$ -thick films of the typical polymers considered in Table 5. The maximum supersaturation ratios were found from Eq. (26) for the choice $I^* = 10^6$ nuclei/ cm^3 s and the corresponding supercooling was derived from water-vapor pressure tables²⁷ so that for $10\text{ C} \leq T_0 \leq 100\text{ C}$, $(p_v/p_0)_{\max}$ is never exceeded. Finally, $0.9(T - T)_{\max}$ was used in Eq. (28) to compute the maximum temperature coefficient of the film because τ_d is the time required to reduce the initial supersaturation by 90 percent.

If the rates in Table 6 are within a few orders of magnitude of the correct values for high-quality films, then the slow environmental cycling typical of

Table 6. Maximum supersaturate ratio and cooling rate for $10\text{ }\mu\text{m}$ -thick films of typical polymer types assuming a water droplet nucleation rate of 10^6 nuclei/cm 3 s and a temperature range of $10\text{ }^\circ\text{C} < T_0 < 100\text{ }^\circ\text{C}$.

Polymer	γ_e ergs/cm 2	$(P_v/P_0)_{\text{max}}$	$(T - T_0)_{\text{max}}$ C	$(\partial T/\partial t)_{\text{max}}$ C/s
Fluorocarbon	52	2.20	-11	-9.9
Hydrocarbon	42	1.75	-8	-7.2
Chlorocarbon	32	1.45	-5	-4.5

Sec. B

present testing procedures is too slow to allow water to condense in the film and attack the substrate as a liquid.²⁸ Instead, the attack should parallel the extremely slow attack on an unprotected, highly passivated substrate surface by unsaturated water vapor. Since this is what experimentalists have found, it appears this mechanism may be the cause.

VI. POLYMER ADSORPTION OF WATER

The wettability of low-energy organic surfaces is determined by the nature and packing of the surface atoms of exposed groups of atoms and is otherwise independent of the nature and arrangement of the underlying molecular structure. The basic explanation for this fact is that in the absence of surface ions or large, uncompensated permanent dipoles, the surface atoms in such solids and liquids attract each other by London forces which vary inversely as the seventh power of the distance. Since these forces are very weak and fall off very rapidly, the equilibrium adsorbed film of vapor or liquid can be very thin.

A liquid spreads to form a film on a polymer if the free surface energy γ_p of the polymer in a vacuum is greater than the liquid-saturated vapor surface energy γ_{lv} plus the polymer-liquid surface energy γ_{pl} , that is if

$$S = \gamma_p - (\gamma_{lv} + \gamma_{pl}) > 0 . \quad (31)$$

Since the highest surface energy of common organic polymers listed in Table 4 is 46 ergs/cm² for poly(hexamethylene adipamide), and γ_{lv} for a water-water vapor surface is 72 ergs/cm², S is always less than zero and water will never spread on polymers.

However, even in the absence of a liquid film on the surface, a polymer may adsorb water vapor in sufficient quantities to increase the optical absorption above 10^{-4} per surface. The free energy change on immersion of a polymer

in a saturated vapor is

$$f_{pv} = \gamma_p - \gamma_{pv} \quad . \quad (32)$$

where γ_{pv} is the free surface energy of a polymer in equilibrium with a saturated vapor. Unfortunately f_{pv} has not been measured for any smooth, low-energy solid surfaces. However, for low-energy solid surfaces it has been found empirically that $f_{pv} \ll \gamma_{lv}$ and that there is negligible vapor adsorption if the liquid exhibits a large contact angle θ on the solid:

$$\gamma_{pv} - \gamma_{pl} = \gamma_{lv} \cos \theta \quad . \quad (33)$$

Bewig and Zisman²⁹ have found adsorption (of much less than a monolayer) of most vapors on both polytetrafluoroethylene and fluorinated poly(ethylene-propylene). Other work cited by Baer¹⁴ indicates that if $\theta > 0$, and particularly if γ_{lv} is several times γ_p , low-energy polymer surfaces are in equilibrium with much less than an adsorbed monolayer of vapor. Thus, adsorbed water vapor should not contribute significantly to the optical absorption of polymer films used as protective environmental coatings on moisture-sensitive optics. This low water adsorption will make polymer coatings extremely important if it is found that water adsorption on nonpolymer high-power optical components causes intolerably great optical absorption.

VII. INFRARED ABSORPTION BY POLYMERS

Most polymers can not be used as environmental coatings on high-power optical components because they have infrared absorptions near $10.6\text{ }\mu\text{m}$ which give absorptions exceeding 10^{-4} per surface even for extremely thin films. The absorption in polymer films comes from a variety of sources in the polymer system: chain modes, branched chain modes, chain termination groups, molecular side groups, included monomers or diamers, polymerization reagents, and extraneous impurities. Except for the chain modes, an initial estimate of the possibility of producing a very low absorption polymer at $10.6\text{ }\mu\text{m}$ can be made by searching infrared correlation charts in the $10\text{-}11\text{ }\mu\text{m}$ region for absorption bands of the components of the polymer system. Such charts, which may be found in Ref. 30 or in Colthup, et al.,³¹ indicate that carbon-carbon double bonds, hydroxyl or carboxyl radicals, oxirane rings, sulfur or halogen ester radicals, and most phosphorous or silicon compounds have absorptions between 10 and $11\text{ }\mu\text{m}$ and should be avoided in polymers used in $10.6\text{ }\mu\text{m}$ optical coatings. In addition, most aromatic or cyclic compounds have weak ring stretching modes and out-of-plane carbon-hydrogen wagging modes which have absorptions between 10 and $11\text{ }\mu\text{m}$. This is the source of much of the absorption in the $10\text{-}11\text{ }\mu\text{m}$ spectral region of atactic polystyrene shown in Fig. 9.

Simple analytic studies of the chain modes have been made by Zbinden,³³ who considered the motions of a linear array of N coupled dipoles of frequency ω_0 . While the total number of modes of the system is N , only the fundamental mode near ω_0 produces an intense absorption band. In this simple chain model,

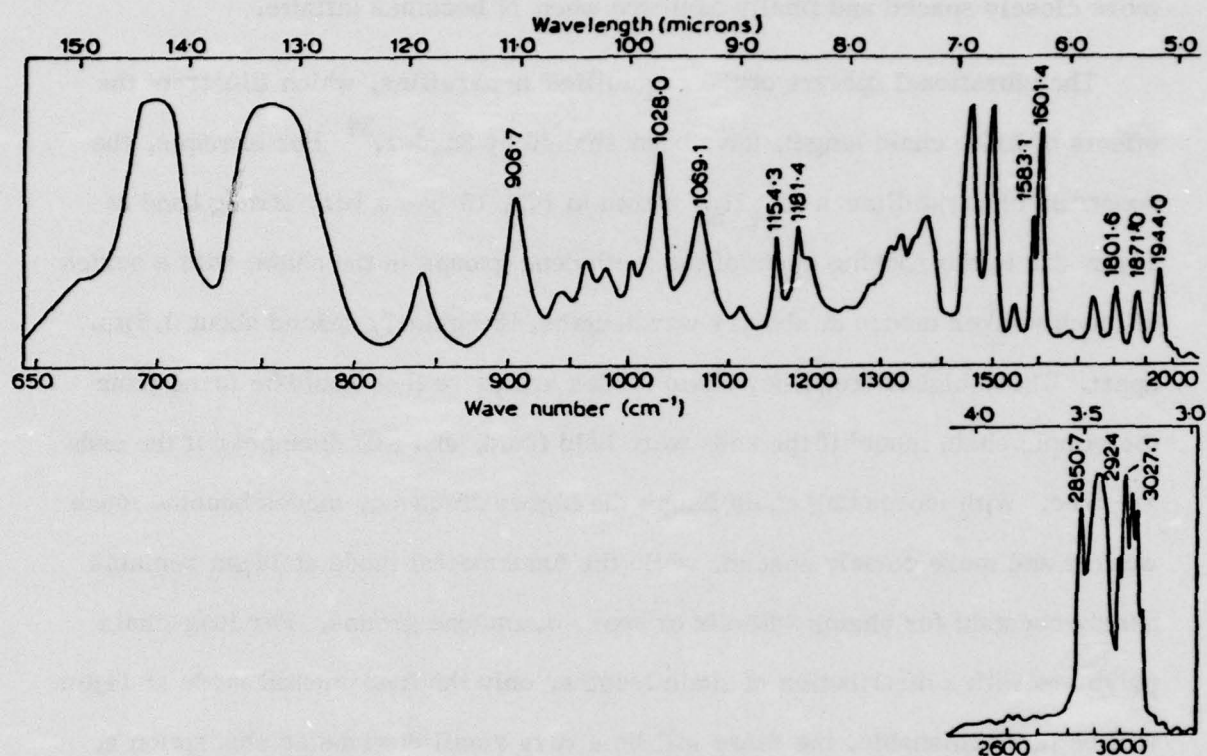


Fig. 9. Spectrum of commercial atactic polystyrene film approximately $25\text{ }\mu\text{m}$ thick.
32
Ordinate of the spectrum is in percent absorption.

the higher frequency modes appear only when the chain is bent, increasing in strength with increasing bending of the chain, but always remaining weak compared to the fundamental mode. As N increases, the component modes become more closely spaced and finally coalesce when N becomes infinite.

The vibrational spectra of the crystalline n-paraffins, which illustrate the effects of finite chain length, have been studied by Snyder.³⁴ For example, the spectrum of crystalline n-C₂₄H₅₀ shown in Fig. 10 has a very strong band at 14 μm due to the rocking mode of the methylene groups in the chain, with a series of much weaker modes at shorter wavelengths, irregularly spaced about 0.5 μm apart. These higher frequency chain modes are those that would be found from the simple chain model if the ends were held fixed, and will disappear if the ends are free. With increasing chain length the higher frequency modes become much weaker and more closely spaced, while the fundamental mode at 14 μm remains nearly constant for chains with six or more methylene groups. For long-chain polymers with a distribution of chain lengths, only the fundamental mode at 14 μm will be distinguishable, but there will be a very small distributed absorption at shorter wavelengths from the weaker, high-frequency chain modes. These modes are extremely important because they are the ones that will probably determine the intrinsic absorption at 10.6 μm for the simpler polymers.

The spectrum of oriented polyethylene in Fig. 11 has the relatively small absorption coefficient of 23 cm^{-1} at 10.6 μm . The small bands that appear on either side of 10.6 μm in the trace of the 0.013-inch thick sample are probably due to either combination bands, side chains, or bent chains in amorphous regions of the polymer sample.

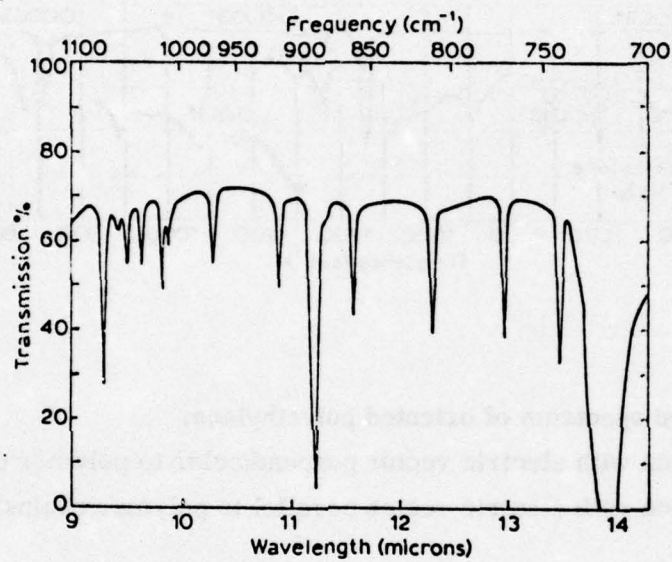


Fig. 10. Spectrum of $n\text{-C}_{24}\text{H}_{50}$ at -160 C.^{35}

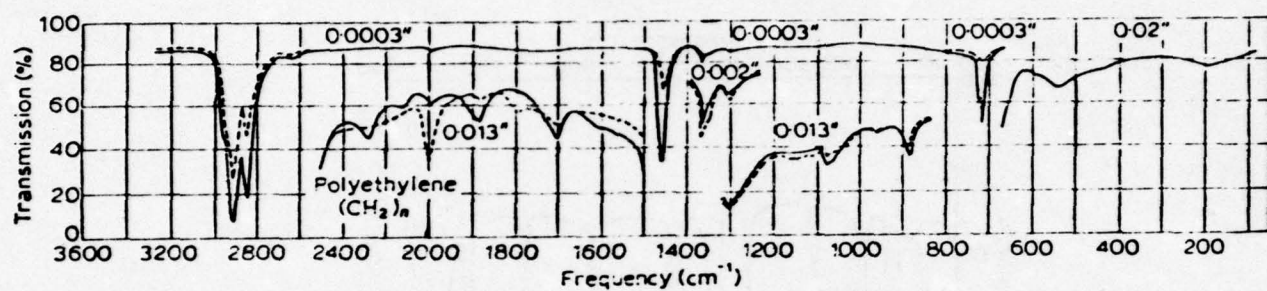
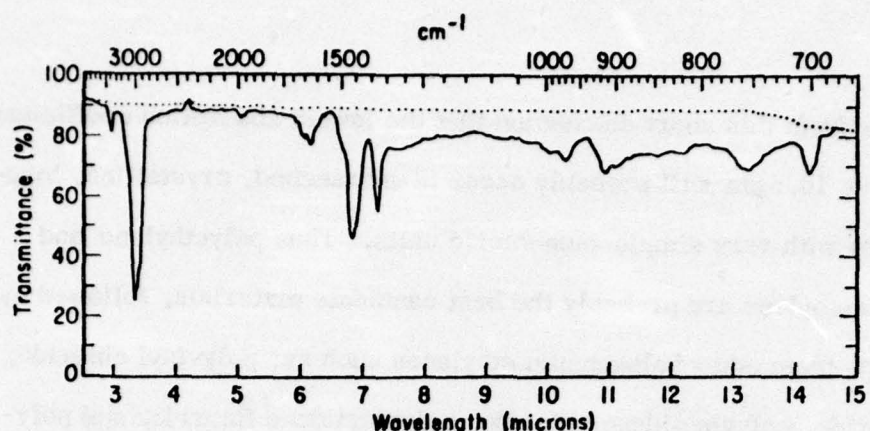


Fig. 11. Infrared spectrum of oriented polyethylene.

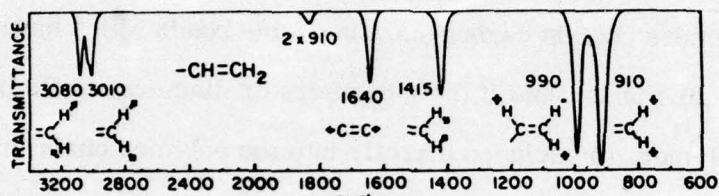
—, radiation with electric vector perpendicular to polymer chains;
- - - - , radiation with electric vector parallel to polymer chains.³⁶

It is clear from this short discussion that the lowest absorption coefficients for polymers at $10.6 \mu\text{m}$ will probably occur in unbranched, crystalline, long-chain polymers with very simple monomeric units. Thus polyethylene and polytetrafluoroethylene are probably the best candidate materials, followed by polymers made from other halogenated ethylenes such as: polyvinyl chloride, polyvinyl fluoride, polyvinylidene chloride, polyvinylidene fluoride, and poly-chlorotrifluoroethylene. The difficulty with these polymer systems is that their monomers or diamers contain carbon-carbon double bonds which have strong absorptions near $10.6 \mu\text{m}$. Thus if the monomers or diamers should become trapped in the polymer, or included directly into the polymer chain in unsaturated form, the spectrum of the polymer will contain these undesirable absorptions.

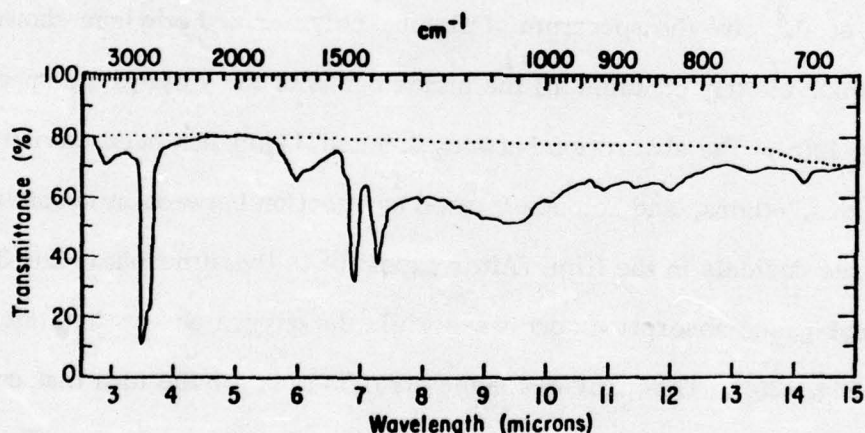
Tibbett, et al.² give the spectrum of plasma-polymerized ethylene shown in Fig. 12(a), which clearly contains all the major bands of the vinyl-group spectrum shown in Fig. 12(b). The absorption between 8.5 and $11 \mu\text{m}$ has been attributed to alkyl hydroxides, ethers, and ketones formed by reaction between atmospheric oxygen and free radicals in the film. After exposure to the atmosphere for 30 days, the vinyl-group absorptions decrease while the oxygen absorptions increase as shown in Fig. 12(c). This provides some confirmation for the idea that unsaturated vinyl bonds are the chief reaction sites for oxygen in the polymer. To avoid these difficulties, Tibbett, et al. polymerized ethane rather than ethylene and found the very simple spectrum shown in Fig. 13, which remained unchanged on exposure to the atmosphere. M. Braunstein recently made microcalorimetric measurements of the absorption coefficient of these polyethane films and found



(a)



(b)



(c)

Fig. 12. (a) Infrared spectrum of uncoated NaCl crystal (dotted line) and the same crystal coated with plasma-polymerized ethylene.² (b) General spectrum of a vinyl group or a vinyl group with an alkane substitute. The arrows indicate atomic movements in the plane of the carbon double bond, while "+" and "-" refer to movement above and below the plane, respectively.³⁷ (c) Infrared spectrum of NaCl coated with plasma-polymerized ethylene after 30 days exposure to the atmosphere.²

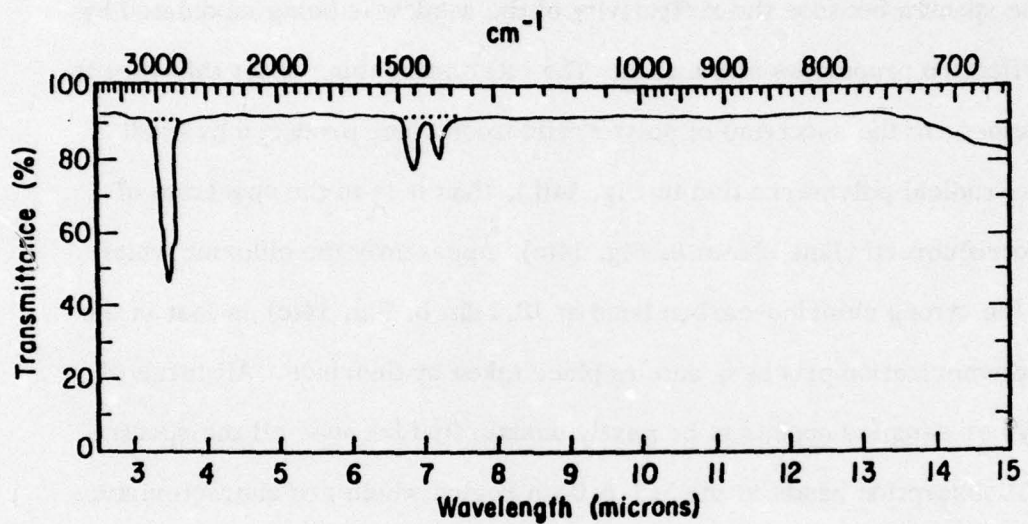


Fig. 13. Infrared spectrum of uncoated NaCl (dotted line), and NaCl coated with plasma-polymerized ethane. The coated spectrum remains unchanged after 30 days exposure to the atmosphere.²

a value of $\beta = 4.7 \text{ cm}^{-1}$.³⁸ This is the lowest reliable value of the absorption coefficient at $10.6 \mu\text{m}$ that we have found for any polymer.

Hollahan, et al.¹ give the spectrum shown in Fig. 14(a) for different thicknesses of plasma-polymerized polychlorotrifluoroethylene deposited on a CsI window. Care should be used in estimating the absorption coefficient of the films from these spectra because the reflectivity of the window is being modulated by the antireflection properties of the film. The interesting thing about this film is that it is closer to the spectrum of polytetrafluoroethylene produced by traditional free-radical polymerization in Fig. 14(b), than it is to the spectrum of polychlorotrifluoroethylene shown in Fig. 14(c). Apparently the chlorine which produces the strong chlorine-carbon band at $10.2 \mu\text{m}$ in Fig. 14(c) is lost in the plasma-polymerization process, and its place taken by fluorines. All three of these polymer samples appear to be partly unsaturated because all the spectra have small absorption bands in the 5.7 - $6.0 \mu\text{m}$ region which are characteristic of substituted tetrafluoroethylene.

The spectra of two other low moisture-permeability polymers are shown in Fig. 15, polypropylene and polyethylene terephthalate. Fig. 15(b) is particularly interesting because it illustrates the differences in absorption that exist between amorphous and crystalline polymers. These differences occur because some vibrations that are present in the amorphous state are not allowed by the symmetry group of the crystalline form, such as those at $11.1 \mu\text{m}$ and $9.6 \mu\text{m}$. Correspondingly, some of the bands that are weak in the amorphous form are stronger in the crystalline form because there is less hindrance of the vibration in the regular crystalline array.

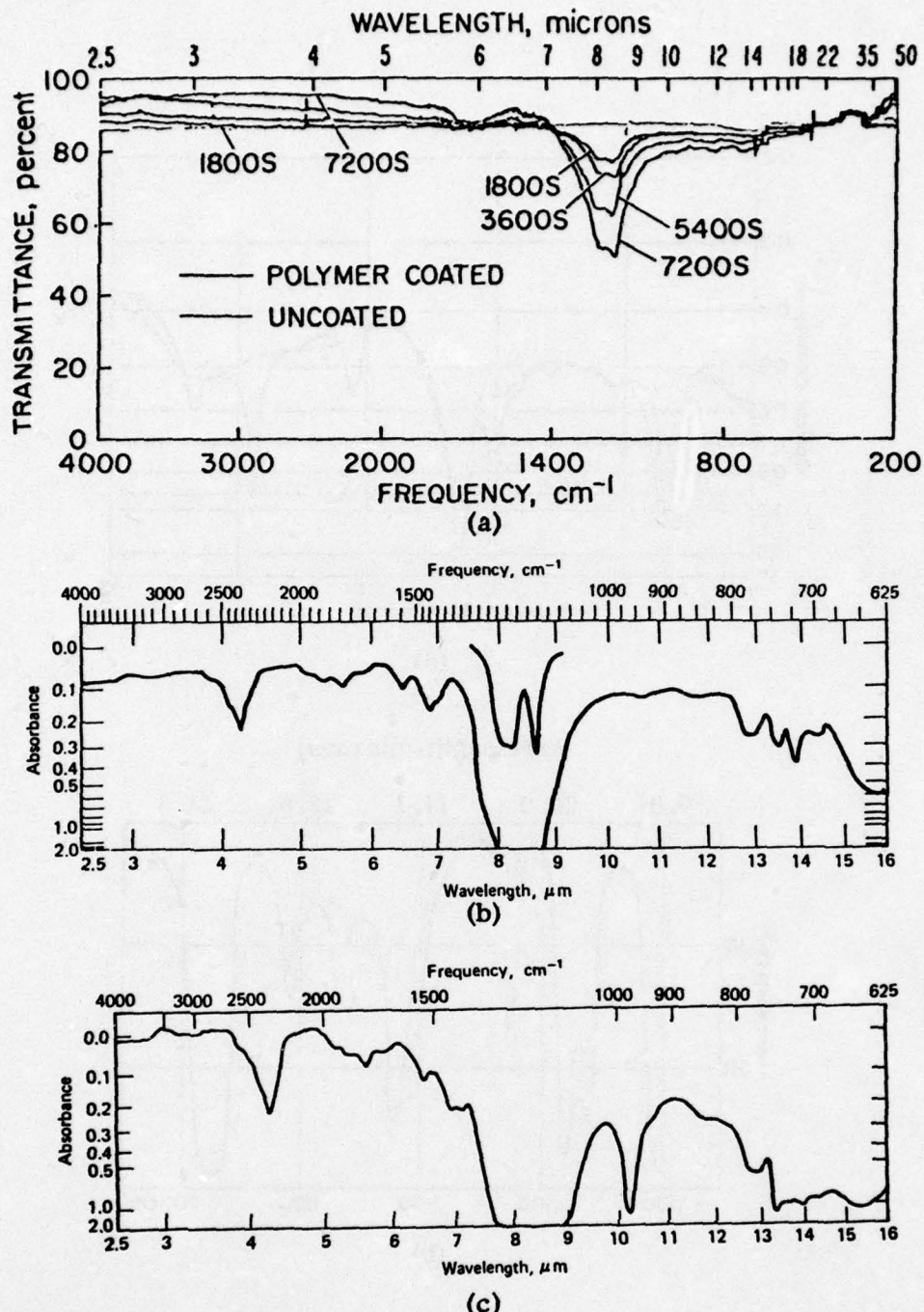
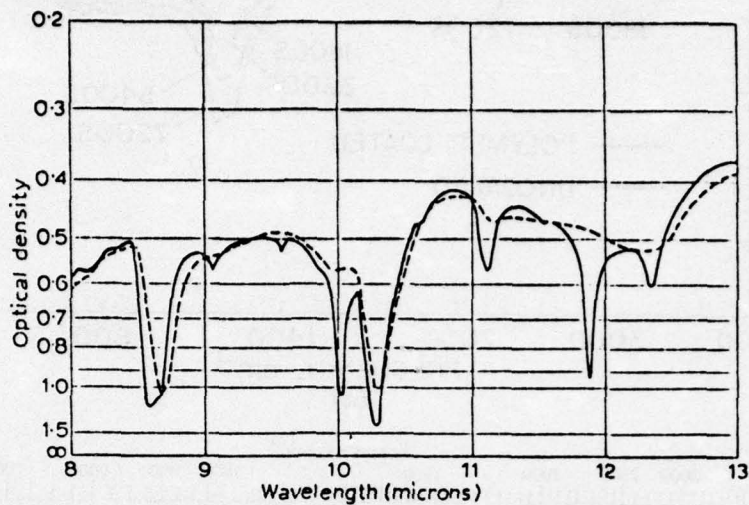
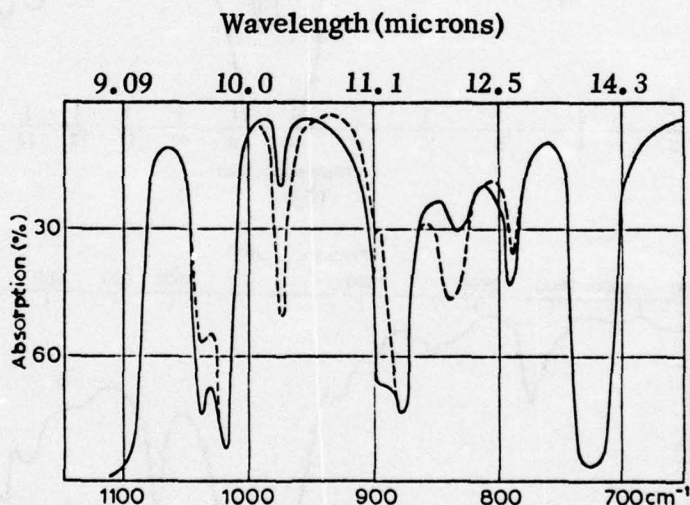


Fig. 14. (a) Infrared spectra of CsI window uncoated, and coated with different thicknesses of plasma-polymerized polychlorotrifluoroethylene. Thicknesses are approximately 0.6 μm per 1800 s of deposition time.¹ (b) Conventionally polymerized polytetrafluoroethylene.³⁹ (c) Conventionally polymerized polychlorotrifluoroethylene showing the C-C1 stretching frequency at 10.2 μm that is absent in (a).³⁹



(a)



(b)

Fig. 15. (a) Infrared spectrum of isotactic polypropylene: —, solid film 76 μ m thick at 20°C; ---, the same film in a molten state between salt plates at 240°C. (b) Infrared spectrum of polyethylene terephthalate: —, totally amorphous; ---, fairly crystalline.⁴⁰

VIII. EXPERIMENTAL TESTING OF POLYMER FILMS

The following list of experiments is suggested to measure various aspects of environmental polymer coatings on soluble substrates, with particular emphasis on those that will establish the physical origins of effectiveness of their moisture-protective properties or their infrared absorption.

Surface energy of crystal substrates. Water droplets on high-quality salt crystals have exhibited large contact angles, indicating that the free surface energy of the solid-gas interface is lower than that of the solid-liquid interface.²⁰ In order to estimate the residual crystal-polymer interface energy and consequently the degree of passification achieved by the coating process, it is necessary to know the initial crystal surface energy. The critical surface energy of wetting for the crystal can be found by measuring the contact angles of progressively lower surface-energy liquids with the crystal, and then extrapolating back to a zero contact angle.¹⁴ To avoid complications arising from dissolving some of the crystal surface or modifying the surface energy of the liquid with dissolved salt, the liquids used for contact angle measurements should not be solvents of the crystal.

Infrared absorption spectra. The infrared absorption spectra of the polymer film is needed to determine the basic polymer structure, the residual impurities from the polymerization process, impurities subsequently acquired from the environment, and the absorption coefficient at the operating wavelengths of the window. The basic polymeric structure of a plasma-polymerized film, which may differ from that produced by traditional polymerization methods with the

same monomer or diamine, can be determined from the spectra of a 10-50 μm thick layer using an ordinary infrared spectrometer. However, the absorption from impurities and the very low absorptions at operating wavelengths may be sensitive to film thickness and should be determined on films close to those used in practice. Laser-calorimeter measurements can be used to determine very small film absorptions at a few operating wavelengths, but attenuated-total-reflectance (ATR) spectroscopy is the best currently available method for measuring the absorption as a function of wavelength. In ATR spectroscopy the beam is propagated (by total internal reflection) between the coated surfaces of a thin plate. The reflecting angle of this mode is determined by refraction into a plate edge normally cut at 45°. This angle may need to be varied for some film-substrate combinations because it will not maintain the total internal reflection condition at either the film-air or film-substrate boundary over the whole range of wavelengths.

Finally, the coatings should be tested at high laser power to ascertain the damage threshold of the film.

Pinholes in polymer films. The initial environmental test is designed to locate pinholes in the coating. The existence of pinholes in a film indicates a failure to produce a contiguous film and as such are not an intrinsic film property, but they will bias subsequent permeability measurements. Pinholes in films deposited on alkali-halide crystals can be located by observing the sample under a microscope while breathing on the sample. Droplets of moisture that condense at pinhole sites leave behind an observable salt crystallite upon evaporation. This procedure has worked well on chemically polished KCl coated with a 0.2 μm

thick film of T1I.⁴¹ The minimum size of pinhole located by this method may be expected to vary inversely with the polymer surface energy. In addition, the method could fail to locate pinholes if the underlying crystal surface is so well passified that the moisture droplet dissolves insufficient salt to leave a visible residue.

Polymer film permeabilities. The permeabilities of pinhole-free plasma-polymerized coatings may differ significantly from those measured in bulk polymers. Once a pinhole-free area of the coating has been located and marked, the film can be removed undamaged by dissolving the salt substrate. The permeability can be measured by the so-called "cup" test since it is most easily adaptable to small, variable-sized samples. A small cup containing water is sealed by securing the sample film over the top. Then the cup is placed in a controlled environment and the weight loss measured as a function of time. From this data the permeability can be computed by Eq. (8). It is expected that films as thin as $0.2 \mu\text{m}$ should be sufficiently strong to withstand careful application of this procedure.

Testing of coated substrate scratches. At 100 percent relative humidity, Young⁹ observed moisture attack on deep surface scratches in NaCl if the thickness of the coating of vitreous As_2S_3 did not exceed the scratch width. This failure was probably due to mechanical failure of the very soft As_2S_3 bridge over the scratch. Under similar conditions, polymer films, with their much higher intrinsic permeabilities, would allow rapid moisture attack at substrate scratches even in the absence of mechanical failure unless there is intimate contact between the film and the substrate. The following procedure is

suggested to investigate the coating of scratches by polymers. First a series of substrates are prepared with unidirectional scratches of known size and shape. If possible, an electron or optical micrograph should be made of each surface prior to depositing a strip of polymer film perpendicular to the scratches. The sample is then exposed to 100 percent relative humidity and the pattern of moisture attack through the film at the scratches, and along the scratches from the edges followed with time. The objective is to observe the attack and characterize the sizes and shapes of scratches that can be effectively protected by polymer coatings. In particular, rapid attack along a scratch from the film edge indicates the coating bridges the scratch rather than filling it, leaving a void next to the crystal surface where water can condense. As a final step the substrate can be completely dissolved away and an electron micrograph made of the back surface of the polymer film. If the polymer coated deep into the scratches, this micrograph should be an inverse replica of the original scratched crystal surface.

Temperature, pressure, and humidity cycling. The final testing of a finished window should include temperature, pressure, and humidity cycling somewhat more stringent than those expected in normal use. However, if the polymer matrix is preventing condensation of moisture, the values of $(\partial T / \partial t)_{\max}$ given in Table 6 indicate that accelerated temperature of pressure cycling will be necessary to verify this mechanism. From Eqs. (28), (29), and (30) the maximum cooling rate can be written as

$$\left(\frac{\partial T}{\partial t} \right)_{\max} \sim \frac{P(T - T_0)_{\max}}{S \cdot t^2} \quad . \quad (31)$$

Therefore, this mechanism is unique in favoring thin, high-permeability films over thick, low-permeability films for providing maximum moisture protection.

Since White⁴² has reported producing pinhole-free polymer films as thin as 3 nm by ultraviolet polymerization, and Cornell and Gregor⁴³ produced pinhole-free films 10 nm thick using magnetically shaped electrodeless rf glow discharges, moisture protection might be achieved with films so thin they barely disturb the performance of antireflection coatings.

The protective ability of this mechanism can be verified by the following experiment. A progression of pinhole-free films of different thicknesses are deposited on very thin, moisture-sensitive substrates, with care being taken to seal the sample against moisture attack at film edges or uncoated surfaces. The most efficient temperature cycling at 100 percent relative humidity can be accomplished by suspending the sample in flowing water at the upper temperature T long enough for the sample to come to thermal equilibrium and the film to come to uniform supersaturation, $P_u / P_0 = 1$. If the water flow is rapidly shifted to the lower temperature T_0 , and the thermal diffusion time is much less than the vapor out-diffusion time given by (29), the polymer-crystal surface should be subject to significant supercooling. A plot of the maximum cooling rate at the onset of significant damage should be approximately a straight line when plotted against λ^2 . Supersaturation could also be achieved by rapid pressure cycling. This has the advantage that the substrate can be any thickness since the diffusion time for vapor pressure changes in the polymer film is the only limitation on the supersaturation achieved within the film for a given pressure change.

Abrasion tests and sealing of coating edges. In addition to previous tests, for field use the window coating will have to pass abrasion tests such as the sand abrasion, scotch tape, eraser rub, and cheesecloth rub tests.²⁸ Also, the edges of the protective coatings must be sealed either by additional coatings that cover the uncoated surfaces of the window, or by moisture-tight seals between the coated window surfaces and the window mounts.

REFERENCES

1. J. R. Hollahan, T. Wydeven, and C. C. Johnson, Appl. Opt. 13, 1844 (1974).
2. J. M. Tibbitt, A. T. Bell, and M. Shen, Proc. Fifth Conference on Infrared Laser Window Materials, ed. by C. R. Andrews and C. L. Strecker, U.S. Air Force Materials Laboratory Special Report, Wright-Patterson AFB, Ohio (1976), p. 205.
3. B. L. Weigand, Third Conference on High Power Infrared Laser Window Materials, ed. by C. A. Pitha, H. Posen, and A. Armington, AFCRL-TR-74-0085, Vol. III, 769 (Air Force Cambridge Research Laboratories, 1974).
4. Handbook of Military Infrared Technology, ed. by W. L. Wolfe (U.S. Government Printing Office, 1965).
- 4a. Sadtler Standard Infrared Spectra, Sadtler Research Laboratories, Inc., 3316 Spring Garden St., Philadelphia, Pa. 19104, IR Spectra Nos. 1924, 7500 and 9000.
- 4b. CRC Handbook of Lasers with Selected Data on Optical Technology, ed. by R. J. Pressley (Chemical Rubber Co., Cleveland, Ohio, 1971), pp. 49, 51, 54, 59, and 151.
5. N. H. Fletcher, Phil. Mag., 18, 1287 (1968).
6. R. C. Evans, An Introduction to Crystal Chemistry, 2nd ed. (Cambridge University Press, Cambridge, England, 1966), pp. 265-303.
7. M. Braunstein, D. Zuccaro, J. E. Rudisill, and A. Braunstein, Proc. Fifth Conference on Infrared Laser Window Materials, ed. by C. R. Andrews and C. L. Strecker, U.S. Air Force Materials Laboratory Special Report, Wright-Patterson AFB, Ohio (1976), p. 135.

8. R. C. Pastor and M. Braunstein, Hughes Research Laboratories Technical Report No. AFWL-TR-72-152, Vol. II, July 1973, p. 113.
9. P. A. Young, Thin Solid Films (Switz.) 6, 423 (1970).
10. Data for Table 1 comes from: CRC Handbook of Chemistry and Physics, 55th ed., ed. by Robert C. Weast (CRC Press, Cleveland, Ohio, 1974), p. B-63; The Merck Index, 8th ed., ed. by P. G. Stecher (Merck and Co., Rahway, N.J., 1968).
11. R. C. Pastor and M. Braunstein, Hughes Research Laboratories Technical Report No. AFWL-TR-72-38, March 1972, p. 6.
12. R. C. Pastor, private communication.
13. G. C. Benson and K. S. Yun in The Solid-Gas Interface, ed. by E. A. Flood (Marcel Dekker, N.Y., 1969), Vol. 1, Chap. 8.
14. C. E. Rogers in Engineering Design for Plastics, ed. by E. Baer (Reinhold, N.Y., 1964) Chap. 9; R. C. Bowers and W. A. Zisman, *ibid.*, Chap. 10.
15. S. M. Lee, Autonetics Technical Report, Contract No. NAS 12-2011, March 1969.
16. J. J. Aklonis, W. J. MacKnight, and M. Shen, Introduction to Polymer Viscoelasticity (Wiley-Interscience, N.Y., 1972), Chap. 4.
17. D. I. McCane in Encyclopedia of Polymer Science and Technology, Vol. 13, pp. 623-670.
18. C. E. Rogers, op. cit., p. 637.
19. P. K. Tien, G. Smolinsky, and R. J. Martin, Appl. Opt. 11, 637 (1972).
20. Photographs of moisture attack on KCl surface defects appear in R. C. Pastor and M. Braunstein, Hughes Research Laboratories Technical Report No. AFWL-TR-72-152, Vol. II, July 1973, pp. 35-37.

21. L. Mandelkern, Crystallization of Polymers (McGraw-Hill, N. Y., 1964).
22. W. A. Zisman in Contact Angle, Wettability, and Adhesion, Vol. 43 of Advances in Chemistry Series, ed. by R. T. Gould (American Chemical Society, Washington, D.C., 1969), p. 20.
23. L. D. Landau and E. M. Lifshitz, Statistical Physics, 2nd ed. (Addison-Wesley, Reading, Mass., 1969), Chap. XV.
24. Ibid., p. 474, problem 1.
25. C. A. Croxton, Liquid State Physics - A Statistical Mechanical Introduction (Cambridge University Press, London, 1974).
26. H. S. Carslaw and J. C. Jaeger, Conduction of Heat in Solids, 2nd ed. (Oxford University Press, London, 1973), p. 98, Fig. 10a.
27. CRC Handbook of Chemistry and Physics, 55th ed., ed. by Robert C. Weast (CRC Press, Cleveland, Ohio, 1974), p. D-158.
28. G. T. Johnston and D. A. Walsh, University of Dayton Research Institute Technical Report No. AFML-TR-75-15, Febr. 1975.
29. K. W. Bewig and W. A. Zisman, Advances in Chemistry, No. 33 (American Chemical Soc. Publ., Washington, D.C., 1961), p. 100.
30. CRC Handbook of Chemistry and Physics, 55th ed., ed. by Robert C. Weast (CRC Press, Cleveland, Ohio, 1974), pp. F-223 to F-242.
31. N. B. Colthup, L. H. Daly, and S. E. Wiberley, Introduction to Infrared and Raman Spectroscopy, 2nd ed. (Academic Press, N. Y., 1975), pp. 374-381.
32. A. Elliott, Infra-red Spectra and Structure of Organic Long-Chain Polymers (St. Martin's Press, N. Y., 1969), p. 27.
33. R. Zbinden, Infrared Spectroscopy of High Polymers (Academic Press, N. Y., 1964).

Sec. B

34. R. G. Snyder, *J. Mol. Spectry.* 4, 411 (1960).
35. R. G. Snyder, *J. Chem. Phys.* 27, 969 (1957).
36. S. Krimm, C. Y. Liang, and G. B. B. M. Sutherland, *J. Chem. Phys.* 25, 549 (1956).
37. N. B. Colthup, L. H. Daly, and S. E. Wiberley, *op. cit.*, p. 247.
38. T. A. Reis, H. Hiratsuka, A. T. Bell, and M. Shen, Eighth Annual Symposium on Optical Materials for High Power Lasers, Boulder, Colo., July, 1976, to be published.
39. D. I. McCane, *op. cit.*, pp. 629 and 659.
40. A. Elliott, *op. cit.*, pp. 109 and 110.
41. E. Bernal G., J. H. Chaffin, B. G. Koepke, R. B. Maciolek, and R. J. Stokes, Honeywell Technical Report HR-75-250-5-26, No. 2, Dec. 1974, pp. 49-53.
42. P. White, *Electrochem. Tech.* 4, 468 (1966).
43. R. A. Connell and L. V. Gregor, *J. Electrochem. Soc.* 112, 1198 (1965).

C. ELECTRONIC PROPERTIES OF THE LiF VALENCE BAND; SURFACE STATES
AND THE LOCAL DENSITY OF STATES NEAR THE SURFACE[†]

D. L. Mills
Department of Physics
University of California
Irvine, California 92717

and

Xonics, Incorporated
Santa Monica, California 90401

Using Sham's tight-binding valence-band wavefunctions and diagonalizing the Hamiltonian matrix for a model 15-layer lithium-fluoride slab, the following results are obtained: A band of surface states, which are spatially confined to the surface layer, are pushed out of the top of the conduction band when the Madelung energy is included. Both bulk and surface-layer densities of states show peaks near the top and bottom of the band, in addition to the narrow surface states. The bulk density of states, which is approached rather closely even in the second atomic layer, generally resembles previously calculated densities but has considerably more resolution.

[†]Supported in part by Grant No. AFOSR 76-2887 of the Air Force Office of Scientific Research, Office of Aerospace Research, U.S.A.F.

AD-A034 088

XONICS INC SANTA MONICA CALIF

THEORETICAL STUDIES OF HIGH-POWER ULTRAVIOLET AND INFRARED MATE--ETC(U)

JUN 76 M SPARKS, C J DUTHLER

F/G 20/6

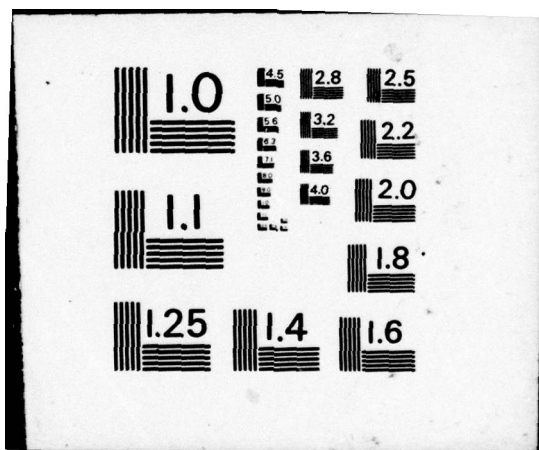
DAHC15-73-C-0127

NL

UNCLASSIFIED

203
ADA034088





In this section, we report studies of some properties of the valence band of LiF. Since the atomic fluorine 2p orbitals have a spatial extent small compared to the lattice constant, a tight-binding description of the valence electrons is appropriate. Such a description of the valence band has been provided by Sham, as part of the present program.

Sham proceeds by presuming the valence electrons are described by Bloch functions of the tight-binding form:

$$\psi_{\vec{k}j}(\vec{x}) = \frac{1}{\sqrt{N}} \sum_{\vec{l}} \sum_{\alpha} c_{\alpha}(\vec{k}j) \varphi_{p_{\alpha}}(\vec{x} - \vec{l}) e^{i\vec{k} \cdot \vec{l}} . \quad (1)$$

In this expression, the subscript j is a band index that labels each of the three valence bands, the sum over \vec{l} ranges over the fluorine sublattice, and $\varphi_{p_{\alpha}}(\vec{x} - \vec{l})$ is a 2p atomic orbital centered on site \vec{l} . Finally, the index α runs over x, y, and z.

The coefficients $c_{\alpha}(\vec{k}j)$ are found by diagonalizing a 3×3 Hamiltonian matrix. In Sham's approach, the tight-binding Hamiltonian matrix contains all non-vanishing overlap integrals between nearest and next nearest neighbor sites in the fluorine sublattice. Numerical values of the various overlap integrals have been calculated by Sham and Duthler, from first principles. Their approach yields energy bands in excellent accord with self consistent Hartree-Fock calculations of Kunz and co-workers.¹ The utility of the tight-binding approach is that we have wave functions of simple form that can be readily generated, and the energy eigenvalues themselves are obtained very easily only by asking for the eigenvalues of a 3×3 matrix.

We report here studies of some basic properties of the LiF valence band, within the framework of Sham's tight-binding scheme described in the preceding paragraphs. With a method described below, we calculate the density of states within the valence band. Within the framework of the most naive interpretation of the photoemission process, this property may be related to the energy distribution of electrons photoemitted from the material. What we have actually calculated is a local density of states, as a function of distance from the crystal surface (for a LiF sample with a (100) surface). This local density of states is identically equal to the bulk density of states in the crystal interior, and through its dependence on distance from the surface we can address the question of how sensitive data such as the photoemission data is to surface properties. In covalent semiconductors, photoemission data is extremely sensitive to the electronic structure of the surface. Surface electronic states show through prominently in the data on these compounds.

In the calculations we have carried out, we begin by considering a slab of material with finite thickness. The electronic wave functions are found for the finite slab, and its electronic properties are then readily studied as a function of distance from the surface. We choose (100) surfaces for the slab, since electrostatic considerations suggest strongly that these electrically neutral, tightly packed surfaces will be encountered in practice.

If we consider the nature of the electron states in a slab with a finite number N of layers, then periodic boundary conditions applied to the two directions parallel to the surface lead one to construct functions with Bloch character in the two directions parallel to the surface. However, since translational invariance no

longer holds in the direction perpendicular to the slab (the z direction here), these functions do not have Bloch character with respect to translations normal to the slab.

Within the framework of the tight-binding model set up by Sham, for the slab the electronic wave functions have the form

$$\psi_{\vec{k}_\parallel n}(\vec{x}) = \sum_{\vec{\ell}_\parallel \ell_z} \sum_{\alpha} A_{\vec{k}_\parallel n}(\ell_z; \alpha) e^{i \vec{k}_\parallel \cdot \vec{\ell}_\parallel} \varphi_{p_\alpha}(\vec{x} - \vec{\ell}) . \quad (2)$$

In this expression, $\varphi_{p_\alpha}(\vec{x} - \vec{\ell})$ is the same atomic p orbital as found in Eq. (1). The sites in the fluorine sublattice are labeled by the vector $\vec{\ell} = \vec{\ell}_\parallel + \hat{z} \ell_z$, where $\vec{\ell}_\parallel$ is the projection of $\vec{\ell}$ onto a plane parallel to the slab surfaces. The factor of $\exp(i \vec{k}_\parallel \cdot \vec{\ell}_\parallel)$ insures that the wave function is a Bloch function with respect to translations parallel to the slab surfaces. The (two-dimensional) wave vector of the Bloch function is \vec{k}_\parallel .

The coefficient $A_{\vec{k}_\parallel n}(\ell_z; \alpha)$ is a measure of the amplitude in the wave function of the p orbital φ_{p_α} associated with the layer ℓ_z . The subscript n is a quantum number which labels the various Bloch states of wave vector \vec{k}_\parallel . On the infinitely extended medium, the wave function is also labeled by three quantum numbers: the three components of the wave vector. Since k_z is no longer a good quantum number for the slab, we must introduce a new label.

One may find the coefficients $A_{\vec{k}_\parallel n}(\ell_z; \alpha)$ along with the energy eigenvalues $E_n(\vec{k}_\parallel)$ by diagonalizing a Hamiltonian matrix for the slab. For the present tight-binding model, if we have a slab of N layers, we are led to a $3N \times 3N$ Hamiltonian matrix. This matrix is set up from the basic 3×3 used

to generate the bulk band structure. For the model of the valence band set up by Sham, the $3N \times 3N$ matrix becomes purely real if one writes it in terms of the representation

$$\tilde{A}_{\vec{k}_\parallel n} = \begin{pmatrix} A_{\vec{k}_\parallel n}(1; x) \\ A_{\vec{k}_\parallel n}(1; y) \\ iA_{\vec{k}_\parallel n}(1; z) \\ \vdots \\ A_{\vec{k}_\parallel n}(N; x) \\ A_{\vec{k}_\parallel n}(N; y) \\ iA_{\vec{k}_\parallel n}(N; z) \end{pmatrix}, \quad (3)$$

that is to say, one uses a representation in which the components $A_{\vec{k}_\parallel n}(\ell_z; z)$ are preceded by an explicit factor of i . In this representation, the Hamiltonian matrix assumes the form

$$\tilde{H} = \begin{pmatrix} \tilde{H}(00) & \tilde{H}(01) & \tilde{H}(02) & 0 & 0 & \cdots \\ \tilde{H}(10) & \tilde{H}(00) & \tilde{H}(01) & \tilde{H}(02) & 0 & \cdots \\ \tilde{H}(20) & \tilde{H}(10) & \tilde{H}(00) & \tilde{H}(01) & \tilde{H}(02) & \\ 0 & \tilde{H}(20) & \tilde{H}(10) & \tilde{H}(00) & \tilde{H}(01) & \\ 0 & 0 & \tilde{H}(20) & \tilde{H}(10) & \tilde{H}(00) & \\ \vdots & \vdots & \vdots & \vdots & \vdots & \end{pmatrix} \quad (4)$$

where the explicit form of the 3×3 submatrices $\tilde{H}(ij)$ are given in the Appendix.

In the Hamiltonian matrix of Eq. (4), we have presumed the tight-binding overlap integrals in the surface to be the same as those in the bulk. This assumption may be relaxed readily if desired, and changes in the overlap integrals (produced, for example, by shifts in the atomic positions near the surface) are easily incorporated into the calculation by modifying entries in the submatrices $\underline{\underline{H}}(i,j)$ near the two extremes of the Hamiltonian matrix.

An important effect we do account for is an energy shift of the surface p orbitals that arises because the Madelung energy of an electron in the surface is higher than when it is in the bulk. This surface Madelung shift has been calculated for the present geometry by Maradudin, and also by the present author. The Madelung surface shift amounts to about 0.4 eV, which is a small fraction ($\approx 12\%$) of the width of the valence band. We shall see that this energy has a dramatic effect on the electronic states near the surface: it pushes a band of surface states out of the top of the valence band, in a limited region of the two-dimensional Brillouin zone near the zone boundary. These surface states introduce sharp structure in the local density of states in the outermost atomic layer of the crystal; this structure disappears quickly as one moves into the crystal interior. We find no electronic surface states in the absence of the Madelung shift, incidentally.

The principal quantity we study is the local density of states, as a function of distance from the surface. By definition, the local density of states is

$$\rho(\vec{x}; E) = \sum_{\vec{k}_{\parallel}} \sum_n \left| \psi_{\vec{k}_{\parallel} n}(\vec{x}) \right|^2 \delta(E - E_n(\vec{k}_{\parallel})) \quad , \quad (5)$$

where the sum on \vec{k}_{\parallel} covers the 2D Brillouin zone for the present structure.

Actually, Eq. (5) is a rather complex function because the atomic orbitals $\varphi_{p_\alpha}(\vec{x} - \vec{k})$ appear explicitly. What we calculate instead is the local density of states averaged over a unit cell in plane ℓ_z :

$$\rho(\ell_z; E) = \int_{\substack{\text{unit cell} \\ \text{in plane } \ell_z}} d^3x \rho(\vec{x}, E) . \quad (6)$$

If the form of the Bloch function given in Eq. (2) is substituted into Eq. (6), and we ignore overlap between atomic orbitals in neighboring cells, then we have the form

$$\rho(\ell_z; E) = \sum_{\vec{k}_{||}} \sum_n \sum_{\alpha} \left| A_{\vec{k}_{||} n}(\ell_z; \alpha) \right|^2 \delta(E - E_n(\vec{k}_{||})) . \quad (7)$$

Before we present the results, we comment on the computational method used to calculate $\rho(\ell_z; E)$. Similar calculations for silicon surfaces and the surfaces of III-V compounds² appear in the literature. These calculations use the Gilat-Raubenheimer method for evaluating the sum over $\vec{k}_{||}$, after replacing the delta function by a gaussian with width of a few tenths of a volt. The second step is useful, because one samples a limited number of $\vec{k}_{||}$ values, and only a discrete eigenvalue spectrum obtains as a consequence.

The calculations here proceed differently. The delta function has been replaced by a Lorentzian with full width at half maximum of 0.2 eV. The "tails" of the Lorentzian help smooth out structure induced artificially by the use of a finite number of eigenvalues in the sample, in the view of the present author. Indeed, the density-of-states curves we find are substantially smoother in appearance than those found in the literature. We believe this is one reason for the improved results.

In the recent literature, there has been considerable attention devoted to performing wave-vector sums through use of "special points" in the Brillouin zone.^{3,4} The idea is that we can get by with rather few points if the points are chosen with certain convergence criteria in mind. Arrays of special points can be found in the literature for various two- and three-dimensional Brillouin zones.³⁻⁵ The present calculations employ Cunningham's net of ten points in the irreducible portion of the Brillouin zone of the square lattice.

In Fig. 1, some principal results of the calculations are displayed. The calculations presented in Fig. 1 ignore the surface Madelung shift; we turn to the effect of this shift later. Since several pieces of information appear in the figure, we comment on them step by step.

The solid line in the figure represents the local density of states six layers in from the surface. This should, in fact, prove an excellent approximation to the bulk density of states in the valence band. One sees two gross features, a broad peak at the energy +30 milli Hartrees, and a sharper feature near -50 milli Hartrees. Upon these two features small amplitude wiggles are superimposed. These small wiggles have their origin in the fact that a finite slab has been employed in the calculations. (Again, the 15-layer slab has been used.) In such a slab, one gets standing wave resonances within the valence bands, and this produces structure in the density of states.

To check if the local density of states has indeed converged to the bulk density of states by the time one moves six atomic layers into the material, we compare the local density of states in layer five with that in layer six. The circles in Fig. 1 show the values of the local density of states in layer five, at selected energies.

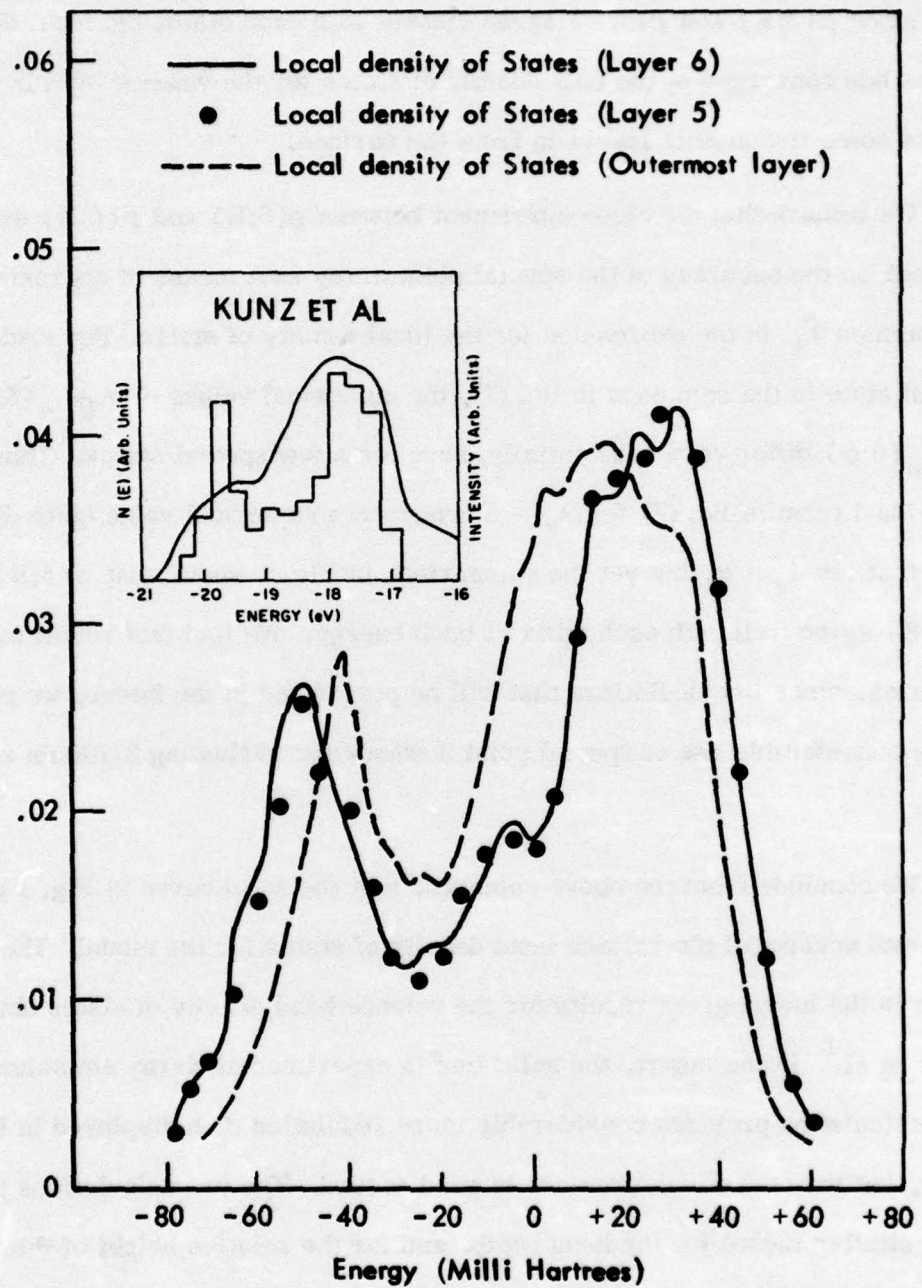


Fig. 1. The local density of states for the valence band of a LiF slab with a (100) surface. In the figure, the solid curve gives the local density of states in the sixth atomic layer in from the surface, and the dots the local density of states in the fifth layer at selected energies. The dashed curve is the local density of states in the surface, and the inset is taken from Ref. 1.

In all cases, the points fall extremely close to the solid curve. Thus, we conclude that since $\rho(5;E)$ and $\rho(6;E)$ agree closely with each other, the local density of states has converged to the bulk density of states for the valence band by the time one is some five atomic layers in from the surface.

We remark that the close agreement between $\rho(5;E)$ and $\rho(6;E)$ serves as a check on the accuracy of the special point array as a means of approximating the sum on \vec{k}_{\parallel} in the expression for the local density of states. For each individual state in the sum on n in Eq. (7), the numerical values of $A_{\vec{k}_{\parallel}n}(5;\alpha)$ and $A_{\vec{k}_{\parallel}n}(6;\alpha)$ differ very substantially, save for a few special states. Thus, each individual term in Eq. (7) for $\ell_z = 5$ assumes a numerical value quite different than that for $\ell_z = 6$, but yet the comparison in Fig. 1 shows that $\rho(5;E)$ and $\rho(6;E)$ agree well with each other at each energy. We find this result most reassuring, since in calculations that will be performed in the future, we plan to make considerable use of special point methods for evaluating Brillouin zone sums.

We conclude from the above remarks, that the solid curve in Fig. 1 gives an accurate account of the valence band density of states for the model. The histogram in the insert gives results for the valence band density of states obtained by Kunz et al.¹ In the insert, the solid line is experimental X-ray emission data. Our calculation provides considerably more resolution than displayed in Kunz's work, but the overall features are in good accord. The two calculations produce very similar values for the band width, and for the relative height of the two prominent peaks.

We remark that for LiF, the photoemission energy distribution curves show a double peak structure (the peaks are not quite resolved, but they are clearly discernible) with relative peak heights consistent with the calculations in Fig. 1. This suggests that in LiF, the photoemission data is not greatly influenced by the variation of matrix elements across the valence band.

The dashed curve in Fig. 1 gives the local density of states in the outermost atomic layer of the crystal, for the case where the surface Madelung shift is ignored. One sees its qualitative shape and form is remarkably similar to the bulk valence band density of states. This is in contrast to the local valence band density of states in silicon, and in the III-V compounds.² As one moves toward the surface, in the present case, the two prominent peaks in the local density of states have smaller splitting than the peaks in the bulk; the apparent valence band width seen by an electron in the surface is smaller than that seen by an electron in the bulk material. The effect is not a large one. The physical origin of this phenomenon is clear. In a simple model with nearest neighbor hopping integral γ , an electron in the FCC structure has twelve neighbors to hop onto, if placed on a given site. The time required to do this is $\hbar / 12\gamma$, and the band width is $\approx 12\gamma$. For an electron in the surface, there are eight neighbors only, and one is led to estimate 8γ as the effective band width in the surface. The model used here is considerably more complex than that considered in this argument, so the argument is reliable only as a qualitative and not a quantitative guide.

One may inquire how far into the bulk one must penetrate before the separation between the two peaks evolves into the bulk splitting. The calculations here show that even in the second atomic layer (first interior layer), the local density

of states is remarkably bulk-like in appearance. This is illustrated in Fig. 2, where the local density of states in the outermost layer is compared with that in the first interior layer. In silicon and in the III-IV compounds, theoretical calculations show that the local density of states changes from surface behavior to bulk behavior in some four or five atomic layers. However, in these compounds the local density of states in the second and third layers shows identifiable and clear deviations from the bulk. Such features are lacking in the present case.

The calculations carried out above provide an accurate description of the bulk density of states in the Sham model of the LiF valence band. In addition, they explore the spatial variation of the local density of states with distance from the surface, for the case where the surface Madelung shift is ignored. We next turn to an assessment of the role of the surface Madelung shift.

In Fig. 3, the solid curve shows the local density of states in the surface layer of the crystal in the presence of the surface Madelung shift. The dashed curve is the local density of states six layers in from the surface. We first remark that in layer 6, the local density of states is little affected by the energy shift of the surface orbitals; save for small details, the dashed curve in Fig. 3 is very similar to the solid curve in Fig. 1.

However, the shape of the local density of states in the surface is quite different. There are now three prominent peaks in $\rho(1; E)$ rather than the two that appear in Fig. 1. In Fig. 3, the lowest energy peak near -30 milli Hartrees is essentially the low energy peak in Fig. 1 shifted upward by the surface Madelung shift. The peak at +30 milli Hartrees in Fig. 3 bears a similar relationship to

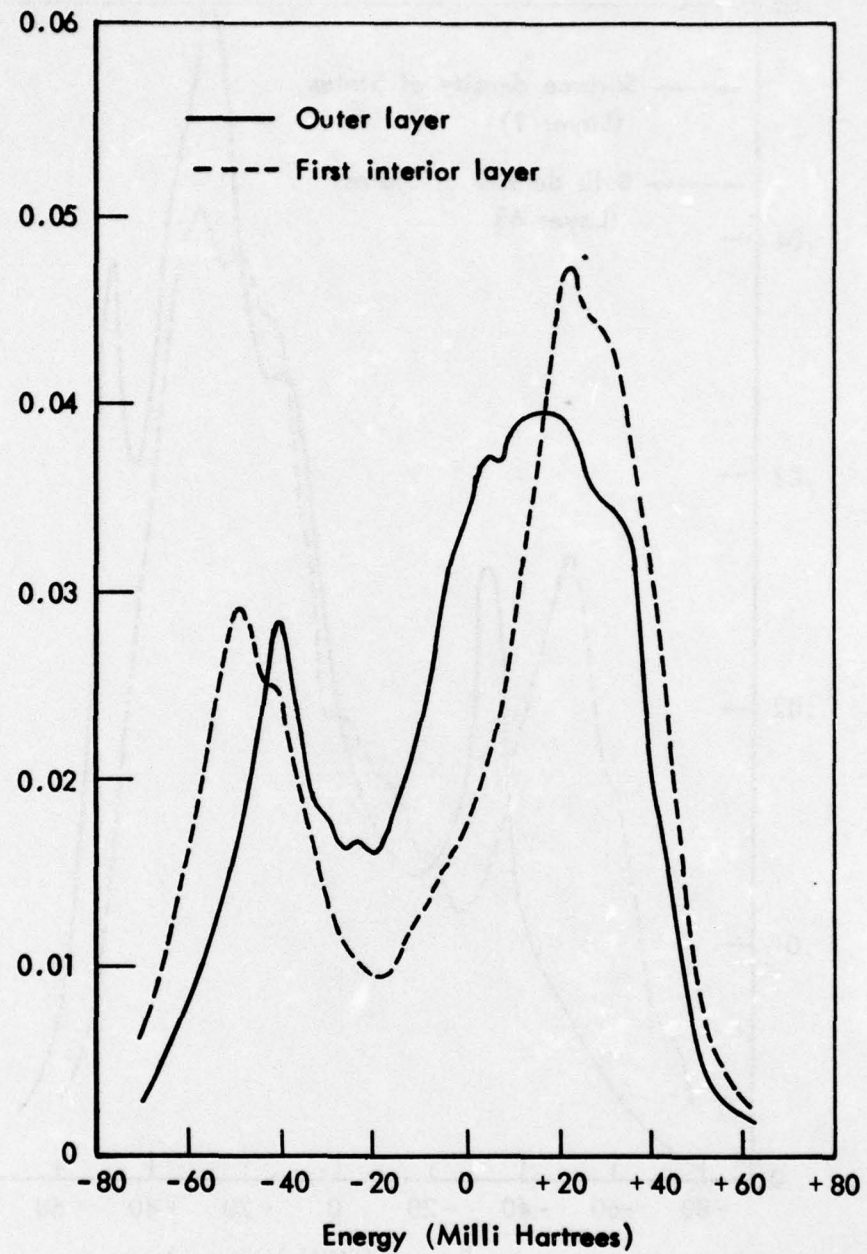


Fig. 2. A comparison of the local valence band density of states for the LiF slab in the outermost atomic layer (solid curve) with that in the first interior layer (dashed curve).

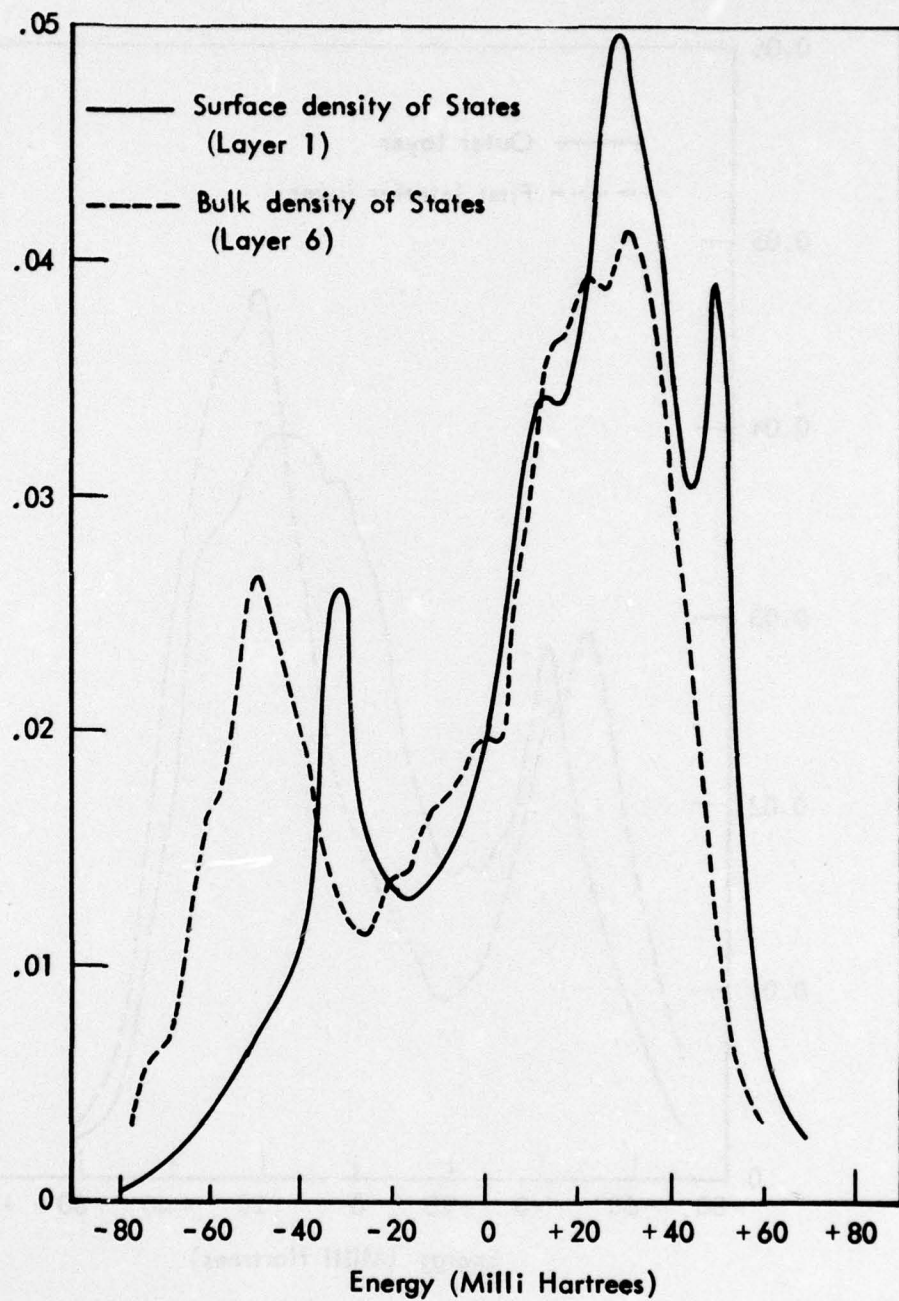


Fig. 3. The local valence band density of states in the outermost layer for the LiF slab (solid curve), for the case where the shift in Madelung energy of the surface orbital is accounted for. Also shown is the local density of states in layer 6, calculated in the presence of the surface orbital shift.

that at +20 milli Hartrees in Fig. 1. These results are surely expected on physical grounds.

The sharp peak near +50 milli Hartrees in Fig. 3 is a qualitatively new feature introduced by the surface Madelung shift. Upon varying the surface orbital energy about the value appropriate to the Madelung shift, we find this feature moves progressively upward as the energy of the surface orbital is moved upward. Quite clearly then, this feature has its origin in surface states pushed upward and out of the valence band by the Madelung shift of the surface orbitals. This identification is confirmed by Fig. 4, where the local density of states near the top of the valence band is plotted as a function of distance from the surface. The sharp peak at +50 milli Hartrees appears only in the density of states of the outermost layer. The surface states are evidently localized in the very near vicinity of the surface.

One may inquire into the nature of these surface states. A particularly interesting question is the extent to which they appear as a consequence of some special feature of the present model, or whether one expects them to persist even in the presence of changes in the nearest neighbor hopping integrals near the surface. We argue that the latter statement is correct.

Examination of the slab eigenvectors shows that the surface states occur near the point $k_{||}^x = \pi/2a_0$, $k_{||}^y = \pi/2a_0$, which lies on the boundary of our two-dimensional Brillouin zone. Right at the point $k_{||}^x = \pi/2a_0$, $k_{||}^y = \pi/2a_0$, the nature of the surface states can be explored by analytic methods. One first writes out the explicit form of the equations for the eigenvectors $A_{k_{||}}^{\rightarrow}(\ell_z; \alpha)$ at this point, and transforms them to the new basis

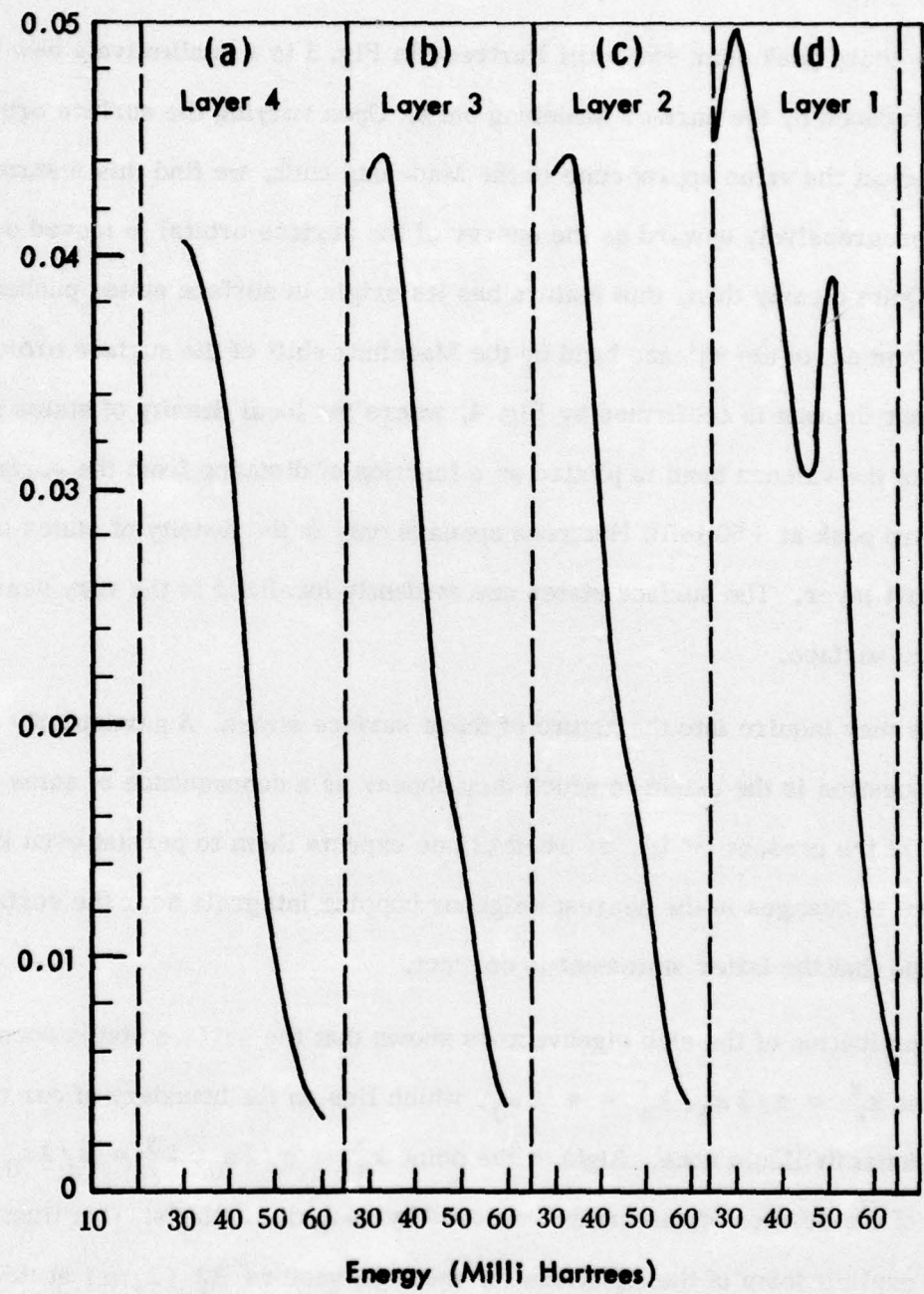


Fig. 4. The sharp feature in the local density of states at the surface, plotted as a function of distance from the surface.

$$B_{\vec{k}_{\parallel}}(\ell_z; +) = \frac{1}{\sqrt{2}} \left(A_{\vec{k}_{\parallel}}(\ell_z; x) + A_{\vec{k}_{\parallel}}(\ell_z; y) \right) \quad (8a)$$

$$B_{\vec{k}_{\parallel}}(\ell_z; -) = \frac{1}{\sqrt{2}} \left(A_{\vec{k}_{\parallel}}(\ell_z; x) - A_{\vec{k}_{\parallel}}(\ell_z; y) \right) \quad (8b)$$

$$B_{\vec{k}_{\parallel}}(\ell_z; z) = A_{\vec{k}_{\parallel}}(\ell_z; z) \quad . \quad (8c)$$

Then one finds the equations decouple into a set which involve $B_{\vec{k}_{\parallel}}(\ell_z; +)$ and $B_{\vec{k}_{\parallel}}(\ell_z; z)$, and a set which involve $B_{\vec{k}_{\parallel}}(\ell_z; -)$ uncoupled from $B_{\vec{k}_{\parallel}}(\ell_z; +)$ and $B_{\vec{k}_{\parallel}}(\ell_z; z)$. The computer results show the surface state arises from the set which involve $B_{\vec{k}_{\parallel}}(\ell_z; -)$. The equations satisfied by $B_{\vec{k}_{\parallel}}(\ell_z; -)$ involve only the next nearest neighbor hopping integrals η and δ ; all the terms which involve the nearest neighbor overlaps α , β , and γ drop out.

As one can see from the numerical values of the hopping integrals given at the end of the Appendix, the next nearest neighbor hopping integrals are very small compared to the nearest neighbor integrals. To a very good approximation, when $\vec{k}_{\parallel} = (\pi/2a_0, \pi/2a_0)$, as far as the $B_{\vec{k}_{\parallel}}(\ell_z; -)$ equations are concerned, the layers behave as they are only very weakly coupled to each other. Thus, the surface Madelung shift easily induces a state highly localized at the surface, split off above the remaining valence band states by an energy very close to the surface Madelung shift. The numerical calculations are quite consistent with this view.

Even if we allow the overlap integrals in and near the surface to change from their bulk values, say because of changes in surface lattice spacing,⁶ it will remain true that the equations for $B_{\vec{k}_{\parallel}}(-; \ell_z)$ will contain only very small next nearest neighbor overlap integrals, and the surface Madelung shift will split states off from the valence band, at this point of the two-dimensional Brillouin zone. It is

for this reason we expect the surface states we find to be a general feature of the LiF surface, and not a special consequence of our neglect of overlap integral changes in the near vicinity of the surface.

As one moves away from the point $(\pi/2 a_0, \pi/2 a_0)$ in the two-dimensional Brillouin zone, we find a band of surface states which merges with the top of the bulk valence bands. For example, we find no surface states at $\vec{k}_{\parallel} = 0$.

At the electron energies (≈ 40 eV) relevant to the photoemission studies of Poole and co-workers,⁷ the electron escape depth is very large compared to the lattice constant. It is the order of ten lattice constants or greater. Thus, the photoemission data probes the bulk properties of the crystal, since we find the local density of states varies appreciably from the bulk valence band density of states only in the outermost atomic layer. Indeed, it is gratifying to see the double peaked structure we find reflected in the photoemission data. The width of the valence band in the Sham model is found to be substantially smaller (by a factor of two) than that assigned to LiF by Poole et al. We believe it is difficult to assign an accurate valence band width to a material such as an alkali halide on the basis of photoemission data taken on thick samples. For example, di Stefano and Spicer⁸ find that for thin samples of CsI, the width of the energy distribution curve is considerably narrower than in thick ones. In large gap materials, where the electron mean free path can be long, the electron has time to engage in phonon scattering, unless the sample is much thinner than the mean free path for phonon emission. The phonon scattering can smear out and broaden the energy distribution observed in photoemission, and lead to an apparent valence band width larger than the true width.

APPENDIX: EXPLICIT FORM OF THE HAMILTONIAN
FOR THE N LAYER LiF SLAB

In this appendix, we list the non-zero elements of the 3×3 submatrices $\tilde{H}(ij)$ that enter the $3N \times 3N$ Hamiltonian matrix defined in Eq. (4). Note that since \tilde{H} is a real symmetric matrix (in a representation where the eigenvector has the form displayed in Eq. (3)), we only need specify $\tilde{H}(00)$, $\tilde{H}(01)$, and $\tilde{H}(02)$, since $\tilde{H}(ji)$ is the transpose of $\tilde{H}(ij)$. In the list below, only the non-zero matrix elements are specific. The numerical values of the overlap parameters α , β , γ , δ , and η employed in the calculation are given at the end of the calculation.

We have for $\tilde{H}(0,0)$ (with $k_{\parallel}^x a_0 = \phi_x$, $k_{\parallel}^y a_0 = \phi_y$, where a_0 is the Li-F separation)

$$H(0,0)_{xx} = 4\alpha \cos(\phi_x) \cos(\phi_y) + 2\eta \cos(2\phi_y) + 2\delta \cos(2\phi_x)$$

$$H(0,0)_{yy} = 4\alpha \cos(\phi_x) \cos(\phi_y) + 2\eta \cos(2\phi_x) + 2\delta \cos(2\phi_y)$$

$$H(0,0)_{zz} = 4\gamma \cos(\phi_x) \cos(\phi_z) + 2\eta (\cos(2\phi_x) + \cos(2\phi_z))$$

$$H(0,0)_{xy} = H(0,0)_{yx} = -4\beta \sin(\phi_x) \sin(\phi_z) .$$

Then for $\tilde{H}(01)$,

$$H(01)_{xx} = 2\gamma \cos(\phi_y) + 2\alpha \cos(\phi_x)$$

$$H(01)_{yy} = 2\gamma \cos(\phi_x) + 2\alpha \cos(\phi_y)$$

Sec. C

$$H(01)_{zz} = 2\alpha (\cos \phi_x + \cos \phi_z)$$

$$H(01)_{xz} = -H(01)_{zx} = +2\beta \sin(\phi_x)$$

$$H(01)_{yz} = -H(01)_{zy} = +2\beta \sin(\phi_y) .$$

Finally, H(02) has only diagonal elements:

$$H(02)_{xx} = H(02)_{yy} = \eta$$

and

$$H(02)_{zz} = \delta .$$

In milli Hartrees, the parameters used in the calculation are those found by Sham:

$$\alpha = 7.3632$$

$$\beta = 9.6918$$

$$\gamma = -2.3286$$

$$\delta = .62936$$

$$\eta = .04599 .$$

REFERENCES

1. D. J. Mickish, A. Barry Kunz, and T. C. Collins, *Phys. Rev. B* 9, 4461 (1974).
2. For example, see K. C. Pandey and J. C. Phillips, *Solid State Commun.* 14, 439 (1974); J. A. Appelbaum and D. R. Hamann, *Phys. Rev. Lett.* 31, 106 (1973); D. J. Chadi and M. L. Cohen, *Phys. Rev. B* 11, 732 (1975); and J. D. Joannopolous and M. L. Cohen, *Phys. Rev. B* 10, 5075 (1974).
3. D. J. Chadi and M. L. Cohen, *Phys. Rev. B* 8, 5747 (1973).
4. S. L. Cunningham, *Phys. Rev. B* 10, 4988 (1974).
5. H. J. Monkhorst and James D. Pack, *Phys. Rev. B* 13, 5188 (1976).
6. For example, see the estimates of surface relaxation effects in NaCl by S. Y. Tong and A. A. Maradudin, *Phys. Rev.* 181, 1318 (1969).
7. R. T. Poole, J. G. Jenkin, J. Liesgand, and R. G. G. Leckey, *Phys. Rev. B* 11, 5179 (1975).
8. T. H. Di Stefano and W. E. Spicer, *Phys. Rev. B* 7, 1554 (1973).

D. LOCALIZED ELECTRONIC STATES IN ALKALI HALIDES
ASSOCIATED WITH A SUBSTITUTIONAL ANION IMPURITY[†]

A. A. Maradudin
Department of Physics
University of California
Irvine, California 92717

and

Xonics, Incorporated
Santa Monica, California 90401

A tight-binding calculation of localized electronic states pushed out of the top of the valence band of an alkali halide by the introduction of a substitutional anion impurity is presented.

[†]Supported in part by Grant No. AFOSR 76-2887 of the Air Force Office of Scientific Research, Office of Aerospace Research, U.S.A.F.

Sec. D

The formulation developed here is for materials with the rocksalt structure. To simplify writing, the case of lithium fluoride is considered.

In the present section the equations whose solutions yield the energies of the localized states are established. These involve certain Green's functions associated with the unperturbed F^- sublattice, as well as overlap integrals between 2 p orbitals on the impurity ion and on its neighbors in the F^- sublattice and similar integrals involving the perturbation of the crystal Hamiltonian caused by the introduction of the impurity ion. The evaluation of these Green's functions and integrals will be described in succeeding reports, together with the solution of the equations for the energies of the localized electronic states.

The valence band in LiF is determined by the three 2 p orbitals centered on each of the ions constituting the F^- sublattice. Therefore, in studying the possibility of the formation of localized electronic states which are pushed out of the top of the valence band by the introduction of a substitutional impurity into the F^- sublattice, it is with only this sublattice that we need to be concerned.

The F^- sublattice in LiF is an fcc lattice. The translation vectors of this lattice are

$$\vec{x}(\ell) = \ell_1 \vec{a}_1 + \ell_2 \vec{a}_2 + \ell_3 \vec{a}_3 , \quad (1)$$

where ℓ_1, ℓ_2, ℓ_3 are any three integers, positive, negative, or zero, and where the three primitive translation vectors are

$$\vec{a}_1 = \frac{a_0}{2} (0, 1, 1) , \quad \vec{a}_2 = \frac{a_0}{2} (1, 0, 1) , \quad \vec{a}_3 = \frac{a_0}{2} (1, 1, 0) . \quad (2)$$

We pick the origin of our coordinate system at the impurity site. The one electron Hamiltonian for the present problem can therefore be written in the form

$$H = \frac{p^2}{2m} + \sum_{\ell} V(\vec{r} - \vec{x}(\ell)) + \Delta V(\vec{r}) \\ \equiv H_0 + \Delta V(\vec{r}) . \quad (3)$$

Here $V(\vec{r})$ is the F^- ion potential seen by the $2p$ electrons while

$$\Delta V(\vec{r}) = U(\vec{r}) - V(\vec{r}) . \quad (4)$$

In Eq. (4) $U(\vec{r})$ is the impurity ion potential seen by the $2p$ electrons of that ion. We assume that the introduction of the substitutional impurity does not alter the O_h symmetry of the impurity site.

The p -like eigenfunctions of $(p^2/2m) + V(\vec{r})$ obey the Schrödinger equation

$$\left[\frac{p^2}{2m} + V(\vec{r}) \right] \phi_{\alpha}(\vec{r}) = \epsilon_0 \phi_{\alpha}(\vec{r}) , \quad \alpha = x, y, z . \quad (5)$$

The p -like eigenfunctions of $(p^2/2m) + U(\vec{r})$ obey

$$\left[\frac{p^2}{2m} + U(\vec{r}) \right] x_{\alpha}(\vec{r}) = \epsilon_1 x_{\alpha}(\vec{r}) , \quad \alpha = x, y, z . \quad (6)$$

The orbitals $\{\phi_{\alpha}(\vec{r})\}$ and $\{x_{\alpha}(\vec{r})\}$ will be assumed to be real and to be orthonormal among themselves.

We wish to solve the Schrödinger equation

$$H\psi(\vec{r}) = E\psi(\vec{r}) . \quad (7)$$

Sec. D

To do so we write

$$\psi(\vec{r}) = \sum_{\alpha} C_{\alpha}(0) \chi_{\alpha}(\vec{r}) + \sum_{\alpha} \sum_{\ell(\neq 0)} C_{\alpha}(\ell) \phi_{\alpha}(\vec{r} - \vec{x}(\ell)) \quad . \quad (8)$$

When we substitute Eq. (8) into Eq. (7) and use the orthonormality of the $\{\chi_{\alpha}(\vec{r})\}$ and the $\{\phi_{\alpha}(\vec{r})\}$ the resulting equation for the expansion coefficients $\{C_{\alpha}(\ell)\}$ can be written in the form

$$\sum_{\ell' \beta} H_{\alpha \beta}(\ell \ell') C_{\beta}(\ell') = E \sum_{\ell' \beta} O_{\alpha \beta}(\ell \ell') C_{\beta}(\ell') \quad . \quad (9)$$

The Hamiltonian matrix $H_{\alpha \beta}(\ell \ell')$ can be written explicitly in the form

$$\begin{aligned} H_{\alpha \beta}(\ell \ell') &= \delta_{\ell 0} \delta_{\ell' 0} \int d^3 r \chi_{\alpha}(\vec{r}) [H_0 + \Delta V] \chi_{\beta}(\vec{r}) + \\ &+ \delta_{\ell 0} (1 - \delta_{\ell' 0}) \int d^3 r \chi_{\alpha}(\vec{r}) [H_0 + \Delta V] \phi_{\beta}(\vec{r} - \vec{x}(\ell')) + \\ &+ (1 - \delta_{\ell 0}) \delta_{\ell' 0} \int d^3 r \phi_{\alpha}(\vec{r} - \vec{x}(\ell)) [H_0 + \Delta V] \chi_{\beta}(\vec{r}) + \\ &+ (1 - \delta_{\ell 0})(1 - \delta_{\ell' 0}) \int d^3 r \phi_{\alpha}(\vec{r} - \vec{x}(\ell)) [H_0 + \Delta V] \phi_{\beta}(\vec{r} - \vec{x}(\ell')) \\ &= H_{\beta \ell}(\ell' \ell) \quad . \end{aligned} \quad (10)$$

The overlap matrix $O_{\alpha \beta}(\ell \ell')$ has the explicit form

$$\begin{aligned} O_{\alpha \beta}(\ell \ell') &= \delta_{\ell 0} \delta_{\ell' 0} \delta_{\alpha \beta} + \delta_{\ell 0} (1 - \delta_{\ell' 0}) \int d^3 r \chi_{\alpha}(\vec{r}) \phi_{\beta}(\vec{r} - \vec{x}(\ell')) \\ &+ (1 - \delta_{\ell 0}) \delta_{\ell' 0} \int d^3 r \phi_{\alpha}(\vec{r} - \vec{x}(\ell)) \chi_{\beta}(\vec{r}) + \\ &+ (1 - \delta_{\ell 0})(1 - \delta_{\ell' 0}) \int d^3 r \phi_{\alpha}(\vec{r} - \vec{x}(\ell)) \phi_{\beta}(\vec{r} - \vec{x}(\ell')) \\ &= O_{\beta \alpha}(\ell' \ell) \quad . \end{aligned} \quad (11)$$

Our next step is to separate the two matrices $H_{\alpha\beta}(\ell\ell')$ and $O_{\alpha\beta}(\ell\ell')$ into their unperturbed and perturbed parts

$$H_{\alpha\beta}(\ell\ell') = H_{\alpha\beta}^{(o)}(\ell\ell') + \Delta H_{\alpha\beta}(\ell\ell') \quad (12)$$

$$O_{\alpha\beta}(\ell\ell') = O_{\alpha\beta}^{(o)}(\ell\ell') + \Delta O_{\alpha\beta}(\ell\ell') \quad . \quad (13)$$

The matrix $H_{\alpha\beta}^{(o)}(\ell\ell')$ is given by

$$\begin{aligned} H_{\alpha\beta}^{(o)}(\ell\ell') &= \int d^3r \phi_{\alpha}(\vec{r} - \vec{x}(\ell)) H_0 \phi_{\beta}(\vec{r} - \vec{x}(\ell)) \\ &= \delta_{\ell 0} \delta_{\ell' 0} \int d^3r \phi_{\alpha}(\vec{r}) H_0 \phi_{\beta}(\vec{r}) + \\ &+ \delta_{\ell 0} (1 - \delta_{\ell' 0}) \int d^3r \phi_{\alpha}(\vec{r}) H_0 \phi_{\beta}(\vec{r} - \vec{x}(\ell)) + \\ &+ (1 - \delta_{\ell 0}) \delta_{\ell' 0} \int d^3r \phi_{\alpha}(\vec{r} - \vec{x}(\ell)) H_0 \phi_{\beta}(\vec{r}) + \\ &+ (1 - \delta_{\ell 0})(1 - \delta_{\ell' 0}) \int d^3r \phi_{\alpha}(\vec{r} - \vec{x}(\ell)) H_0 \phi_{\beta}(\vec{r} - \vec{x}(\ell')) \\ &= H_{\beta\alpha}^{(o)}(\ell'\ell) \quad . \quad (14) \end{aligned}$$

Subtracting this expression from that given by Eq. (10), we obtain

$$\begin{aligned} \Delta H_{\alpha\beta}(\ell\ell') &= \delta_{\ell 0} \delta_{\ell' 0} \left\{ \int d^3r \chi_{\alpha}(\vec{r}) [H_0 + \Delta V] \chi_{\beta}(\vec{r}) - \right. \\ &\quad \left. - \int d^3r \phi_{\alpha}(\vec{r}) H_0 \phi_{\beta}(\vec{r}) \right\} + \\ &+ \delta_{\ell 0} (1 - \delta_{\ell' 0}) \left\{ \int d^3r \chi_{\alpha}(\vec{r}) [H_0 + \Delta V] \phi_{\beta}(\vec{r} - \vec{x}(\ell')) - \right. \\ &\quad \left. + \int d^3r \phi_{\alpha}(\vec{r}) [H_0 + \Delta V] \chi_{\beta}(\vec{r} - \vec{x}(\ell')) \right\} \end{aligned}$$

$$\begin{aligned}
& - \int d^3r \phi_{\alpha}(\vec{r}) H_0 \phi_{\beta}(\vec{r} - \vec{x}(\ell)) \Big\} + \\
& + (1 - \delta_{\ell 0}) \delta_{\ell' 0} \left\{ \int d^3r \phi_{\alpha}(\vec{r} - \vec{x}(\ell)) [H_0 + \Delta V] \chi_{\beta}(\vec{r}) - \right. \\
& \left. - \int d^3r \phi_{\alpha}(\vec{r} - \vec{x}(\ell)) H_0 \phi_{\beta}(\vec{r}) \right\} + \\
& + (1 - \delta_{\ell 0})(1 - \delta_{\ell' 0}) \int d^3r \phi_{\alpha}(\vec{r} - \vec{x}(\ell)) \Delta V \phi_{\beta}(\vec{r} - \vec{x}(\ell')) . \quad (15)
\end{aligned}$$

The unperturbed overlap matrix is given by

$$O_{\alpha\beta}^{(0)}(\ell\ell') = \int d^3r \phi_{\alpha}(\vec{r} - \vec{x}(\ell)) \phi_{\beta}(\vec{r} - \vec{x}(\ell')) = O_{\beta\alpha}^{(0)}(\ell'\ell) . \quad (16)$$

It follows that the perturbing overlap matrix is given by

$$\begin{aligned}
\Delta O_{\alpha\beta}(\ell\ell') = & \delta_{\ell 0}(1 - \delta_{\ell' 0}) \int d^3r [\chi_{\alpha}(\vec{r}) - \phi_{\alpha}(\vec{r})] \times \phi_{\beta}(\vec{r} - \vec{x}(\ell')) + \\
& + (1 - \delta_{\ell 0}) \delta_{\ell' 0} \int d^3r \phi_{\alpha}(\vec{r} - \vec{x}(\ell)) [\chi_{\beta}(\vec{r}) - \phi_{\beta}(\vec{r})] . \quad (17)
\end{aligned}$$

We now turn to a study of the properties of the four matrices $H_{\alpha\beta}^{(0)}(\ell\ell')$, $O_{\alpha\beta}^{(0)}(\ell\ell')$, $\Delta H_{\alpha\beta}(\ell\ell')$, and $\Delta O_{\alpha\beta}(\ell\ell')$.

We note first of all that $H_{\alpha\beta}^{(0)}(\ell\ell')$ and $O_{\alpha\beta}^{(0)}(\ell\ell')$ have the property that

$$H_{\alpha\beta}^{(0)}(\ell + m \ell' + m) = H_{\alpha\beta}^{(0)}(\ell\ell') \quad (18)$$

$$O_{\alpha\beta}^{(0)}(\ell + m \ell' + m) = O_{\alpha\beta}^{(0)}(\ell\ell') . \quad (19)$$

Thus these two matrices depend on the cell indices ℓ and ℓ' only through their difference.

The fcc lattice belongs to the space group O_h^5 (as does the rocksalt lattice). The operations of this group are written in the Seitz¹ notation as $\{\overleftrightarrow{S} | \vec{x}(m)\}$. Here \overleftrightarrow{S} is a 3×3 real, orthogonal matrix representative of one of the rotations (proper or improper) which constitute the point group of the space group of the crystal (O_h in the present case). $\vec{x}(m)$ is a lattice translation vector. This operation is defined by its effect on the position vector $\vec{x}(l)$

$$\{\overleftrightarrow{S} | \vec{x}(m)\} \vec{x}(l) = \overleftrightarrow{S} \vec{x}(l) + \vec{x}(m) \equiv \vec{x}(L) \quad . \quad (20)$$

The last equation expresses the fact that because $\{\overleftrightarrow{S} | \vec{x}(m)\}$ is a symmetry operation it must send a lattice vector $\vec{x}(l)$ into another lattice vector, which we denote by $\vec{x}(L)$. We will use the convention of denoting by upper case letters the site into which a site labeled by the corresponding lower case letter is sent by a space group operation. Finally, we emphasize that we use the active convention, in which the space group moves the points of the crystal with respect to a fixed set of coordinate axes.

The site symmetry of each lattice site of an fcc lattice is that of the point group O_h . Under the operations of this group the orbitals $\{\phi_\alpha(\vec{r})\}$ and $\{x_\alpha(\vec{r})\}$ transform according to

$$P_s \phi_\alpha(\vec{r}) \equiv \phi_\alpha(\overleftrightarrow{S}^{-1} \vec{r}) = \sum_\beta \Gamma_{\beta\alpha}^{(4-)}(S) \phi_\beta(\vec{r}) \quad (21)$$

$$P_s x_\alpha(\vec{r}) \equiv x_\alpha(\overleftrightarrow{S}^{-1} \vec{r}) = \sum_\beta \Gamma_{\beta\alpha}^{(4-)}(S) \phi_\beta(\vec{r}) \quad (22)$$

where $\Gamma^{(4-)}(S)$ is the matrix representing the operation S of the group O_h in the irreducible representation Γ_4^- . This representation is the polar vector

irreducible representation, whose basis functions are x, y, z , and it is the irreducible representation according to which p-like orbitals transform. In the case of the group O_h we have the simplifying result that

$$\overleftrightarrow{\Gamma}^{(4-)}(S) = \overleftrightarrow{S} . \quad (23)$$

If we use the fact that the unperturbed Hamiltonian H_0 is invariant under all operations of the space group O_h^5 , we obtain the following transformation laws for the matrices $H_{\alpha\beta}^{(o)}(LL')$ and $O_{\alpha\beta}^{(o)}(LL')$ when the crystal is subjected to an operation from this group

$$H_{\alpha\beta}^{(o)}(LL') = \sum_{\mu\nu} S_{\alpha\mu} S_{\beta\nu} H_{\mu\nu}^{(o)}(LL') \quad (24)$$

$$O_{\alpha\beta}^{(o)}(LL') = \sum_{\mu\nu} S_{\alpha\mu} S_{\beta\nu} O_{\mu\nu}^{(o)}(LL') . \quad (25)$$

If we assume that these two matrices vanish unless $\ell = \ell'$ or ℓ and ℓ' are nearest and next nearest neighbors, we obtain the following results for the nonzero elements of these matrices:

$$\overleftrightarrow{H}^{(o)}(000;000) = \begin{pmatrix} \alpha_0 & 0 & 0 \\ 0 & \alpha_0 & 0 \\ 0 & 0 & \alpha_0 \end{pmatrix} \quad (26)$$

$$\overleftrightarrow{H}^{(o)}(000;110) = \overleftrightarrow{H}^{(o)}(000;\bar{1}\bar{1}0) = \begin{pmatrix} \alpha & \beta & 0 \\ \beta & \alpha & 0 \\ 0 & 0 & \gamma \end{pmatrix} \quad (27a)$$

$$\overleftrightarrow{H}^{(o)}(000;\bar{1}10) = \overleftrightarrow{H}^{(o)}(000;1\bar{1}0) = \begin{pmatrix} \alpha & -\beta & 0 \\ -\beta & \alpha & 0 \\ 0 & 0 & \gamma \end{pmatrix} \quad (27b)$$

$$\leftrightarrow_{\mathbf{H}}^{(o)}(000;101) = \leftrightarrow_{\mathbf{H}}^{(o)}(000;\bar{1}0\bar{1}) = \begin{pmatrix} \alpha & 0 & \beta \\ 0 & \gamma & 0 \\ \beta & 0 & \alpha \end{pmatrix} \quad (27c)$$

$$\leftrightarrow_{\mathbf{H}}^{(o)}(000;\bar{1}01) = \leftrightarrow_{\mathbf{H}}^{(o)}(000;10\bar{1}) = \begin{pmatrix} \alpha & 0 & -\beta \\ 0 & \gamma & 0 \\ -\beta & 0 & \alpha \end{pmatrix} \quad (27d)$$

$$\leftrightarrow_{\mathbf{H}}^{(o)}(000;011) = \leftrightarrow_{\mathbf{H}}^{(o)}(000;0\bar{1}\bar{1}) = \begin{pmatrix} \gamma & 0 & 0 \\ 0 & \alpha & \beta \\ 0 & \beta & \alpha \end{pmatrix} \quad (27e)$$

$$\leftrightarrow_{\mathbf{H}}^{(o)}(000;0\bar{1}1) = \leftrightarrow_{\mathbf{H}}^{(o)}(000;01\bar{1}) = \begin{pmatrix} \gamma & 0 & 0 \\ 0 & \alpha & -\beta \\ 0 & -\beta & \alpha \end{pmatrix} \quad (27f)$$

$$\leftrightarrow_{\mathbf{H}}^{(o)}(000;200) = \leftrightarrow_{\mathbf{H}}^{(o)}(000;\bar{2}00) = \begin{pmatrix} \delta & 0 & 0 \\ 0 & \epsilon & 0 \\ 0 & 0 & \epsilon \end{pmatrix} \quad (28a)$$

$$\leftrightarrow_{\mathbf{H}}^{(o)}(000;020) = \leftrightarrow_{\mathbf{H}}^{(o)}(000;0\bar{2}0) = \begin{pmatrix} \epsilon & 0 & 0 \\ 0 & \delta & 0 \\ 0 & 0 & \epsilon \end{pmatrix} \quad (28b)$$

$$\leftrightarrow_{\mathbf{H}}^{(o)}(000;002) = \leftrightarrow_{\mathbf{H}}^{(o)}(000;00\bar{2}) = \begin{pmatrix} \epsilon & 0 & 0 \\ 0 & \epsilon & 0 \\ 0 & 0 & \delta \end{pmatrix} \quad (28c)$$

$$\leftrightarrow_{\mathbf{O}}^{(o)}(000;000) = \begin{pmatrix} 1 & 0 & 0 \\ 0 & 1 & 0 \\ 0 & 0 & 1 \end{pmatrix} \quad (29)$$

The forms of the remaining nonzero matrices $\overset{\leftrightarrow}{O}^{(o)}(\ell\ell')$ are obtained from the corresponding $\overset{\leftrightarrow}{H}^{(o)}(\ell\ell')$ matrices on replacing $\alpha, \beta, \gamma, \delta, \epsilon$ by $\alpha', \beta', \gamma', \delta', \epsilon'$, respectively.

We now turn to the perturbing matrices $\Delta H_{\alpha\beta}(\ell\ell')$ and $\Delta O_{\alpha\beta}(\ell\ell')$.

In the presence of a substitutional impurity a crystal is no longer invariant under all the operations of its space group. It is invariant only under that subgroup which consists of operations which leave the impurity site fixed while they send the crystal into itself. This subgroup is called the point group of the impurity site. We will denote it by G . In the present case it is the point group O_h . Although this group is the same group as the point group of the space group in the present case, we will denote its operations by $\{R\}$, and their 3×3 real orthogonal matrix representatives by $\{\overset{\leftrightarrow}{R}\}$, in order to make clear in any equation whether we are dealing with perfect crystal space group operations or with operations from the point group of the impurity site.

An atomic position vector $\vec{x}(\ell)$ is transformed under an operation from G according to

$$\sum_{\beta} R_{\alpha\beta} x_{\beta}(\ell) = x_{\alpha}(L) \quad R \subset G \quad . \quad (30)$$

It is then straightforward to establish the transformation laws for the matrices $\Delta H_{\alpha\beta}(\ell\ell')$ and $\Delta O_{\alpha\beta}(\ell\ell')$ when the crystal is subjected to an operation from G . These are

$$\Delta H_{\alpha\beta}(LL') = \sum_{\mu\nu} R_{\alpha\mu} R_{\beta\nu} \Delta H_{\mu\nu}(\ell\ell') \quad (31)$$

$$\Delta O_{\alpha\beta}(LL') = \sum_{\mu\nu} R_{\alpha\mu} R_{\beta\nu} \Delta O_{\alpha\beta}(\ell\ell') \quad . \quad (32)$$

With the aid of these results we find in the two center approximation, and with the assumption that only the impurity site and its nearest and next nearest neighbors are touched by the introduction of the impurity ion, that the only non-zero matrices $\vec{\Delta}H(\mathcal{M})$ have the following forms:

$$\overset{\leftrightarrow}{\Delta}H(000;000) = \begin{pmatrix} a_0 & 0 & 0 \\ 0 & a_0 & 0 \\ 0 & 0 & a_0 \end{pmatrix} \quad (33)$$

$$\overset{\leftrightarrow}{\Delta}H(000;110) = \overset{\leftrightarrow}{\Delta}H(000;\bar{1}\bar{1}0) = \begin{pmatrix} a & b & 0 \\ b & a & 0 \\ 0 & 0 & c \end{pmatrix} \quad (34a)$$

$$\overset{\leftrightarrow}{\Delta}H(000;\bar{1}10) = \overset{\leftrightarrow}{\Delta}H(000;1\bar{1}0) = \begin{pmatrix} a & -b & 0 \\ -b & a & 0 \\ 0 & 0 & c \end{pmatrix} \quad (34b)$$

$$\overset{\leftrightarrow}{\Delta}H(000;101) = \overset{\leftrightarrow}{\Delta}H(000;\bar{1}0\bar{1}) = \begin{pmatrix} a & 0 & b \\ 0 & c & 0 \\ b & 0 & a \end{pmatrix} \quad (34c)$$

$$\overset{\leftrightarrow}{\Delta}H(000;\bar{1}01) = \overset{\leftrightarrow}{\Delta}H(000;10\bar{1}) = \begin{pmatrix} a & 0 & -b \\ 0 & c & 0 \\ -b & 0 & a \end{pmatrix} \quad (34d)$$

$$\overset{\leftrightarrow}{\Delta}H(000;011) = \overset{\leftrightarrow}{\Delta}H(000;0\bar{1}\bar{1}) = \begin{pmatrix} c & 0 & 0 \\ 0 & a & b \\ 0 & b & a \end{pmatrix} \quad (34e)$$

$$\Delta H(000;0\bar{1}1) = \Delta H(000;01\bar{1}) = \begin{pmatrix} c & 0 & 0 \\ 0 & a & -b \\ 0 & -b & a \end{pmatrix} \quad (34f)$$

$$\Delta H(110;110) = \Delta H(\bar{1}\bar{1}0;\bar{1}\bar{1}0) = \begin{pmatrix} d & f & 0 \\ f & d & 0 \\ 0 & 0 & e \end{pmatrix} \quad (35a)$$

$$\Delta H(\bar{1}10;\bar{1}10) = \Delta H(1\bar{1}0;1\bar{1}0) = \begin{pmatrix} d & -f & 0 \\ -f & d & 0 \\ 0 & 0 & e \end{pmatrix} \quad (35b)$$

$$\Delta H(101;101) = \Delta H(\bar{1}0\bar{1};\bar{1}0\bar{1}) = \begin{pmatrix} d & 0 & f \\ 0 & e & 0 \\ f & 0 & d \end{pmatrix} \quad (35c)$$

$$\Delta H(\bar{1}01;\bar{1}01) = \Delta H(10\bar{1};10\bar{1}) = \begin{pmatrix} d & 0 & -f \\ 0 & e & 0 \\ -f & 0 & d \end{pmatrix} \quad (35d)$$

$$\Delta H(011;011) = \Delta H(0\bar{1}\bar{1};0\bar{1}\bar{1}) = \begin{pmatrix} e & 0 & 0 \\ 0 & d & f \\ 0 & f & d \end{pmatrix} \quad (35e)$$

$$\Delta H(0\bar{1}1;0\bar{1}1) = \Delta H(01\bar{1};01\bar{1}) = \begin{pmatrix} e & 0 & 0 \\ 0 & d & -f \\ 0 & -f & d \end{pmatrix} \quad (35f)$$

$$\overset{\leftrightarrow}{\Delta H}(000;200) = \overset{\leftrightarrow}{\Delta H}(000;\bar{2}00) = \begin{pmatrix} g & 0 & 0 \\ 0 & h & 0 \\ 0 & 0 & h \end{pmatrix} \quad (36a)$$

$$\overset{\leftrightarrow}{\Delta H}(000;020) = \overset{\leftrightarrow}{\Delta H}(000;0\bar{2}0) = \begin{pmatrix} h & 0 & 0 \\ 0 & g & 0 \\ 0 & 0 & h \end{pmatrix} \quad (36b)$$

$$\overset{\leftrightarrow}{\Delta H}(000;002) = \overset{\leftrightarrow}{\Delta H}(000;00\bar{2}) = \begin{pmatrix} h & 0 & 0 \\ 0 & h & 0 \\ 0 & 0 & g \end{pmatrix} \quad (36c)$$

$$\overset{\leftrightarrow}{\Delta H}(200;200) = \overset{\leftrightarrow}{\Delta H}(\bar{2}00;\bar{2}00) = \begin{pmatrix} m & 0 & 0 \\ 0 & n & 0 \\ 0 & 0 & n \end{pmatrix} \quad (37a)$$

$$\overset{\leftrightarrow}{\Delta H}(020;020) = \overset{\leftrightarrow}{\Delta H}(0\bar{2}0;0\bar{2}0) = \begin{pmatrix} n & 0 & 0 \\ 0 & m & 0 \\ 0 & 0 & n \end{pmatrix} \quad (37b)$$

$$\overset{\leftrightarrow}{\Delta H}(002;002) = \overset{\leftrightarrow}{\Delta H}(00\bar{2};00\bar{2}) = \begin{pmatrix} n & 0 & 0 \\ 0 & n & 0 \\ 0 & 0 & m \end{pmatrix} \quad (37c)$$

The forms of the nonzero matrices $\overset{\leftrightarrow}{\Delta O}(\ell\ell')$ can be obtained from the results given by Eqs. (34) and (36) on replacing a, b, c, g, h by a', b', c', g', h' , respectively. (Note from Eq. (17) that $\overset{\leftrightarrow}{\Delta O}(\ell\ell')$ vanishes identically for $\ell = \ell'$.)

In what follows we will refer to the three orbitals on the impurity site and on the ions of the F' sublattice with which it interacts directly, as constituting the space of the impurity ion.

With the preceding results in hand we return to Eq. (9) which, in view of Eqs. (12) and (13), we rewrite in the form

$$\begin{aligned} \sum_{\alpha\beta} \left[H_{\alpha\beta}^{(o)}(\ell\ell') - E O_{\alpha\beta}^{(o)}(\ell\ell') \right] C_{\beta}(\ell') \\ = \sum_{\alpha\beta} \left[E \Delta O_{\alpha\beta}(\ell\ell') - \Delta H_{\alpha\beta}(\ell\ell') \right] C_{\beta}(\ell') . \end{aligned} \quad (38)$$

The elements of the two matrices on the right-hand side of this equation are non-zero only in the space of the impurity ion. To solve it we therefore introduce the Green's function matrix $G_{\alpha\beta}(\ell\ell'; E)$ defined by

$$\sum_{\alpha\beta} \left[E O_{\alpha\beta}^{(o)}(\ell\ell') - H_{\alpha\beta}^{(o)}(\ell\ell') \right] G_{\beta\gamma}(\ell'\ell''; E) = \delta_{\alpha\gamma} \delta_{\ell\ell''} . \quad (39)$$

In terms of this matrix Eq. (38) can be rewritten equivalently as

$$C_{\alpha}(\ell) = \sum_{\beta} \sum_{\gamma} G_{\alpha\beta}(\ell\ell'; E) \left[\Delta H_{\beta\gamma}(\ell'\ell'') - E \Delta O_{\beta\gamma}(\ell'\ell'') \right] C_{\gamma}(\ell'') . \quad (40)$$

Because of the localized nature of the matrices ΔH and ΔO , the only coefficients $\{C_{\alpha}(\ell)\}$ which appear on the right-hand side of this equation are those corresponding to the space of the impurity. Consequently, Eq. (40) expresses the coefficient $C_{\alpha}(\ell)$ associated with any site of the crystal as a linear combination of the few coefficients in the space of the impurity. If we now restrict the indices (ℓ, α) in Eq. (40) to those corresponding to ions in the space of the impurity, and denote the coefficients $\{C_{\alpha}(\ell)\}$ in this space by $\{C_{\alpha}^{(o)}(\ell)\}$, we obtain a set of homogeneous equations for the determination of the latter:

$$C_{\alpha}^{(0)}(\ell) = \sum_{\ell' \beta} \sum_{\ell'' \gamma} G_{\alpha \beta}(\ell \ell'; E) \left[\Delta H_{\beta \gamma}(\ell' \ell'') - E \Delta O_{\beta \gamma}(\ell' \ell'') \right] C_{\gamma}^{(0)}(\ell'') . \quad (41)$$

In this equation all indices $(\ell, \alpha), (\ell', \beta), (\ell'', \gamma)$ are confined to the space of the impurity. Equating to zero the determinant of the coefficients in Eq. (41) we obtain the equation for the energies of the impurity levels lying above the top of the valence band:

$$\det \left[\delta_{\alpha \gamma} \delta_{\ell \ell''} - \sum_{\ell' \beta} G_{\alpha \beta}(\ell \ell'; E) \left[\Delta H_{\beta \gamma}(\ell' \ell'') - E \Delta O_{\beta \gamma}(\ell' \ell'') \right] \right] = 0 . \quad (42)$$

It should be noted that in the approximation in which the impurity ion interacts with only its nearest neighbors the matrix whose determinant is being evaluated in Eq. (42) is a 39×39 matrix; if the impurity is assumed to interact with its nearest and next nearest neighbors, this matrix is a 57×57 matrix. We will see below, however, that group theory enables us to block diagonalize these matrices so that the dimensionalities of the determinants which must actually be evaluated are quite small.

Central to this approach to the calculation of impurity levels are the elements of the Green's function matrix $G_{\alpha \beta}(\ell \ell'; E)$. We now turn to their evaluation.

We begin by exploiting the translational symmetry of the unperturbed crystal to expand $G_{\alpha \beta}(\ell \ell'; E)$ in the form

$$G_{\alpha \beta}(\ell \ell'; E) = \frac{1}{N} \sum_{\vec{k}} g_{\alpha \beta}(\vec{k} | E) e^{i \vec{k} \cdot (\vec{x}(\ell) - \vec{x}(\ell'))} , \quad (43)$$

where the N allowed values of \vec{k} are uniformly and densely distributed throughout the first Brillouin zone for the fcc lattice. If we also use the expansion

$$\delta_{\ell\ell'} = \frac{1}{N} \sum_{\vec{k}} e^{i\vec{k} \cdot (\vec{x}(\ell) - \vec{x}(\ell'))} \quad , \quad (44)$$

then on substituting Eqs. (43)-(44) into Eq. (39) we obtain the equation for the coefficients $g_{\alpha\beta}(\vec{k} | E)$:

$$\sum_{\beta} D_{\alpha\beta}(\vec{k} | E) g_{\beta\gamma}(\vec{k} | E) = \delta_{\alpha\gamma} \quad , \quad (45)$$

where

$$D_{\alpha\beta}(\vec{k} | E) = E O_{\alpha\beta}^{(0)}(\vec{k}) - H_{\alpha\beta}(\vec{k}) \quad (46)$$

with

$$O_{\alpha\beta}^{(0)}(\vec{k}) = \sum_{\ell'} O_{\alpha\beta}^{(0)}(\ell\ell') e^{i\vec{k} \cdot (\vec{x}(\ell) - \vec{x}(\ell'))} \quad (47)$$

$$H_{\alpha\beta}^{(0)}(\vec{k}) = \sum_{\ell'} H_{\alpha\beta}^{(0)}(\ell\ell') e^{i\vec{k} \cdot (\vec{x}(\ell) - \vec{x}(\ell'))} \quad . \quad (48)$$

It follows from Eq. (45) that

$$g_{\alpha\beta}(\vec{k} | E) = D_{\alpha\beta}^{-1}(\vec{k} | E) \quad . \quad (49)$$

If we make use of the results given by Eqs. (26)-(29) we can write the following explicit expressions for the elements of the matrices $H_{\alpha\beta}^{(0)}(\vec{k})$ and $O_{\alpha\beta}^{(0)}(\vec{k})$:

$$\begin{aligned} H_{xx}^{(0)}(\vec{k}) = & \alpha_0 + 4\alpha \cos \frac{a_0}{2} k_x \left(\cos \frac{a_0}{2} k_y + \cos \frac{a_0}{2} k_z \right) + \\ & + 4\gamma \cos \frac{a_0}{2} k_y \cos \frac{a_0}{2} k_z + 2\delta \cos k_x a_0 + \\ & + 2\epsilon \left(\cos k_y a_0 + \cos k_z a_0 \right) \end{aligned} \quad (50a)$$

Sec. D

$$H_{xy}^{(o)}(\vec{k}) = -4\beta \sin \frac{a_0}{2} k_x \sin \frac{a_0}{2} k_y \quad (50b)$$

$$\begin{aligned} O_{xx}^{(o)}(\vec{k}) = & 1 + 4\alpha' \cos \frac{a_0}{2} k_x \left(\cos \frac{a_0}{2} k_y + \cos \frac{a_0}{2} k_z \right) + \\ & + 4\gamma' \cos \frac{a_0}{2} k_y \cos \frac{a_0}{2} k_z + 2\delta' \cos k_x a_0 + \\ & + 2\epsilon' (\cos k_y a_0 + \cos k_z a_0) \end{aligned} \quad (50c)$$

$$O_{xy}^{(o)}(\vec{k}) = -4\beta' \sin \frac{a_0}{2} k_x \sin \frac{a_0}{2} k_y . \quad (50d)$$

The remaining matrix elements can be obtained by cyclic permutations of the subscripts.

The evaluation of the Green's functions $G_{\alpha\beta}^{(\ell\ell')}(E)$ can be greatly simplified by the use of symmetry arguments. We note first that if we combine Eqs. (24), (25), (46)-(48), we can establish the following transformation law for the matrix $D_{\alpha\beta}(\vec{k}|E)$ when the unperturbed crystal is subjected to an operation from its space group:

$$D_{\alpha\beta}(\overset{\leftrightarrow}{S} \vec{k} | E) = \sum_{\mu\nu} S_{\alpha\mu} S_{\beta\nu} D_{\mu\nu}(\vec{k} | E) . \quad (51)$$

(It is this result which underlies the comment following Eq. (50).) It follows, therefore, that the matrix $g_{\alpha\beta}(\vec{k}|E)$ obeys the same transformation law

$$g_{\alpha\beta}(\overset{\leftrightarrow}{S} \vec{k} | E) = \sum_{\mu\nu} S_{\alpha\mu} S_{\beta\nu} g_{\mu\nu}(\vec{k} | E) . \quad (52)$$

Moreover, because every ion is at a center of inversion in the unperturbed crystal, Eq. (43) can be rewritten as

$$G_{\alpha\beta}(\ell\ell'; E) = \frac{1}{N} \sum_{\vec{k}} g_{\alpha\beta}(\vec{k}|E) \cos \vec{k} \cdot (\vec{x}(\ell) - \vec{x}(\ell')) , \quad (53)$$

since $g_{\alpha\beta}(-\vec{k}|E) = g_{\alpha\beta}(\vec{k}|E)$. Now \vec{k} is a dummy summation variable. We can therefore replace it by $\overset{\leftrightarrow}{S}\vec{k}$, where $\overset{\leftrightarrow}{S}$ represents one of the operations of the point group of the space group of the host crystal. We do this for each element of this group in turn; sum the results over all group elements, and divide by the order of the group. In this way we obtain the result that

$$\begin{aligned} G_{\alpha\beta}(\ell\ell'; E) &= \frac{1}{h} \sum_{S \in O_h} \frac{1}{N} \sum_{\vec{k}} g_{\alpha\beta}(\overset{\leftrightarrow}{S}\vec{k}|E) \times \cos \overset{\leftrightarrow}{S}\vec{k} \cdot (\vec{x}(\ell) - \vec{x}(\ell')) \\ &= \frac{1}{h} \sum_{S \in O_h} \frac{1}{N} \sum_{\vec{k}} \sum_{\mu\nu} S_{\alpha\mu} g_{\mu\nu}(\vec{k}|E) S_{\nu\beta}^{-1} \times \\ &\quad \times \cos \vec{k} \cdot \overset{\leftrightarrow}{S}^{-1}(\vec{x}(\ell) - \vec{x}(\ell')) , \end{aligned} \quad (54)$$

where h is the order of the group ($h = 48$ in the present case). This result can be simplified a bit. Since the point group O_h is the direct product of the group C_i and the group O , where C_i is the group of order 2 whose elements are the identity and the inversion, and because the effects of inversion have already been taken into account in the replacement of $\exp(i\vec{k} \cdot (\vec{x}(\ell) - \vec{x}(\ell')))$ by $\cos \vec{k} \cdot (\vec{x}(\ell) - \vec{x}(\ell'))$ in Eq. (53), we can replace O_h by O in Eq. (54) and take $h = 24$. When we do this we obtain finally $(\vec{x}(\ell) - \vec{x}(\ell')) \equiv \vec{x}$

$$\begin{aligned} G_{xx}(\ell\ell'; E) &= \frac{1}{6N} \sum_{\vec{k}} \left\{ g_{xx}(\vec{k}|E) \cos k_x x \times \right. \\ &\quad \times \left. (\cos k_y y \cos k_z z + \cos k_y z \cos k_z y) + g_{yy}(\vec{k}|E) \times \right. \\ &\quad \times \left. (\cos k_x x \cos k_z z + \cos k_x z \cos k_z x) \right\} \end{aligned}$$

$$\begin{aligned}
 & \times \cos k_y x (\cos k_z z \cos k_x y + \cos k_z y \cos k_x z) + \\
 & + g_{zz}(\vec{k}|E) \cos k_z x (\cos k_x y \cos k_y z + \cos k_x z \cos k_y y) \} \\
 \end{aligned} \tag{55}$$

$$\begin{aligned}
 G_{xy}(\ell\ell'; E) = \frac{1}{6N} \sum_{\vec{k}} \left\{ g_{xy}(\vec{k}|E) [\sin k_x x \sin k_y y + \right. \\
 & + \sin k_y x \sin k_x y] \cos k_z z + g_{yz}(\vec{k}|E) [\sin k_y x \sin k_z y + \\
 & + \sin k_z x \sin k_y y] \cos k_x z + g_{zx}(\vec{k}|E) [\sin k_z x \sin k_x y + \\
 & \left. + \sin k_x x \sin k_z y] \cos k_y z \right\} . \\
 \end{aligned} \tag{56}$$

The remaining elements of $G_{\alpha\beta}(\ell\ell'; E)$ are obtained from these by cyclic permutations of subscripts.

For both $G_{xx}(\ell\ell'; E)$ and $G_{xy}(\ell\ell'; E)$ the summands in Eqs. (55) and (56), respectively, are invariant against all operations of the point group O_h , for all ℓ and ℓ' . These expressions, therefore, are in forms to which special point integration methods² can be applied.

We now show how group theory can be used to block diagonalize the matrices $G_{\alpha\beta}(\ell\ell'; E)$, $\Delta H_{\alpha\beta}(\ell\ell')$ and $\Delta O_{\alpha\beta}(\ell\ell')$ in the space of the impurity.³ We first determine the number of times each irreducible representation of O_h is contained in the (reducible) representation of this group provided by the matrices $\{S_{\alpha\beta}(\ell\ell'; R)\}$ which are defined by

$$S_{\alpha\beta}(\ell\ell'; R) = R_{\alpha\beta} \delta(\vec{R}^{-1} \vec{x}(\ell), \vec{x}(\ell')) . \tag{57}$$

These matrices commute with the matrices $G_{\alpha\beta}(\ell\ell'; E)$, $\Delta H_{\alpha\beta}(\ell\ell')$, and $\Delta O_{\alpha\beta}(\ell\ell')$ in the space of the impurity, as can be seen from Eqs. (31), (32), and (52)-(53). The number of times the s^{th} irreducible representation of O_h is contained in this representation is given by

$$c_s = \frac{1}{h} \sum_{R \in G} \chi(R) \chi^{(s)}(R)^* \quad (58)$$

where $\chi^{(s)}(R)$ is the character of the s^{th} irreducible representation of O_h , and

$$\begin{aligned} \chi(R) &= \sum_{\alpha\ell} S_{\alpha\ell}(\ell\ell; R) \\ &= \sum_{\alpha} R_{\alpha\ell} \sum_{\ell} \delta(\vec{R}^{-1} \vec{x}(\ell), \vec{x}(\ell)) \\ &= (\pm 1 + 2 \cos \phi) N(R) \quad . \end{aligned} \quad (59)$$

In Eq. (59) ϕ is the angle through which the crystal is rotated about the impurity site; the plus sign obtains if the operation R is a proper rotation, while the minus sign applies if it is an improper rotation (that is, rotation through an angle ϕ followed by reflection in the plane perpendicular to the rotation axis; and $N(R)$ is the number of lattice sites in the space of the impurity left unmoved by the symmetry operation R . In the present case we obtain the following results.

A. Nearest Neighbor Impurity Interaction

If the impurity ion interacts with only its nearest neighbors in the F^- sub-lattice, then from Eq. (59) we obtain the following character table:

Sec. D

R	E	8C ₃	3C ₂	6C ₄	6C' ₂	I	8S ₆	3σ _h	6S ₄	6σ _d
χ(R)	39	0	-1	1	-3	-3	0	5	-1	3

Thus the representation Γ of O_h generated by the matrices $\{S_{\alpha\beta}(\ell\ell'; R)\}$ in this case reduces according to⁴

$$\Gamma = \Gamma_1^+ \oplus \Gamma_2^+ \oplus 2\Gamma_3^+ \oplus 2\Gamma_4^+ \oplus 2\Gamma_5^+ \oplus \Gamma_2^- \oplus \Gamma_3^- \oplus 4\Gamma_4^- \oplus 2\Gamma_5^- . \quad (60)$$

B. Next Nearest Neighbor Impurity Interaction

If the impurity ion interacts with its nearest and next nearest neighbors in the F^- sublattice, then Eq. (59) yields the following character table:

R	E	8C ₃	3C ₂	6C ₄	6C' ₂	I	8S ₆	3σ _h	6S ₄	6σ _d
χ(R)	57	0	-3	3	-3	-3	0	9	-1	5

The representation Γ of O_h generated by the matrices $\{S_{\alpha\beta}(\ell\ell'; R)\}$ therefore reduces in this case according to

$$\Gamma = 2\Gamma_1^+ \oplus \Gamma_2^+ \oplus 3\Gamma_3^+ \oplus 3\Gamma_4^+ \oplus 3\Gamma_5^+ \oplus \Gamma_2^- \oplus \Gamma_3^- \oplus 6\Gamma_4^- \oplus 3\Gamma_5^- . \quad (61)$$

The preceding results imply that if the matrix of the determinant in Eq. (42) is block diagonalized by group theoretic methods, the largest determinant that has to be solved in the case that the impurity is assumed to interact with only its nearest neighbors in the F^- sublattice is a 4×4 determinant, for levels of Γ_4^- symmetry; in the case that the impurity is assumed to interact with its nearest

and next nearest neighbors on the F' sublattice the largest determinant to be solved is a 6×6 determinant, also for levels of Γ_4' symmetry.

To effect this block diagonalization we introduce symmetry coordinates in the following way.³ Let the vector $\{\phi_\alpha(\ell)\}$ be an arbitrary vector in the space of the impurity. Construct from it the vectors $\{\psi_\alpha^{(s\mu)}(\ell)\}$ in the following way:

$$\psi_\alpha^{(s\mu)}(\ell) = \frac{f_s}{h} \sum_{R \in G} \Gamma_{\mu\mu}^{(s)}(R)^* \sum_{\ell' \beta} S_{\alpha\beta}(\ell\ell'; R) \phi_\beta(\ell') . \quad (62)$$

Here s labels the irreducible representations of the point group G ; f_s is the dimensionality of the irreducible representation s ; h is the order of G ; $\Gamma_{\mu\nu}^{(s)}(R)$ is a matrix representative of the operation R in the irreducible representation s ; and $S_{\alpha\beta}(\ell\ell'; R)$ has been defined in Eq. (57). The vector $\psi_\alpha^{(s\mu)}(\ell)$ obtained in this way belongs to the μ^{th} row of the s^{th} irreducible representation of G .⁽³⁾ It can be shown to depend on as many independent, nonzero parameters as the number of times (c_s) the representation s is contained in the reducible representation of G provided by the matrices $\{S_{\alpha\beta}(\ell\ell'; R)\}$. From the vector $\psi_\alpha^{(s\mu)}(\ell)$ we construct c_s vectors $\{\psi_\alpha^{(sa\mu)}(\ell)\}$ ($a = 1, 2, \dots, c_s$) by equating each of the c_s independent parameters on which it depends to unity in turn, with all the remaining parameters being set equal to zero, and normalizing the resulting vectors to unity. The c_s vectors obtained in this way will often be mutually orthogonal, but not always. In the latter case they can be orthogonalized by the Schmidt process. The set of vectors $\{\psi_\alpha^{(sa\mu)}(\ell)\}$ ($\mu = 1, 2, \dots, f_s$; $a = 1, 2, \dots, c_s$) obtained in this way is called a set of symmetry coordinates. Each vector $\psi_\alpha^{(sa\mu)}(\ell)$ ($a = 1, 2, \dots, c_s$) belongs to the μ^{th} row of the s^{th} irreducible representation of G . The set is orthonormal and complete in the space of the impurity:

$$\sum_{\ell\alpha} \psi_{\alpha}^{(sa\mu)}(\ell)^* \psi_{\alpha}^{(s'a'\mu')(\ell)} = \delta_{ss'} \delta_{aa'} \delta_{\mu\mu'}. \quad (63a)$$

$$\sum_{s\mu} \psi_{\alpha}^{(sa\mu)}(\ell)^* \psi_{\beta}^{(sa\mu)(\ell')} = \delta_{\ell\ell'} \delta_{\alpha\beta}. \quad (63b)$$

The usefulness of the vectors $\{\psi_{\alpha}^{(sa\mu)}(\ell)\}$ lies in the fact that a matrix element of any matrix $M_{\alpha\beta}(\ell\ell'; E)$ which commutes with all the matrices $\{S_{\alpha\beta}(\ell\ell'; R)\}$ taken between two vectors $\psi_{\alpha}^{(sa\mu)}(\ell)$ and $\psi_{\alpha}^{(s'a'\mu')(\ell)}$ vanishes unless $s = s'$ and $\mu = \mu'$:

$$\begin{aligned} \bar{M}(sa\mu; s'a'\mu') &= \sum_{\ell\alpha} \sum_{\ell'\beta} \psi_{\alpha}^{(sa\mu)}(\ell)^* M_{\alpha\beta}(\ell\ell'; E) \times \psi_{\beta}^{(s'a'\mu')(\ell')} \\ &= \frac{1}{f_s} \delta_{ss'} \delta_{\mu\mu'} \sum_{\lambda=1}^{f_s} \bar{M}(sa\lambda; s'a'\lambda). \end{aligned} \quad (64)$$

Moreover, when $s = s'$ and $\mu = \mu'$ $\bar{M}(sa\mu; sa'\mu')$ is independent of μ . We can therefore rewrite Eq. (64) as

$$\bar{M}(sa\mu; s'a'\mu') = \delta_{ss'} \delta_{\mu\mu'} \bar{M}^{(s)}(aa'). \quad (65)$$

Thus, if we denote the matrix of the determinant in Eq. (42) by $\Delta_{\alpha\beta}(\ell\ell'; E)$,

$$\begin{aligned} \Delta_{\alpha\beta}(\ell\ell'; E) &= \delta_{\alpha\beta} \delta_{\ell\ell'} - \sum_{\ell''\gamma} G_{\alpha\gamma}(\ell\ell''; E) \times \\ &\times \left[\Delta H_{\gamma\beta}(\ell''\ell') - E \Delta O_{\gamma\beta}(\ell''\ell') \right], \end{aligned} \quad (66)$$

and note that each of the matrices entering it commutes with all the matrices $\{S_{\alpha\beta}(\ell\ell'; R)\}$, we know from Eqs. (64) and (65) that the matrix element of $\Delta_{\alpha\beta}(\ell\ell'; E)$ between the vectors $\psi_{\alpha}^{(sa\mu)}(\ell)$ and $\psi_{\beta}^{(s'a'\mu')(\ell')}$ is

$$\begin{aligned}\bar{\Delta}(s a \mu; s' a' \mu') &= \delta_{ss'} \delta_{\mu\mu'} \bar{\Delta}(s a \mu; s a' \mu) \\ &= \delta_{ss'} \delta_{\mu\mu'} \bar{\Delta}^{(s)}(a a'; E) \quad ,\end{aligned}\quad (67)$$

where

$$\bar{\Delta}^{(s)}(a a'; E) = \delta_{aa'} - \sum_{a''=1}^{c_s} \bar{G}^{(s)}(a a''; E) \times \left[\bar{\Delta}H^{(s)}(a'' a') - E \bar{\Delta}O^{(s)}(a'' a') \right] \quad (68)$$

and

$$\bar{G}^{(s)}(a a'; E) = \sum_{\ell\alpha} \sum_{\ell'\beta} \psi_{\alpha}^{(sa\mu)}(\ell)^* G_{\alpha\beta}(\ell\ell'; E) \psi_{\beta}^{(sa'\mu)}(\ell') \quad (69a)$$

$$\bar{\Delta}H^{(s)}(a a') = \sum_{\ell\alpha} \sum_{\ell'\beta} \psi_{\alpha}^{(sa\mu)}(\ell)^* \Delta H_{\alpha\beta}(\ell\ell') \psi_{\beta}^{(sa'\mu)}(\ell') \quad (69b)$$

$$\bar{\Delta}O^{(s)}(a a') = \sum_{\ell\alpha} \sum_{\ell'\beta} \psi_{\alpha}^{(sa\mu)}(\ell)^* \Delta O_{\alpha\beta}(\ell\ell') \psi_{\beta}^{(sa'\mu)}(\ell') \quad . \quad (69c)$$

Consequently, from Eq. (67) we see that the determinant $\det \Delta_{\alpha\beta}(\ell\ell'; E)$ factors into the product of determinants of smaller dimensions

$$\det \Delta_{\alpha\beta}(\ell\ell'; E) = \prod_s \left[\det \bar{\Delta}^{(s)}(a a'; E) \right]^{f_s} \quad . \quad (70)$$

The energies of the localized states are therefore obtained from the solutions of the determinantal equations

$$\begin{aligned}\det \bar{\Delta}^{(s)}(a a'; E) &= 0 \quad (f_s \text{ times}) \\ a, a' &= 1, 2, \dots, c_s \quad .\end{aligned}\quad (71)$$

We have implemented the preceding procedure in the case that the impurity ion is assumed to interact with only its nearest neighbors in the F^- sublattice.

Sec. D

The symmetry coordinates $\{\psi_{\alpha}^{(s\alpha\mu)}(\ell)\}$ are presented in Table 1. In Table 2 is presented the form of the Green's function matrix in the space of the impurity ion, while in Table 3 is shown the form of the perturbing matrix $\Delta H_{\alpha\beta}(\ell\ell')$.

The form of the perturbing matrix $\Delta O_{\alpha\beta}(\ell\ell')$ is obtained from the latter by setting $a_0 = d = e = f = 0$, and replacing a, b, c by a', b', c' , respectively.

By the use of these results we have worked out the forms of the matrices $\bar{G}^{(s)}(aa'; E)$, $\bar{\Delta H}^{(s)}(aa')$, and $\bar{\Delta O}^{(s)}(aa')$ for the irreducible representation $s = \Gamma_4^-$. This is a particularly interesting case because Γ_4^- is the polar vector irreducible representation of the group O_h , and it is to states of this symmetry that electric dipole transitions from a totally symmetric ground state are allowed. These states should therefore contribute to the absorption of electromagnetic radiation by the crystal. The results are

$$\bar{G}^{(4-)}(aa'; E) = \begin{pmatrix} A & \bar{B} & \frac{1}{\sqrt{2}}C & \sqrt{8}G_1 \\ \bar{B} & \bar{D} & \frac{1}{\sqrt{2}}E & \sqrt{8}\bar{G}_3 \\ \frac{1}{\sqrt{2}}C & \frac{1}{\sqrt{2}}E & F & 2G_2 \\ \sqrt{8}G_1 & \sqrt{8}\bar{G}_3 & 2G_2 & G_0 \end{pmatrix} \quad (72)$$

where

$$A = G_0 + 2G_2 + G_4 + G_5 + G_6 + 2G_9 \quad (73a)$$

$$B = G_8 + 2G_{11} \quad (73b)$$

$$C = 4G_1 + 4G_{10} \quad (73c)$$

$$D = \bar{G}_0 + 2G_3 + G_4 + G_5 + \bar{G}_6 + 2\bar{G}_{12} \quad (73d)$$

$$E = 4\bar{G}_{11} \quad (73e)$$

$$F = G_0 + 2G_5 + G_7 ; \quad (73f)$$

Table 1. Symmetry coordinates for an impurity ion which interacts only with its nearest neighbors. We express the coordinates of the lattice sites through the three integers $\iota_1, \iota_2, \iota_3$ in the expression $x(\iota) = (a_0/2)(\iota_1, \iota_2, \iota_3)$, where a_0 is the lattice parameter.

	A_{1g}	A_{2g}	$E_g^{(11)}$	$E_g^{(21)}$	$E_g^{(12)}$	$E_g^{(22)}$	$T_{1g}^{(11)}$	$T_{1g}^{(21)}$	$T_{1g}^{(12)}$	$T_{1g}^{(22)}$	$E_{1g}^{(13)}$	$E_{1g}^{(23)}$	$E_{2g}^{(11)}$	$E_{2g}^{(21)}$	$E_{2g}^{(12)}$	$E_{2g}^{(22)}$	$E_{2g}^{(13)}$	$E_{2g}^{(23)}$
$\psi_x(000)$	0	0	0	0	0	0	0	0	0	0	0	0	0	0	0	0	0	0
$\psi_y(000)$	0	0	0	0	0	0	0	0	0	0	0	0	0	0	0	0	0	0
$\psi_z(000)$	0	0	0	0	0	0	0	0	0	0	0	0	0	0	0	0	0	0
$\psi_x(110)$	1	1	1	T	T	T	0	0	0	0	0	0	T	0	0	0	0	0
$\psi_y(110)$	1	T	1	T	1	1	0	0	0	0	0	0	1	0	0	0	0	T
$\psi_z(110)$	0	0	0	0	0	0	0	T	T	0	0	0	0	1	1	0	0	0
$\psi_x(\bar{1}10)$	T	T	T	1	1	1	0	0	0	0	0	0	T	0	0	0	0	T
$\psi_y(\bar{1}10)$	1	T	1	T	1	1	0	0	0	0	0	0	T	0	0	0	0	1
$\psi_z(\bar{1}10)$	0	0	0	0	0	0	0	1	T	0	0	0	0	T	1	1	0	0
$\psi_x(\bar{1}\bar{1}0)$	1	T	2	0	T	0	1	0	0	0	0	0	0	1	0	0	0	0
$\psi_y(\bar{1}\bar{1}0)$	0	0	0	0	0	0	0	0	0	1	0	0	T	0	0	1	0	T
$\psi_z(\bar{1}\bar{1}0)$	1	1	1	1	T	1	T	0	0	0	0	0	0	1	0	0	0	0
$\psi_x(\bar{1}01)$	T	1	2	0	2	0	1	0	0	0	0	0	0	1	0	0	0	0
$\psi_y(\bar{1}01)$	0	0	0	0	0	0	0	0	0	1	0	0	1	0	0	1	0	1
$\psi_z(\bar{1}01)$	1	1	1	1	T	1	1	0	0	0	0	0	T	0	0	0	0	0
$\psi_x(011)$	0	0	0	0	0	0	0	1	0	0	0	0	1	0	0	0	T	0
$\psi_y(011)$	1	1	2	0	2	0	0	0	0	0	1	0	0	0	0	1	0	0
$\psi_z(011)$	1	T	1	1	1	T	0	0	0	T	0	0	0	0	1	0	0	0
$\psi_x(0\bar{1}1)$	0	0	0	0	0	0	0	1	0	0	T	0	0	0	1	0	0	0
$\psi_y(0\bar{1}1)$	T	T	2	0	T	0	0	0	0	1	0	0	0	0	0	1	0	0
$\psi_z(0\bar{1}1)$	1	T	1	1	T	0	0	0	0	1	0	0	T	0	0	0	T	0
$\psi_x(\bar{1}\bar{1}\bar{1}0)$	T	T	T	1	1	1	0	0	0	0	0	0	1	0	0	0	0	1
$\psi_y(\bar{1}\bar{1}\bar{1}0)$	T	1	T	1	T	T	0	0	0	0	0	0	T	0	0	0	0	1
$\psi_z(\bar{1}\bar{1}\bar{1}0)$	0	0	0	0	0	0	0	0	1	1	0	0	0	T	T	0	0	0
$\psi_x(\bar{1}\bar{1}1\bar{0})$	1	1	1	T	T	T	0	0	0	0	0	0	1	0	0	0	0	1
$\psi_y(\bar{1}\bar{1}1\bar{0})$	T	1	T	1	T	T	0	0	0	0	0	0	1	0	0	0	0	T
$\psi_z(\bar{1}\bar{1}1\bar{0})$	0	0	0	0	0	0	0	0	T	1	0	0	0	1	T	0	0	0
$\psi_x(\bar{1}1\bar{1}0)$	T	1	2	0	2	0	T	0	0	0	0	0	0	T	0	0	0	0
$\psi_y(\bar{1}1\bar{1}0)$	0	0	0	0	0	0	0	0	T	0	0	0	1	0	0	1	0	0
$\psi_z(\bar{1}1\bar{1}0)$	T	1	1	T	T	T	0	0	0	0	0	0	1	0	0	0	0	T
$\psi_x(1\bar{1}\bar{1}\bar{0})$	T	T	T	T	1	T	1	0	0	0	0	0	T	0	0	0	0	0
$\psi_y(1\bar{1}\bar{1}\bar{0})$	1	T	2	0	T	0	0	0	0	T	0	0	0	0	T	0	0	0
$\psi_z(1\bar{1}\bar{1}\bar{0})$	0	0	0	0	0	0	0	0	T	0	0	0	T	0	0	T	0	0
$\psi_x(1\bar{1}1\bar{0})$	T	1	T	T	T	1	0	0	0	0	0	0	1	0	0	0	0	0
$\psi_y(1\bar{1}1\bar{0})$	0	0	0	0	0	0	0	0	T	0	0	0	1	0	0	T	0	0
$\psi_z(1\bar{1}1\bar{0})$	T	1	1	T	T	T	0	0	0	0	0	0	1	0	0	0	0	T
$\psi_x(10\bar{1}\bar{0})$	1	T	2	0	T	0	0	0	0	T	0	0	0	T	0	0	0	T
$\psi_y(10\bar{1}\bar{0})$	0	0	0	0	0	0	0	0	T	0	0	0	T	0	0	T	0	T
$\psi_z(10\bar{1}\bar{0})$	T	T	T	T	1	T	T	0	0	0	0	0	0	1	0	0	0	0
$\psi_x(0\bar{1}1\bar{0})$	0	0	0	0	0	0	0	0	T	0	0	0	T	0	0	0	0	1
$\psi_y(0\bar{1}1\bar{0})$	T	T	2	0	T	0	0	0	0	T	0	0	0	0	0	T	0	0
$\psi_z(0\bar{1}1\bar{0})$	T	1	T	T	T	1	0	0	0	0	0	0	1	0	0	T	0	0
$\psi_x(01\bar{1}\bar{0})$	0	0	0	0	0	0	0	0	T	0	0	0	T	0	0	T	0	T
$\psi_y(01\bar{1}\bar{0})$	1	1	T	0	2	0	0	0	0	T	0	0	0	0	0	T	0	0
$\psi_z(01\bar{1}\bar{0})$	T	1	T	T	T	1	0	0	0	0	0	0	0	0	0	1	0	0

Table 1. (Continued)

Table 2. The form of the Green's function matrix in the space of the impurity ion.

	000	110	T10	101	T01	011	0T1	T10	1T0	T0T	10T	0TT	01T
000	$G_0 G_0$	$G_1 G_2 0$	$G_1 \bar{G}_3 0$	$G_0 G_3$	$G_0 \bar{G}_3$	$G_2 0 0$	$G_2 0 0$	$G_1 G_3 0$	$G_1 \bar{G}_3 0$	$G_0 G_3$	$G_0 \bar{G}_3 0$	$G_1 0 0$	$G_1 0 0$
	$0 G_0 0$	$G_1 G_2 0$	$\bar{G}_3 G_0 0$	$0 G_1 0$	$0 G_2 0$	$0 G_3 0$	$0 G_4 0$	$0 G_1 \bar{G}_3$	$0 G_2 \bar{G}_3$	$0 G_3 \bar{G}_3$	$0 G_4 \bar{G}_3$	$0 G_1 0$	$0 G_1 \bar{G}_3$
	$0 0 G_0$	$0 0 G_1$	$0 0 G_2$	$G_1 0 G_1$	$\bar{G}_3 0 G_1$	$0 G_3 G_1$	$0 G_4 G_1$	$0 G_3 G_1$	$0 G_4 G_1$	$0 G_3 G_1$	$0 G_4 G_1$	$0 G_3 G_1$	$0 G_3 G_1$
110	$G_1 G_2 0$	$G_0 0 0$	$G_0 0 0$	$G_0 0 0$	$G_1 G_1 \bar{G}_1$	$G_1 0 \bar{G}_3$	$G_{10} G_{11} \bar{G}_{11}$	$G_0 G_2 0$	$G_0 G_2 0$	$G_0 G_2 0$	$G_0 G_2 0$	$G_{10} G_{11} \bar{G}_{11}$	$G_0 G_2 0$
	$G_3 G_0 0$	$0 G_0 0$	$0 G_5 0$	$0 G_1 \bar{G}_3$	$G_{10} G_{11} \bar{G}_{11}$	$0 G_2 0$	$G_{10} G_{11} \bar{G}_{11}$	$G_0 G_3 0$	$G_0 G_3 0$	$G_0 G_3 0$	$G_0 G_3 0$	$G_{10} G_{11} \bar{G}_{11}$	$G_0 G_3 0$
	$0 0 G_2$	$0 0 G_5$	$0 \bar{G}_1 G_1$	$\bar{G}_1 \bar{G}_1 G_{10}$	$\bar{G}_1 \bar{G}_1 G_{10}$	$\bar{G}_1 \bar{G}_1 G_{10}$	$0 G_1 G_{10}$	$0 G_1 G_{10}$	$0 G_1 G_{10}$	$0 G_1 G_{10}$	$0 G_1 G_{10}$	$0 G_1 G_{10}$	$0 G_1 G_{10}$
T10	$G_1 \bar{G}_3 0$	$G_0 0 0$	$G_0 0 0$	$G_0 0 0$	$G_1 \bar{G}_4 G_4$	$G_1 0 G_3$	$G_{10} G_{11} \bar{G}_{11}$	$G_0 \bar{G}_1 G_1$	$G_0 \bar{G}_1 G_1$	$G_0 \bar{G}_1 G_1$	$G_0 \bar{G}_1 G_1$	$G_{10} G_{11} \bar{G}_{11}$	$G_0 \bar{G}_1 G_1$
	$\bar{G}_3 G_0 0$	$0 G_0 0$	$0 G_0 0$	$0 G_0 0$	$\bar{G}_4 G_{10} \bar{G}_{11}$	$0 G_1 \bar{G}_3$	$0 G_2 0$	$\bar{G}_1 G_1 \bar{G}_1$	$0 G_2 0$	$0 G_2 0$	$0 G_2 0$	$\bar{G}_4 G_{10} \bar{G}_{11}$	$0 G_2 0$
	$0 0 G_3$	$0 0 G_5$	$0 \bar{G}_1 G_1$	$\bar{G}_1 \bar{G}_1 G_{10}$	$\bar{G}_1 \bar{G}_1 G_{10}$	$\bar{G}_1 \bar{G}_1 G_{10}$	$0 G_1 G_{10}$	$0 G_1 G_{10}$	$0 G_1 G_{10}$	$0 G_1 G_{10}$	$0 G_1 G_{10}$	$\bar{G}_1 \bar{G}_1 G_{10}$	$\bar{G}_1 \bar{G}_1 G_{10}$
101	$G_1 G_2 0$	$G_2 0 0$	$G_2 \bar{G}_3 G_3$	$G_3 0 0$	$G_4 0 0$	$G_1 \bar{G}_3 0$	$G_1 G_3 0$	$G_2 G_{10} G_{11}$	$G_2 G_{10} G_{11}$	$G_2 G_{10} G_{11}$	$G_2 G_{10} G_{11}$	$G_{10} G_{11} \bar{G}_{11}$	$G_2 G_{10} G_{11}$
	$0 G_2 0$	$0 G_1 \bar{G}_3$	$\bar{G}_4 G_{10} \bar{G}_{11}$	$0 G_0 0$	$0 G_5 0$	$\bar{G}_3 G_0 0$	$G_3 G_1 0$	$G_4 G_{10} G_{11}$	$G_4 G_{10} G_{11}$	$G_4 G_{10} G_{11}$	$G_4 G_{10} G_{11}$	$G_{11} G_{10} \bar{G}_{11}$	$\bar{G}_4 G_{10} \bar{G}_{11}$
	$G_3 0 G_1$	$0 \bar{G}_1 G_1$	$G_4 \bar{G}_1 G_1$	$G_4 \bar{G}_1 G_1$	$0 0 G_6$	$0 0 G_5$	$0 0 G_1$	$0 0 G_1$	$0 0 G_1$	$0 0 G_1$	$0 0 G_1$	$G_3 G_1 G_1$	$G_3 G_1 G_1$
T01	$G_1 0 \bar{G}_3$	$G_1 G_4 \bar{G}_4$	$G_2 0 0$	$G_4 0 0$	$G_0 0 0$	$G_1 G_3 0$	$G_1 \bar{G}_3 0$	$G_2 0 0$	$G_2 0 0$	$G_2 0 0$	$G_2 0 0$	$G_{10} G_{11} \bar{G}_{11}$	$G_2 0 0$
	$0 G_4 0$	$G_{10} G_{11} \bar{G}_{11}$	$0 G_1 \bar{G}_3$	$0 G_5 0$	$0 G_0 0$	$G_3 G_1 0$	$\bar{G}_2 G_1 G_1$	$0 G_4 0$	$0 G_4 0$	$0 G_4 0$	$0 G_4 0$	$\bar{G}_{12} G_{10} \bar{G}_{11}$	$G_{12} G_{10} \bar{G}_{11}$
	$\bar{G}_3 0 G_1$	$\bar{G}_{11} \bar{G}_{11} G_{10}$	$0 \bar{G}_3 G_0$	$0 0 G_5$	$0 0 G_1$	$0 0 G_1$	$0 0 G_1$	$G_1 G_{10} G_{11}$	$G_1 G_{10} G_{11}$	$G_1 G_{10} G_{11}$	$G_1 G_{10} G_{11}$	$\bar{G}_{11} G_{11} G_1$	$\bar{G}_{11} G_{11} G_1$
011	$G_3 0 0$	$G_1 0 \bar{G}_3$	$G_1 0 G_3$	$\bar{G}_3 G_0 0$	$G_1 G_3 0$	$G_0 0 0$	$G_0 0 0$	$G_{10} G_{11} G_{11}$	$G_{10} G_{11} G_{11}$	$G_{10} G_{11} G_{11}$	$G_{10} G_{11} G_{11}$	$G_3 0 0$	$G_3 0 0$
	$0 G_3 G_3$	$0 G_2 0$	$0 G_1 0$	$\bar{G}_3 G_1 0$	$G_3 G_1 0$	$0 G_0 0$	$0 G_0 0$	$G_{11} G_9 G_9$	$G_{11} G_9 G_9$	$G_{11} G_9 G_9$	$G_{11} G_9 G_9$	$G_{11} G_9 G_9$	$0 G_3 G_3$
	$0 G_3 G_1$	$\bar{G}_1 G_1 0$	$G_1 0 G_1$	$0 0 G_3$	$0 0 G_0$	$G_0 0 G_5$	$G_1 G_{10} G_{11}$	$\bar{G}_{11} G_9 G_9$	$\bar{G}_{11} G_9 G_9$	$\bar{G}_{11} G_9 G_9$	$\bar{G}_{11} G_9 G_9$	$G_{11} G_9 G_9$	$0 G_3 G_3$
0T1	$G_2 0 0$	$G_{10} G_{11} \bar{G}_{11}$	$G_{10} \bar{G}_1 G_{11}$	$G_3 G_3 0$	$G_1 \bar{G}_3 0$	$G_2 0 0$	$G_2 0 0$	$G_1 0 G_3$	$G_1 0 \bar{G}_3$	$G_{10} G_{11} \bar{G}_{11}$	$G_{10} G_{11} \bar{G}_{11}$	$G_7 0 0$	$G_7 0 0$
	$0 G_1 \bar{G}_3$	$G_{10} G_{11} \bar{G}_{11}$	$\bar{G}_1 G_9 \bar{G}_9$	$G_3 G_0 0$	$\bar{G}_2 G_0 0$	$0 G_4 0$	$0 G_4 0$	$0 G_1 0$	$0 G_1 0$	$0 G_1 0$	$0 G_1 0$	$G_{12} G_{10} \bar{G}_{11}$	$G_8 0 0$
	$0 \bar{G}_3 G_1$	$\bar{G}_{11} \bar{G}_{11} G_{10}$	$0 0 G_3$	$0 0 G_3$	$0 0 G_3$	$0 0 G_3$	$0 0 G_3$	$G_3 G_1 0$	$G_3 G_1 0$	$G_3 G_1 0$	$G_3 G_1 0$	$\bar{G}_3 G_1 G_1$	$\bar{G}_3 G_1 G_1$
T10	$G_1 G_2 0$	$G_2 G_3 0$	$G_3 G_2 0$	$G_0 0 0$	$G_1 G_1 \bar{G}_1$	$G_1 0 G_3$	$G_1 0 \bar{G}_3$	$G_2 0 0$	$G_2 0 0$	$G_2 0 0$	$G_2 0 0$	$G_{10} G_{11} \bar{G}_{11}$	$G_2 0 0$
	$G_3 G_1 0$	$G_3 G_0 0$	$G_2 G_1 0$	$G_0 0 0$	$G_1 G_1 \bar{G}_1$	$G_1 0 G_3$	$G_1 0 \bar{G}_3$	$G_2 0 0$	$G_2 0 0$	$G_2 0 0$	$G_2 0 0$	$G_{10} G_{11} \bar{G}_{11}$	$G_2 0 0$
	$0 0 G_3$	$0 0 G_5$	$0 0 G_7$	$0 0 G_7$	$0 0 G_7$	$0 0 G_7$	$0 0 G_7$	$G_1 G_{10} G_{11}$	$G_1 G_{10} G_{11}$	$G_1 G_{10} G_{11}$	$G_1 G_{10} G_{11}$	$G_{11} G_{10} \bar{G}_{11}$	$G_2 0 0$
10T	$G_1 \bar{G}_3 0$	$G_2 \bar{G}_3 0$	$G_3 \bar{G}_3 0$	$G_0 0 0$	$G_1 \bar{G}_4 G_4$	$G_1 0 G_3$	$G_1 0 \bar{G}_3$	$G_2 0 0$	$G_2 0 0$	$G_2 0 0$	$G_2 0 0$	$G_{10} G_{11} \bar{G}_{11}$	$G_2 0 0$
	$\bar{G}_3 G_0 0$	$0 G_4 0$	$\bar{G}_4 G_6 0$	$0 G_5 0$	$0 G_6 0$	$0 G_7 0$	$0 G_8 0$	$\bar{G}_1 G_9 G_9$	$0 G_2 0$	$0 G_3 0$	$0 G_4 0$	$\bar{G}_{11} \bar{G}_{11} G_9$	$0 G_5 0$
	$0 0 G_3$	$0 0 G_5$	$0 0 G_7$	$0 0 G_7$	$0 0 G_7$	$0 0 G_7$	$0 0 G_7$	$\bar{G}_1 G_{10} G_{11}$	$\bar{G}_1 G_{10} G_{11}$	$\bar{G}_1 G_{10} G_{11}$	$\bar{G}_1 G_{10} G_{11}$	$\bar{G}_{11} \bar{G}_{11} G_9$	$0 G_5 0$
TOT	$G_1 0 G_3$	$G_1 G_4 G_4$	$G_2 0 0$	$G_0 0 G_8$	$G_5 0 0$	$G_1 G_{10} G_{11}$	$G_{10} G_{11} \bar{G}_{11}$	$G_1 0 \bar{G}_3$	$G_1 0 \bar{G}_3$	$G_1 0 \bar{G}_3$	$G_1 0 \bar{G}_3$	$G_0 G_9 G_9$	$G_1 0 G_3$
	$0 G_2 0$	$G_{10} G_{11} \bar{G}_{11}$	$0 G_1 G_3$	$0 G_3 0$	$G_5 0 0$	$G_{11} G_{10} G_{11}$	$\bar{G}_{11} G_{10} \bar{G}_{11}$	$0 G_1 \bar{G}_3$	$0 G_1 \bar{G}_3$	$0 G_1 \bar{G}_3$	$0 G_1 \bar{G}_3$	$0 G_0 G_9$	$G_1 0 G_3$
	$G_3 0 G_1$	$\bar{G}_{11} \bar{G}_{11} G_{10}$	$0 G_1 G_1$	$G_8 0 G_4$	$G_9 0 G_4$	$G_{11} G_{10} G_{11}$	$\bar{G}_1 G_{10} G_{11}$	$0 \bar{G}_1 G_1$	$0 \bar{G}_1 G_1$	$0 \bar{G}_1 G_1$	$0 \bar{G}_1 G_1$	$0 G_0 G_9$	$G_1 0 G_3$
10T	$G_1 0 \bar{G}_3$	$G_2 \bar{G}_3 0$	$G_3 \bar{G}_3 0$	$G_0 0 0$	$G_1 \bar{G}_4 G_4$	$G_1 0 G_3$	$G_1 0 \bar{G}_3$	$G_2 0 0$	$G_2 0 0$	$G_2 0 0$	$G_2 0 0$	$G_{10} G_{11} \bar{G}_{11}$	$G_2 0 0$
	$0 G_1 \bar{G}_3$	$0 G_1 \bar{G}_3$	$0 G_1 \bar{G}_3$	$0 G_1 \bar{G}_3$	$0 G_1 \bar{G}_3$	$0 G_1 \bar{G}_3$	$0 G_1 \bar{G}_3$	$G_1 G_{10} G_{11}$	$G_1 G_{10} G_{11}$	$G_1 G_{10} G_{11}$	$G_1 G_{10} G_{11}$	$G_{11} G_{10} \bar{G}_{11}$	$G_2 0 0$
	$\bar{G}_3 0 G_1$	$\bar{G}_1 \bar{G}_1 G_1$	$\bar{G}_1 \bar{G}_1 G_1$	$\bar{G}_1 \bar{G}_1 G_1$	$\bar{G}_1 \bar{G}_1 G_1$	$\bar{G}_1 \bar{G}_1 G_1$	$\bar{G}_1 \bar{G}_1 G_1$	$\bar{G}_1 \bar{G}_1 G_1$	$\bar{G}_1 \bar{G}_1 G_1$	$\bar{G}_1 \bar{G}_1 G_1$	$\bar{G}_1 \bar{G}_1 G_1$	$\bar{G}_1 \bar{G}_1 G_1$	$G_1 0 G_3$
01T	$G_2 0 0$	$G_{10} G_{11} \bar{G}_{11}$	$G_{10} \bar{G}_1 \bar{G}_1$	$G_{10} G_{11} \bar{G}_{11}$	$G_7 0 0$	$G_7 0 0$	$G_7 0 0$	$G_7 0 0$	$G_7 0 0$	$G_7 0 0$	$G_7 0 0$	$G_{10} G_{11} \bar{G}_{11}$	$G_7 0 0$
	$0 G_1 G_3$	$G_{11} G_9 G_9$	$G_{11} G_9 G_9$	$G_{11} G_9 G_9$	$G_{11} G_9 G_9$	$G_{11} G_9 G_9$	$G_{11} G_9 G_9$	$G_{11} G_9 G_9$	$G_{11} G_9 G_9$	$G_{11} G_9 G_9$	$G_{11} G_9 G_9$	$G_{11} G_9 G_9$	$G_7 0 0$
	$0 G_1 G_1$	$G_{11} G_{11} G_{10}$	$G_{11} G_{11} G_{10}$	$G_{11} G_{11} G_{10}$	$G_{11} G_{11} G_{10}$	$G_{11} G_{11} G_{10}$	$G_{11} G_{11} G_{10}$	$G_{11} G_{11} G_{10}$	$G_{11} G_{11} G_{10}$	$G_{11} G_{11} G_{10}$	$G_{11} G_{11} G_{10}$	$G_{11} G_{11} G_{10}$	$G_7 0 0$
01T	$G_2 0 0$	$G_1 0 G_3$	$G_1 0 \bar{G}_3$	$G_{10} \bar{G}_1 \bar{G}_1$	$G_{10} \bar{G}_1 \bar{G}_1$	$G_8 0 0$	$G_8 0 0$	$G_7 0 0$	$G_7 0 0$	$G_7 0 0$	$G_7 0 0$	$G_{10} G_{11} \bar{G}_{11}$	$G_8 0 0$
	$0 G_1 \bar{G}_3$	$0 G_1 \bar{G}_3$	$0 G_1 \bar{G}_3$	$0 G_1 \bar{G}_3$	$0 G_1 \bar{G}_3$	$0 G_1 \bar{G}_3$	$0 G_1 \bar{G}_3$	$0 G_1 \bar{G}_3$	$0 G_1 \bar{G}_3$	$0 G_1 \bar{G}_3$	$0 G_1 \bar{G}_3$	$0 G_1 \bar{G}_3$	$G_8 0 0$
	$0 \bar{G}_3 G_1$	$G_3 G_0 G_1$	$\bar{G}_3 G_0 G_1$	$G_{11} G_9 G_9$	$G_{11} G_9 G_9$	$G_8 0 G_4$	$G_8 0 G_4$	$G_7 0 G_4$	$G_7 0 G_4$	$G_7 0 G_4$	$G_7 0 G_4$	$G_{11} G_{11} G_{10}$	$G_8 0 0$

$$\begin{aligned}
 \vec{x}(L) - \vec{x}(L') &= \frac{a_0}{2} (L_1, L_2, L_3) \\
 G_0 &= G_{xx}(000) \quad G_2 = G_{zz}(110) \quad G_5 = G_{yy}(200) \quad G_8 = G_{xy}(220) \quad G_{11} = G_{xy}(211) \\
 G_1 &= G_{xx}(110) \quad G_3 = G_{xy}(110) \quad G_6 = G_{xx}(220) \quad G_9 = G_{xx}(211) \quad G_{12} = G_{yz}(211) \\
 G_4 &= G_{xx}(200) \quad G_7 = G_{zz}(220) \quad G_{10} = G_{yy}(211) \quad G_{13} = G_{yz}(000)
 \end{aligned}$$

Table 3. The form of the perturbing matrices ΔH .

$$\overline{\Delta H}^{(4-)}(aa') = \begin{pmatrix} d & \bar{f} & 0 & \sqrt{8}a \\ f & d & 0 & \sqrt{8}\bar{b} \\ 0 & 0 & e & 2c \\ \sqrt{8}a & \sqrt{8}\bar{b} & 2c & a_0 \end{pmatrix} \quad (74)$$

$$\overline{\Delta O}^{(4-)}(aa') = \begin{pmatrix} 0 & 0 & 0 & \sqrt{8}a' \\ 0 & 0 & 0 & \sqrt{8}\bar{b}' \\ 0 & 0 & 0 & 2c' \\ \sqrt{8}a' & \sqrt{8}\bar{b}' & 2c' & 0 \end{pmatrix} \quad (75)$$

This concludes the analysis required for the determination of the electric dipole active impurity states associated with a substitutional impurity in the F^- sublattice of LiF. In subsequent reports the results presented here will be used to obtain quantitative results for the impurity levels.

REFERENCES

1. F. Seitz, *Ann. Math.* 37, 17 (1936).
2. See, for example, D. J. Chadi and M. L. Cohen, *Phys. Rev. B* 8, 5747 (1973).
3. See, for example, Section VIII.7 of Theory of Lattice Dynamics in the Harmonic Approximation, by A. A. Maradudin, E. W. Montroll, G. H. Weiss, and I. P. Ipatova (Academic Press, New York, 1971).
4. We use here the notation of G. F. Koster, J. O. Dimmock, R. G. Wheeler, and H. Statz, Properties of the Thirty-Two Point Groups (M. I. T. Press, Cambridge, Mass., 1963).

**E. CLASSICAL TRANSPORT EQUATION FOR
ELECTRON-AVALANCHE BREAKDOWN**

T. D. Holstein
Department of Physics
University of California
Los Angeles, California 90024

and

Xonics, Incorporated
Santa Monica, California 90401

In this first phase of investigation of electron-avalanche breakdown, the classical transport equation to be used is derived from the Boltzmann equation. A quasi-isotropy approximation and the Fokker-Planck expansion are used, and a current density, a conductivity tensor, and relaxation rates are introduced.

The preliminary theory of electron-avalanche breakdown presented in the Fifth Technical Report (30 June 1975) explained experimental results satisfactorily for the first time. However, additional work is needed to determine the validity of the theory. The results below represent the first phase of the reinvestigation of the electron-avalanche breakdown problem, as was discussed further in Sec. A.

We start from the Boltzmann transport equation

$$\frac{\partial f}{\partial t} + \frac{e\tilde{\mathcal{E}}(t)}{n} \cdot \text{grad}_k f = \left(\frac{\partial f}{\partial t} \right)_{\text{coll}} . \quad (1)$$

Here, $f = f_k(t)$ is the time-dependent electron distribution in k space, $\tilde{\mathcal{E}}(t) = \tilde{\mathcal{E}}_0 \cos \omega t$ is the impressed laser field, and

$$\left(\frac{\partial f}{\partial t} \right)_{\text{coll}} = \sum_{k'} \left[f_{k'} W(\tilde{k} \rightarrow \tilde{k}') - f_k W(\tilde{k}' \rightarrow \tilde{k}) \right] , \quad (2)$$

where $W(\tilde{k} \rightarrow \tilde{k}')$ is the collisional transition probability between states \tilde{k} and \tilde{k}' .

We generally have

$$W(\tilde{k} \rightarrow \tilde{k}') = \sum_i w_i(\tilde{k}, \tilde{k}') \delta(E_k - E_{k'} - \Delta_{kk'}^{(i)}) \quad (3)$$

where the subscript, i , refers to a particular type of collision (e.g., electron scattering with emission or absorption of various types of phonons) and where $\Delta_{kk'}^{(i)}$, represents the associated energy loss (or gain).

It may be remarked that, for electron-phonon collisions, $\Delta_{kk'}$ is relatively small (< 0.05 eV), i.e., the collisions are quasi-elastic. This feature will

Sec. E

permit substantial simplification of the analysis to be given below, especially in the energy region below the threshold for exciton formation, which we now discuss. We rewrite (1) in the form

$$\frac{\partial f}{\partial t} + \frac{e\mathbf{E}(t)}{\hbar} \cdot \mathbf{grad}_{\mathbf{k}} f - \left(\frac{\partial f}{\partial t} \right)_{\text{in coll}} = \left(\frac{\partial f}{\partial t} \right)_{e \& \text{coll}} \quad (4)$$

where

$$\left(\frac{\partial f}{\partial t} \right)_{e \& \text{coll}} = \sum_{\mathbf{k}'} (f_{\mathbf{k}'} - f_{\mathbf{k}}) w(\mathbf{k}, \mathbf{k}') \delta(E_{\mathbf{k}} - E_{\mathbf{k}'}) \quad (5)$$

(with $w(\mathbf{k}, \mathbf{k}') \equiv \sum_i w_i(\mathbf{k}, \mathbf{k}')$ taken to be symmetrical with respect to interchange of \mathbf{k} and \mathbf{k}')¹ and $\left(\frac{\partial f}{\partial t} \right)_{\text{in coll}}$ is the remainder of the collision term; it may be written as

$$\begin{aligned} \left(\frac{\partial f}{\partial t} \right)_{\text{in coll}} = \sum_{\mathbf{k}', i} & \left[f_{\mathbf{k}'} w_i(\mathbf{k}', \mathbf{k}) [\delta(E_{\mathbf{k}'} - E_{\mathbf{k}} - \Delta_{\mathbf{k}\mathbf{k}'}) - \delta(E_{\mathbf{k}'} - E_{\mathbf{k}})] \right. \\ & \left. - f_{\mathbf{k}} w_i(\mathbf{k}, \mathbf{k}') [\delta(E_{\mathbf{k}} - E_{\mathbf{k}'} - \Delta_{\mathbf{k}\mathbf{k}'}) - \delta(E_{\mathbf{k}} - E_{\mathbf{k}})] \right]. \end{aligned} \quad (6)$$

The stage has now been set for introducing the principal assumption of this -- as well as other derivations -- of the energy transport equation, namely, the assumption of quasi-isotropy of the distribution function in \mathbf{k} space. Strictly speaking, this phraseology pertains to the usual case of spherical energy surfaces, for which it describes the situation in which $f_{\mathbf{k}}$ depends principally on the magnitude of \mathbf{k} . In our case, we generalize by writing

$$f_{\mathbf{k}} = f(E_{\mathbf{k}}) + f_{\mathbf{k}}^{(1)} \quad (7)$$

where $f_k^{(1)}$ is taken to be small compared to $f(E_k)$, and is ultimately to be determined by a suitably prescribed iteration procedure. We incidentally note that, by definition,

$$f(E) = \frac{\sum_k f_k \delta(E - E_k)}{\sum_k \delta(E - E_k)} \quad (8)$$

so that the corresponding integral of $f_k^{(1)}$ vanishes.

Let us integrate (4) over a surface of constant energy, E . This is done by multiplying by $\delta(E - E_k)$ and summing over k . Introducing the density-of-states function

$$N(E) \equiv \sum_k \delta(E - E_k) \quad (9)$$

we have

$$\begin{aligned} N(E) \frac{\partial f(E)}{\partial t} + \sum_k e \mathbf{v}_k \cdot \mathbf{v}_k \frac{\partial}{\partial E} \delta(E - E_k) f_k^{(1)} \\ = \sum_{kk',i} \delta(E - E_k) \left[f(E_{k'}) w_i(k, k') \delta(E_{k'} - E_k - \Delta_{kk'}^{(i)}) \right. \\ \left. - f(E_k) w_i(k, k') \delta(E_k - E_{k'} - \Delta_{kk'}^{(i)}) \right] \\ = \int [f(E') K(E', \Delta E) - f(E) K(E, \Delta E)] d\Delta E \end{aligned} \quad (10)$$

where $E' = E + \Delta E$ and where

$$K(E, \Delta E) \equiv \sum_{kk',i} \delta(E - E_k) \delta(E - \Delta E - E_{k'}) w_i(k, k') \delta(E_k - E_{k'} - \Delta_{kk'}^{(i)}). \quad (11)$$

The Fokker-Planck expansion is now applied to the right-hand side of (10), yielding

$$N(E) \frac{\partial f(E)}{\partial t} + \frac{\partial}{\partial E} \langle \tilde{\mathbf{E}}(t) \cdot \tilde{\mathbf{J}}(E, t) \rangle = \frac{\partial}{\partial E} \left[N(E) \frac{\Delta(E)}{\tau(E)} f(E) \right] \quad (12)$$

where

$$N(E) \frac{\Delta(E)}{\tau(E)} = \int (\Delta E) K(E, \Delta E) dE = \sum_{kk', i} \delta(E - E_k) w^{(i)}(\tilde{k}, \tilde{k}') \times \Delta^{(i)}(\tilde{k}, \tilde{k}') \times \delta(E_k - E_{k'} - \Delta_{kk'}^{(i)}) \quad . \quad (13)$$

Thus $\Delta(E)$ is the average energy loss per collision (with $1/\tau(E)$ representing the total collision rate). Also

$$\tilde{\mathbf{J}}(E, t) \equiv \sum_k \delta(E - E_k) e \tilde{\mathbf{v}}_k f_k^{(1)}(t) \quad (14)$$

is manifestly the "monoenergetic" current density (to be evaluated below). Finally, the braced expression, $\langle \dots \rangle$, is a time average over a period $2\pi/\omega$ of the external laser field. It is thereby assumed that the variation of $f(E)$ over this time interval is negligible.²

An explicit expression for $\tilde{\mathbf{J}}(E, t)$ has now to be obtained. To achieve this objective, we consider the equation satisfied by $f_k^{(1)}(t)$, which reads

$$\frac{\partial f_k^{(1)}}{\partial t} + e \tilde{\mathbf{E}}(t) \cdot \tilde{\mathbf{v}}_k \frac{\partial f(E)}{\partial E} = \sum_{k'} (f_{k'} - f_k) w(\tilde{k}, \tilde{k}') \delta(E_k - E_{k'}) \quad . \quad (15)$$

Equation (15) is a linearized version of (4), wherein the "small" terms, such as that proportional to $\tilde{\mathbf{E}}(t)$, have been approximated by the replacement of f_k by $f(E_k)$. (From a logical point of view, an additional "driving" term of this sort,

involving the inelastic collision operator, should have been included. However, as one may readily demonstrate, the resulting contribution to $f_{\mathbf{k}}^{(1)}(t)$ is even with respect to reflection of \mathbf{k} through the origin, and would hence give no contribution to $\mathbf{J}(\mathbf{E}, t)$.

Ignoring the time variation of $f(E_{\mathbf{k}})$ (as discussed in the text subsequent to (14)), and taking $\mathbf{g}(t) = R \mathbf{g}_0 \exp(-i\omega t)$, we may replace $\partial/\partial t$ in (15) by $-i\omega$, thereby obtaining

$$-e \mathbf{g}_0 \cdot \mathbf{v}_{\mathbf{k}} \frac{\partial f(E_{\mathbf{k}})}{\partial E_{\mathbf{k}}} = i\omega f_{\mathbf{k}} + \sum_{\mathbf{k}'} \left[f_{\mathbf{k}'} - f_{\mathbf{k}} - w(\mathbf{k}, \mathbf{k}') \delta(E_{\mathbf{k}} - E_{\mathbf{k}'}) \right]$$

the formal solution of which is written as

$$f_{\mathbf{k}} = -\phi_{\mathbf{k}}(\omega) \cdot e \frac{\partial f_0}{\partial E_{\mathbf{k}}} \quad (16a)$$

where $\phi_{\mathbf{k}}(\omega)$ obeys the equation

$$\mathbf{v}_{\mathbf{k}} = i\omega \mathbf{g}_{\mathbf{k}} + \sum_{\mathbf{k}'} [\mathbf{g}_{\mathbf{k}'} - \phi_{\mathbf{k}}] w(\mathbf{k}, \mathbf{k}') \delta(E_{\mathbf{k}} - E_{\mathbf{k}'}) \quad (16b)$$

Inserting (16) into (14), we have

$$\begin{aligned} \mathbf{J}(\mathbf{E}, t) &= \sum_{\mathbf{k}} \delta(\mathbf{E} - \mathbf{E}_{\mathbf{k}}) e^2 v_{\mathbf{k}} \phi_{\mathbf{k}}(\omega) \cdot \frac{\partial f}{\partial E_{\mathbf{k}}} \\ &= -R \left\{ \mathbf{g}(\mathbf{E}, \omega) \cdot e_0 e^{-i\omega t} \frac{\partial f_0}{\partial E} \right\} \end{aligned} \quad (17)$$

where

$$\mathbf{g}(\mathbf{E}, \omega) = \sum_{\mathbf{k}} \delta(\mathbf{E} - \mathbf{E}_{\mathbf{k}}) e^2 v_{\mathbf{k}} \phi_{\mathbf{k}}(\omega)$$

is the monoenergetic conductivity tensor; as is known, for cubic crystals, it reduces to a scalar quantity; i.e.,

$$\underline{J}(E, t) = -R \left\{ \sigma(E, \omega) \underline{\varrho}_0 e^{-i\omega t} \frac{\partial f(E)}{\partial E} \right\} \quad (18)$$

with

$$\sigma(E, \omega) = \frac{1}{3} \sum_k \delta(E - E_k) e^2 \underline{v}_k \cdot \underline{\varrho}_k(\omega) \quad . \quad (19)$$

We now substitute (18) into (12), obtaining

$$N(E) \frac{\partial f(E)}{\partial t} = \frac{e_0^2}{6} \frac{\partial}{\partial E} R \sigma(E, \omega) \frac{\partial f(E)}{\partial E} + \frac{\partial}{\partial E} \left[N(E) \frac{\Delta(E)}{\tau(E)} f(E) \right] \quad . \quad (20)$$

Let us note that, in the usual spherical approximation -- with E_k dependent only on the magnitude of \underline{k} , and with $w(\underline{k}, \underline{k}')$ a function of just the magnitudes of \underline{k} and \underline{k}' and of the angle $\psi_{kk'}$ between them -- it is always possible to replace the collision integral by a relaxation-time expression, i.e.,

$$\sum_{k'} [\underline{\varrho}_{k'} - \underline{\varrho}_k] w(\underline{k}, \underline{k}') \delta(E_k - E_{k'}) \rightarrow -\frac{\varphi_k}{\tau_r} \quad (21)$$

where

$$1/\tau_r(E) \equiv \sum_{k'} w(\underline{k}, \underline{k}') (1 - \cos \psi_{kk'}) \delta(E_k - E_{k'}) \quad (22)$$

is the "transport" relaxation rate. Introducing (21) into (17), we have

$$\underline{\varrho}_k = \frac{\underline{v}_k \tau_r}{1 + i\omega \tau_r} \quad (23a)$$

whence

$$\begin{aligned}
 \sigma(E, \omega) &= \frac{\left[\sum_k \delta(E - E_k) e^2 v_k^2 / 3 \right] \tau_r(E)}{1 - i\omega \tau_r(E)} \\
 &= \frac{N(E) e^2 \langle v^2(E) \rangle \tau_r(E) / 3}{1 - i\omega \tau_r(E)} \tag{23b}
 \end{aligned}$$

where $\langle v^2(E) \rangle$ denotes an average of v_k^2 over a surface of constant energy.

Upon substituting (23) into (20), one has

$$\begin{aligned}
 N(E) \frac{\partial f(E)}{\partial t} &= \frac{e_0^2}{6} \frac{\partial}{\partial E} \left(\frac{N(E) e^2 \langle v^2(E) \rangle \tau_r(E)}{1 + \omega^2 \tau_r^2(E)} \frac{\partial f}{\partial E} \right) \\
 &+ \frac{\partial}{\partial E} \left[N(E) \frac{\Delta(E)}{\tau_r(E)} f(E) \right] . \tag{24}
 \end{aligned}$$

It may be remarked that, in the more general case of cubic symmetry, an expression of the form of (24), with $1/\tau_r$ given by the relation

$$\frac{1}{\tau_r(E)} = \frac{1}{N(E)} \sum_{kk'} \delta(E - E_k) \delta(E_k - E_{k'}) w(k, k') (1 - \tilde{v}_k \cdot \tilde{v}_{k'} / v_k^2) \tag{25}$$

is still a useful approximation; in particular, it has the following two properties:

- (1) In the high-frequency limit $\omega \tau_r \gg 1$, it coincides with the first non-vanishing term obtained from a perturbation solution of (17) in powers of $(\omega \tau_r)^{-2}$.
- (2) In the d.c. limit, variational theory may be used to show that the coefficient of $\partial f / \partial E$ in the square bracket of (24) is a lower bound to the correct $\sigma(E, 0)$, with an error quadratic in the deviation of the "trial" function, $\varphi_k(\text{var}) = \tilde{v}_k$ from the actual solution of (16).

Equation (20) and its approximate form (24) (with some subsequent straightforward modifications introduced in the text) constitute the basis of the classical energy-transport theory used in this paper.

It remains, finally, to carry out some estimate of the validity of the approximation of generalized quasi-isotropy introduced with Eq. (7). Our task is to demonstrate the relative smallness of $f_k^{(1)}$ (as given, e.g., by (16a) and (23a)) compared to $f(E)$. For this purpose it is clearly necessary to know $\partial f / \partial E$ as a function of primary parameters. As pointed out above, experience has shown that this is feasible only on an *aposteriori* basis. In what follows, we give the simplest illustrative example; the state of affairs in other cases of interest will be discussed in due course.

Let us consider the situation in which exciton and electron-hole forming collisions may be ignored. Then, Eq. (24), with $\partial f / \partial t = 0$, applies. A first integration can immediately be carried out, yielding

$$0 = \frac{\epsilon_0^2}{6} \frac{e^2 v^2(E) \tau_r(E)}{1 + i\omega^2 \tau_r^2(E)} \frac{\partial f}{\partial E} + \frac{\Delta(E)}{\tau(E)} f(E) \quad (26)$$

where the constant of integration has been set equal to zero, to assure $f(E) \rightarrow 0$ as $E \rightarrow \infty$. From (26) we obtain an explicit expression for $\partial f / \partial E$ in terms of $f(E)$ and the primary parameters. Introducing this expression into (23a) and (16a), we have, for the component of $f_k^{(1)}$ in phase with the external field (which we denote as $f_k^{(1)'} \rangle$)

$$\begin{aligned} f_k^{(1)'} / f(E) &= \frac{e\epsilon_0 v(E) \tau_r}{1 + \omega^2 \tau_r^2} \frac{6(1 + \omega^2 \tau_r^2(E))}{\epsilon_0^2 e^2 v^2(E) \tau_r(E)} \frac{\Delta(E)}{\tau(E)} \\ &= \frac{6 \Delta(E)}{e \epsilon v(E) \tau(E)} \end{aligned} \quad (27)$$

Sec. E

To extract some physical meaning from this result, we define an effective energy-dependent electron temperature via the equation

$$\frac{1}{kT_e(E)} = - \frac{d \log f(E)}{d E} . \quad (28)$$

Equation (28) together with (26) yields

$$kT_e(E) = \frac{e^2 \epsilon_0^2}{6} \frac{v^2(E) \tau_r(E) \tau(E)}{(1 + \omega^2 \tau_r^2) \Delta(E)}$$

or

$$e \epsilon_0 v(E) = \left[\frac{6(1 + \omega^2 \tau_r^2(E)) \Delta(E)}{\tau_r(E) \tau(E)} \right]^{1/2} \left(kT_e(E) \right)^{1/2}$$

which, when inserted into (27), gives

$$\frac{f_k^{(1)'}(E)}{f(E)} = \left[\frac{\Delta(E)}{\tau(E)} \frac{\tau_r(E)}{1 + \omega^2 \tau_r^2} \frac{1}{kT_e(E)} \right]^{1/2} \lesssim \left(\frac{\Delta(E)}{kT_e(E)} \right)^{1/2} \quad (29)$$

if we take $\tau_r(E) \sim \tau(E)$. The parameter contained in square brackets is usually quite small. In fact, if we consider $kT_e(E)$ as characterizing the energy spread of the distribution function, the parameter on the right-hand side of (29) is known to be small -- at least in the energy region below the exciton threshold.

REFERENCES

1. This property is certainly valid in the Born approximation, in which it is possible to treat all electron-phonon collisions.
2. This approximation is valid when energy loss and gain processes are slow, relative to the external frequency, ω ; said condition is hereby assumed to hold once and for all.

F. EVALUATION OF TWO-CENTER INTEGRALS
OF SLATER ATOMIC ORBITALS*

K. G. Hamilton
Department of Physics
University of California, San Diego
La Jolla, California 92037

and

Xonics, Incorporated
Santa Monica, California 90401

Expressions are given from which the values of overlap integrals $\int \chi_a \chi_b d^3 r$, kinetic-energy integrals $-\frac{1}{2} \int \chi_a \nabla^2 \chi_b d^3 r$, and nuclear-Coulomb-attraction integrals $z \int \chi_a (1/r_a) \chi_b d^3 r$ are obtained in closed form for any Slater-atomic-orbitals χ having principal quantum numbers from 1 to 6, thus extending Roothaan's useful tabulations.

The calculation of electronic energy bands in a solid, or of energy levels in a molecule or atom, can be written as the simultaneous matrix diagonalization problem

$$(\mathcal{K}_{ij} - E S_{ij}) x_j = 0 \quad , \quad (1)$$

in which each subscript labels both orbital and site. Formulation of the matrix problem requires, first of all, estimates of the Hamiltonian elements

$$\mathcal{K}_{ij} = \int \varphi_i^*(\mathbf{r}) \mathcal{K} \varphi_j(\mathbf{r}) d^3\mathbf{r} \quad , \quad (2)$$

and the wavefunction overlaps

$$S_{ij} = \int \varphi_i^*(\mathbf{r}) \varphi_j(\mathbf{r}) d^3\mathbf{r} \quad . \quad (3)$$

using some basis set $\{\phi_i\}$.

If the basis set is orthonormal, then the overlap matrix becomes the Kronecker delta, and Eq. (1) simplifies to the problem of diagonalizing \mathcal{K} by itself; this is the case for the Hückel approximation in molecular orbital theory,¹ as well as the hydrogen-atom problem of elementary quantum mechanics. In general, however, it is not practical to make an a priori choice of basis set having this fortunate characteristic, so that it is usually necessary to solve Eq. (1) with a non-diagonal S .

In 1930, Slater² proposed a method for obtaining approximate analytic atomic wavefunctions of the form

$$x_{nlm}(\mathbf{r}, \zeta) = N r^{n-1} e^{-\zeta r} Y_{lm}(\theta, \phi) \quad , \quad (4)$$

Sec. F

in which the normalization factor is

$$N = (2\zeta)^{\frac{n+1}{2}} / [(2n!)^{1/2}] \quad (5)$$

and $Y_{\ell m}$ are the spherical harmonics. Such functions have proven to be very useful approximations over the years, despite their lack of nodes, which the radial part of an atomic wavefunction must have. This shortcoming can be rectified by considering a sum of Slater functions,

$$\Psi_{nlm}(\mathbf{r}) = \sum_i a_i x_{n_i \ell m}(\mathbf{r}, \zeta_i) \quad . \quad (6)$$

If an adequate number of terms are used in the summation, then the mathematical function Ψ can be made arbitrarily close to the true physical wavefunction by a judicious choice of the parameters a_i , n_i , and ζ_i . In particular, the Hartree-Fock equations can be, and have been,³ solved using trial wavefunctions of this form, with the solution being specified in terms of the adjustable parameters.

If Slater functions (or, equivalently, sums of Slater functions) are used for the basis set in Eqs. (1) through (3), then a number of mathematical conveniences are obtained. To begin with, two-center overlap elements

$$S = \int x_{n_a \ell_a m}(\mathbf{r} - \mathbf{r}_a) x_{n_b \ell_b m}(\mathbf{r} - \mathbf{r}_b) d^3 r \quad , \quad (7)$$

can be evaluated in closed form. (It should be noted that the magnetic quantum number, m , is the same in both of these wavefunctions — if the orbitals have different values of this parameter, then the integral is zero under all circumstances. Here the Roothaan⁴ coordinate system with z axes along the site

centers, $\tilde{r}_a - \tilde{r}_b \sim z$, is used.) The evaluation of such integrals involves a transformation to prolate spheroidal coordinates, and some evaluations of these integrals have been made previously.^{4,5} If this transformation is made, then the five simplest classes of overlap integrals are listed below:

$$\underline{\ell_a = 0, \ell_b = 0, m = 0}$$

$$S(n_a s, n_b s) = \frac{1}{2} N_a N_b \left(\frac{1}{2} R\right)^{n_a + n_b + 1} \int_1^\infty d\xi \int_{-1}^{+1} d\eta (\xi + \eta)^{n_a} \times$$

$$\times (\xi - \eta)^{n_b} e^{-\rho(\xi + \eta\tau)} \quad (7)$$

$$\underline{\ell_a = 0, \ell_b = 1, m = 0}$$

$$S(n_a s, n_b p) = \frac{1}{2} \sqrt{3} N_a N_b \left(\frac{1}{2} R\right)^{n_a + n_b + 1} \int_1^\infty d\xi \int_{-1}^{+1} d\eta (\xi + \eta)^{n_a} \times$$

$$\times (\xi - \eta)^{n_b - 1} (\xi\eta - 1) e^{-\rho(\xi + \eta\tau)} \quad (8)$$

$$\underline{\ell_a = 1, \ell_b = 0, m = 0}$$

$$S(n_a p, n_b s) = \frac{1}{2} \sqrt{3} N_a N_b \left(\frac{1}{2} R\right)^{n_a + n_b + 1} \int_1^\infty d\xi \int_{-1}^{+1} d\eta (\xi + \eta)^{n_a - 1} \times$$

$$\times (\xi - \eta)^{n_b} (\xi\eta + i) e^{-\rho(\xi + \eta\tau)} \quad (9)$$

$$\underline{\ell_a = 1, \ell_b = 1, m = 0}$$

$$S(n_a p, n_b p, \sigma) = \frac{3}{2} N_a N_b \left(\frac{1}{2} R\right)^{n_a + n_b + 1} \int_1^\infty d\xi \int_{-1}^{+1} d\eta (\xi + \eta)^{n_a - 1} \times$$

$$\times (\xi - \eta)^{n_b - 1} (\xi^2 \eta^2 - 1) e^{-\rho(\xi + \eta\tau)} \quad (10)$$

Sec. F

$$\underline{\ell_a = 1, \ell_b = 1, m = 1}$$

$$S(n_a p, n_b p, \pi) = \frac{3}{4} N_a N_b \left(\frac{1}{2} R\right)^{n_a + n_b + 1} \int_1^\infty d\xi \int_{-1}^{+1} d\eta (\xi + \eta)^{n_a - 1} \times \\ \times (\xi - \eta)^{n_b - 1} (\xi^2 - 1) (1 - \eta^2) e^{-\rho(\xi + \eta\tau)} . \quad (11)$$

In these equations, the internuclear distance is

$$R = r_b - r_a , \quad (12)$$

while

$$\rho = \frac{1}{2} (\zeta_a + \zeta_b) R \quad (13)$$

and

$$\tau = (\zeta_a - \zeta_b) / (\zeta_a + \zeta_b) . \quad (14)$$

It must be noted that a sign reversal has been introduced into the sp and $p\sigma$ integrals, relative to some other tabulations. This is a consequence of making the assumption that p-orbitals have the same directionality convention for both sites: it is understood that the positive lobe of a $p\sigma (\ell=1, m=0)$ orbital points to the right, where a is the left-hand site and b the right-hand site.

By expanding the polynomial portion of the integrands, it is possible to express any one of the overlap integrals as

$$S = N_c N_a N_b \left(\frac{1}{2} R\right)^{n_a + n_b + 1} \sum_{n,m} C_{nm} \int_1^\infty \xi^n e^{-\rho\xi} d\xi \int_{-1}^{+1} \eta^m e^{-\tau\rho\eta} d\eta . \quad (15)$$

Such an integral can then be written in terms of the elementary functions

$$A_n(\rho) = \int_1^{\infty} \xi^n e^{-\rho \xi} d\xi = \frac{n!}{\rho^{n+1}} e^{-\rho} \sum_{k=0}^n \frac{\rho^k}{k!} \quad (16)$$

and

$$B_m(\tau\rho) = \int_{-1}^{+1} \eta^m e^{-\tau\rho\eta} d\eta \quad . \quad (17)$$

If $\tau \neq 0$, then

$$B_m(\tau\rho) = -A_m(\tau\rho) - (-1)^m A_m(-\tau\rho) \quad , \quad (18)$$

whereas the $\tau = 0$ case simply has the value

$$B_m = \begin{cases} \frac{2}{m+1} & , \quad m \text{ even} \\ 0 & , \quad m \text{ odd} \end{cases} \quad . \quad (19)$$

All of the overlap integrals involving s and p orbitals for $0 \leq n_a, n_b \leq 6$ are listed in Table I. In order to avoid repeating the normalization factors, the bare integrals

$$T = \sum_{nm} C_{nm} A_n B_m \quad (20)$$

are given; the complete overlap requires the extra operation

$$S = N_c N_a N_b \left(\frac{1}{2} R \right)^{n_a + n_b + 1} T \quad . \quad (21)$$

Roofaan⁴ gave certain overlaps in an expanded form, which involved additional secondary parameters, and required separate formulae for the $\tau = 0$

and $\tau \neq 0$ case. In comparison to Roothaan's equations, the AB form is simpler, and is therefore to be preferred for practical computation. Roothaan's tabulations were for the values $n = 1$ and 2 , and the present results are for $n = 1-6$.

The following procedure can be used to evaluate the numerical value of an overlap, given Table I and a calculator.

1. R, ρ , and τ must be evaluated (Eqs. (12)-(14)).
2. The first polynomial

$$A_0(\rho) = \frac{1}{\rho} e^{-\rho} \quad (22)$$

should be computed.

3. The recursion relation

$$A_n(\rho) = \frac{n}{\rho} A_{n-1}(\rho) + A_0(\rho) \quad (23)$$

can then be used to prepare a table of A versus n , up to the required maximum n value.

4. If $\tau = 0$, then the B polynomials can be computed from Eq. (19). Skip to step 6.
5. If $\tau \neq 0$, then:
 - a. Repeat steps 2 and 3, to obtain a table of $A_m(\tau\rho)$.
 - b. Repeat steps 2 and 3, to obtain a table of $A_m(-\tau\rho)$.
 - c. Use Eq. (18) to work out the required values of $B_m(\tau\rho)$.
6. Using the values of A_n and B_m thus obtained, compute T from the appropriate Table I formula.
7. As specified in Eq. (21), multiply T by the normalization factors, to find S .

The Hamiltonian matrix elements specified by Eq. (2) can be obtained by expressing them in terms of the simple overlap integrals which can now be evaluated. For example, the kinetic energy operator can be seen to have the property

$$\nabla^2 \chi_{n\ell m}(r, \zeta) = \zeta^2 \left\{ \chi_{n\ell m}(r, \zeta) - 2 \sqrt{\frac{2n}{2n-1}} \chi_{n-1, \ell m}(r, \zeta) \right. \\ \left. + \frac{4[n(n-1) - \ell(\ell+1)]}{\sqrt{(2n)(2n-1)(2n-2)(2n-3)}} \chi_{n-2, \ell m}(r, \zeta) \right\}, \quad (24)$$

while the nuclear Coulomb attraction can be written as

$$\frac{1}{r} \chi_{n\ell m}(r, \zeta) = \frac{2\zeta}{\sqrt{(2n)(2n-1)}} \chi_{n-1, \ell m}(r, \zeta). \quad (25)$$

These two operators generate Slater functions of lower principal quantum number, including such objects as 0s and 1p wavefunctions. While these functions are not physically meaningful as atomic orbitals, they are mathematically useful for Eqs. (24) and (25); consequentially, overlaps involving such functions are included in Table I.

REFERENCES

* This paper will be submitted to the Journal of Chemical Physics.

1. H. E. Zimmerman, Quantum Mechanics for Organic Chemists (Academic Press, New York, 1975).
2. J. C. Slater, Phys. Rev. 36, 57 (1930).
3. E. Clementi and C. Roetti, Atomic Data and Nuclear Data Tables 14, 177 (1974).
4. C. C. J. Roothaan, J. Chem. Phys. 19, 1445 (1951).
5. R. S. Mulliken, C. A. Rieke, D. Orloff, and H. Orloff, J. Chem. Phys. 17, 1248 (1949).

Table I. Unnormalized Overlap Integrals

$T(0s0s) = A_0 B_0$
$T(0s1s) = A_1 B_0 - A_0 B_1$
$T(0s1p) = -A_0 B_0 + A_2 B_2$
$T(0s2s) = A_2 B_0 - 2A_1 B_1 + A_0 B_2$
$T(0s2p) = -A_1 B_0 + (A_0 + A_2) B_1 - A_1 B_2$
$T(0s3s) = A_3 B_0 - 3A_2 B_1 + 3A_1 B_2 - A_0 B_3$
$T(0s3p) = -A_2 B_0 + (2A_1 + A_3) B_1 + (-A_0 - 2A_2) B_2 + A_1 B_3$
$T(0s4s) = A_4 B_0 - 4A_3 B_1 + 6A_2 B_2 - 4A_1 B_3 + A_0 B_4$
$T(0s4p) = -A_3 B_0 + (3A_2 + A_4) B_1 + (-3A_1 - 3A_3) B_2 + (A_0 + 3A_2) B_3 - A_1 B_4$
$T(0s5s) = A_5 B_0 - 5A_4 B_1 + 10A_3 B_2 - 10A_2 B_3 + 5A_1 B_4 - A_0 B_5$
$T(0s5p) = -A_4 B_0 + (4A_3 + A_5) B_1 + (-6A_2 - 4A_4) B_2 + (4A_1 + 6A_3) B_3$ $+ (-A_0 - 4A_2) B_4 + A_1 B_5$
$T(0s6s) = A_6 B_0 - 6A_5 B_1 + 15A_4 B_2 - 20A_3 B_3 + 15A_2 B_4 - 6A_1 B_5 + A_0 B_6$
$T(0s6p) = -A_5 B_0 + (5A_4 + A_6) B_1 + (-10A_3 - 5A_5) B_2 + (10A_2 + 10A_4) B_3$ $+ (-5A_1 - 10A_3) B_4 + (A_0 + 5A_2) B_5 - A_1 B_6$
$T(1s1s) = A_2 B_0 - A_0 B_2$
$T(1s1p) = -A_1 B_0 - A_0 B_1 + A_2 B_1 + A_1 B_2$
$T(1s2s) = A_3 B_0 - A_2 B_1 - A_1 B_2 + A_0 B_3$
$T(1s2p) = -A_2 B_0 + A_3 B_1 + A_0 B_2 - A_1 B_3$
$T(1s3s) = A_4 B_0 - 2A_3 B_1 + 2A_1 B_3 - A_0 B_4$
$T(1s3p) = -A_3 B_0 + (A_2 + A_4) B_1 + (A_1 - A_3) B_2 + (-A_0 - A_2) B_3 + A_1 B_4$
$T(1s4s) = A_5 B_0 - 3A_4 B_1 + 2A_3 B_2 + 2A_2 B_3 - 3A_1 B_4 + A_0 B_5$
$T(1s4p) = -A_4 B_0 + (2A_3 + A_5) B_1 - 2A_4 B_2 - 2A_1 B_3 + (A_0 + 2A_2) B_4 + A_1 B_5$

Table I. Unnormalized Overlap Integrals (Cont'd)

$$\begin{aligned}
T(1s5s) &= A_6 B_0 - 4A_5 B_1 + 5A_4 B_2 - 5A_2 B_4 + 4A_1 B_5 - A_0 B_6 \\
T(1s5p) &= -A_5 B_0 + (3A_4 + A_6) B_1 + (-2A_3 - 3A_5) B_2 + (-2A_2 + 2A_4) B_3 \\
&\quad + (3A_1 + 2A_3) B_4 + (-A_0 - 3A_2) B_5 + A_1 B_6 \\
T(1s6s) &= A_7 B_0 - 5A_6 B_1 + 9A_5 B_2 - 5A_4 B_3 - 5A_3 B_4 + 9A_2 B_5 - 5A_1 B_6 + A_0 B_7 \\
T(1s6p) &= -A_6 B_0 + (4A_5 + A_7) B_1 + (-5A_4 - 4A_6) B_2 + 5A_5 B_3 + 5A_2 B_4 \\
&\quad + (-4A_1 - 5A_3) B_5 + (A_0 + 4A_2) B_6 - A_1 B_7 \\
T(1p1p\sigma) &= -A_0 B_0 + A_2 B_2 \\
T(1p1p\pi) &= (-A_0 + A_2) B_0 + (A_0 - A_2) B_2 \\
T(1p2s) &= A_2 B_0 + (-2A_1 + A_3) B_1 + (A_0 - 2A_2) B_2 + A_1 B_3 \\
T(1p2p\sigma) &= -A_1 B_0 + A_0 B_1 + A_3 B_2 - A_2 B_3 \\
T(1p2p\pi) &= (-A_1 + A_3) B_0 + (A_0 - A_2) B_1 + (A_1 - A_3) B_2 + (-A_0 + A_2) B_3 \\
T(1p3s) &= A_3 B_0 + (-3A_2 + A_4) B_1 + (3A_1 - 3A_3) B_2 + (-A_0 + 3A_2) B_3 - A_1 B_4 \\
T(1p3p\sigma) &= -A_2 B_0 + 2A_1 B_1 + (-A_0 + A_4) B_2 - 2A_3 B_3 + A_2 B_4 \\
T(1p3p\pi) &= (-A_2 + A_4) B_0 + (2A_1 - 2A_3) B_1 + (-A_0 + 2A_2 - A_4) B_2 \\
&\quad + (-2A_1 + 2A_3) B_3 + (A_0 - A_2) B_4 \\
T(1p4s) &= A_4 B_0 + (-4A_3 + A_5) B_1 + (6A_2 - 4A_4) B_2 + (-4A_1 + 6A_3) B_3 \\
&\quad + (A_0 - 4A_2) B_4 + A_1 B_5 \\
T(1p4p\sigma) &= -A_3 B_0 + 3A_2 B_1 + (-3A_1 + A_5) B_2 + (A_0 - 3A_4) B_3 + 3A_3 B_4 - A_2 B_5 \\
T(1p4p\pi) &= (-A_3 + A_5) B_0 + (3A_2 - 3A_4) B_1 + (-3A_1 + 4A_3 - A_5) B_2 \\
&\quad + (A_0 - 4A_2 + 3A_4) B_3 + (3A_1 - 3A_3) B_4 + (-A_0 + A_2) B_5 \\
T(1p5s) &= A_5 B_0 + (-5A_4 + A_6) B_1 + (10A_3 - 5A_5) B_2 + (-10A_2 + 10A_4) B_3 \\
&\quad + (5A_1 - 10A_3) B_4 + (-A_0 + 5A_2) B_5 - A_1 B_6 \\
T(1p5p\sigma) &= -A_4 B_0 + 4A_3 B_1 + (-6A_2 + A_6) B_2 + (4A_1 - 4A_5) B_3 \\
&\quad + (-A_0 + 6A_4) B_4 - 4A_3 B_5 + A_2 B_6
\end{aligned}$$

Table I. Unnormalized Overlap Integrals (Cont'd)

$$\begin{aligned}
T(1p5p\pi) &= (-A_4 + A_6)B_0 + (4A_3 - 4A_5)B_1 + (-6A_2 + 7A_4 - A_6)B_2 \\
&\quad + (4A_1 - 8A_3 + 4A_5)B_3 + (-A_0 + 7A_2 - 6A_4)B_4 + (-4A_1 + 4A_3)B_5 \\
&\quad + (A_0 - A_2)B_6 \\
T(1p6s) &= A_6B_0 + (-6A_5 + A_7)B_1 + (15A_4 - 6A_6)B_2 + (-20A_3 + 15A_5)B_3 \\
&\quad + (15A_2 - 20A_4)B_4 + (-6A_1 + 15A_3)B_5 + A_1B_7 \\
T(1p6p\sigma) &= -A_5B_0 + 5A_4B_1 + (-10A_3 + A_7)B_2 + (10A_2 - 5A_6)B_3 \\
&\quad + (-5A_1 + 10A_5)B_4 + (A_0 - 10A_4)B_5 + 5A_3B_6 - A_2B_7 \\
T(1p6p\pi) &= (-A_5 + A_7)B_0 + (5A_4 - 5A_6)B_1 + (-10A_3 + 11A_5 - A_7)B_2 \\
&\quad + (10A_2 - 15A_4 + 5A_6)B_3 + (-5A_1 + 15A_3 - 10A_5)B_4 \\
&\quad + (A_0 - 11A_2 + 10A_4)B_5 + (5A_1 - 5A_3)B_6 + (-A_0 + A_2)B_7 \\
T(2s2s) &= A_4B_0 - 2A_2B_2 + A_0B_4 \\
T(2s2p) &= -A_3B_0 + (-A_2 + A_4)B_1 + (A_1 + A_3)B_2 + (A_0 - A_2)B_3 - A_1B_4 \\
T(2s3s) &= A_5B_0 - A_4B_1 - 2A_3B_2 + 2A_2B_3 + A_1B_4 - A_0B_5 \\
T(2s3p) &= -A_4B_0 + A_5B_1 + 2A_2B_2 - 2A_3B_3 - A_0B_4 + A_1B_5 \\
T(2s4s) &= A_6B_0 - 2A_5B_1 - A_4B_2 + 4A_3B_3 - A_2B_4 - 2A_1B_5 + A_0B_6 \\
T(2s4p) &= -A_5B_0 + (A_4 + A_6)B_1 + (2A_3 - A_5)B_2 + (-2A_2 - 2A_4)B_3 \\
&\quad + (-A_1 + 2A_3)B_4 + (A_0 + A_2)B_5 - A_1B_6 \\
T(2s5s) &= A_7B_0 - 3A_6B_1 + A_5B_2 + 5A_4B_3 - 5A_3B_4 - A_2B_5 + 3A_1B_6 - A_0B_7 \\
T(2s5p) &= -A_6B_0 + (2A_5 + A_7)B_1 + (A_4 - 2A_6)B_2 + (-4A_3 - A_5)B_3 \\
&\quad + (A_2 + 4A_4)B_4 + (2A_1 - A_3)B_5 + (-A_0 - 2A_2)B_6 - A_1B_7 \\
T(2s6s) &= A_8B_0 - 4A_7B_1 + 4A_6B_2 + 4A_5B_3 - 10A_4B_4 + 4A_3B_5 + 4A_2B_6 \\
&\quad - 4A_1B_7 + A_0B_8 \\
T(2s6p) &= -A_7B_0 + (3A_6 + A_8)B_1 + (-A_5 - 3A_7)B_2 + (-5A_4 + A_6)B_3 \\
&\quad + (5A_3 + 5A_5)B_4 + (A_2 - 5A_4)B_5 + (-3A_1 - A_3)B_6 \\
&\quad + (A_0 + 3A_2)B_7 - A_1B_8
\end{aligned}$$

Table I. Unnormalized Overlap Integrals (Cont'd)

$$\begin{aligned}
T(2p\,2p\sigma) &= -A_2 B_0 + (A_0 + A_4) B_2 - A_2 B_4 \\
T(2p\,2p\pi) &= (-A_2 + A_4) B_0 + (A_0 - A_4) B_2 + (-A_0 + A_2) B_4 \\
T(2p\,3s) &= A_4 B_0 + (-2A_3 + A_5) B_1 - 2A_4 B_2 + 2A_1 B_3 + (-A_0 + 2A_2) B_4 - A_1 B_5 \\
T(2p\,3p\sigma) &= -A_3 B_0 + A_2 B_1 + (A_1 + A_5) B_2 + (-A_0 - A_4) B_3 - A_3 B_4 + A_2 B_5 \\
T(2p\,3p\pi) &= (-A_3 + A_5) B_0 + (A_2 - A_4) B_1 + (A_1 - A_5) B_2 + (-A_0 + A_4) B_3 \\
&\quad + (-A_1 + A_3) B_4 + (A_0 - A_2) B_5 \\
T(2p\,4s) &= A_5 B_0 + (-3A_4 + A_6) B_1 + (2A_3 - 3A_5) B_2 + (2A_2 + 2A_4) B_3 \\
&\quad + (-3A_1 + 2A_3) B_4 + (A_0 - 3A_2) B_5 + A_1 B_6 \\
T(2p\,4p\sigma) &= -A_4 B_0 + 2A_3 B_1 + A_6 B_2 + (-2A_1 - 2A_5) B_3 + A_0 B_4 + 2A_3 B_5 - A_2 B_6 \\
T(2p\,4p\pi) &= (-A_4 + A_6) B_0 + (2A_3 - 2A_5) B_1 + (A_4 - A_6) B_2 + (-2A_1 + 2A_5) B_3 \\
&\quad + (A_0 - A_2) B_4 + (2A_1 - 2A_3) B_5 + (-A_0 + A_2) B_6 \\
T(2p\,5s) &= A_6 B_0 + (-4A_5 + A_7) B_1 + (5A_4 - 4A_6) B_2 + 5A_5 B_3 - 5A_2 B_4 \\
&\quad + (4A_1 - 5A_3) B_5 + (-A_0 + 4A_2) B_6 - A_1 B_7 \\
T(2p\,5p\sigma) &= -A_5 B_0 + 3A_4 B_1 + (-2A_3 + A_7) B_2 + (-2A_2 - 3A_6) B_3 \\
&\quad + (3A_1 + 2A_5) B_4 + (-A_0 + 2A_4) B_5 - 3A_3 B_6 + A_2 B_7 \\
T(2p\,5p\pi) &= (-A_5 + A_7) B_0 + (3A_4 - 3A_6) B_1 + (-2A_3 + 3A_5 - A_7) B_2 \\
&\quad + (-2A_2 - A_4 + 3A_6) B_3 + (3A_1 - A_3 - 2A_5) B_4 \\
&\quad + (-A_0 + 3A_2 - 2A_4) B_5 + (-3A_1 + 3A_3) B_6 + (A_0 - A_2) B_7 \\
T(2p\,6s) &= A_7 B_0 + (-5A_6 + A_8) B_1 + (9A_5 - 5A_7) B_2 + (-5A_4 + 9A_6) B_3 \\
&\quad + (-5A_3 - 5A_5) B_4 + (9A_2 - 5A_4) B_5 + (-5A_1 + 9A_3) B_6 \\
&\quad + (A_0 - 5A_2) B_7 + A_1 B_8 \\
T(2p\,6p\sigma) &= -A_6 B_0 + 4A_5 B_1 + (-5A_4 + A_8) B_2 - 4A_7 B_3 + (5A_2 + 5A_6) B_4 \\
&\quad - 4A_1 B_5 + (A_0 - 5A_4) B_6 + 4A_3 B_7 - A_2 B_8 \\
T(2p\,6p\pi) &= (-A_6 + A_8) B_0 + (4B_5 - 4B_7) B_1 + (-5A_4 + 6A_6 - A_8) B_2 \\
&\quad + (-4A_5 + 4A_7) B_3 + (5A_2 - 5A_6) B_4 + (-4A_1 + 4A_3) B_5 \\
&\quad + (A_0 - 6A_2 + 5A_4) B_6 + (4A_1 - 4A_3) B_7 + (-A_0 + A_2) B_0
\end{aligned}$$

Table I. Unnormalized Overlap Integrals (Cont'd)

$$\begin{aligned}
 T(3s\ 3s) &= A_6 B_0 - 3A_4 B_2 + 3A_2 B_4 - A_0 B_6 \\
 T(3s\ 3p) &= -A_5 B_0 + (-A_4 + A_6) B_1 + (2A_3 + A_5) B_2 + (2A_2 - 2A_4) B_3 \\
 &\quad + (-A_1 - A_3) B_4 + (-A_0 + A_2) B_5 + A_1 B_6 \\
 T(3s\ 4s) &= A_7 B_0 - A_6 B_1 - 3A_5 B_2 + 3A_4 B_3 + 3A_3 B_4 - 3A_2 B_5 - A_1 B_6 + A_0 B_7 \\
 T(3s\ 4p) &= -A_6 B_0 + A_7 B_1 + 3A_4 B_2 - 3A_5 B_3 - 3A_2 B_4 + 3A_3 B_5 + A_0 B_6 - A_1 B_7 \\
 T(3s\ 5s) &= A_8 B_0 - 2A_7 B_1 - 2A_6 B_2 + 6A_5 B_3 - 6A_3 B_5 + 2A_2 B_6 + 2A_1 B_7 - A_0 B_8 \\
 T(3s\ 5p) &= -A_7 B_0 + (A_6 + A_8) B_1 + (3A_5 - A_7) B_2 + (-3A_4 - 3A_6) B_3 \\
 &\quad + (-3A_3 + 3A_5) B_4 + (3A_2 + 3A_4) B_5 + (A_1 - 3A_3) B_6 \\
 &\quad + (-A_0 - A_2) B_7 + A_1 B_8 \\
 T(3s\ 6s) &= A_9 B_0 - 3A_8 B_1 + 8A_6 B_3 - 6A_5 B_4 - 6A_4 B_5 + 8A_3 B_6 - 3A_1 B_8 + A_0 B_9 \\
 T(3s\ 6p) &= -A_8 B_0 + (2A_7 + A_9) B_1 + (2A_6 - 2A_8) B_2 + (-6A_5 - 2A_7) B_3 \\
 &\quad + 6A_6 B_4 + 6A_3 B_5 + (-2A_2 - 6A_4) B_6 + (-2A_1 + 2A_3) B_7 \\
 &\quad + (A_0 + 2A_2) B_8 - A_1 B_9 \\
 T(3p\ 3p\sigma) &= -A_4 B_0 + (2A_2 + A_6) B_2 + (-A_0 - 2A_4) B_4 + A_2 B_6 \\
 T(3p\ 3p\pi) &= (-A_4 + A_6) B_0 + (2A_2 - A_4 - A_6) B_2 + (-A_0 - A_2 + 2A_4) B_3 \\
 &\quad + (A_0 - A_2) B_6 \\
 T(3p\ 4s) &= A_6 B_0 + (-2A_5 + A_7) B_1 + (-A_4 - 2A_6) B_2 + (4A_3 - A_5) B_3 \\
 &\quad + (-A_2 + 4A_4) B_4 + (-2A_1 - A_3) B_5 + (A_0 - 2A_2) B_6 + A_1 B_7 \\
 T(3p\ 4p\sigma) &= -A_5 B_0 + A_4 B_1 + (2A_3 + A_7) B_2 + (-2A_2 - A_6) B_3 \\
 &\quad + (-A_1 - 2A_5) B_4 + (A_0 + 2A_4) B_5 + A_3 B_6 - A_2 B_7 \\
 T(3p\ 4p\pi) &= (-A_5 + A_7) B_0 + (A_4 - A_6) B_1 + (2A_3 - A_5 - A_7) B_2 \\
 &\quad + (-2A_2 + A_4 + A_6) B_3 + (-A_1 - A_3 + 2A_5) B_4 \\
 &\quad + (A_0 + A_2 - 2A_4) B_5 + (A_1 - A_3) B_6 + (-A_0 + A_2) B_7
 \end{aligned}$$

Table I. Unnormalized Overlap Integrals (Cont'd)

$$\begin{aligned}
T(3p\ 5s) &= A_7 B_0 + (-3A_6 + A_8) B_1 + (A_5 - 3A_7) B_2 + (5A_4 + A_6) B_3 \\
&\quad + (-5A_3 + 5A_5) B_4 + (-A_2 - 5A_4) B_5 + (3A_1 - A_3) B_6 \\
&\quad + (-A_0 + 3A_2) B_7 - A_1 B_8 \\
T(3p\ 5p\sigma) &= -A_6 B_0 + 2A_5 B_1 + (A_4 + A_8) B_2 + (-4A_3 - 2A_7) B_3 + (A_2 - A_6) B_4 \\
&\quad + (2A_1 + 4A_5) B_5 + (-A_0 - A_4) B_6 - 2A_3 B_7 + A_2 B_8 \\
T(3p\ 5p\pi) &= (-A_6 + A_8) B_0 + (2A_5 - 2A_7) B_1 + (A_4 - A_8) B_2 + (-4A_3 + 2A_5) \\
&\quad + 2A_7 B_3 + (A_2 - 2A_4 + A_6) B_4 + (2A_1 + 2A_3 - 4A_5) B_5 \\
&\quad + (-A_0 + A_4) B_6 + (-2A_1 + 2A_3) B_7 + (A_0 - A_2) B_8 \\
T(3p\ 6s) &= A_8 B_0 + (-4A_7 + A_9) B_1 + (4A_6 - 4A_8) B_2 + (4A_5 + 4A_7) B_3 \\
&\quad + (-10A_4 + 4A_6) B_4 + (4A_3 - 10A_5) B_5 + (4A_2 + 4A_4) B_6 \\
&\quad + (-A_1 + A_3) B_7 + (A_0 - 4A_2) B_8 + A_1 B_9 \\
T(3p\ 6p\sigma) &= -A_7 B_0 + 3A_6 B_1 + (-A_5 + A_9) B_2 + (-5A_4 - 3A_8) B_3 \\
&\quad + (5A_3 + A_7) B_4 + (A_2 + 5A_6) B_5 + (3A_1 - 5A_5) B_6 \\
&\quad + (A_0 - A_4) B_7 + 3A_3 B_8 - A_2 B_9 \\
T(3p\ 6p\pi) &= (-A_7 + A_9) B_0 + (3A_6 - 3A_8) B_1 + (-A_5 + 2A_7 - A_9) B_2 \\
&\quad + (-5A_4 + 2A_6 + 3A_8) B_3 + (5A_3 - 4A_5 - A_7) B_4 \\
&\quad + (A_2 + 4A_4 - 5A_6) B_5 + (-3A_1 - 2A_3 + 5A_5) B_6 \\
&\quad + (A_0 - 2A_2 + A_4) B_7 + (3A_1 - 3A_3) B_8 + (-A_0 + A_2) B_9 \\
T(4s\ 4s) &= A_8 B_0 - 4A_6 B_2 + 6A_4 B_4 - 4A_2 B_6 + A_0 B_8 \\
T(4s\ 4p) &= -A_7 B_0 + (-A_6 + A_8) B_1 + (3A_5 + A_7) B_2 + (3A_4 - 3A_6) B_3 \\
&\quad + (-3A_3 - 3A_5) B_4 + (-3A_2 + 3A_4) B_5 + (A_1 + 3A_3) B_6 \\
&\quad + (A_0 - A_2) B_7 - A_1 B_8 \\
T(4s\ 5s) &= A_9 B_0 - A_8 B_1 - 4A_7 B_2 + 4A_6 B_3 + 6A_5 B_4 - 6A_4 B_5 - 4A_3 B_6 \\
&\quad + 4A_2 B_7 + A_1 B_8 - A_0 B_9
\end{aligned}$$

Table I. Unnormalized Overlap Integrals (Cont'd)

$$\begin{aligned}
 T(4s5p) &= -A_8 B_0 + A_9 B_1 + 4A_6 B_2 - 4A_7 B_3 - 6A_4 B_4 + 6A_5 B_5 \\
 &\quad + 4A_2 B_6 - 4A_3 B_7 - A_0 B_8 + A_1 B_9 \\
 T(4s6s) &= A_{10} B_0 - 2A_9 B_1 - 3A_8 B_2 + 8A_7 B_3 + 2A_6 B_4 - 12A_5 B_5 \\
 &\quad + 2A_4 B_6 + 8A_3 B_7 - 3A_2 B_8 - 2A_1 B_9 + A_0 B_{10} \\
 T(4s6p) &= -A_9 B_0 + (A_8 + A_{10}) B_1 + (4A_7 - A_9) B_2 + (-4A_6 - 4A_8) B_3 \\
 &\quad + (-6A_5 + 4A_7) B_4 + (6A_4 + 6A_6) B_5 + (4A_3 - 6A_5) B_6 \\
 &\quad + (-4A_2 - 4A_4) B_7 + (-A_1 + 4A_3) B_8 + (A_0 + A_2) B_9 - A_1 B_{10} \\
 T(4p4p\sigma) &= -A_6 B_0 + (3A_4 + A_8) B_2 + (-3A_2 - 3A_6) B_4 + (A_0 + 3A_4) B_6 - A_2 B_8 \\
 T(4p4p\pi) &= (-A_6 + A_8) B_0 + (3A_4 - 2A_6 - A_8) B_2 + (-3A_2 + 3A_6) B_4 \\
 &\quad + (A_0 + 2A_2 - 3A_4) B_6 + (-A_0 + A_2) B_8 \\
 T(4p5s) &= A_8 B_0 + (-2A_7 + A_9) B_1 + (-2A_6 - 2A_8) B_2 + (6A_5 - 2A_7) B_3 \\
 &\quad + 6A_6 B_4 - 6A_3 B_5 + (2A_2 - 6A_4) B_6 + (2A_1 + 2A_3) B_7 \\
 &\quad + (-A_0 + 2A_2) B_8 - A_1 B_9 \\
 T(4p5p\sigma) &= -A_7 B_0 + A_6 B_1 + (3A_5 + A_9) B_2 + (-3A_4 - A_8) B_3 \\
 &\quad + (-3A_3 - 3A_7) B_4 + (3A_2 + 3A_6) B_5 + (A_1 + 3A_5) B_6 \\
 &\quad + (-A_0 - 3A_4) B_7 - A_3 B_8 + A_2 B_9 \\
 T(4p5p\pi) &= (-A_7 + A_9) B_0 + (A_6 - A_8) B_1 + (3A_5 - 2A_7 - A_9) B_2 \\
 &\quad + (-3A_4 + 2A_6 + A_8) B_3 + (-3A_3 + 3A_7) B_4 + (3A_2 - 3A_6) B_5 \\
 &\quad + (A_1 + 2A_3 - 3A_5) B_6 + (-A_0 - 2A_2 + 3A_4) B_7 + (-A_1 + A_3) B_8 \\
 &\quad + (A_0 - A_2) B_9 \\
 T(4p6s) &= A_9 B_0 + (-3A_8 + A_{10}) B_1 - 3A_9 B_2 + 8A_6 B_3 + (-6A_5 + 8A_7) B_4 \\
 &\quad + (-6A_4 - 6A_6) B_5 + (8A_3 - 6A_5) B_6 + 8A_4 B_7 - 3A_1 B_8 \\
 &\quad + (A_0 - 3A_2) B_9 + A_1 B_{10}
 \end{aligned}$$

Table I. Unnormalized Overlap Integrals (Cont'd)

$$\begin{aligned}
T(4p\ 6p\sigma) &= -A_8 B_0 + 2A_7 B_1 + (2A_6 + A_{10}) B_2 + (-6A_5 - 2A_9) B_3 \\
&\quad - 2A_8 B_4 + (6A_3 + 6A_7) B_5 - 2A_2 B_6 + (-2A_1 - 6A_5) B_7 \\
&\quad + (A_0 + 2A_4) B_8 + 2A_3 B_9 - A_2 B_{10} \\
T(4p\ 6p\pi) &= (-A_8 + A_{10}) B_0 + (2A_7 - 2A_9) B_1 + (2A_6 - A_8 - A_{10}) B_2 \\
&\quad + (-6A_5 + 4A_7 + 2A_9) B_3 + (-2A_6 + 2A_8) B_4 + (6A_3 - 6A_7) B_5 \\
&\quad + (-2A_2 + 2A_4) B_6 + (-2A_1 - 4A_3 + 6A_5) B_7 + (A_0 + A_2 - 2A_4) B_8 \\
&\quad + (2A_1 - 2A_3) B_9 + (-A_0 + A_2) B_{10} \\
T(5s\ 5s) &= A_{10} B_0 - 5A_8 B_2 + 10A_6 B_4 - 10A_4 B_6 + 5A_2 B_8 - A_0 B_{10} \\
T(5s\ 5p) &= -A_9 B_0 + (-A_8 + A_{10}) B_1 + (4A_7 + A_9) B_2 + (4A_6 - 4A_8) B_3 \\
&\quad + (-6A_5 - 4A_7) B_4 + (-6A_4 + 6A_6) B_5 + (4A_3 + 6A_5) B_6 \\
&\quad + (4A_2 - 4A_4) B_7 + (-A_1 - 4A_3) B_8 + (-A_0 + A_2) B_9 + A_1 B_{10} \\
T(5s\ 6s) &= A_{11} B_0 - A_{10} B_1 - 5A_9 B_2 + 5A_8 B_3 + 10A_7 B_4 - 10A_6 B_5 \\
&\quad - 10A_5 B_6 + 10A_4 B_7 + 5A_3 B_8 - 5A_2 B_9 - A_1 B_{10} + A_0 B_{11} \\
T(5s\ 6p) &= -A_{10} B_0 + A_{11} B_1 + 5A_8 B_2 - 5A_9 B_3 - 10A_6 B_4 + 10A_7 B_5 \\
&\quad + 10A_4 B_6 - 10A_5 B_7 - 5A_2 B_8 + 5A_3 B_9 + A_0 B_{10} - A_1 B_{11} \\
T(5p\ 5p\sigma) &= -A_8 B_0 + (4A_6 + A_{10}) B_2 + (-6A_4 - 4A_8) B_4 + (4A_2 + 6A_6) B_6 \\
&\quad + (-A_0 - 4A_4) B_8 + A_2 B_{10} \\
T(5p\ 5p\pi) &= (-A_8 + A_{10}) B_0 + (4A_6 - 3A_8 - A_{10}) B_2 + (-6A_4 + 2A_6 + 4A_8) B_4 \\
&\quad + (4A_2 + 2A_4 - 6A_6) B_6 + (-A_0 - 3A_2 + 4A_4) B_8 + (A_0 - A_2) B_{10} \\
T(5p\ 6s) &= A_{10} B_0 + (-2A_9 + A_{11}) B_1 + (-3A_8 - 2A_{10}) B_2 + (8A_7 - 3A_9) B_3 \\
&\quad + (2A_6 + 8A_8) B_4 + (-12A_5 + 2A_7) B_5 + (2A_4 - 12A_6) B_6 \\
&\quad + (8A_3 + 2A_5) B_7 + (-3A_2 + 8A_4) B_8 + (-2A_1 - 3A_3) B_9 \\
&\quad + (A_0 - 2A_2) B_{10} + A_1 B_{11}
\end{aligned}$$

Table I. Unnormalized Overlap Integrals (Cont'd)

$$\begin{aligned}
 T(5p6p\sigma) = & -A_9 B_0 + A_8 B_1 + (4A_7 + A_{11}) B_2 + (-4A_6 - A_{10}) B_3 \\
 & + (-6A_5 - 4A_9) B_4 + (6A_4 + 4A_8) B_5 + (4A_3 + 6A_7) B_6 \\
 & + (-4A_2 - 6A_6) B_7 + (-A_1 - 4A_5) B_8 + (A_0 + 4A_4) B_9 \\
 & + A_3 B_{10} - A_2 B_{11}
 \end{aligned}$$

$$\begin{aligned}
 T(5p6p\pi) = & (-A_9 + A_{11}) B_0 + (A_8 - A_{10}) B_1 + (4A_7 - 3A_9 - A_{11}) B_2 \\
 & + (-4A_6 + 3A_8 + A_{10}) B_3 + (-6A_5 + 2A_7 + 4A_9) B_4 \\
 & + (6A_4 - 2A_6 - 4A_8) B_5 + (4A_3 + 2A_5 - 6A_7) B_6 \\
 & + (-4A_2 - 2A_4 + 6A_6) B_7 + (-A_1 - 3A_3 + 4A_5) B_8 \\
 & + (A_0 + 3A_2 - 4A_4) B_9 + (A_1 - A_3) B_{10} + (-A_0 + A_2) B_{11}
 \end{aligned}$$

$$\begin{aligned}
 T(6s6s) = & A_{12} B_0 - 6A_{10} B_2 + 15A_8 B_4 - 20A_6 B_6 + 15A_4 B_8 \\
 & - 6A_2 B_{10} + A_0 B_{12}
 \end{aligned}$$

$$\begin{aligned}
 T(6s6p) = & -A_{11} B_0 + (-A_{10} + A_{12}) B_1 + (5A_9 + A_{11}) B_2 + (5A_8 - 5A_{10}) B_3 \\
 & + (-10A_7 - 5A_9) B_4 + (-10A_6 + 10A_8) B_5 + (10A_5 + 10A_7) B_6 \\
 & + (10A_4 - 10A_6) B_7 + (-5A_3 - 10A_5) B_8 + (-5A_2 + 5A_4) B_9 \\
 & + (A_1 + 5A_3) B_{10} + (A_0 - A_2) B_{11} - A_1 B_{12}
 \end{aligned}$$

$$\begin{aligned}
 T(6p6p\sigma) = & -A_{10} B_0 + (5A_8 + A_{12}) B_2 + (-10A_6 - 5A_{10}) B_4 + (10A_4 + 10A_8) B_6 \\
 & + (-5A_2 - 10A_6) B_8 + (A_0 + 5A_4) B_{10} - A_2 B_{12}
 \end{aligned}$$

$$\begin{aligned}
 T(6p6p\pi) = & (-A_{10} + A_{12}) B_0 + (5A_8 - 4A_{10} - A_{12}) B_2 \\
 & + (-10A_6 + 5A_8 + 5A_{10}) B_4 + (10A_4 - 10A_8) B_6 \\
 & + (-5A_2 - 5A_4 + 10A_6) B_8 + (A_0 + 4A_2 - 5A_4) B_{10} \\
 & + (-A_0 + A_2) B_{12}
 \end{aligned}$$

G. QUASISELECTION RULES FOR MULTIPHONON
ABSORPTION IN ALKALI HALIDES*

C. J. Duthler

Our last multiphonon calculation shows that infrared absorption in alkali halides is dominated by processes with an odd number of optical output phonons. The results afford a practical computation scheme that greatly reduces the effort of calculation and explains the recent observation of a well-defined peak in the low-temperature infrared absorption of several alkali halides at a frequency corresponding to the sum of three optical phonons. The odd-optical-phonon quasiselection rule results from the relative ionic displacements for optical modes being approximately in phase with the individual ion displacements, while the relative ionic displacements for acoustical modes are approximately 90° out of phase. The further realization that the magnitude of the Fourier-transformed optical-mode relative displacement is nearly independent of the wave vector greatly reduces calculation effort by reducing an extremely tedious multiple sum to a thermally and frequency weighted density of states of distinct phonon branches. The theory avoids the two inadequacies of diatomic-molecule approaches to multiphonon absorption: (a) that peaks near all integral multiples of the fundamental frequency are predicted and that (b) molecular models have led to gross overestimates of vertex correction factors, which are shown here to be negligible.

I. INTRODUCTION

The advent of high-power infrared lasers has stimulated considerable recent interest in the small amount of absorption of transparent solids in the far wings of their infrared absorption bands.¹ In alkali halides at frequencies greater than approximately twice the fundamental Reststrahl frequency, the absorption coefficient β is observed to decrease exponentially with increasing frequency.² Until recently no structure has been observed in the high-frequency, multiphonon region. Recent experiments by Harrington *et al.*³ at low temperature (80 K) show a well-defined peak in the absorption coefficient of several alkali halides at a frequency corresponding to the sum of three optical phonons. No corresponding peak is observed at the two- or four-optical-phonon summation frequencies and the three-optical-phonon summation band is observed to be most pronounced in crystals having a large mass ratio between the heavy and light crystal ions. These observations suggest an odd-even selection rule that allows odd numbered optical-phonon summation bands. Such a selection rule is derived in this paper and is called a quasiselection rule since it is approximate (unallowed transition matrix elements small, but nonzero).

Previous theories⁴⁻⁹ generally predict a smoothly exponentially decreasing absorption coefficient in the multiphonon region in agreement with previous room-temperature experiments. Structure in the multiphonon absorption coefficient can arise from structure in both the multiphonon density of states and transition matrix elements. Evidence is presented in the present paper that much of the fine-scale structure in the multiphonon density of states is smoothed out by the short lifetime, hence large spectral width, of the final-state optical phonons at room temperature.

The remaining broad structure observed by Harrington et al.³ is shown to result from transition matrix elements which favor transitions to final states containing an odd number of optical phonons.

Many past theories treat the lattice as a set of molecular oscillators on which a density of states is impressed. Such past theories have neglected the suppression of even-numbered optical phonon summation bands and any structure in the absorption coefficient, if predicted, occurs at both even- and odd-numbered combinations.

The present paper is based on a perturbation-theory calculation on actual crystal phonons by Sparks and Sham.⁴ An error in the Sparks and Sham⁴ paper is corrected which, when corrected, leads to multiphonon quasiselection rules. Further reasonable approximations greatly simplify the otherwise very tedious perturbation-theory calculation.

Previously, selection rules were derived for the two-phonon region. An exact group-theory selection rule forbids final-state phonons on the same phonon branch.^{10,11} Subsequently Duthler and Sparks¹² derived a two-phonon quasiselection rule which favors final states consisting of an optical plus an acoustical phonon over final states consisting of two optical or two acoustical phonons. This quasi-selection rule yields four quasiallowed combinations of phonon bands: TA + TO, LA + TO, TA + LO, and LA + LO, where O and A denote optical and acoustical branches, and T and L denote transverse and longitudinal. Typically four two-phonon absorption peaks are observed in alkali halides¹³ in agreement with the quasiselection rule and in contrast with numerous additional peaks possible from the joint density of states. Eldridge and co-workers¹⁴ have examined the absorption peaks in LiF in detail. Strong two-phonon summation peaks were traced to

the combination of branches and the particular region of the Brillouin zone contributing to the peak. Four strong contributions were found for combinations of optical plus acoustical branches, although branch identification is somewhat difficult in LiF due to dispersion curve crossings.

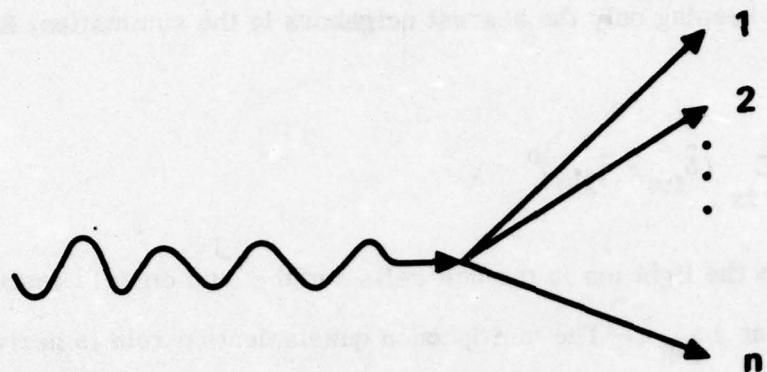
II. ABSORPTION MECHANISM

There are two possible mechanisms for multiphonon infrared absorption in dielectric crystals: In the higher-order-dipole-moment mechanism the absorbed photon directly creates n final-state phonons, as is illustrated in Fig. 1(a). In the anharmonic lattice mechanism only the fundamental Reststrahl (TO, zero momentum) phonon couples to the radiation field. In this case illustrated in Fig. 1(b), the intermediate-state Reststrahl phonon is driven off resonance and decays into n final-state phonons. It was previously thought that the anharmonic lattice mechanism is dominant in alkali halides, although this is now questioned especially at large n .¹⁵ The leading terms in the transition matrix elements for the two mechanisms are expected to be similar^{16,17} with the result that the quasiselection rules derived in the following section for the anharmonic lattice mechanism should also be valid for the higher-order-dipole-moment mechanism.

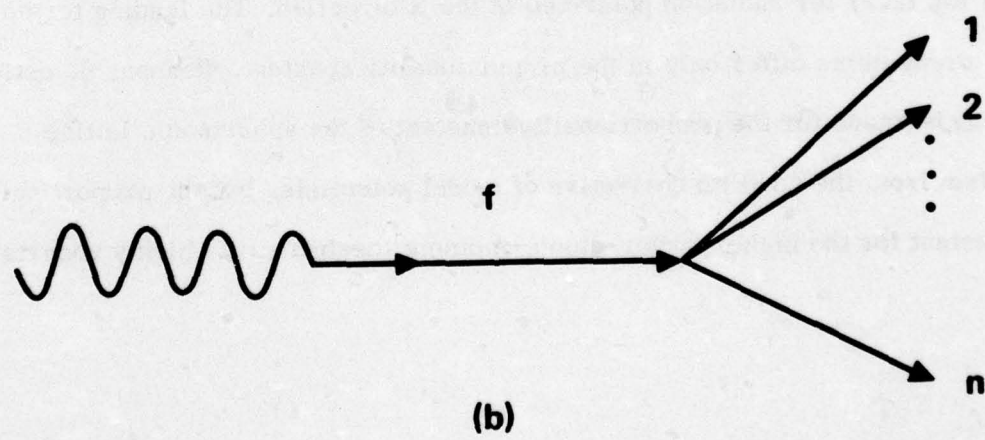
To illustrate the equivalent functional form of the leading terms of the two mechanisms, consider the interaction Hamiltonian for radiation absorption by the anharmonic lattice mechanism. Assuming a central-force lattice potential, the n phonon anharmonic lattice interaction Hamiltonian is proportional to the n th power of the relative displacement of ion pairs:

$$\mathcal{H}_{\text{anh}}^{(n)} \propto \sum_{\ell} \sum_{m} (\hat{\delta}_{\ell m} \cdot \vec{u}_{\ell m})^n (\hat{u}_f \cdot \hat{\delta}_{\ell m}) . \quad (2.1)$$

Here $\vec{u}_{\ell m} = \vec{u}_{\ell} - \vec{u}_m$ where \vec{u}_{ℓ} and \vec{u}_m are the displacements of the ℓ th and m th ions from equilibrium. The unit vector $\hat{\delta}_{\ell m}$ is directed from the equilibrium positions of the ℓ th ion to the m th ion and \hat{u}_f is the unit polarization vector for the ion motion in the fundamental mode.



(a)



(b)

Fig. 1. In the higher-order-dipole-moment mechanism the absorbed photon directly creates n final-state phonons (a). Only the fundamental Reststrahl phonon couples to the radiation field in the anharmonic lattice mechanism (b).

In rocksalt structure crystals the absorption coefficient is independent of the direction of propagation. Choosing the x direction for the radiation polarization ($\hat{u}_f = \hat{x}$) and keeping only the nearest neighbors in the summation, Eq. (2.1) becomes

$$\kappa_{\text{anh}}^{(n)} \propto \sum_{\ell} \sum_{m=\pm x} (\hat{\delta}_{\ell m} \cdot \vec{u}_{\ell m})^n , \quad (2.2)$$

where now ℓ labels the light ion in the unit cells and the sum on m is restricted to nearest neighbors at $\pm a_{nn} \hat{x}$. The multiphonon quasiselection rule is derived from the term under the summation with the relative ionic displacement expressed in terms of crystalline normal modes.

It is reasonable to expect that the higher-order dipole moment which arises from the n th power of the relative ionic displacement is dominated by contributions of nearest neighbor pairs and is directed along the line connecting the ion centers. If these conditions are satisfied, at least the leading terms of the interaction Hamiltonian for the higher-order-dipole-moment mechanism have the same form as Eq. (2.2) for radiation polarized in the x direction. The leading terms of the two mechanisms differ only in the proportionality constant. Reasonable estimates can be made for the proportionality constant of the anharmonic lattice mechanism from the $(n+1)$ th derivative of model potentials, but the proportionality constant for the higher-order-dipole-moment mechanism is highly uncertain.

III. DERIVATION OF QUASISELECTION RULE

The infrared dielectric constant for the anharmonic lattice mechanism is

$$\epsilon(\omega) = \epsilon_{\infty} + (\epsilon_0 - \epsilon_{\infty}) \omega_f^2 / [\omega^2 - \omega_f^2 - i\omega_f \Gamma(\omega)] , \quad (3.1)$$

where ϵ_0 and ϵ_{∞} are the static and high-frequency dielectric constants, ω_f is the frequency of the fundamental Reststrahl mode, and $\Gamma(\omega)$ is the frequency dependent relaxation frequency of the fundamental mode. The absorption coefficient is given by $\beta = k_0 \epsilon_1 / n_R$ where k_0 is the vacuum propagation constant of the radiation, ϵ_1 is the imaginary part of the dielectric constant, and n_R is the real part of the refractive index $n = \epsilon^{1/2}$. For frequencies away from the resonant frequency, peaks in the relaxation frequency will be reflected in peaks in the absorption coefficient.

Sparks and Sham⁴ have derived formal expressions for the relaxation frequency using the perturbation-theory result that the probability per unit time of a transition between two states is $2\pi/\hbar$ times the square of the transition matrix element. The total relaxation frequency of the fundamental mode is the sum of processes involving all numbers of phonons with the contribution from the n phonon summation process shown in Fig. 1b being

$$\Gamma_n(\omega) = \frac{2\pi}{\hbar} (n+1)^2 n! \sum_{Q_1 \dots Q_n} \left| \Lambda(f Q_1 \dots Q_n) \right|^2 \Delta \left(\sum_{j=1}^n \vec{q}_j \right) \delta \left(\omega - \sum_{j=1}^n \omega_{Q_j} \right) \tilde{n}_n , \quad (3.2)$$

where Q denotes the phonon mode having wave vector \vec{q} , branch b and frequency ω_Q ; Δ is the modified Kronecker δ which is unity when the argument is zero or a reciprocal lattice vector and zero otherwise; and

Sec. G

$$\tilde{n}_n = \prod_{j=1}^n \frac{n_{Q_j} + 1}{n_{\omega} + 1} , \quad (3.3)$$

where n_Q and n_ω are Bose-Einstein occupation numbers of the phonon mode Q and frequency ω , respectively.

The total renormalized vertex $\Lambda(fQ_1 \cdots Q_n)$ is approximated by the simple vertex $V(fQ_1 \cdots Q_n)$ multiplied by a vertex renormalization factor

$$\Lambda(fQ_1 \cdots Q_n) = \Lambda_n V(fQ_1 \cdots Q_n) . \quad (3.4)$$

The simple vertex $V(Q_1 \cdots Q_m)$ involves all derivatives of the potential through order m , but no products of derivatives as does the renormalized vertex. Sparks and Sham⁴ justify retaining only the m th-order derivative of the assumed nearest-neighbor, central-force potential $\phi^{(m)} = d^m \phi / dr^m$, and obtain

$$V(Q_1 \cdots Q_m) = (N/m!) \phi^{(m)} \sum_{\gamma=1}^6 \prod_{j=1}^m U_\gamma(Q_j) \left(\hbar/2N m \omega_{Q_j} \right)^{1/2} , \quad (3.5)$$

where N is the number of unit cells in the crystal and $m_<$ is the mass of the light ion in the unit cell. The sum on γ runs over the nearest neighbor heavy ions which, in rocksalt structure crystals, are located at the six positions $\pm a_{nn} \hat{x}$, $\pm a_{nn} \hat{y}$, and $\pm a_{nn} \hat{z}$ from each light ion with the directions to these positions being given by the unit vectors \hat{x}_γ . The quantity

$$U_\gamma(Q) = \hat{x}_\gamma \cdot \left[\vec{w}_{<Q_j} - (m_</m_>)^{1/2} \vec{w}_{>Q_j} e^{i\vec{Q} \cdot \hat{x}_\gamma a_{nn}} \right] \quad (3.6)$$

is the \hat{x}_γ component of the Fourier transformed relative displacement of the light ion from the heavy ion located at $\hat{x}_\gamma a_{nn}$. The polarization vectors $\vec{w}_{<Q}$ and $\vec{w}_{>Q}$

are implicitly defined by the equation expressing the displacement $\vec{u}_{\ell\tau}$ of an ion from its equilibrium position $\vec{x}_{\ell\tau}$ in terms of phonon modes:

$$\vec{u}_{\ell\tau} = \sum_Q \left(\hbar/2 N m_\tau \omega_Q \right)^{1/2} e^{i \vec{q} \cdot \vec{x}_{\ell\tau}} A_Q \vec{w}_{\tau Q} , \quad (3.7)$$

where τ denotes the ion type and $A_Q = a_Q + a_Q^\dagger$ with a_Q and a_Q^\dagger being phonon creation and annihilation operators. With the convention used in writing Eq. (3.7), the components of the polarization vectors $\vec{w}_{\tau Q}$ are real numbers.

For the fundamental Reststrahl mode, the Fourier transformed relative displacement in Eq. (3.6) becomes

$$U_\gamma(f) = \hat{x}_\gamma \cdot \hat{w}_f (m_\gamma / m_r)^{1/2} , \quad (3.8)$$

where m_r is the reduced mass of the two ions in a unit cell.

Substituting this result for one of the phonon modes in Eq. (3.5) and using Eqs. (3.3) and (3.4), the relaxation frequency in Eq. (3.2) can be written

$$\Gamma_n(\omega) = \frac{2\pi}{\hbar^2} \frac{1}{n!} \left(\frac{\hbar}{2m_\gamma} \right)^{n+1} \left(\frac{m_\gamma}{m_r} \right) \omega^{-1} (n\omega + 1)^{-1} \left(\phi^{(n+1)} \right)^2 \Lambda_n^2 \Sigma_n , \quad (3.9)$$

where the dynamical information of the phonons is contained in Σ_n :

$$\begin{aligned} \Sigma_n = & \sum_{\gamma=1}^6 \sum_{\ell=1}^6 (\hat{x}_\gamma \cdot \hat{w}_f) (\hat{x}_{\gamma'} \cdot \hat{w}_f) N^{-n} \\ & \times \sum_{Q_1 \dots Q_n} N \Delta \left(\sum_{j=1}^n \vec{q}_j \right) \delta \left(\omega - \sum_{j=1}^n \omega_{Q_j} \right) \prod_{j=1}^n U_\gamma(Q_j) U_{\gamma'}^*(Q_j) \omega_{Q_j}^{-1} [n_{Q_j} + 1] . \end{aligned} \quad (3.10)$$

This result for Σ_n is identical to that given in Eq. (2.21) of Sparks and Sham.⁴ In going from their Eq. (2.21) to Eq. (2.24) Sparks and Sham⁴ made an algebraic error when expressing Σ_n in terms of real and imaginary parts of $U_x(Q)$. Rather than simply correcting the algebra in Ref. 4, a different approach is taken from this point on in the present paper.

In rocksalt structure crystals the absorption is independent of the direction of propagation. Hence, for convenience we choose $\hat{\omega}_f = \hat{x}$. With this choice the only terms surviving the sums over nearest neighbors in Eq. (3.10) are those located at $\pm \hat{x} a_{nn}$. Interchanging sums on γ and Q , Eq. (3.10) becomes

$$\begin{aligned} \Sigma_n = N^{-n} \sum_{Q_1 \dots Q_n} N \Delta \left(\sum_{j=1}^n \vec{q}_j \right) \delta \left(\omega - \sum_{j=1}^n \omega_{Q_j} \right) \\ \times \sum_{\gamma=\pm x} \sum_{\gamma'=\pm x} (\hat{x}_\gamma \cdot \hat{x}) (\hat{x}_{\gamma'} \cdot \hat{x}) \prod_{j=1}^n U_\gamma(Q_j) U_{\gamma'}^*(Q_j) \omega_{Q_j}^{-1} [n_{Q_j} + 1] . \end{aligned} \quad (3.11)$$

An examination of Eq. (3.6) reveals that the components of the Fourier transformed relative displacements in the positive and negative x directions are related by

$$U_{-x}(Q) = -U_x^*(Q) . \quad (3.12)$$

Using this result in the sums on γ , Eq. (3.11) can be written

$$\begin{aligned} \Sigma_n = N^{-n} \sum_{Q_1 \dots Q_n} N \Delta \left(\sum_{j=1}^n \vec{q}_j \right) \delta \left(\omega - \sum_{j=1}^n \omega_{Q_j} \right) \\ \times \left[\prod_{j=1}^n 2 |U_x(Q_j)|^2 \omega_{Q_j}^{-1} (n_{Q_j} + 1) \right] \left[1 + (-1)^{n+1} \cos \left(2 \sum_{j=1}^n \varphi_{Q_j} \right) \right] , \end{aligned} \quad (3.13)$$

where the x component of the Fourier transformed relative displacement has been written in terms of its magnitude and phase φ_Q :

$$U_x(Q) = w_{<Qx} - (m_{<}/m_{>})^{1/2} w_{>Qx} e^{i q_x a_{nn}} = |U_x(Q)| e^{i \varphi_Q}. \quad (3.14)$$

Writing Σ_n in Eq. (3.13) in terms of the magnitude and phase of $U_x(Q)$ puts Σ_n in a form in which the quasiselection rule is manifest. An examination of the polarization vectors of phonons throughout the Brillouin zone reveals that the phases of optical and acoustical phonons are approximately 0° and -90° , respectively. These approximate phases can be derived from either a simple diatomic linear lattice model or from more realistic three-dimensional models. Substitution of the phases in the cosine term of Eq. (3.13) yields the quasiselection rule that the fundamental Reststrahl phonon prefers to split into final states containing an odd number of optical phonons (transition matrix elements large). Final states containing an even number of optical phonons are less favored (transition matrix elements small). Other statements of the quasiselection rule are possible. It is stated in terms of the optical phonons in the final states since, as will be demonstrated later, those final states containing primarily optical phonons dominate the absorption spectrum. The quasiselection rule places no restriction on the number of acoustical phonons in the final state.

For example in the two-phonon region, the square bracketed term containing the cosine factor in Eq. (3.13) becomes $1 - \cos(180^\circ) = 2$ for an optical plus an acoustical final-state phonons. For two optical or two acoustical final-state phonons this term is approximately zero. In the three-phonon region, three optical final-state phonons yield $1 - \cos(540^\circ) = 2$ while two optical phonons

plus an acoustical phonon yield approximately $1 - \cos(360^\circ) = 0$. Hence quasiallowed final states are one optical phonon plus any number of acoustical phonons, three optical phonons plus any number of acoustical phonons, etc.

Departures of the phases from their idealized values prevent the quasi-selection rule from being exact, although typically there is a large degree of cancellation in the sum of the departures of the n phonons. For example, the exact two-phonon selection rule that the two final-state phonons cannot be on the same branch follows from the fact that the phases of the two phonons are equal and opposite because of equal and opposite momenta in spite of departures of the phases from their idealized values.

Crystal structures other than the rocksalt structure have not been examined yet. In other structures, such as the zincblende structure, the quasiselection rule derived here is not expected to be valid because the sum over nearest neighbors in Eq. (3.10) is expected to yield a different algebraic form than Eq. (3.13). The possibility of a different quasiselection rule in such crystals awaits further investigation.

The derivation of the phases of $U_x(Q)$ for acoustical and optical phonon branches using a diatomic linear lattice is instructive. Consider a diatomic linear lattice having spring constant C and nearest neighbor spacing a with light ions at positions $2sa$ and heavy ions at positions $(2s+1)a$, where s is an integer. Analogous to Eq. (3.7) the displacements of the light and heavy ions for standing-wave normal modes are written

Sec. G

$$u_{2s} = m_{<}^{-1/2} w_{<} \cos [2sqa] \quad (3.15)$$

and

$$u_{2s+1} = m_{>}^{-1/2} w_{>} \cos [(2s+1)qa] \quad (3.16)$$

The relative displacement of ions within a unit cell is

$$\begin{aligned} u_{2s} - u_{2s+1} &= m_{<}^{-1/2} \operatorname{Re} \left[w_{<} - (m_{<}/m_{>})^{1/2} w_{>} e^{iqa} \right] e^{i2sqa} \\ &= m_{<}^{-1/2} |U_x(Q)| \cos [2sqa + \phi_Q] \quad (3.17) \end{aligned}$$

where Re denotes the real part. The quantity within the square bracket of Eq. (3.17) is identical to $U_x(Q)$ in Eq. (3.14). Components $w_{<}$ and $w_{>}$ of the normalized polarization vector are obtained from the equation of motion and have the ratio

$$w_{<}/w_{>} = (2C\sqrt{m_{<}}/\sqrt{m_{>}}) \cos qa / (2C - \omega^2 m_{<}) \quad (3.18)$$

where ω is the frequency of the normal mode obtained from

$$\omega^2 = C/m_r \pm C \left[1/m_r^2 - (4/m_{<} m_{>}) \sin^2 qa \right]^{1/2} \quad (3.19)$$

The displacements of the ions from their equilibrium positions are plotted at the top of Fig. 2 for acoustical and optical normal modes of a diatomic chain having equal mass positive and negative ions. The relative displacements of the ions within each unit cell, obtained by taking the difference of heavy and light ion displacements and referencing the difference to the light ion position,

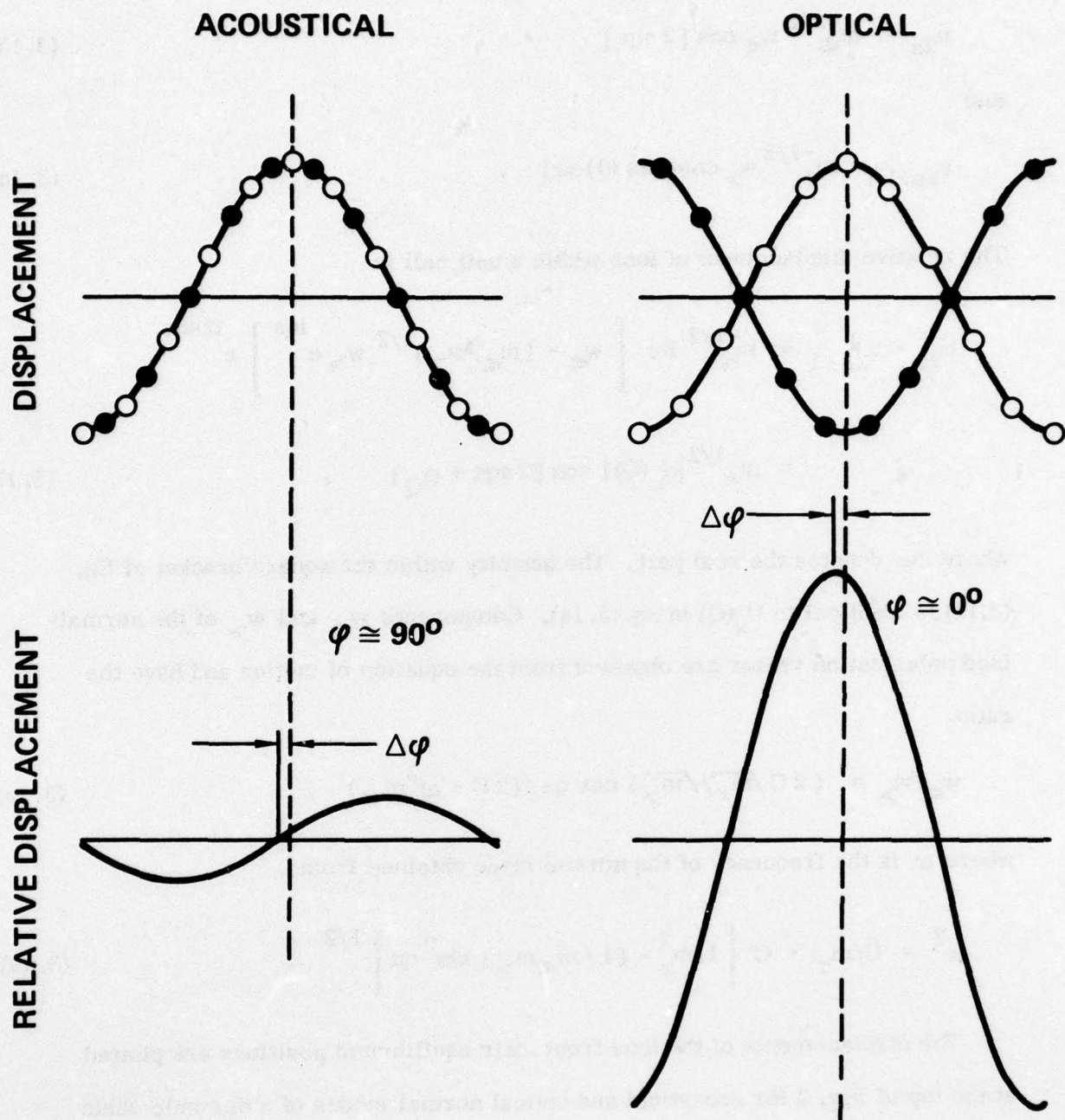


Fig. 2. Ion displacements for acoustical and optical normal modes of a linear diatomic lattice with ions of equal mass, upper curves. Relative displacement of ions, lower curves. The relative displacement curve for the optical mode is approximately in phase with the ion displacements, while the relative displacement curve for the acoustical mode is spatially displaced approximately 90° .

are plotted at the bottom of Fig. 2. Notice that the relative displacement curve for the optical mode is approximately in phase with the displacements, while the relative displacement curve for the acoustical mode is spatially displaced approximately 90° with the two relative displacement curves having a mutual spatial displacement of 90° . The departure $\Delta\varphi$ of the spatial phases from the idealized values of 0° and -90° results from the lattice spacing being finite compared to the normal-mode wavelength.

In Fig. 3 the optical and the acoustical spatial phases are plotted as functions of the normal-mode wave number for four heavy to light ion mass ratios. The magnitude of the departure of the phase from the idealized value depends on the mass ratio and the position in the Brillouin zone. The idealized phase values are attained at the center and edge of the zone for all mass ratios, and are attained throughout the Brillouin zone for an infinite mass ratio. The maximum departure occurs for equal masses near the zone boundary.

Often the sum of the departures of the spatial phases from their idealized values is small or zero. In the diatomic linear lattice model the quasiselection rule is exact (sum departures zero) for the following cases: 1) For two final-state phonons the phase departures of the two phonons are equal and opposite because of momentum conservation. 2) For crystals having positive and negative ions of equal mass, the linear dependence of the spatial phase on phonon momentum yields a zero sum for all numbers of final-state phonons if the momenta sum to zero. (For the less likely cases where three or more final-state phonons sum to an odd-numbered reciprocal lattice vector, an exact violation of the quasiselection rule results.) 3) For crystals having an infinite mass ratio between heavy and light ions there is zero deviation from the idealized phases.

AD-A034 088

XONICS INC SANTA MONICA CALIF

THEORETICAL STUDIES OF HIGH-POWER ULTRAVIOLET AND INFRARED MATE--ETC(U)

JUN 76 M SPARKS, C J DUTHLER

F/G 20/6

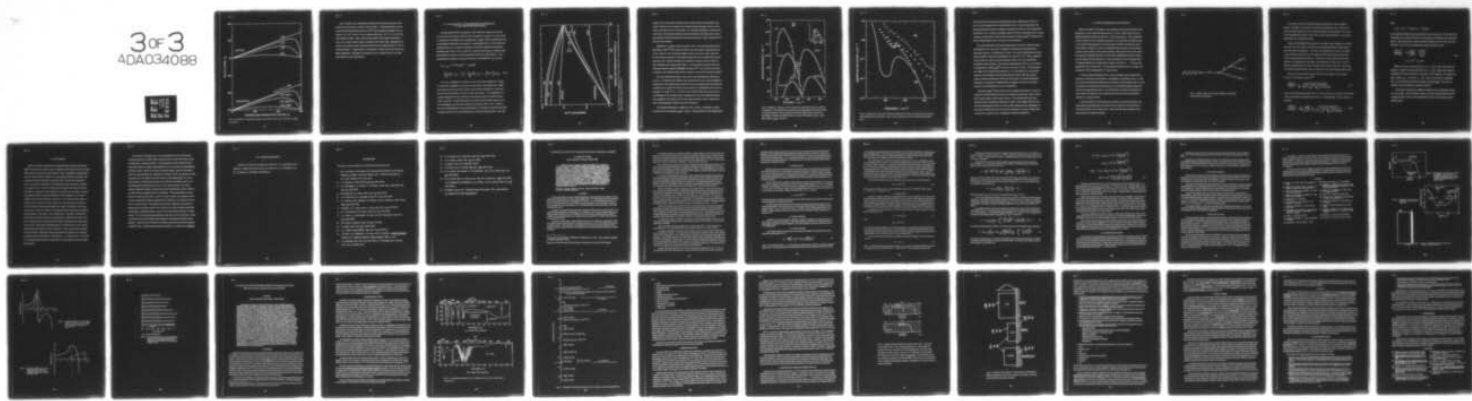
DAHC15-73-C-0127

NL

UNCLASSIFIED

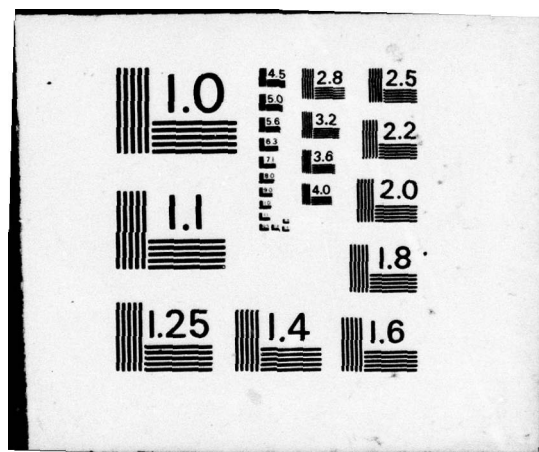
3 of 3
ADA034088

REF FILE



END

DATE
FILMED
2 -77



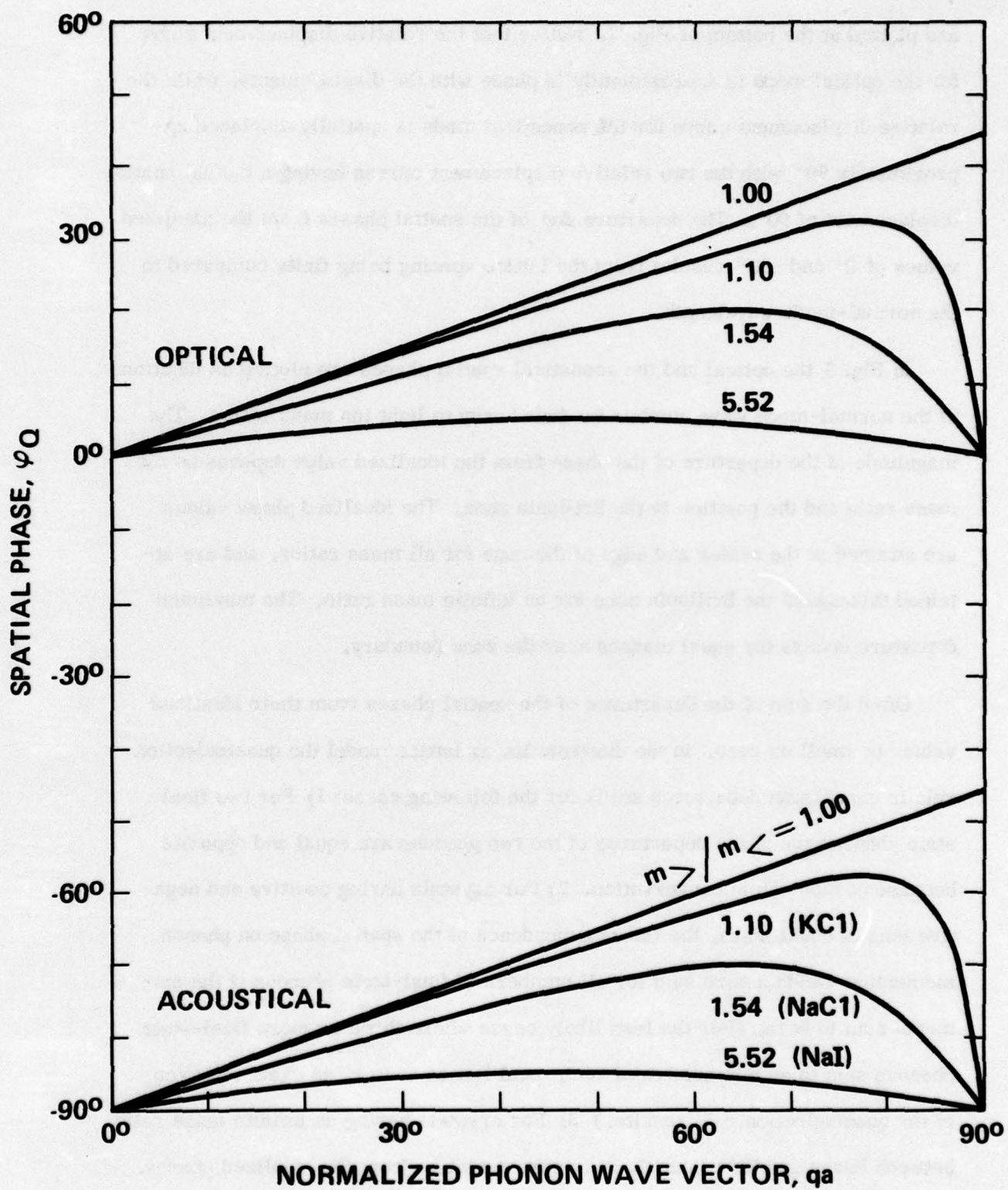


Fig. 3. Dependence of the spatial phase on the phonon wave vector and heavy to light ion masses.

More realistic three-dimensional models yield momentum and mass ratio dependent spatial phases similar to those in Fig. 3. Using polarization vectors from the deformable dipole model for Na^{18} the following mean phases are obtained: 2.8° , 2.8° , and 3.9° for the optical modes and -74° , -71° , and -65° for the acoustical modes. These values for the optical modes agree with those in Fig. 3 for a linear diatomic lattice having the same mass ratio, although the departure of the phases of the acoustical modes from the idealized value of -90° is somewhat larger. A large degree of cancellation is again found in the sum of the phase departures, although the cancellation is now complete only for two final-state phonons on the same branch.

IV. CALCULATION OF THE ANHARMONIC CONTRIBUTION TO THE ABSORPTION COEFFICIENT

The perturbation-theory calculation of the relaxation frequency from Eqs. (3.9) and (3.13) is greatly simplified if the magnitude of $U_x(Q_j)$ for a given branch is replaced by the Brillouin zone averaged value $U_x(b_j)$. (This is equivalent to neglecting phonon momentum conservation.) Assuming that this is valid and that the quasiselection rule is exactly satisfied, the extremely complicated momentum-dependent sum in Eq. (3.13) is reduced to a thermal and frequency weighted multi-phonon density of states in which the phonon branches are kept distinct. For a quasiallowed combination of phonon branches, the contribution to Σ_n becomes

$$\Sigma_{b_1 \dots b_n} = 4N^{-n} |U_x(b_1)|^2 \dots |U_x(b_n)|^2 \times \left\{ \sum_{\vec{q}_j} \omega_{Q_j}^{-1} [n_{Q_j} + 1] \right\} \dots \left\{ \sum_{\vec{q}_j} \omega_{Q_j}^{-1} [n_{Q_j} + 1] \right\} \delta(\omega - \sum_{j=1}^n \omega_{Q_j}) . \quad (4.1)$$

The error resulting from taking the mean value of the magnitude of $U_x(Q_j)$ is small if the magnitude is insensitive to position in the Brillouin zone. Magnitudes obtained from the linear diatomic chain model are plotted as a function of normal mode wavenumber in Fig. 4 for four mass ratios. The assumption of a constant magnitude is best satisfied for the optical branch of crystals having a large mass ratio. Acoustical branches of crystals having equally massive positive and negative ions are most sensitive to the phonon wave vector. However, the error resulting from the strong dependence of $|U_x(Q_j)|$ of acoustical branches on phonon wave vector is ameliorated by the following considerations: First, the

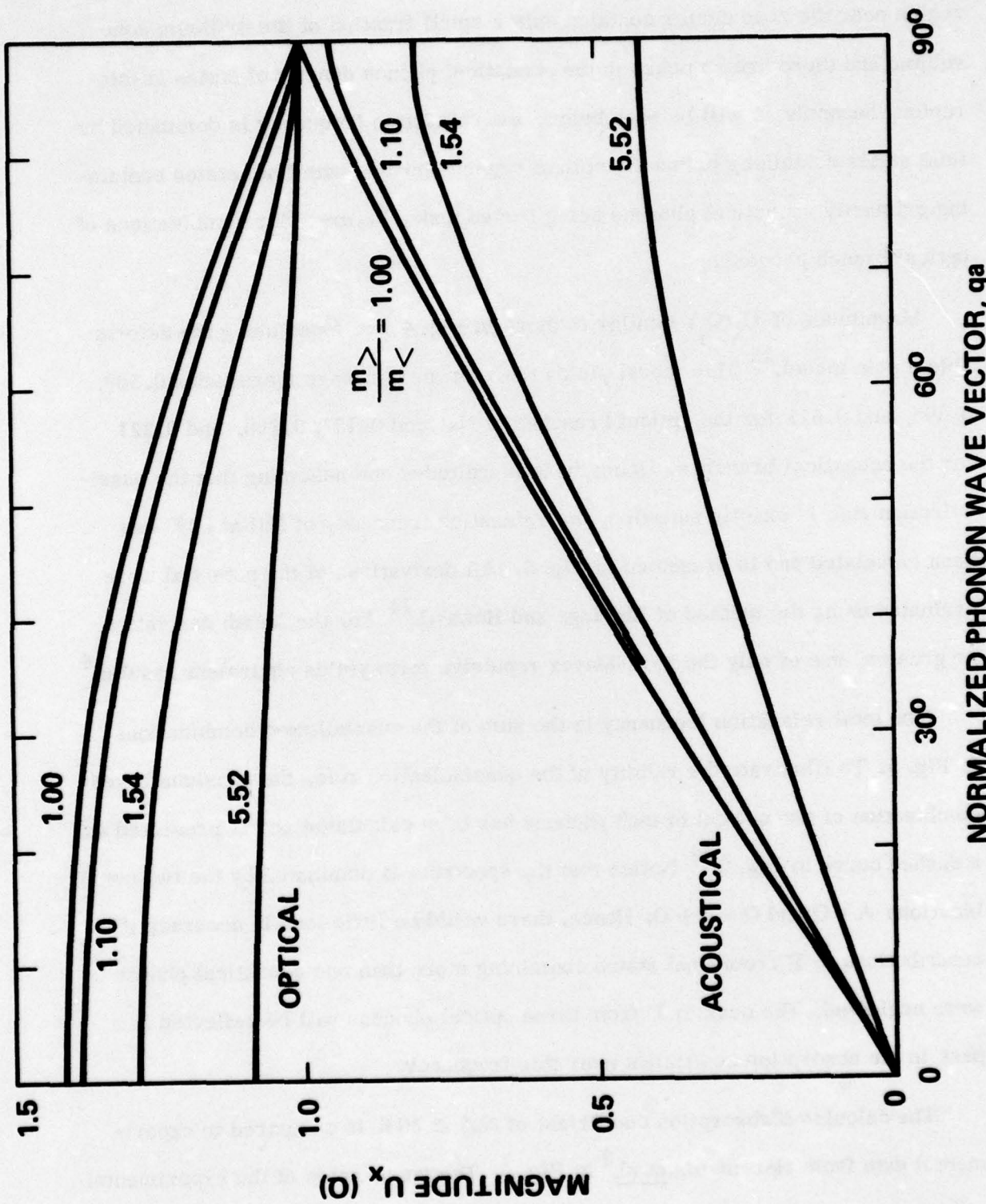


Fig. 4. Dependence of the magnitude of the Fourier transformed relative displacement on the phonon wave vector and heavy to light ion mass ratio.

region near the zone center contains only a small fraction of the Brillouin zone volume and there are no peaks in the acoustical phonon density of states in this region. Secondly as will be seen below, the relaxation frequency is dominated by final states containing primarily optical branch phonons with final states containing primarily acoustical phonons being buried under lower-order combinations of optical branch phonons.

Magnitudes of $U_x(Q_j)$ similar to those in Fig. 4 are found using the deformable dipole model.¹⁸ This model yields the root mean square magnitudes 0.589, 0.595, and 0.611 for the optical branches of NaI and 0.137, 0.188, and 0.221 for the acoustical branches. Using these magnitudes and assuming that the quasi-selection rule is exactly satisfied, the relaxation frequency of NaI at 80 K has been calculated and is presented in Fig. 5. All derivatives of the potential were evaluated using the method of Eldridge and Howard.¹⁴ For the fourth derivative, or greater, use of only the Born-Mayer repulsive term yields equivalent results.⁴

The total relaxation frequency is the sum of the quasiallowed combinations in Fig. 5. To illustrate the validity of the quasiselection rule, the quasiunallowed combination of two optical branch phonons has been calculated and is presented as a dashed curve in Fig. 5.¹² Notice that the spectrum is dominated by the two combinations A + O and O + O + O. Hence, there would be little loss in accuracy if contributions to Γ from final states containing more than one acoustical phonon were neglected. The peak in Γ from three optical phonons will be reflected in a peak in the absorption coefficient near this frequency.

The calculated absorption coefficient of NaI at 80 K is compared to experimental data from Harrington *et al.*³ in Fig. 6. The frequencies of the experimental

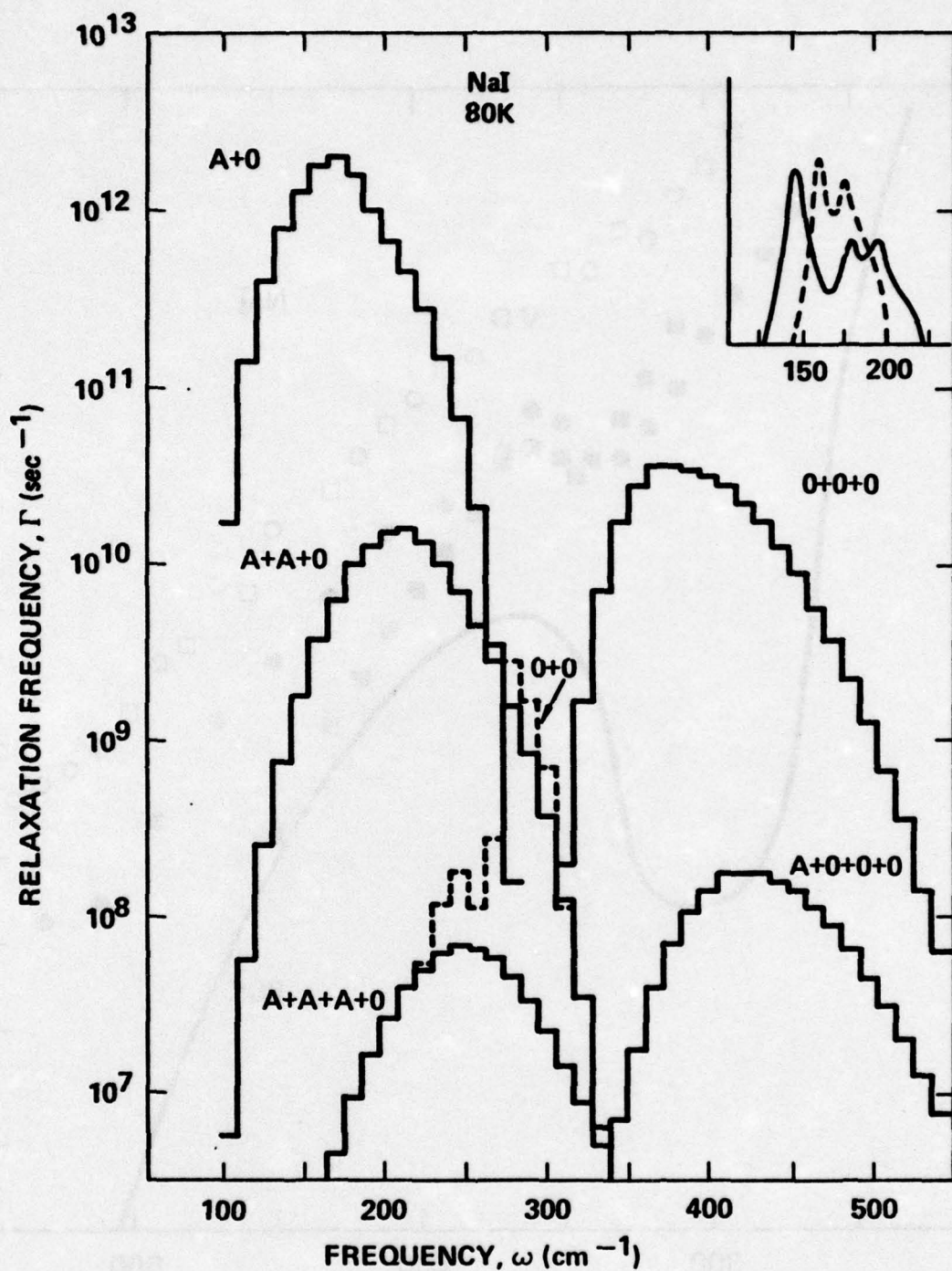


Fig. 5. Relaxation frequency of the fundamental Reststrahl mode as a function of frequency. The dashed curve presents the quasiunallowed contribution from two optical phonons. Inset presents the spectral width function of the zero-momentum LO phonon at 300 K (solid curve) and 90 K (dashed curve). (Inset after Cowley, et al., Ref. 20.)

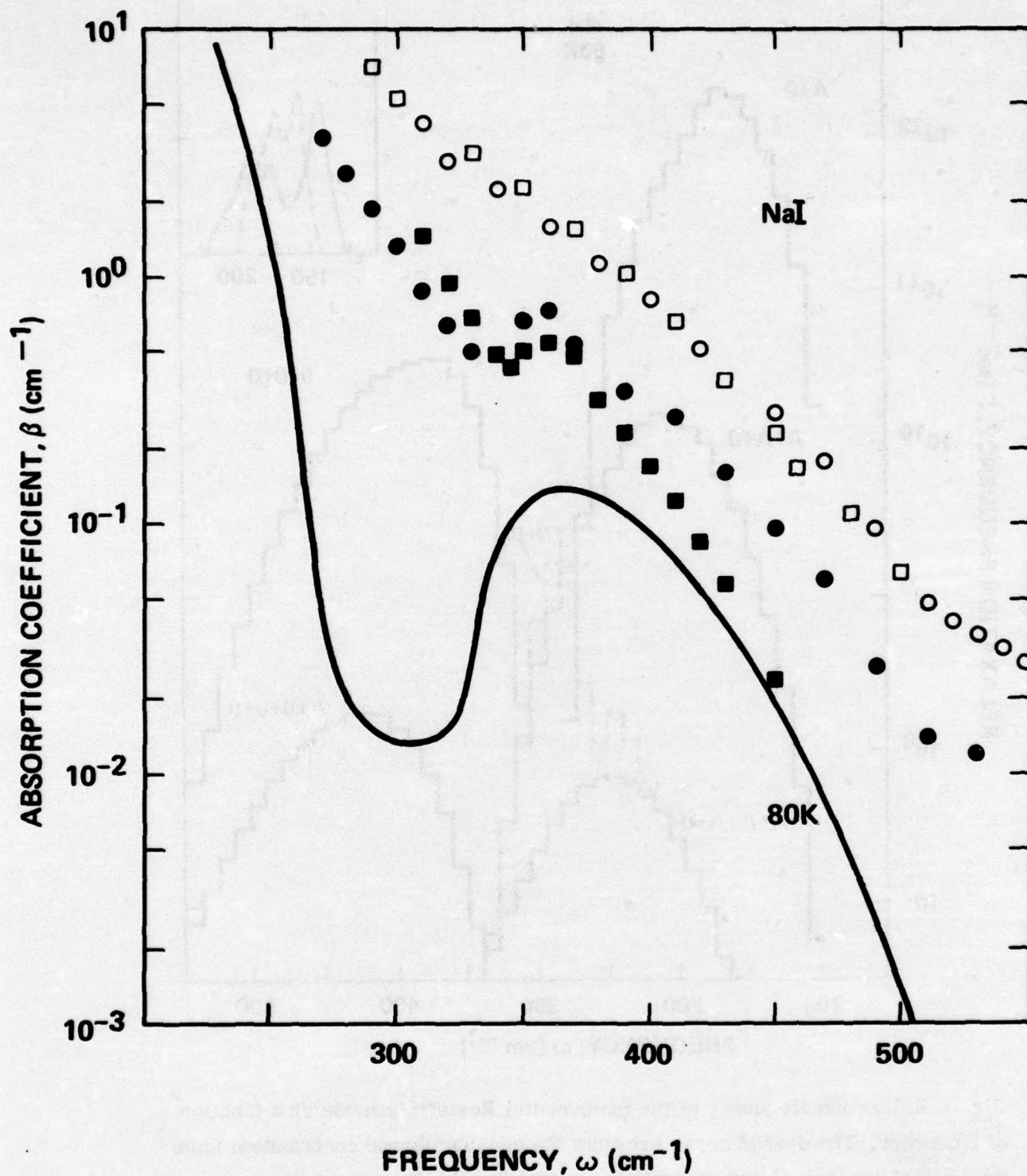


Fig. 6. Comparison of the 80 K theoretical absorption coefficient (solid curve) to the 80 K data (solid circles and squares). Open circles and squares present 300 K experimental data.

and theoretical three-phonon summation bands agree, although the theoretical curve is much sharper than the experimental curve. At room temperature the experimental peak is almost completely smoothed out while the room temperature theoretical curve is nearly as strongly peaked as the low-temperature curve. Using a density of states from a shell-model calculation of Cowley *et al.*¹⁹ yields an even more strongly peaked curve at nearly the same frequency.

The increased width in the experimental peak is not due to violations of the quasiselection rule, but rather is thought to result from the linewidth of the final-state phonons. In calculating Γ in Fig. 5 it is tacitly assumed that the final-state linewidth is less than the histogram bin width of 11 cm^{-1} . This is satisfied for the acoustical and some optical phonons at 80 K , but is not satisfied for longitudinal-optical phonons. The spectral width function of the $q = 0$, LO phonon as calculated by Cowley *et al.*²⁰ is shown in the inset in Fig. 5. The large spectral width of the LO phonons broadens the O + A contribution to Γ on the high frequency side and fills in the sharp dip between the two- and three-phonon regions. Beside broadening the 80 K theoretical peak, the strong temperature dependence of the spectral width function is thought to account for the disappearance of the distinct peak at room temperature.

Harrington *et al.*³ observe that the three-optical-phonon peak is most pronounced in crystals having a large heavy to light ion mass ratio. Such crystals have frequency gaps in their phonon spectra. Consequently they have more structure in their multiphonon densities of states. This together with the facts that the idealized phase values are more nearly attained and the magnitudes of the relative displacements are more nearly constant in the case of large mass ratios, favors structure in the multiphonon absorption coefficient.

V. VERTEX RENORMALIZATION FACTORS

Sparks and Sham⁴ treat higher-order diagrams involving intermediate-state phonons as a vertex renormalization factor Λ_n to the simple vertex where the fundamental phonon splits directly into n final-state phonons. The contribution of these diagrams to the relaxation frequency can be explicitly calculated using a more general quasiselection rule and the above method of calculation where mean values of $|U_x(Q)|$ are used. Perturbation-theory analysis of the general n phonon vertex yields a cosine factor similar to that in Eq. (3.13) from which a more general quasiselection rule is derived that quasiallowed vertices contain an even number of optical phonons. In this more general case incoming as well as outgoing phonons are counted and the number and wave vectors of the incoming phonons are not restricted. The previously considered case of a single zero momentum, TO incoming phonon is a special case.

For three final-state phonons there is only one higher-order diagram containing an intermediate-state phonon. This diagram is sketched in Fig. 7. At the first vertex the fundamental phonon must split into an optical phonon plus an acoustical phonon with splitting into two optical or two acoustical phonons being unallowed by the quasiselection rule. The intermediate-state phonon, labeled by m , can be either the optical or the acoustical phonon with the final-state phonon, labeled by l , being the other.

In the case where the intermediate-state phonon is the optical phonon, the above general quasiselection rule requires that it split into an optical plus an acoustical phonon at the second vertex. Hence the final state consists of one optical plus two acoustical phonons.

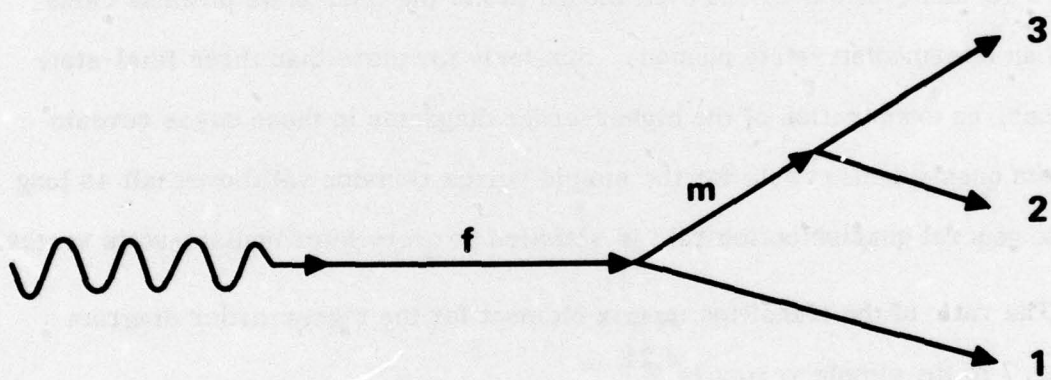


Fig. 7. Higher-order three-phonon diagram involving an intermediate-state phonon.

In the other case where the intermediate-state phonon is the acoustical phonon, this phonon is allowed by the general quasiselection rule to decay into either two optical phonons or two acoustical phonons at the second vertex. Hence the two possible final states in this case are three optical phonons or one optical phonon plus two acoustical phonons.

These two quasiallowed final states for the higher-order diagram are exactly the same as for the simple vertex where the fundamental phonon splits directly into three final-state phonons. Therefore the quasiselection rule for the simple vertex remains valid over-all even though two of the final-state phonons came from an intermediate-state phonon. Similarly for more than three final-state phonons, an examination of the higher-order diagrams in these cases reveals that the quasiselection rule for the simple vertex remains valid over-all as long as the general quasiselection rule is satisfied at every intermediate-state vertex.

The ratio of the transition matrix element for the higher-order diagram in Fig. 7 to the simple vertex is^{4,21}

$$\frac{\langle f | \mathcal{K}'_3 | i \rangle}{\langle f | \mathcal{K}_3 | i \rangle} = \sum_{b_m} \frac{4\omega_m V(fQ_m Q_1) V(Q_m Q_2 Q_3)}{3\hbar[(\omega - \omega_{Q_1})^2 - \omega_{Q_m}^2] V(fQ_1 Q_2 Q_3)} , \quad (5.1)$$

where for fixed initial and final states it is only necessary to sum over the branches of the intermediate-state phonon denoted by m. Evaluating the vertices, Eq. (5.1) becomes

$$\frac{\langle f | \mathcal{K}'_3 | i \rangle}{\langle f | \mathcal{K}_3 | i \rangle} = \frac{4}{9^m} \frac{[\phi^{(3)}]^2}{[\phi^{(4)}]} \sum_{b_m} \frac{\alpha(fQ_m Q_1) \alpha(Q_m Q_2 Q_3)}{[(\omega - \omega_{Q_1})^2 - \omega_{Q_m}^2] \alpha(fQ_1 Q_2 Q_3)} , \quad (5.2)$$

where

$$\alpha(Q_1 \cdots Q_n) = 2 |U_x(Q_1)| \cdots |U_x(Q_n)|$$

for quasiallowed diagrams and approximately zero otherwise. For the final state consisting of three optical phonons the intermediate-state phonon is an acoustical phonon. Approximating the square bracketed frequency term by $4\omega_f^2$ and multiplying by 3 for the three quasiallowed acoustical branches yields

$$\frac{\langle f | x'_3 | i \rangle}{\langle f | x_3 | i \rangle} = \frac{2}{3} \frac{[\phi^{(3)}]^2}{[\phi^{(4)}]} \frac{|U_x(A)|^2}{m \omega_f^2} \quad (5.3)$$

$$= 1.5 \times 10^{-2} \quad \text{for NaI} \quad .$$

Hence the vertex correction factor is $\Lambda_3 = 1.015$ which implies that the quantity ξ defined by Sparks and Sham⁴ is $\xi = 0.020$. Rather than explicitly evaluating the vertex corrections to the higher-order diagrams, this quantity is used to obtain $\Lambda_4 = 1.04$ and $\Lambda_5 = 1.08$. These corrections are negligible. They are much smaller than those obtained by McGill et al.⁶ and are even smaller than those obtained by Sparks and Sham.⁴

Corrections arising from confluence diagrams in the multiphonon region are still smaller. Since confluence diagrams contain predominantly incoming acoustical phonons, the over-all quasiselection rule for allowed final states remains valid.

VI. CONCLUSIONS

Many of the basic assumptions and approximations made by Sparks and Sham⁴ remain in the present paper, although several improvements have been made and new results have been obtained. These assumptions and approximations are summarized as follows: (1) As justified by Sparks and Sham,⁴ the perturbation-theory approach is assumed valid. (2) Only the anharmonic-lattice mechanism is included in the calculation of the absorption coefficient. It is argued in Sec. II that the inclusion of the higher-order dipole-moment mechanism is expected to only change the strength of the interaction, leaving the phonon dynamics and the quasiselection rule unchanged. (3) A nearest-neighbor central-force potential is assumed. Use of only the Born-Mayer repulsive term for three, or more, phonons is convenient, but not essential. (4) The lifetimes of final-state phonons are taken to be infinite in the calculated curves. However, evidence is presented that the large spectral width of optical phonons, especially at room temperature, contributes considerable broadening to the theoretical curves bringing the calculated line shape of the three-optical-phonon summation band into better agreement with experiment. (5) An error in the Sparks and Sham paper,⁴ on which the use of the central-limit theorem was based, has been corrected. In the present paper multiple sums over phonon modes have been approximated by Brillouin zone averages in which the phonon branches are kept distinct. It is shown in Sec. IV that this is a reasonable approximation, especially for optical phonons which dominate the spectrum.

The results of this paper are: (1) A quasiselection rule is derived that infrared absorption in alkali halide crystals tends to create final states having an odd number of optical phonons. This quasiselection rule follows from the observation that the relative motion between ions in a unit cell is approximately spatially in phase with the ion motion for optical modes, while the acoustical modes are approximately 90° spatially out of phase with the ion motions. (2) The quasiselection rule explains the observations of Harrington *et al.*³ of a three-optical-phonon summation-band peak in the absorption coefficient with no corresponding peak being observed at two or four optical phonons. (3) Using a constant magnitude Fourier transformed relative displacement greatly reduces the effort of the perturbation-theory calculation. This approximation is justified by the demonstration that, at least for optical modes, the magnitude of the Fourier transformed relative displacement is insensitive to the phonon momentum for a given branch. This allows an extremely complicated momentum dependent sum over phonon modes to be reduced to an easily evaluated thermally and frequency weighted density of states in which the phonon branches are kept distinct. (4) A more general quasiselection rule allows easy evaluation of vertex correction factors from higher-order diagrams containing intermediate-state phonons. These factors are found to be smaller than those estimated by Sparks and Sham,⁴ and, in agreement with Sparks and Sham, are found to be negligible.

VII. ACKNOWLEDGMENTS

I thank Dr. M. Hass for bringing the data of Dr. J. A. Harrington to my attention. Helpful discussions with Dr. M. Hass, Dr. J. A. Harrington, and Dr. M. Sparks are gratefully acknowledged.

REFERENCES

* This paper will be published in *The Physical Review (in press)*.

1. See for example, "Proceedings of the International Conference on the Optical Properties of Highly Transparent Solids, 1975," edited by B. Bendow and S. S. Mitra (Plenum, New York, 1975).
2. T. F. Deutsch, *J. Phys. Chem. Solids* 34, 2091 (1973).
3. J. A. Harrington, C. J. Duthler, F. W. Patten, and M. Hass, *Solid State Commun.* 18, 1043 (1976).
4. M. Sparks and L. J. Sham, *Phys. Rev. B* 8, 3037 (1973).
5. D. L. Mills and A. A. Maradudin, *Phys. Rev. B* 8, 1617 (1973).
6. T. C. McGill, R. W. Hellwarth, M. Mangir, and H. V. Winston, *J. Phys. Chem. Solids* 34, 2105 (1973).
7. B. Bendow, S. C. Ying, and S. P. Yukon, *Phys. Rev. B* 8, 1679 (1973).
8. K. V. Namjoshi and S. S. Mitra, *Phys. Rev. B* 9, 815 (1974).
9. L. L. Boyer, J. A. Harrington, M. Hass, and H. B. Rosenstock, *Phys. Rev. B* 11, 1665 (1975).
10. M. Lax and E. Burstein, *Phys. Rev.* 97, 39 (1955).
11. R. Loudon, *Phys. Rev.* 137, A1784 (1965).
12. C. J. Duthler and M. Sparks, *Phys. Rev. B* 9, 830 (1974).
13. C. Smart, G. R. Wilkinson, A. M. Karo, and J. R. Hardy, in *Lattice Dynamics*, edited by R. F. Wallis (Pergamon, Oxford, England, 1965), p. 387.
14. J. E. Eldridge, *Phys. Rev. B* 6, 1510 (1972); J. E. Eldridge and R. Howard, *Phys. Rev. B* 7, 4652 (1973).

Sec. G

15. P. N. Keating and G. Rupprecht, *Phys. Rev.* 138, A866 (1965).
16. R. A. Cowley, *Advan. Phys.* 12, 421 (1963).
17. M. Sparks, *Phys. Rev. B* 10, 2581 (1974).
18. A. M. Karo and J. R. Hardy, *Phys. Rev.* 129, 2024 (1963).
19. R. A. Cowley, W. Cochran, B. N. Brockhouse, and A. D. B. Woods, *Phys. Rev.* 131, 1030 (1963).
20. E. R. Cowley and R. A. Cowley, *Proc. Roy. Soc. London, Ser. A* 287, 259 (1965); A. D. B. Woods, B. N. Brockhouse, R. A. Cowley, and W. Cochran, *Phys. Rev.* 131, 1025 (1963).
21. M. Sparks, Xonics, Inc. Technical Report, December 1972, under Contract No. DAHC15-72-C-0129 (unpublished).

H. IRRADIANCE LIMITS FOR VACUUM ULTRAVIOLET MATERIAL FAILURE*

C. J. Duthler and M. Sparks

Xonics, Incorporated, Van Nuys, California 91406

Calculated values of irradiance I at which materials fail in 7.2 eV pulses of 10 nsec duration by various mechanisms indicate that metallic mirrors melt at very low values, typically $I \approx 20 \text{ MW/cm}^2$. Improving the aluminum, which is the only good metallic vuv reflector, would increase I by a factor of only three. The lowest of the thresholds for transparent materials are $\sim 140 \text{ MW/cm}^2$ for the intrinsic reversible process of optical distortion caused by the conduction electrons generated by two-photon absorption and $\sim 200 \text{ MW/cm}^2$ for the intrinsic irreversible process of thermal fracture by two-photon absorption. Other thresholds are: $\sim 1 \text{ GW/cm}^2$ for fracture from enhanced stimulated Raman scattering in Raman-active materials; $\sim 1.6 \text{ GW/cm}^2$ for melting from two-photon absorption; $\sim 2 \text{ GW/cm}^2$ for optical distortion from the nonlinear refractive index (bound electrons); and $\sim 100 \text{ GW/cm}^2$ for thermal fracture from extrinsic one-photon absorption with $\beta = 0.1 \text{ cm}^{-1}$. Included in the calculations are the Joule heating by the generated electrons, which is greater than the direct heating by the absorption process, and electron-avalanche multiplication. Thermally induced optical distortion has a higher threshold than that for the optical distortion by generated conduction electrons.

Key words: Nonlinear index of refraction; optical distortion; thermal fracture; two-photon absorption.

I. Introduction

Our theoretical studies of materials damage by high-power, vacuum-ultraviolet (vuv) radiation were motivated by the successful operation of lasers in this wavelength region [1]¹. High output powers have been achieved from the rare-gas excimer lasers with wavelengths of 174 nm ($\hbar\omega = 7.2 \text{ eV}$) for the xenon laser [2], 146 nm (8.5 eV) for the krypton laser [3], and 126 nm (9.8 eV) for the argon laser [4]. At the present time there have been no experiments on materials damage in the vuv, other than that observed with the first lasers, which were materials limited [2,5].

The laser cavity-mode pattern was burned into the thin-film aluminum mirrors in these first lasers. The threshold irradiance (intensity) for this damage was $I \approx 20 \text{ MW/cm}^2$. Since orders-of-magnitude greater power would be feasible if suitable mirrors were available, there is great interest in obtaining improved reflectors. Transparent materials for high-power use as windows, lenses, reflecting devices, and other optical components are of even greater interest.

Consider the intrinsic limit for metallic reflectors in the vuv. For a metal to be a good reflector it must have a plasma frequency large compared to the frequency of interest, and it must not have interband transitions in the region of interest. These conditions are best satisfied in the vuv by aluminum. Silver and gold, which are commonly used in the visible and infrared, are transparent in the vuv since their plasma wavelengths are greater than 200 nm.

* This paper was published in NBS Special Publication No. 435, "Laser Induced Damage in Optical Materials: 1975."

¹ Figures in brackets indicate the literature references at the end of this paper.

Sec. H

The reflectance of aluminum as a function of frequency is shown in figure 1. In the infrared, values of the reflectance as large as 99 percent are obtained. Aluminum is somewhat anomalous in that it has interband transitions in the near infrared. With extreme care in sample preparation under exacting laboratory conditions, values of reflectance approaching 92 percent have been obtained from the visible to the vuv [6]. Below the plasma wavelength of 81.4 nm (15.2 eV), aluminum is transparent except for interband transitions.

Chow and Sparks [7] have shown that the 92 percent reflectance, observed with the best samples at 174 nm, is within two percent of the intrinsic limit. In commercially available mirrors the absorptance in the vuv typically is 20 percent or greater, as denoted by the dashed curves in figure 1. Mills and Maradudin [8] have studied these greater values of absorptance, which result from enhanced coupling to aluminum surface plasmons caused by a rough surface or rough Al_2O_3 or MgF_2 overcoating.

In view of the extreme difficulty of achieving the intrinsic reflectance limit of aluminum and considering the large absorptance at the intrinsic limit, significant improvements in the failure thresholds of metallic reflectors do not seem possible. Improved reflectance has been obtained using a stack of very thin aluminum layers separated by approximately one-quarter wave layers of MgF_2 [9]. The damage threshold of these multilayer structures remains to be investigated. However, even greater damage thresholds should be attainable from the use of transparent materials as multilayer dielectric reflectors, or as total internal reflection devices.

Problems of transparent materials for high-power vuv use also are severe. There are few materials with sufficiently great electronic band gap E_g to avoid the great linear absorption above the absorption edge. Those having the largest band gaps are ionic materials composed of light ions from the edges of the periodic table. Materials having E_g greater than 7.2 eV include: LiF (~13), MgF_2 (~11), KF (10.9), NaF (>10.5), RbF (10.4), CsF (10), LiCl (~10), CaF_2 (~10), SrF_2 (>9), BaF_2 (>9), NaCl (8.6), KCl (8.5), LiBr (~8.5), Al_2O_3 (8.3), RbCl (8.2), KBr (7.8), NaBr (7.7), SiO_2 (~7.7), and MgO (7.3). All transparent materials will suffer the effects of two-photon absorption at the xenon laser frequency. The 13 eV band gap of LiF, which is the largest band gap of all transparent solids, is less than twice the photon energy of the xenon laser with $2\hbar\omega_L = 14.4$ eV.

Many of these materials are not expected to be useful as practical high-power vuv windows. The alkaline-earth halides are superior to the alkali halides with respect to hygroscopic properties and fracture strengths. Sapphire and quartz have highly desirable chemical and mechanical properties, but their band gaps of 8.3 eV and 7.7 eV, respectively, are very close to the xenon laser photon energy of 7.2 eV. The steepness of the electronic absorption edge appears to allow their use as xenon laser windows unless further study reveals such effects as anomalous frequency dependence of the absorption coefficient or a large nonlinear refractive index.

For construction of dielectric reflectors, there is a paucity of large index materials so that it may be necessary to use moderately absorbing materials. The absorption coefficient of such materials as NdF_3 and LaF_3 needs further investigation.

Aged LiF can suffer increased absorption from vuv induced color centers. It is not yet known if two-photon absorption at 7.2 eV will result in similar creation of color centers in LiF or other materials.

The frequency dependence of the linear absorption coefficient β of such ionic materials as alkali halides is shown schematically in figure 2. In the infrared, the intrinsic absorption mechanism is the creation of phonons which results in a large peak in β at the reststrahl frequency followed by a broad, exponentially decreasing multi-phonon tail. At the CO_2 laser frequency many materials are impurity limited with absorption coefficients as low as 10^{-4} cm^{-1} being obtained. In the ultraviolet the intrinsic absorption mechanism is the excitation of electrons from the valence band to the conduction band. In contrast to the infrared, the electronic "Urbach tail" is relatively sharp (typically $\sim 10^8 \text{ cm}^{-1}/\text{eV}$ for the rate of reduction of the absorption coefficient β) so that materials can be used close to the edge without suffering excessive linear intrinsic absorption.

Presently available materials have extrinsic absorption coefficients ranging from 0.1 to 1 cm^{-1} for vuv frequencies below the intrinsic absorption edge [10]. Even though these values are quite large, improving the

materials to reduce the linear absorption will not result in a greater threshold for the case of a single 10 nsec pulse, unless the one-photon induced optical-distortion mechanism of section 3D is operative. Even then, the threshold would be increased from $\sim 60 \text{ MW/cm}^2$ to only $\sim 140 \text{ GW/cm}^2$, which is set by the two-photon induced electron optical distortion. However, in cw or repeated pulse systems it is expected that lowering the value of β should increase the threshold substantially. If such systems become of interest, the present analyses could be extended easily to include these cases.

2. Metallic Reflectors

Materials damage in the first xenon lasers occurred with the laser cavity-mode pattern being burned into the thin-film aluminum mirrors. The mechanism for damage in this case can be understood with the aid of figure 3, where a cross section of one of the laser-cavity mirrors is sketched. The mirror consists of a coating of aluminum approximately 100 Å thick on a magnesium fluoride substrate. At the xenon-laser wavelength of 174 nm, commercially available aluminum reflectors typically have 20 percent absorptance, and the intrinsic limit is approximately 6 percent.

In order to determine the threshold for metallic-reflector damage, the surface temperature T of the mirror is calculated by dividing the energy absorbed $IA\alpha t$ by the volume of heated material αd . Here I is the incident irradiance, α the absorptance, A the surface area that is irradiated, t is the pulse duration, and $d = (\pi K t / 4 C)^{1/2} = 2 \times 10^{-5} \mu\text{m}$ (for a 10 nsec pulse in MgF_2) is the thermal diffusion depth. Also, K is the thermal conductivity and C the heat capacity per unit volume. Equating this energy density $IA\alpha t / d$ to CT gives

$$T = (4t/\pi CK)^{1/2} IA . \quad (1)$$

Notice that the energy is absorbed in the thin aluminum film, while the volume of heated material is determined by the thermal diffusion into the magnesium fluoride.

For short pulse durations, failure occurs by melting of the aluminum film since aluminum has a lower melting point than MgF_2 , and thermal stresses in the small volume of heated material are insufficient to cause fracture. Using $\alpha = 0.2$, $K = 0.11 \text{ W/cm K}$, and $C = 4.1 \text{ J/cm}^3 \text{ K}$ in eq. (1) yields a failure intensity of 20 MW/cm^2 . The failure intensity decreases as the square root of the pulse duration, while the power density increases as $t^{1/2}$.

3. Transparent Materials

In addition to use in thin-film dielectric reflectors, transparent materials are of course needed for windows, lenses, and other optical components. Single-shot thresholds are calculated in the following for failure of bulk transparent materials by various mechanisms. These bulk thresholds can be used as a guide for thin films or for multiple shots.

A. Two-Photon Absorption

The two-photon absorption coefficient β_2 can be calculated using golden-rule perturbation theory which yields the formal expression [11, 12]

$$\beta_2 = \frac{4\pi\epsilon^{1/2}}{\hbar c n_L} \sum_f \sum_h \delta(E) \left| \sum_h \frac{X_{fh} X_{hi}}{E_f - E_h - \hbar\omega} \right|^2 . \quad (2)$$

where ϵ is the dielectric constant, n_L is the laser-photon occupation number, and $\delta(E)$ is an energy-conserving delta function. In eq. (2), X_{fh} and X_{hi} are matrix elements of the interaction Hamiltonian (which can be written

Sec. H

in terms of dipole matrix elements) between the initial state *i* (valence band) or the final state *f* (conduction band) and an intermediate state *h*. The matrix elements are summed over all possible initial, final, and intermediate states that conserve over-all energy. Possible intermediate states are higher conduction bands, exciton levels, lower valence bands, and the conduction band itself with intra-band transitions.

Present knowledge of the band structure of large-band-gap insulators, even LiF, is insufficient to predict which intermediate states are dominant or to calculate the two-photon absorption coefficient to better than an order-of-magnitude accuracy. Tentatively, it appears that a lower valence band may be the dominant intermediate state for LiF at the xenon-laser frequency. Simple arguments indicate that two-photon absorption is parity forbidden at the absorption edge in LiF. For slightly larger energies, two-photon absorption is allowed. Neglecting the wave-vector dependence of the transition matrix elements gives the frequency dependence $\beta_2 = \beta_{20} (\omega - \omega_g/2)^{1/2}$, where β_{20} is constant and $\hbar\omega_g$ is the band gap. This approximate frequency dependence, which is obtained from the joint density of states of parabolic conduction and valence bands, agrees qualitatively with experimental results for two-photon absorption coefficient in heavier alkali halides [13].

The two-photon absorption coefficient is proportional to the intensity and can be written formally as

$$\beta_2 = (I/I_0) 1 \text{ cm}^{-1} . \quad (3)$$

At the xenon-laser frequency in LiF, an order-of-magnitude estimate of the characteristic intensity at which $\beta = 1 \text{ cm}^{-1}$ is $I_0 = 1.2 \text{ GW/cm}^2$ [12].

B. Optical Distortion

There are two nonlinear mechanisms for optical distortion in the vacuum ultraviolet. First, the process of two-photon absorption creates conduction electrons, which in turn, can scatter incident radiation. The second mechanism is the usual nonlinear index, n_2 , of the bound electrons in the solid, which is the dominant mechanism for optical distortion and catastrophic self focusing in infrared Nd-glass lasers. In the vicinity of two-photon absorption bands, the nonlinear index can be resonantly enhanced. The two mechanisms are not independent since n_2 is obtained from the real part of the third-order susceptibility, and two-photon absorption from the imaginary part.

The change in the refractive index from conduction electrons created by two-photon absorption is estimated using the Drude-theory result

$$\delta n = -\omega^2/2 n_0 \omega_p^2 . \quad (4)$$

where

$$\omega_p^2 = 4\pi N e^2 / m .$$

In eq. (4), ω_p^2 is the plasma frequency, e is the electronic charge, m is the reduced effective mass of the electrons, and n_0 is the linear refractive index. At the threshold for optical distortion, the number of free carriers is approximately equal to the integrated number of photons absorbed, neglecting relaxation, although the number is slightly larger as a result of electron-avalanche creation of additional pairs.

Our criterion for optical distortion is that the change in the optical path length at the center of the beam is 1/8 wave:

$$\lambda/8 = (\delta n) z , \quad (5)$$

where z is the thickness of the material, which is taken to be 1 cm. Using the absorption coefficient in eq. (3) for LiF yields the free carrier threshold intensity $I = 160 \text{ MW/cm}^2$ for a 10 nsec duration xenon-laser pulse.

Sec. H

The change in the refractive index from the nonlinear index of bound electrons is $\delta n = n_2 E^2$, where E is the rms electric field. The typical value of $n_2 = 10^{-13}$ esu, observed in the visible and infrared, yields a threshold of $I = 7 \text{ GW/cm}^2$ for optical distortion. However, resonant enhancement of n_2 by two-photon absorption in the uv reduces this threshold.

A simple model of the nonlinear index that preserves much of basic physics has been considered by Fournier and Snitzer. [14] This model considers a solid composed of noninteracting molecules having three electronic levels. The nonlinear index in this case is

$$n_2 = \frac{4\pi N}{n_0} \left(\frac{n_0 + 1}{3} \right)^4 \frac{e^4}{h^3} \left(\frac{n}{2m} \right)^2 \frac{f_{01} f_{12}}{\omega_{12} (\omega^2 - \omega_0^2)^2} \left[\frac{(\omega_0^2 + 5\omega^2)}{(\omega_0^2 - 4\omega^2)} + 2 \right] . \quad (6)$$

where n_0 is the linear refractive index, $\hbar\omega_0$ is the energy of the electronic excited states, $\hbar\omega_{12}$ is the energy difference of the excited states, and f_{01} and f_{12} are the oscillator strengths for the transitions between subscripted levels. Since our primary interest is in the frequency dependence of n_2 , eq. (6) is written in terms of the low frequency nonlinear index n_{20} :

$$n_2 = \frac{1}{3} n_{20} \frac{\omega_0^4}{(\omega^2 - \omega_0^2)^2} \left[\frac{(\omega_0^2 + 5\omega^2)}{(\omega_0^2 - 4\omega^2)} + 2 \right] . \quad (7)$$

Methods of estimating n_{20} from linear optical constants have been proposed [14, 15].

The first term within the square brackets of eq. (7) has a resonance at one-half the one-photon absorption frequency ω_0 . The nonlinear index is plotted as a function of frequency from eq. (7) in figure 4. In the absence of damping very large values of n_2 would be obtained near $\omega_0/2$. To keep n_2 finite, a small amount of damping has been added, which leads to a broadened two-photon absorption line at $\omega_0/2$ shown by the dashed curve in figure 4.

The molecular model is not realistic for solids such as alkali halides, which have broad two-photon absorption bands. For LiF, two-photon transitions from the valence band to the lowest conduction band extend from $\omega_g/2$ to approximately ω_g . To estimate the frequency dependence of n_2 in this case, eq. (7) is integrated over a distribution of oscillator frequencies having density $(\omega - \omega_g)^{1/2}$, which yields

$$n_2 = n_{20} \frac{1}{2(\omega_m - \omega_g)^{3/2}} \int_{\omega_g}^{\omega_m} \frac{\omega^4 (\omega' - \omega_g)^{1/2}}{(\omega^2 - \omega'^2)^2} \left[\frac{(\omega^2 + 5\omega^2)}{(\omega'^2 - 4\omega^2)} + 2 \right] d\omega' . \quad (8)$$

This integral is approximated by replacing ω' in the slowly varying terms of the integrand by ω_g , which gives

$$n_2 = \frac{2}{3} n_{20} \frac{\omega_g^4}{(\omega^2 - \omega_g^2)^2} + \frac{1}{2} n_{20} \frac{\omega_g^4 (\omega_g^2 + 5\omega_g^2)}{(\omega_m - \omega_g)^{3/2} (\omega^2 - \omega_g^2)^2} \int_{\omega_g}^{\omega_m} \frac{(\omega' - \omega_g)^{1/2} d\omega'}{(\omega'^2 - 4\omega^2)} . \quad (9)$$

Notice that eq. (9) has the form of a Kramers-Kronig integral over the two-photon absorption band. Even though the individual oscillators diverge at one-half the resonant frequency, the integral over the oscillators remains finite, except at ω_g , and has the value

Sec. H

$$J(\omega < \omega_g/2) = \frac{1}{2\omega} (\omega_g + 2\omega)^{1/2} \tan^{-1} \left[\left(\frac{\omega_m - \omega_g}{\omega_g + 2\omega} \right)^{1/2} \right]$$

$$- \frac{1}{2\omega} (\omega_g - 2\omega)^{1/2} \tan^{-1} \left[\left(\frac{\omega_m - \omega_g}{\omega_g + 2\omega} \right)^{1/2} \right]$$

and

$$J(\omega_g/2 < \omega < \omega_g) = \frac{1}{2\omega} (\omega_g + 2\omega)^{1/2} \tan^{-1} \left[\left(\frac{\omega_m - \omega_g}{\omega_g + 2\omega} \right)^{1/2} \right]$$

$$- \frac{1}{2\omega} (2\omega - \omega_g)^{1/2} \ln \left| \frac{(2\omega - \omega_g)^{1/2} + (\omega_m - \omega_g)^{1/2}}{(2\omega - \omega_g)^{1/2} - (\omega_m - \omega_g)^{1/2}} \right| \quad (10)$$

The nonlinear index obtained from eqs. (9) and (10) is plotted as a function of frequency in figure 5. The maximum positive value of $n_2 \approx 3n_{20}$ occurs at $\omega_g/2$. As the frequency increases, n_2 passes through zero (no optical distortion) and attains large negative values near ω_g . However, close to ω_g , one-photon effects will dominate. The xenon-laser frequency equals $0.55\omega_g$ in LiF. Using $n_2 = 3n_{20}$ with $n_{20} = 10^{-13}$ esu yields a threshold of $I = 2 \text{ GW/cm}^2$ for optical distortion in LiF. This is a factor of 12 greater than the estimated threshold for optical distortion from conduction electrons.

Although optical distortion from the nonlinear index of bound electrons is negligible at the xenon-laser frequency in LiF, there are other cases for which it may be important. The degree of resonance enhancement at $\omega_g/2$ increases with decreasing two-photon absorption band width. If a material has a strong sharp two-photon absorption band with the laser frequency adjacent to, but not within, the band, two-photon creation of free carriers will not occur, and the nonlinear index will be considerably enhanced. Large negative values of n_2 are predicted for ω just below ω_g for broad-band materials. This negative value of n_2 could yield strong nonlinear defocusing, but the three-band model used may not be valid in this frequency range. Then a more realistic model including effects of higher bands is needed for accurate predictions.

The frequency dependence of the nonlinear index has not been measured experimentally. A factor of 100 resonant enhancement of three-wave mixing (also obtained from the third-order susceptibility) has been observed in diamond by Levenson et al., [16] when the difference frequency was resonant with the Raman frequency.

Optical distortion from heating of the material by absorbed radiation, which is the dominant mechanism for distortion in cw $10.6 \mu\text{m}$ lasers, is negligible on the 10 nsec time scale of the xenon laser (except for rapidly repeated pulses). The lack of thermal distortion results from the fact that, first, recombination of the electron-hole pairs is negligible on this time scale. Even if the pairs degraded rapidly into heat, there would be no optical distortion since the thermal expansion of the lattice (which dominates dn/dT) is slow.

C. Irreversible Damage Thresholds

Heat generated by two-photon absorption will result in thermal fracture of transparent materials. This will occur on a time scale of microseconds during which the thermal stresses in the material approach their equilibrium values. The previous analysis of Sparks and Chow [17] indicates that a LiF window fractures when the temperature at the center of the window is 7 K greater than at the edge. Using the two-photon absorption coefficient in eq. (3), and allowing for electron-avalanche creation of additional conduction electrons, and Joule heating of these electrons yields a fracture threshold of $I = 1.6 \text{ GW/cm}^2$ for LiF.

Sec. H

The electron-avalanche creation of conduction electrons and Joule heating of these carriers is highly nonlinear [18]. A factor of only three greater irradiance will result in two orders of magnitude greater heating in LiF.

Local fracture from absorbing inclusions, if present, will have the lowest permanent damage threshold. Since absorbing inclusions are expected to absorb at least as much energy in the vuv as in the infrared, the failure power density of 2 J/cm^2 (200 MW/cm^2 with a 10 nsec pulse) observed for many materials in the infrared, is expected to apply in the vuv [19]. This failure mechanism, being extrinsic, can be removed by materials improvement, in principle.

D. Other Failure Mechanisms

In Raman-active crystals, enhanced stimulated Raman scattering can lead to materials damage from heating by phonons created in the scattering process. Sparks has estimated the threshold irradiance of 2 GW/cm^2 for thermal fracture by this mechanism [20]. Of the candidate 7.2 eV window materials, Raman scattering is symmetry allowed in the alkaline-earth halides, but not in the alkali halides.

Another form of optical distortion is nonlinear generation of harmonic frequencies in transparent materials. Frequency doubling occurs in materials lacking a center of inversion which, of the candidate materials, includes only crystalline SiO_2 . Frequency tripling can occur in materials having a center of inversion, but the effects of frequency tripling are expected to be less severe than those from two-photon absorption.

Linear, extrinsic absorption can lead to optical distortion and thermal fracture, as with intrinsic two-photon absorption. The efficiency of generation of conduction electrons by linear, extrinsic absorption is not known. If each photon absorbed generates a conduction electron, it is estimated that an impurity absorption coefficient of $\beta = 0.15 \text{ cm}^{-1}$ will yield an optical distortion threshold of 60 MW/cm^2 . At higher intensities nonlinear mechanisms dominate. An irradiance of $I = 30 \text{ GW/cm}^2$ is required for thermal fracture from extrinsic one-photon heating with $\beta = 0.15 \text{ cm}^{-1}$, compared to $I = 2 \text{ GW/cm}^2$ for two-photon heating.

Such crystalline defects as F centers have been observed to be created by light absorption [21]. It is possible that unavoidable two-photon absorption will create defects, which in turn yield an increasing extrinsic absorption coefficient at 7.2 eV. This remains to be investigated.

4. Summary and Conclusions

The various failure thresholds are presented graphically in figure 6. Unless otherwise noted, these thresholds are most appropriate for a single, 10 nsec duration, xenon-laser pulse in LiF. The mechanism having the lowest threshold of $I = 20 \text{ MW/cm}^2$ is melting of thin-film aluminum mirrors. With transparent materials, the lowest reversible threshold is $I = 140 \text{ MW/cm}^2$ for optical distortion by free carriers created by intrinsic, two-photon absorption. Depending on the efficiency for the creation of free carriers, extrinsic absorption coefficients greater than approximately $\beta = 10^{-1} \text{ cm}^{-1}$ are required for lower optical distortion thresholds. Light absorption is known to create crystalline defects. Two-phonon creation of defects may lead to unacceptably large linear absorption coefficients in aged materials.

The lowest irreversible damage threshold of 200 MW/cm^2 occurs for localized fracture from absorbing inclusions. This mechanism being extrinsic, can be eliminated in principle. The lowest intrinsic threshold results from thermal fracture from two-photon heating and has the threshold of 1.6 GW/cm^2 for LiF. Assuming a comparable two-photon absorption coefficient for other materials, the threshold for thermal fracture is expected to be greater for the materials having greater fracture strengths. The threshold in MgF_2 is estimated as 4 GW/cm^2 . Thermal fracture from an extrinsic absorption coefficient of $\beta = 0.1 \text{ cm}^{-1}$ is negligible compared to that from two-photon absorption.

Sec. H

The threshold of 2 GW/cm^2 for optical distortion from the nonlinear index of bound electrons in LiF is negligible compared to the distortion from free carriers. This mechanism may be dominant in other materials if the laser frequency is adjacent to, but not within, a sharp, strong two-photon absorption line. Another nonlinear mechanism that can lead to failure is enhanced stimulated Raman scattering. In materials with allowed Raman scattering (includes alkaline-earth halides), heating from Raman-created phonons results in fracture at $I = 2 \text{ GW/cm}^2$.

An accuracy of only one order of magnitude is expected for the above thresholds because of an order-of-magnitude uncertainty in the two-photon absorption coefficient. Our present efforts are directed toward a better understanding of the linear optical properties of wide-band-gap materials so that better estimates of two-photon absorption and other nonlinear effects can be made.

5. References

- [1] Rhodes, C. K., IEEE J. Quant. Elect. QE-10, 153 (1974).
- [2] Hughes, W. M., Shannon, J., Kolbi, A., Ault, E., and Bhaumik, M., Appl. Phys. Lett. 23, 385 (1973).
- [3] Hoff, P. W., Swingle, J. C., and Rhodes, C. K., Appl. Phys. Lett. 23, 245 (1973).
- [4] Hughes, W. M., Shannon, J., and Hunter, R., Appl. Phys. Lett. 24, 488 (1974).
- [5] Laser Focus, p. 10, May (1973).
- [6] Feuerbacher, B. P. and Steinmann, W., Opt. Commun. 1, 81 (1969).
- [7] Chow, H. C. and Sparks, M., J. Appl. Phys. 46, 1307 (1975).
- [8] Maradudin, A. A. and Mills, D. L., Phys. Rev. B 11, 1392 (1975); Mills, D. L. and Maradudin, A. A., Phys. Rev., in press.
- [9] Spiller, E., Optik 39, 118 (1973).
- [10] Tomiki, T. and Miyata, T., J. Phys. Soc. Japan 27, 658 (1969).
- [11] Braunstein, R., Phys. Rev. 125, 475 (1962).
- [12] Sparks, M. and Sham, L. J., to be published.
- [13] Hopfield, J. J. and Worlock, J. M., Phys. Rev. 137, A1455 (1965); Frölich, D. and Staginnus, B., Phys. Rev. Lett. 19, 496 (1967).
- [14] Fournier, J. T. and Snitzer, E., IEEE J. Quant. Elect. QE-10, 473 (1974).
- [15] Wang, C. C., Phys. Rev. B 2, 2045 (1970).
- [16] Levenson, M. D., Flytzanis, C., and Bloembergen, N., Phys. Rev. B 6, 3962 (1972).
- [17] Sparks, M. and Chow, H. C., J. Appl. Phys. 45, 1510 (1974).
- [18] Sparks, M., these proceedings, and to be published.
- [19] Sparks, M. and Duthler, C. J., J. Appl. Phys. 44, 3038 (1973); Duthler, C. J., Appl. Phys. Lett. 24, 5 (1974).
- [20] Sparks, M., J. Appl. Phys. 46, 2134 (1975).
- [21] Warneck, P., J. Opt. Soc. Am. 55, 921 (1965).

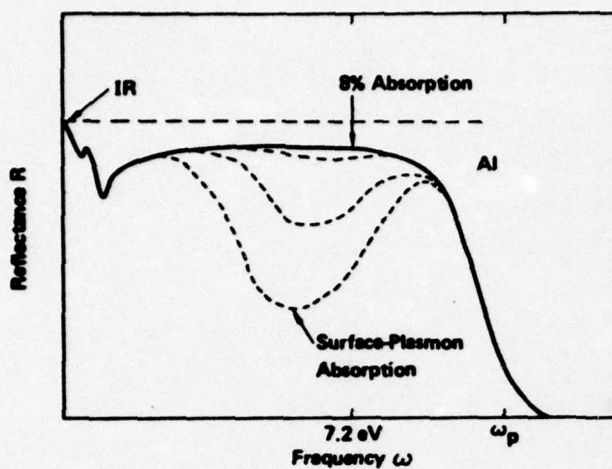


Figure 1. Reflectance of aluminum as a function of frequency. At 7.2 eV, the intrinsic absorptance is 8%. More typically, the absorptance is limited by surface plasmons as shown by dashed curves.

Figure 2. Absorption coefficient of an ionic solid as a function of frequency.

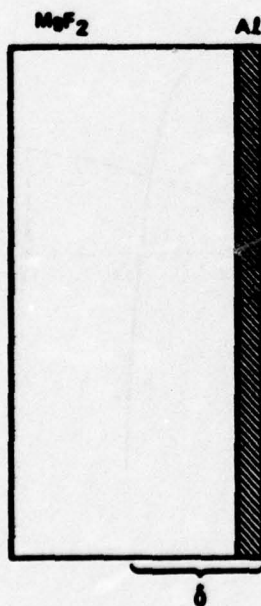
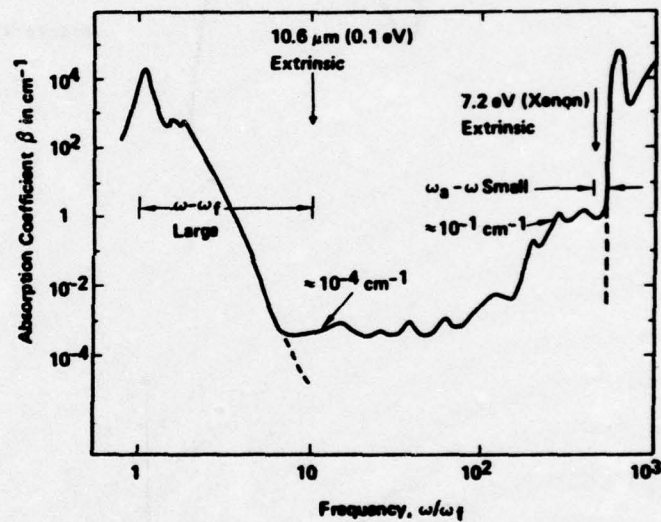


Figure 3. Sketch of aluminum-film laser-cavity mirror. The heat diffusion depth is δ .

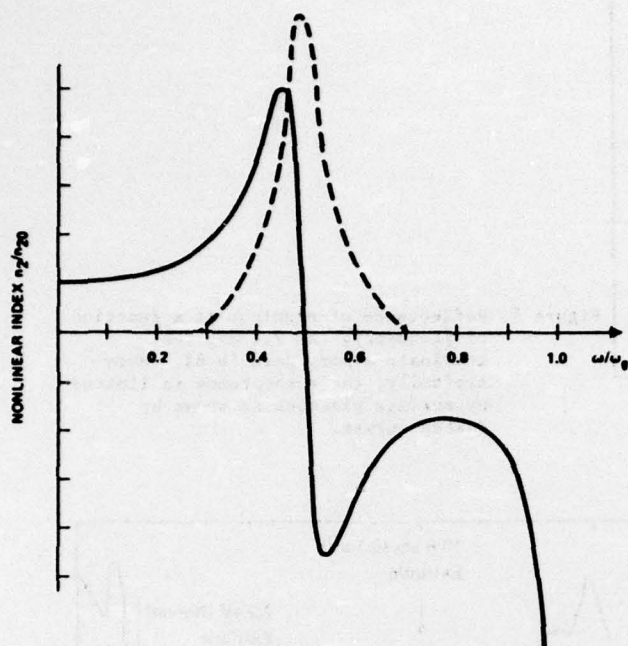


Figure 4. Frequency dependence of the nonlinear refractive index for a solid consisting of molecular oscillators. Two-photon absorption is denoted by dashed curve.

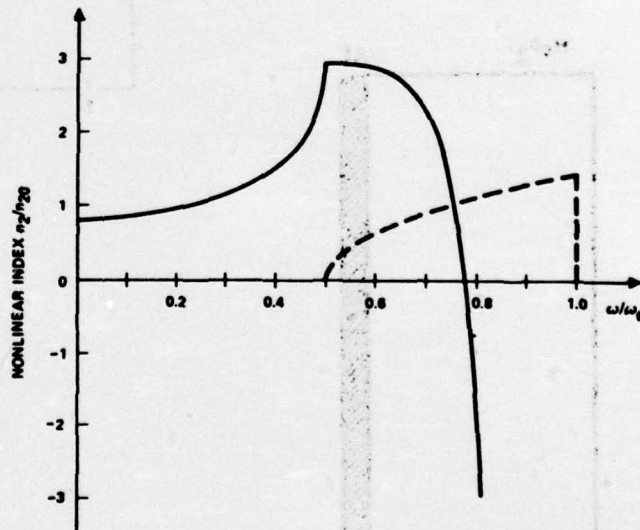
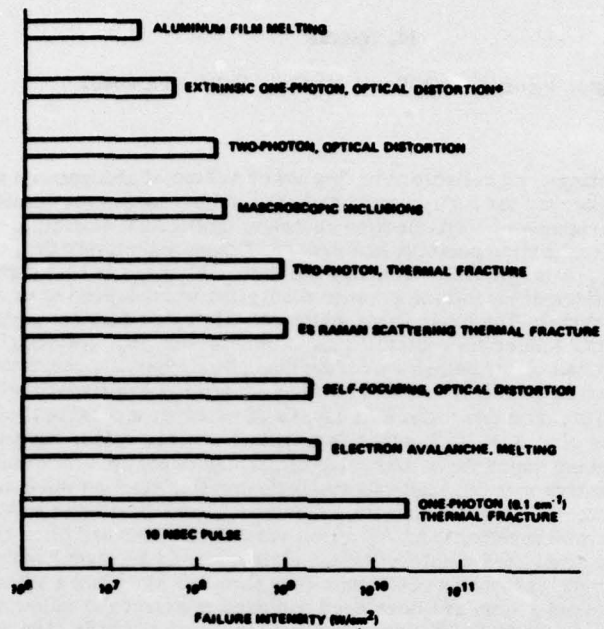


Figure 5. Frequency dependence of the nonlinear refractive index for a broad-band solid, such as LiF. Two-photon absorption is denoted by dashed curve.



*ONLY IF ELECTRONS GENERATED; SEE TEXT.

Figure 6. Failure irradiances for various mechanisms. Except for mirror melting and Raman scattering fracture, these thresholds are most appropriate for a single 7.2 eV xenon-pulse incident on LiF.

I. MATERIALS FOR HIGH-POWER WINDOW AND MIRROR COATINGS AND MULTILAYER-DIELECTRIC REFLECTORS*

M. Sparks

Xonics, Incorporated, Santa Monica, California 90401

Antireflection coatings and reflectors having lower values of absorptance than are presently available are needed for high-power, and even some low-power, applications. Intrinsic values of absorptance of antireflection coatings, multilayer-dielectric reflectors, and metallic-reflection-enhancing coatings are orders of magnitude lower than current experimental values A_{exp} . A major factor limiting the values of A_{exp} is that a given coating material usually has orders of magnitude greater absorption when deposited as a film than when grown as a bulk crystal. The most likely source of this extra film absorptance A_f is contamination of the film. Numerous contaminants include water, HCO_3^- , ClO_3^- , NO_3^- , OH^- , and CN^- . Contamination can occur before or during deposition, upon exposure to the atmosphere (where absorption by porous films and surface adsorption are important), or during use or storage. At $10.6\mu m$ only two molecular layers of water or a packing density of 99.95% are formally required to give $A_f = 10^{-4}$, which is a typical desired value. High-packing-density films should be vacuum vapor deposited using ultraclean deposition conditions including thorough baking of the entire system, high-purity single-crystal starting materials, special care in evaporation, state-of-the-art substrate preparation, and ultrahigh vacuum. Spectroscopic and calorimetric measurements of $A_f(\omega)$ on very thick films and on normal-thickness films, both deposited on attenuated-total-reflection plates, should be made. Material-selection guidelines, including a bulk absorption coefficient less than 0.5 cm^{-1} and a value of the index of refraction in the required range, are developed and used to select the following $10.6\mu m$ candidate materials: ThF_4 , NaF , BaF_2 , SrF_2 , $NaCl$, KCl , $KGaF_4$, As_2S_3 , As_2Se_3 , ZnS , $ZnSe$, and TlI . Distinguishing absorption on the coating surface from that in the bulk of the coatings by utilizing the nearly zero electric field on the surfaces of certain coatings is proposed. Inclusion damage is expected at $\sim 1-10\text{ J/cm}^2$ for nanosecond pulses or ~ 10 to several hundred J/cm^2 for microsecond pulses. Intrinsic damage is expected by heating at $\sim 100\text{ J/cm}^2$ for a $10\mu s$ pulse and $A_f = 10^{-3}$, or by such nonlinear processes as electron-avalanche breakdown at $\sim 10\text{ J/cm}^2$ (i.e. $1 = 10\text{ GW per cm}^2$) for a 10 ns pulse. Strongly absorbing $1\text{-}\mu m$ -radius inclusions spaced $175\mu m$ apart in the coating give rise to absorptance $A_f \approx 10^{-4}$. Thermally induced stresses in a 2 mm -diameter detached film segment may be sufficient to cause additional detachment and a runaway process.

1. Introduction

Deposition of thin dielectric films is of great interest for (1) antireflection coatings, where the reflectance is to be reduced, and for (2) multilayer-dielectric reflectors and (3) metallic coatings, where the reflectance is to be increased. Some high-power systems of current interest cannot be operated without antireflection coatings on the windows. The best uncoated metallic mirrors have high intrinsic values of normal incidence absorptance, ranging from approximately one-half percent at $10.6\mu m$, to approximately two percent at 500 nm , to approximately 10 percent from 400 nm to 100 nm (12.5 eV). Much lower values of absorptance are needed in some high-power systems. By contrast, multilayer-dielectric reflectors (and window and mirror coatings) have much lower intrinsic values of absorptance, probably less than 10^{-8} in many cases, for all wavelengths from the vacuum ultraviolet through the infrared to $\sim 10\mu m$. Since the lowest current experimental values of absorptance are a few times 10^{-4} for window and mirror coatings and multilayer-dielectric mirrors, it is possible that technical improvements in film deposition techniques could result in lower absorptance for all three of the film devices.

In view of the current difficulties in obtaining satisfactory coatings for high-power infrared windows and mirrors, a study of the problems of these coatings was made. [1]¹ The present paper is a summary of the results,

*Prepared for the 8th Annual Symposium on Optical Materials for High Power Lasers, Boulder, Colorado, July 1976

¹Figures in brackets indicate the literature references at the end of this paper.

most of which also apply to multilayer-dielectric reflectors and to wavelength regions other than the infrared. It is emphasized that the study was limited to a near-term program of obtaining coatings in a research-laboratory environment in the shortest period of time for the lowest cost. Fundamental investigations and manufacturing of field-use components were not explicitly included in the study, although it is necessary to keep the ultimate use in mind even during the research-laboratory stage of the investigation.

2. High Absorptance of Films

In addition to the already stringent requirements of coatings for low-power use, the high-power coatings must have low optical absorptance. Required values for the film absorptance per surface A_f have not been established for any of the major systems of interest. A typical desired value is $A_f = 10^{-4}$, which is chosen to make the absorptance of two coated surfaces equal to that of the window for the typical case of a 2 cm-thick window with absorption coefficient $\beta_b = 10^{-4}$. The value of the film absorption coefficient β_f corresponding to $A_f = 10^{-4}$ and a typical thickness of 2 μm is $\beta_f = 0.5 \text{ cm}^{-1}$. Since much greater values of absorption coefficient can be tolerated in the film ($\sim 0.5 \text{ cm}^{-1}$) than in the bulk ($\sim 10^{-4} \text{ cm}^{-1}$), it would appear that obtaining materials for films should be much easier than for windows. However, the absorption coefficient of a given material usually is much greater when deposited as a thin film than when grown as a bulk crystal. As a typical example a material with a bulk value of $\beta_b = 10^{-4} \text{ cm}^{-1}$ may have a film value of $\beta_f = 10 \text{ cm}^{-1}$. This much greater absorptance in film form than in bulk form is one of the most serious coatings problems, though by no means the only one.

In general the source of the extra absorptance in films is not known. It is suggested that contamination of the film is by far the most likely candidate for explaining this extra absorptance. Water is the most important contaminant for the 2 to 15 μm wavelength region, but there are many others. The contamination can be in the bulk of the film, adsorbed on the surface of the film, or in pores in the film. The contamination can occur during deposition, from the residual gas for example, after deposition, by surface adsorption or by absorption into the pores for example, or before deposition, by substrate contamination for example.

As seen in figure 1a, liquid water absorbs strongly from 2 μm through 15 μm . The absorption coefficient at 10.6 μm is $\sim 10^3 \text{ cm}^{-1}$, and the values at the other prominent laser frequencies are shown by the vertical lines. In passing notice that this top figure illustrates the invalidity of the myth that the frequency must be near an absorption line in order to have great absorptance. From ~ 6.5 to $10.5 \mu\text{m}$ there is very little structure in the absorption spectrum, but the absorption coefficient has the very large value of 10^3 cm^{-1} . The broad absorption from ~ 11 to $15 \mu\text{m}$ results from the hydrogen-hydrogen interactions in the liquid water, and this absorption is missing in the water-vapor spectrum, which is shown in figure 1b. In fact, careful measurements [3] indicate that the absorption coefficient of water vapor at 10.6 μm may be orders of magnitude smaller than that of liquid water.

For adsorbed water, only 1 nm is required formally (using $\beta = 10^3 \text{ cm}^{-1}$ for liquid water) to give 10^{-4} absorptance. Pores in films are known to readily absorb water from the atmosphere on removal from the vacuum-deposition chamber, and a fraction of 5×10^{-4} of pores filled with water formally gives an absorptance of 10^{-4} .

At 10.6 μm , molecules containing O_3 are particularly offensive since they usually absorb near 10.6 μm . There are many known molecules that are strongly absorbing in the infrared. Deutsch [4] observed molecular absorption on sample surfaces in attenuated-total-reflection studies. Duthler [5] showed that molecular-ion absorption was an important source of bulk absorption, pointed out the relation to matrix-isolation spectroscopy studies, and catalogued strongly absorbing molecular ions. Phil Klein [6] has argued that molecules containing carbon probably cause a wide absorption band extending from ~ 2 to $\sim 5 \mu\text{m}$.

There are absorption bands of molecules and molecular ions extending throughout the range from 2 to 12 μm as seen in figure 2. These and other film contaminants include the following:

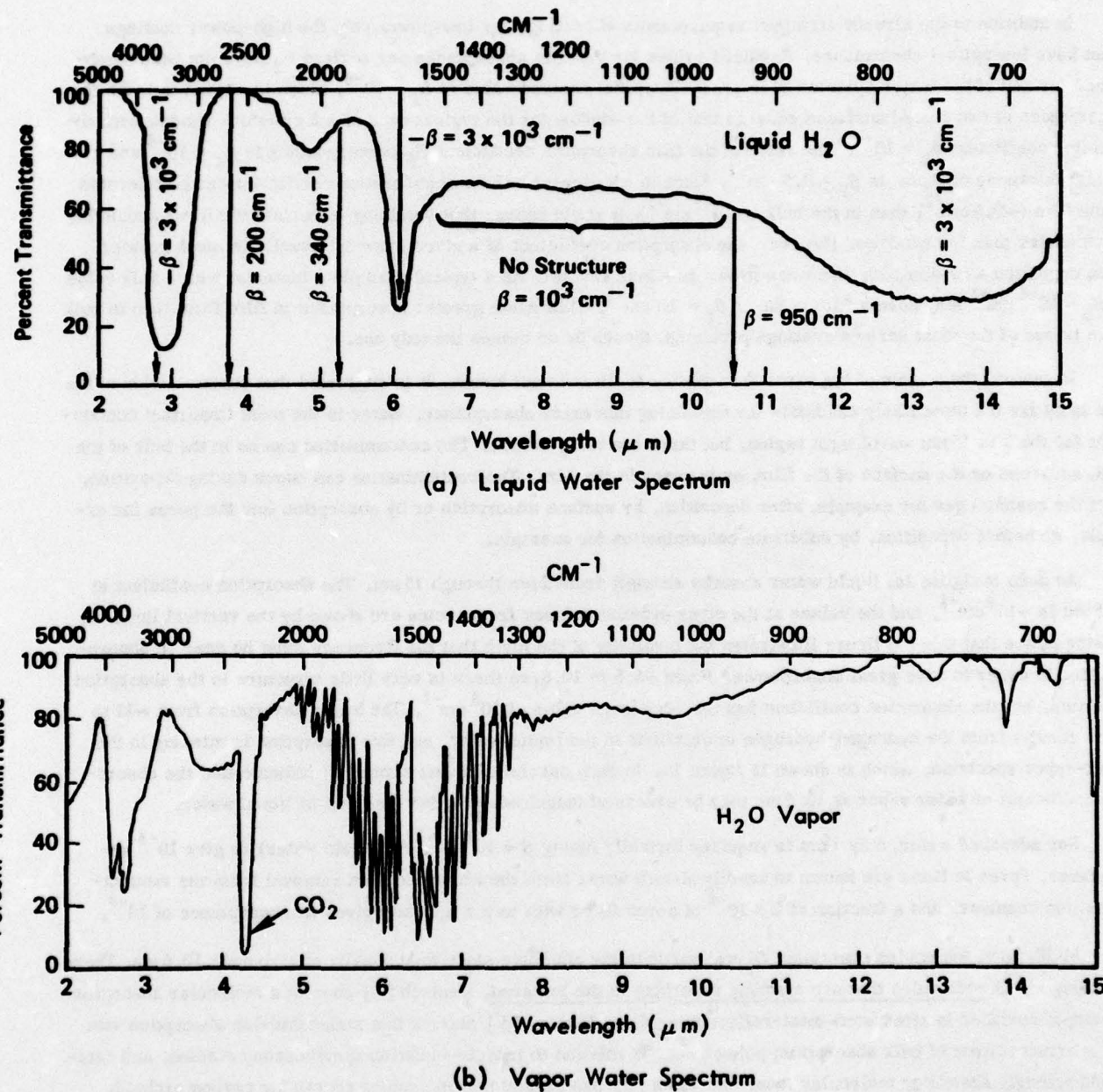


Fig. 1. Transmission spectra of (a) liquid water and of (b) water vapor.
From Ref. 2.

Sec. I

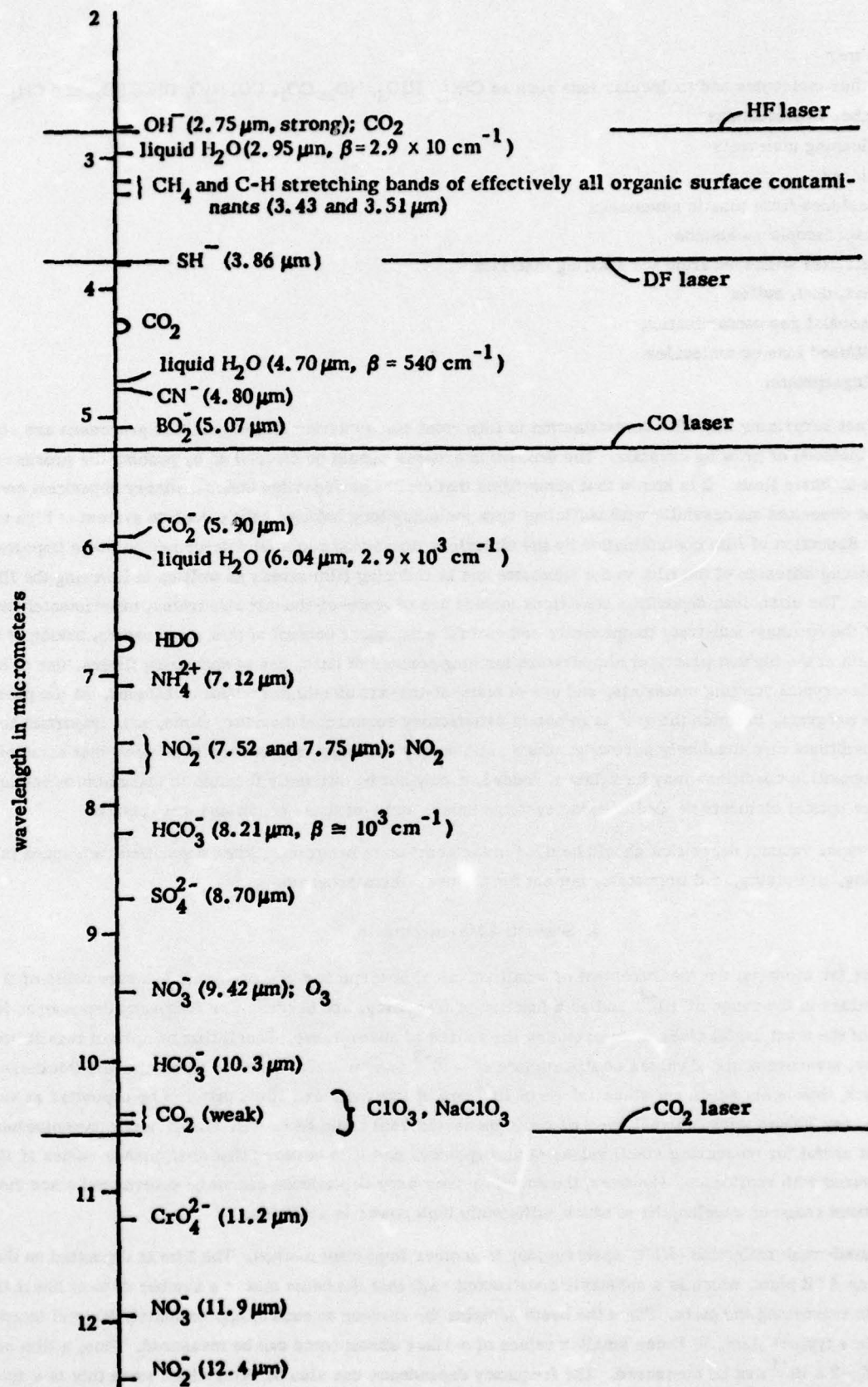


Fig. 2. Positions of absorption peaks of some possible coating contaminants.

Sec. I

- Water
- Other molecules and molecular ions such as CHO_3 , ClO_3 , NO_2 , CO_2 , CO , N_2O , DHO , SO_4 , and CH_4
- Other hydrocarbons
- Cleaning materials
- Rinses
- Residues from plastic containers
- Macroscopic inclusions
- Particles spattered from the starting material
- Dirt, dust, pollen
- Residual gas contamination
- Diffused ions or molecules
- Fingerprints.

It is not surprising that film contamination is important since current film-deposition processes are simply very dirty methods of growing crystals. The deposition process should be cleaned up by pushing the process to the current ultimate limit. It is known that some films that cannot be deposited under ordinary deposition conditions can be deposited successfully with sufficient care including long baking of the complete system at high temperatures. Reduction of film contamination by the ultraclean deposition conditions described below is important in obtaining strong adhesion of the film to the substrate and in reducing film stress as well as in lowering the film absorptance. The ultraclean deposition conditions include use of state-of-the-art substrates, experimental determination of the optimum substrate temperature and careful subsequent control of this temperature, baking of the entire system at the highest practical temperature for long periods of time, use of spattering filters, use of high-purity single-crystal starting materials, and use of state-of-the-art ultrahigh vacuum techniques. At the present stage of the program, in which the goal is to obtain satisfactory research-laboratory films, it is important to have all these conditions met absolutely perfectly. Once satisfactory coatings are obtained it is hoped that some of the stringent deposition conditions may be relaxed. Indeed, it may not be currently feasible to manufacture coatings for the large optical elements needed in some systems unless some of these conditions are relaxed.

Only vapor vacuum deposition should be used in the near-term program. Other deposition techniques may be interesting, promising, and important, but not for the near-term program.

3. Suggested Measurements

Just as for windows, the measurement of small values of absorptance is a problem. Measurements of absorptance values in the range of 10^{-4} , and as a function of frequency, are needed. The frequency dependence is of course one of the most useful clues in determining the source of absorptance. Recall that by normal transmittance spectroscopy, measurements of values of absorptance of $\sim 10^{-2}$ can be made. For the films of usual thickness, say $2\text{ }\mu\text{m}$ thick, this is not sufficient since values of 10^{-4} are of interest. For films that can be deposited as very thick layers, say $200\text{ }\mu\text{m}$ thick, normal spectroscopic measurements could be useful. Calorimetric measurements are the most useful for measuring small values of absorptance, and it is believed that absorptance values of 10^{-4} can be measured with confidence. However, the complete frequency dependence cannot be determined since there is not a continuous range of wavelengths at which sufficiently high power is available.

Attenuated-total-reflection (ATR) spectroscopy is another important method. The film is deposited on the surfaces of an ATR plate, which is a substrate constructed such that the beam makes a number of total internal reflections in traversing the plate. Since the beam samples the surface at each of approximately 50 total internal reflections in a typical plate, 50 times smaller values of surface absorptance can be measured. Thus, a film absorptance of $\sim 2 \times 10^{-4}$ can be measured. The frequency dependence can also be determined since this is a spectroscopic measurement. The main difficulty is in interpreting the experimental results, and in particular in obtaining the numerical value of the absorptance.

Sec. I

Figure 3a is an illustration of the liquid-water absorption spectrum for a water-contaminated thorium-tetra-fluoride film deposited on a zinc-selenide ATR plate. This spectrum leaves little doubt that there is water contamination in this sample. Figure 3b illustrates one of the difficulties in extracting the value of film absorptance from the curves and in interpreting the ATR spectrum results in general. Here the transmittance increased when the film was deposited. Thus, even a rough estimate of the absorptance cannot be obtained.

An important factor that has not been emphasized in previous ATR measurements of film absorptance is that the angle of the ATR plate should be adjusted for the particular film-substrate combination, rather than using such a fixed angle as 45 degrees for all measurements. A simple calculation illustrates that for barium fluoride the index of refraction is very close to the value at which total internal reflection occurs for a 45 degree plate. In fact at a wavelength value near $5\text{ }\mu\text{m}$ the index of barium fluoride drops to the value at which total internal reflection is no longer possible, and some leakage out of the ATR plate is expected. It seems likely that the reduction in transmittance from approximately 4 to $8\text{ }\mu\text{m}$ in figure 3b is due to this lack of total internal reflection.

In general the total internal reflection can occur either at the surface of the film or at the interface of the film and the substrate. The angle of the ATR plate should be chosen such that the total internal reflection is at the film surface in order to give the greatest electric field and the greatest absorptance in the film. The conditions on the angle, which are easy to derive and are discussed elsewhere, [1] are as follows: For the case of $n_f > n_s$, where n_f is the index of refraction of the film material and n_s is the index of refraction of the substrate, total internal reflection is possible only at the film surface. In this case the ATR plate angle θ must satisfy the inequality $\theta > \sin^{-1}(1/n_s)$, which is the general condition for total internal reflection (for arbitrary values of n_s and n_f). For the case of $n_f < n_s$, total internal reflection is possible at either the film surface or at the substrate-film interface. As mentioned above, in order to have the maximum absorptance in the film the total internal reflection should occur at the film surface. This requires that θ satisfies the double inequality $\sin^{-1}(1/n_s) < \theta < \sin^{-1}(n_f/n_s)$.

There is a possibility of distinguishing between absorption on the surface of the film, at the film-substrate interface, or in the bulk of the film. The reason is that at the surface of a metal the electric field is very small, as illustrated schematically in figure 4. For a dielectric coating that is one-half of an optical wavelength thick, the electric field is also nearly equal to zero on the outside surface of the coating. For a quarter-optical-wavelength-thick dielectric coating the electric field has a large value at the surface, and for a dielectric coating deposited on a dielectric substrate the electric field is not equal to zero at either the interface or the surface. Thus, by measuring the absorptance under various conditions it is possible in principle to distinguish between absorption at the interface, absorption at the surface of the film, and absorption in the bulk of the film. In particular, distinguishing optical absorption by adsorbed layers from that by other sources should be possible. Either ATR or calorimetric measurements could be used.

This measurement technique is included in the category of measurements which are interesting, but not for the near-term program. There are many promising methods of measuring absorptance including ellipsometry, emissivity, surface acoustical-wave-type measurements, low-temperature measurements, alpha phones, and a number of others. Even the simplest sounding of these methods has turned out in the past to be technically difficult, and the development of new measurement techniques should not be included in the near-term program.

4. Material Selection Guidelines and Suggested Materials

Since there are no coatings available with $A_f = 10^{-4}$ for any of the infrared frequencies of interest and only a small handful of coating materials have been investigated, it is important to select new candidates with the highest probability of success. For window materials, values of the total power through a window under various conditions were convenient figures of merit. [8, 9] The dependence $P(\beta, \sigma, C, K, \dots)$ of the power P , calculated by making simplifying assumptions, on such parameters as the absorption coefficient β , material strength σ , heat capacity C , and thermal conductivity K clearly shows the relative importance of these parameters. For example, diamond is a

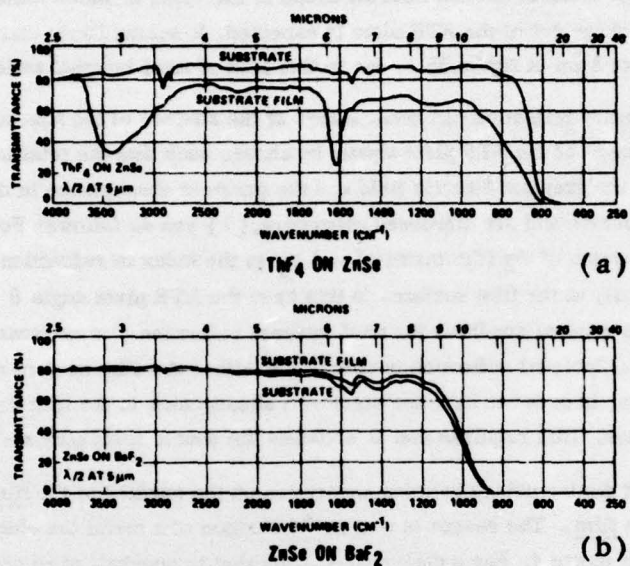


Fig. 3. Attenuated-total-reflection spectra, from Ref. 7. (a) This ATR spectrum for a ThF_4 coating deposited on a ZnSe substrate clearly shows the spectrum of contaminating water. (b) This ATR spectrum of ZnSe on BaF_2 illustrates the difficulty of interpreting ATR-spectrum results (an apparent increase in transmittance when the coating was deposited) and illustrates a decrease in transmittance with increasing wavelength, probably resulting from a lack of total internal reflection.

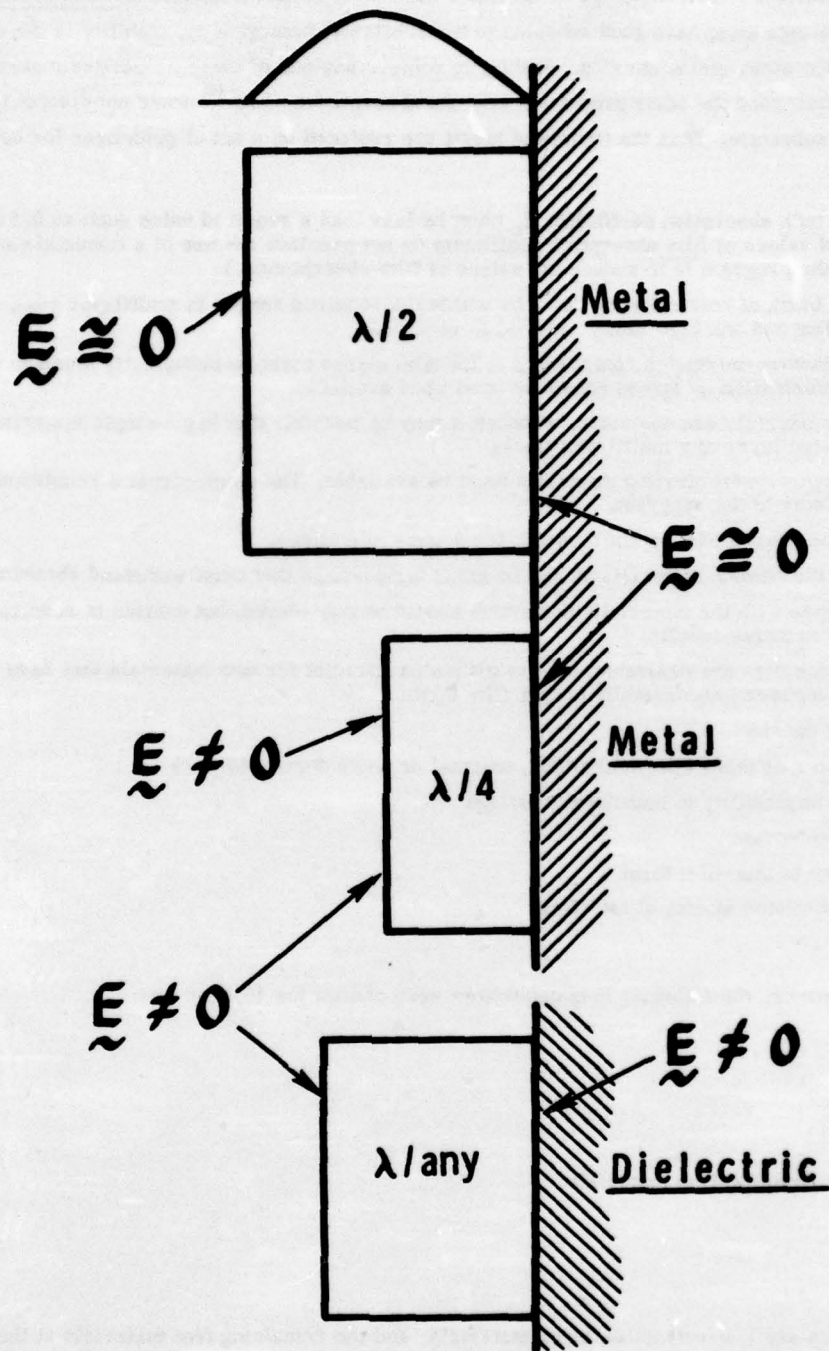


Fig. 4. Schematic illustration of coatings used to distinguish between absorption at the film surface, in the bulk of the film, and at the film-substrate interface.

Sec. I

good material in some applications because its great strength and thermal conductivity more than compensate for its high $10.6\text{ }\mu\text{m}$ absorption coefficient. Coatings on the other hand must satisfy a number of independent requirements. For example, coatings must have good adhesion to the substrate, homogeneity, stability in the atmosphere, and low absorptance, reflectance, and scattering. Failure to achieve any one of these properties makes the coating unacceptable, no matter how good the other properties are. An absorptance of 10^{-10} would not compensate for the inability to adhere to the substrate. Thus the figures of merit are replaced by a set of guidelines for selecting candidate materials:

- The value of the bulk absorption coefficient β_b must be less than a required value such as 0.5 cm^{-1} . (Large measured values of film absorption coefficient do not preclude the use of a material since a major goal of the program is to reduce the values of film absorptance.)
- The value of the index of refraction n_r must be within the required range. In multilayer coatings, at least one low-index and one high-index material is required.
- The thermal-expansion-mismatch contribution to the film stress must be sufficiently small to prevent failure. Other information on stress should be used when available.
- Nonhygroscopic materials are desirable, although it may be possible that hygroscopic materials can be used as an inside layer of a multilayer stack.
- High-purity, single-crystal starting materials must be available. The single-crystal requirement may be relaxed later in the program.
- Materials must be nonradioactive and nontoxic for some applications.
- The hardness of the outside materials should be great for coatings that must withstand abrasion.
- Previous experience with the materials in question should be considered, but caution is required to avoid misleading negative results.
- The following properties are desirable, but are difficult to predict for new materials that have not been previously deposited successfully in thin-film form:

film packing density
stability (water or other chemical attack, thermal or photo decomposition)
deposition compatibility in multilayer coatings
adhesion to substrate
stoichiometry in thin-film form
no adverse diffusion effects at interface
homogeneity.

By using these guidelines, the following best candidates were chosen for $10.6\text{ }\mu\text{m}$ use:

- ThF_4
- $\text{Na}(\text{F}, \text{Cl})$ [10]
- KCl
- $(\text{Ba}, \text{Sr})\text{F}_2$
- KGaF_4 and other Cryolite-type materials
- $\text{As}_2(\text{S}_3, \text{Se}_3)$
- $\text{Zn}(\text{S}, \text{Se})$
- TiI_3 .

The fluorides and chlorides are low-refractive-index materials, and the remaining five materials at the bottom of the list are high-index materials. These candidates are discussed, and a list of other good candidate materials and a preliminary discussion of materials for use at 2 to $6\text{ }\mu\text{m}$ are given elsewhere. [1]

Of the unacceptable and unlikely candidates for $10.6\text{ }\mu\text{m}$ coatings, the following are important: Materials containing the light elements H, He, Li, Be, C, N, and O. The light masses are expected to give rise to a fundamental resonance too near $10.6\text{ }\mu\text{m}$, making $\beta_b > 0.5\text{ cm}^{-1}$. Note that the vast number of materials containing oxygen and carbon are expected to be unsatisfactory. Many oxides are known to have $\beta_b > 0.5\text{ cm}^{-1}$ at $10.6\text{ }\mu\text{m}$. Although it is not certain that some oxides and carbon-containing materials will not have a sufficiently low absorption coefficient, the generally high absorption at $10.6\text{ }\mu\text{m}$ of these materials make them less likely candidates.

The absorption coefficients of the fluorides are marginal. Fluorides that are known to have too great absorptance at $10.6\text{ }\mu\text{m}$ include LiF , $(\text{Ca, Mg})\text{F}_2$, AlF_3 , and NaAlF_4 (cryolite). Potassium fluoride is more hygroscopic than KCl or KBr . Lead fluoride would have to be deposited with greater packing density than that which has been obtained previously (0.9). Thallium fluoride is a less desirable candidate since thallium is toxic. The rare-earth fluorides ($\text{Ce, La, Nd, Pr, Yb}\text{F}_3$) probably will not have $\beta_f < 0.5\text{ cm}^{-1}$, although this is not certain. Other unlikely and unacceptable materials are listed elsewhere. [1]

5. Protective Coatings

Protective coatings for such hygroscopic window and coating materials as alkali halides have been discussed in the literature for some time. [11] In addition to the prevention of water-vapor penetration, it may become extremely important to develop a thin coating to reduce adsorption of water and other contaminants on the surface of optical components. It was shown [1] that information in the literature suggests the following results: (a) It is not likely that polycrystalline films can protect large areas of alkali halides from moisture attack. [11] (b) It is possible, though not certain, that polycrystalline films can be sufficiently dense and sufficiently hydrophobic to allow $A_g = 10^{-4}$ to be attained in carefully prepared films. [11] (c) Very thin glassy films were found not to protect alkali halides. [11] (d) Thick glassy films, say $1\text{ }\mu\text{m}$ thick on well polished substrates, did protect alkali halides. However, on long exposure to humidity, moisture attack that started at the edges of the sample eventually covered the entire substrate under the coating. [11] (e) Polymer films will be considered further in order to determine the possibility of their providing sufficient moisture protection in spite of the known great moisture vapor transmission rates and to determine the possibility of reducing their normally great optical absorption to acceptably low values. (f) The possibility of using very thin polymer films as hydrophobic outside layers over antireflection coatings to reduce adsorption on the surface will also be investigated. (g) Priority of future research on such amorphous semiconductors as germanium is low since the likelihood of obtaining β_f less than 0.5 cm^{-1} is small.

The main concern about polymer coatings in the past was that of obtaining pin-hole-free coatings in order to prevent moisture attack of the underlying antireflection coating or substrate. This is indeed important since it is known that moisture will attack underlying substrates through pin holes in polymer films. Unfortunately, in addition to this technical problem there are two fundamental properties of polymer films that possibly could prevent their use as moisture-protection films.

First, the rate at which moisture vapor permeates through a polymer is one of the routinely measured properties of polymers. Formally using the measured values of this moisture-vapor transmission rate through unsupported (i.e., not deposited on substrates) polymer films suggests that pin-hole-free polymer films would not be useful in preventing water from penetrating through the polymer to a substrate or an antireflection coating. However, the moisture-vapor transmission rate could be drastically different for a polymer deposited on a solid from that of an unsupported polymer film. The results from the literature and from workers in the field are conflicting, in some cases suggesting that moisture-vapor protection is possible and in other cases suggesting that it is not. We suspect that inhibition of the moisture-vapor transmission at the polymer-substrate interface is important if polymers do indeed provide sufficient moisture-vapor protection.

In considering the problem of moisture-vapor transmission through polymer coatings, it must be recalled that these coatings are extremely thin and that only two monolayers of water transmitted through the film could cause unacceptably great optical absorptance. According to available data, absorption of water by plastic films (as opposed to water-vapor transmission through the films) probably will be tolerable at $2.8, 3.8, 5.3$, and $10.6\text{ }\mu\text{m}$.

The second fundamental problem with polymer coatings is that the published infrared spectra of all polymers that we have found to date show values of absorptance that are too great to allow $A_g = 10^{-4}$ for either antireflection coatings or for very thin protective coatings. Professor M. Shen and coworkers at the University of California at Berkeley have deposited polyethane coatings by a plasma deposition method which is believed to give pin-hole-

Sec. I

free coatings. [12] Measurements of the absorption coefficient of these coatings made at the Hughes Research Laboratory gave values of $\beta_f = 3-7 \text{ cm}^{-1}$. Shen and coworkers plan to reduce the contamination of the film in the hopes of reducing this value of the film absorption coefficient.

6. Stresses

The stress in a thin film is believed to consist of three components, one from the mismatch of the thermal expansion coefficient of the film and the substrate, one from contaminants in the film, and one from an intrinsic contribution. The contribution from the mismatch of the thermal expansion coefficient is well understood, and very simple calculations give the observed values of this component of stress. For any proposed film-substrate combination this thermal-expansion mismatch component of stress should be calculated in order to determine if the film can withstand this stress. Examples are given in the complete report. [1] Unfortunately, the thermal-expansion mismatch contribution to the stress is often less than that of the other two contributions.

Film contamination typically leads to compressive stresses. Campbell [13] states that, "In impure films in which oxygen and other materials are incorporated into the structure during growth, the resultant stresses are usually sufficiently high to overshadow any of the "pure film" effects. The stresses are then usually compressive, at least in the initial stages of growth and provided that the reacting species migrate through growing film to the interface. Compressive stresses are observed in thermally grown, anodized, and certain sputtered and evaporated films. If the ion migration takes place from the interface to the film surface, tensile stresses will be observed." Of great importance for the power of stress are the packing density and the water vapor absorption. During exposure to atmosphere very often a stress relief takes place.

The intrinsic contribution to the stress in a film is not well understood. It is not possible to predict in advance what the stress will be in a new film material on a given substrate. However, for film materials that have been previously deposited it is possible to predict with a fair degree of success what the stress will be for a given film-substrate combination or for a particular multilayer coating on a given substrate.

7. Laser Heating and Damage

There are three damage or failure regimes of interest in general. The first is damage or optical distortion resulting from heating by ordinary linear absorption in the coating. The second is the absorption by macroscopic imperfections such as inclusions. It is well known that inclusions are extremely important in laser damage under short-pulse operation. It has also been pointed out [14] that inclusions can increase the average heating in addition to causing the well known damage. The absorption can, in general, be linear or nonlinear. The third is the intrinsic nonlinear damage mechanism such as electron-avalanche breakdown.

The results of the heating and damage studies are very briefly as follows:

- For $2A_f = A_b = 2 \times 10^{-4}$, the film and bulk contributions to the spatial average of the window temperature, which determines the thermally induced optical distortion, are equal and have a typical value $T_{\text{tot}} = 1.0 \text{ K}$, which is sufficient to cause thermally induced optical-distortion failure in some cases.
- In a typical system with repeated short pulses, only the time-average heating need be considered (apart from inclusion damage, nonlinear effects and possible more stringent conditions of future systems).
- The linear absorption (below the damage threshold) by strongly absorbing ($\sigma_{\text{abs}} = \pi a^2$) one-micron-radius inclusions with an average spacing of $175 \mu\text{m}$ gives rise to absorptance $A_f = 10^{-4}$.
- Inclusion damage is expected to occur at energy densities $It_p \approx 1-10 \text{ J/cm}^2$ for nanosecond pulses or at $It_p \approx 10$ to several hundred joules per square centimeter for microsecond pulses. In principle, values of $It_p < 1 \text{ J/cm}^2$ are possible for nanosecond through microsecond pulses.
- Intrinsic damage of coatings is expected to occur at $It_p \approx 10^3 \text{ J/cm}^2$ for a pulse of duration $t_p = 10 \mu\text{s}$ and $A_f = 10^{-3}$ as a result of linear heating of the coating, or at $It_p \approx 100 \text{ J/cm}^2$ (or $I \approx 10 \text{ GW/cm}^2$) for a 10 ns pulse of ~ 1 to $10 \mu\text{m}$ radiation as a result of electron-avalanche breakdown or perhaps another nonlinear process.

Sec. I

- The calculated value of 25 K temperature rise for a detached film segment of diameter $D = 2$ mm under continuous illumination at 10^3 W/cm² and $A_f = 10^{-4}$ is surprisingly small.
- The temperature is proportional to D^2 for a detached segment.
- The thermally induced stress corresponding to $T = 25$ K has a typical value of 20 MPa (3×10^3 psi), which may be sufficient to cause further detachment, then further temperature increase since $T \sim D^2$, and possibly a runaway condition resulting in damage.

In pulsed operation, for short pulse durations $t_p \ll \tau_f$, where $\tau_f = C L_f^2 / 4K$ has a typical value of $0.4 \mu s$, the detachment causes little additional temperature rise since thermal diffusion into the substrate already was negligible. For values of energy density near the threshold for failure (of the undetached areas of the film), the size of the detached area probably will be increased, and various types of fracture both in and out of the plane of the film could cause failure, especially in subsequent pulses.

For very long pulse durations $t_p \gg \tau_D$, where $\tau_D = C(D/2)^2 / 4K$ has a typical value of 2.5×10^{-2} s for detached diameter $D = 1$ mm, the above steady-state results are approached. For intermediate pulse durations $\tau_f < t_p < \tau_D$, the detachment causes a greater temperature rise $T = IA t_p / CL_f$ than the corresponding value $T = IA t_p / CL_{z=0}$, with $L_{z=0} = (\pi K t_p / 4C)^{1/2}$, for unimpeded thermal diffusion into the substrate.

8. Acknowledgements

In preparing the report of which the present paper is a summary, comments were solicited from a representative sample of active workers in the field of coatings for high-power infrared optics. I am indebted to a number of people for a great amount of assistance, and I deeply appreciate the time and effort they have contributed. At the beginning of the program the current status of coatings of high-power infrared materials was discussed with the following investigators: Dr. R. R. Austin, Dr. H. E. Bennett, Dr. E. Bernal G., Mr. A. Braunstein, Mr. M. Braunstein, Dr. T. F. Deutsch, Dr. T. M. Donovan, Dr. C. J. Duthler, Dr. S. Geller, Dr. A. J. Glass, Dr. M. Hass, Dr. A. R. Hilton, Dr. T. D. Holstein, Dr. J. Kershenstein, Dr. G. E. Kuhl, Dr. J. R. Kurdock, Dr. J. Lehman, Dr. J. H. Marburger, Dr. D. Milam, Dr. P. A. Miles, Dr. T. Norwood, Dr. H. Posen, Dr. G. Ruse, Mr. C. S. Sahagian, Dr. M. Shen, Maj. J. L. Stapp, Dr. C. M. Stickley, Dr. L. Van Ultert, Dr. B. L. Weigand, Dr. R. W. White, and Capt. H. V. Winsor.

I want to thank the following for their comments on a preliminary draft of the report: [1] Dr. R. R. Austin, Dr. E. Bernal G., Mr. A. Braunstein, Dr. T. M. Donovan, Dr. M. Hass, Dr. L. P. Mott, and Dr. H. Posen. Dr. Guy Ruse, University of Colorado, stressed the importance of thorough baking of the entire system and pointed out that this was essential in attaining stable films of certain compounds.

9. References

- [1] Sparks, M., Xonics, Inc. Sixth Technical Report, Contract DAHC15-73-C-0127, December (1975).
- [2] Sadtler Standard Infrared Prism Spectra, Midget Edition (Sadtler Research Labs, Philadelphia, Pa., 1959).
- [3] CRC Handbook of Lasers with Selected Data on Optical Technology, ed. R. J. Pressley (Chemical Rubber Co., Cleveland, Ohio, 1971).
- [4] Deutsch, T. F., J. Electron. Mats. 4, 663 (1975).
- [5] Duthler, C. J., J. Appl. Phys. 45, 2668 (1974); Proceedings of 4th Annual Conference on Infrared Laser Window Materials, Tucson, Ariz., Nov. 18-20, 1974 (January 1975).
- [6] Klein, P., this proceedings (to be published).
- [7] Willingham, C., Bua, D., Statz, H., and Horrigan, F., Raytheon Research Division Final Technical Report, Contract DAAH01-74-C-0719, August (1975).
- [8] Horrigan, F., Klein, C., Rudko, R., and Wilson, D., Microwaves 8, 68 (1969).
- [9] Sparks, M., J. Appl. Phys. 42, 5029 (1971).
- [10] Such symbols as Na(F, Cl) denote the set of materials NaF and NaCl.
- [11] Young, P. A., Thin Solid Films 6, 423 (1970).
- [12] Reis, T. A., Hirsuka, S., Bell, A. T., and Shen, M., this proceedings (to be published).
- [13] Campbell, D. S. in Handbook of Thin Film Technology, ed. L. L. Maissel and R. Glang (McGraw-Hill, New York, 1970).
- [14] Duthler, C. J. and Sparks, M., J. Appl. Phys. 44, 3038 (1973).